

SIMRAC

D R A F T

Final Project Report

**Title: SEISMOLOGY FOR ROCKBURSTS
PREVENTION, CONTROL AND
PREDICTION**

**Authors: A J Mendecki; A van Z Brink; R W E Green;
P Mountfort; A Dzhafarov; J Niewiadomski;
A Kijko; M Sciocatti; S Radu;
G van Aswegen; P Hewlett; E de Kock;
T Stankiewicz;**

**Research
Agency: ISS International Limited**

**Project No: GAP 017
Date: April 1996**

CONTENTS

SUMMARY

CHAPTER 1 Characteristics of Seismic Monitoring Systems for Mines

- 1.1 Transducers
- 1.2 Data Transmission
- 1.3 Data Acquisition in a Distributed System
- 1.4 Central Control Site

CHAPTER 2 Configuration and Sensitivity of Seismic Networks

- 2.1 Optimum Spatial Distribution of Seismic Stations
- 2.2 Maps of Expected Location Error and Sensitivity
- 2.3 Quality Index for Configuration of Seismic Stations

CHAPTER 3 Location of Seismic Events and Velocity Inversion

- 3.1 Location of Seismic Events
- 3.2 L_1 Adaptive Norm and Simplex Minimization Procedure
- 3.3 Velocity Inversion
 - 3.3.1 Travel Time Equations and Solution

CHAPTER 4 Seismic Raytracing

- 4.1 Shooting and Bending
- 4.2 Point-to-curve
- 4.3 Finite-difference
- 4.4 Wavefront Construction

CHAPTER 5 Seismic Wave Attenuation and Site Effect

- 5.1 Attenuation and Site Effect
- 5.2 Applications

CHAPTER 6 Source Parameters

- 6.1 Finding the Arrival Time and Rotation of the Seismogram
- 6.2 Spectral Analysis
- 6.3 Moment Tensor
- 6.4 Spectral Source Parameters

CHAPTER 7 Statistical Analysis of Seismicity

- 7.1 Gutenberg-Richter Relation
- 7.2 Integrated Volume of Ground Motion
- 7.3 Space-Time Clustering of Seismicity
- 7.4 Probability Model for Seismic Event Occurrence Based on Temporal Variations of Stress-Strain Release
- 7.5 Probability Model for Seismic Event Occurrence Based on Fractal Formalism
 - 7.5.1 Building the model
 - 7.5.2 Fractal based parameterization of the model
 - 7.5.3 Parameters estimation
- 7.6 Correlation Between Seismicity in Adjacent Mining Areas
- 7.7 Significance of Difference
 - 7.7.1 Two random variables
 - 7.7.2 Difference in relation to average

CHAPTER 8 Limits of Predictability

- 8.1 Phase Space
- 8.2 Reconstruction of the Phase Space from Seismic Data
- 8.3 Fractal Correlation Dimension
- 8.4 Numerical Results
- 8.5 Lyapunov Exponent and Limits of Predictability

CHAPTER 9 Quantitative Seismology and Rock Mass Stability

- 9.1 Seismic Moment, Source Size and Stress Drop
- 9.2 Seismic Energy
- 9.3 Apparent Stress and Energy Index
- 9.4 Source Volume, Clustering of Sources and Seismic Damage
- 9.5 Seismic Strain and Seismic Stress
- 9.6 Seismic Softening
- 9.7 Seismic Viscosity and Deborah Number
- 9.8 Seismic Diffusion
- 9.9 Seismic Schmidt Number
- 9.10 Unstable Deformation and Unstable System
- 9.11 Nucleation of Instability
- 9.12 Phenomonological Model and Time to Failure

CHAPTER 10 Application of Quantitative Seismology in Mines

10.1 Introduction

10.1.1 From micro tremors to earthquakes

10.1.2 The purpose of seismic monitoring in mines

10.2 Criteria for the Recognition of Potential Instabilities

10.2.1 Stress

10.2.2 Strain rate

10.2.3 Gradients in stress and strain

10.3 Analysis and Interpretation of Seismic Events

10.3.1 Location and source parameters

10.3.2 Location, source parameters and mechanism

10.4 Analysis and Interpretation of Seismicity

10.4.1 Quantitative comparisons of seismicity

10.4.2 Contouring seismicity parameters - some principles

10.4.3 Delineation of geological structures

10.4.4 Statistical analysis of source mechanisms

10.4.5 Quantification of discontinuity behaviour

10.4.6 Detection of potential instabilities in space

10.4.7 Detection of potential instabilities in time

10.4.8 Definition of clusters

10.5 Velocity of Ground Motion Estimates

10.5.1 Scaling Laws

10.5.2 Applications

10.5.3 Optimum time windows

10.6 Benchmark Case Studies

10.6.1 Stuirmanspan fault

10.6.1 Postma dyke

10.6.2 Western Holdings No. 6 Shaft Pillar

10.6.3 Trough dyke

10.7.4 81-122 longwall

SEISMOLOGY FOR ROCKBURST PREVENTION, CONTROL AND PREDICTION

GAP 017 (1993 – 1995)

Summary of Final Report

Routine seismic monitoring was introduced in mines over 30 years ago with two major objectives in mind:

- to locate major seismic events and thus guide rescue operations
- to detect potential instabilities

The first objective was achieved fairly quickly, but, due to the development in mining communication systems, its strategic importance has diminished. The very limited success with rockburst prediction can be attributed to two reasons:

- the non-quantitative description of a seismic event, by so-called Richter or Local Magnitude, and the focus of seismicity analysis on the magnitude-based statistical Gutenberg-Richter relation and its parameters
- analogue technology based seismic monitoring systems that provided limited dynamic range, noisy and poorly-calibrated data

The progress in theoretical, computational and observational seismology over the last 25 years (*e.g.* Brune 1970; Backus and Mulcahy 1976a, 1976b; Aki and Richards 1980; Scholz, 1988; Kostrov and Das 1988; see Gibowicz and Kijko 1994, for an excellent review) and the introduction in 1988, in South Africa, of the world's first mine-worthy digital seismic data acquisition system (Mendecki *et al* 1988) enabled the implementation of real time quantitative seismology as a management tool for continuous monitoring of the rock mass response to mining (Mendecki 1993).

The primary output of the project "Seismology for Rockburst Prevention, Control and Prediction" was to develop methodologies for long-, intermediate- and short-term rockburst prediction based on quantitative data provided by the modern seismic networks. The intention was that the developed methodology should be objective, *i.e.* based on sound physical principles rather than on loosely defined patterns or trends observed under certain circumstances which are often strongly site dependent. Thus, investigations into "seismicity and geological features" or "seismicity and mine layout" were considered not entirely objective since there are no two identical geological features nor two identical mining and geological situations. Some faults or dykes are very dangerous, producing large and dynamic seismic events resulting in rockbursts while mining is carried out in their vicinity, while others, or even the same features at different

locations, behave differently, yielding a number of smaller and/or slower seismic events. Moreover, it has been shown in our study that there is strong interaction in seismicity over long distances, *e.g.*, correlation of up to 80% in seismic activity and seismic energy release over 1 km distance at one of the gold mines. However, there are underlying fundamental physical processes leading to large instabilities – to identify and to quantify them on the basis of information provided by the seismic monitoring systems is the main objective of this project.

Seismic monitoring consists of data acquisition, seismological processing, quantification of rock mass response to mining and finally the interpretation in terms of potential for larger instabilities. Each of these stages must be conducted with great care for meaningful results. Thus, the successful application of seismic monitoring depends on strict technical requirements for data acquisition, sound principles of seismological processing and adherence to the fundamentals of physics rather than only to one's experience during interpretation of data.

The following summarize the major results of the project.

SEISMIC DATA ACQUISITION SYSTEM

Transducers

The sensor specifications of most concern for seismic monitoring are frequency range (bandwidth) and dynamic range in amplitude. Fig.1 shows how the dominant frequency generated by a seismic event varies with magnitude for a range of stress conditions and rock properties. Fig.2 shows sensor velocity limits as a function of frequency.

Extensive experience has been gained with two types of sensor:

a. 4.5 Hz geophones (velocity transducers)

- have a low noise level, set by background noise in mines to about 10^{-7} m/s.
- wide dynamic range, up to 120 dB at 4.5 Hz
- limited bandwidth, from 2 Hz to about 300 Hz, which in Fig.1 corresponds to corner frequencies between 4 Hz and 60 Hz.
- These frequencies propagate well through the rock, so the geophones may be widely separated, 5 stations within 5 km of the source.
- These sensors suffer from displacement clipping, so must not be too close to large events

- b. 10 kHz, 300mV/g piezoelectric accelerometers:
- have a noise level, set by internal amplifiers, of about 10 μ g
 - have a dynamic range, set by internal amplifiers, of about 120dB
 - wide bandwidth, from 1 Hz to 10 kHz (event corner frequencies from 5 Hz to 2 kHz in Fig.1).
 - the higher frequencies do not propagate well so the accelerometers must be closely spaced, 5 stations within 300 m of the source of a $m_M = -3$ event.
 - are relatively insensitive to low frequencies so there is no problem with clipping on nearby large events.
 - are 5 to 10 times more expensive per unit than geophones, and more are required for covering the same volume.

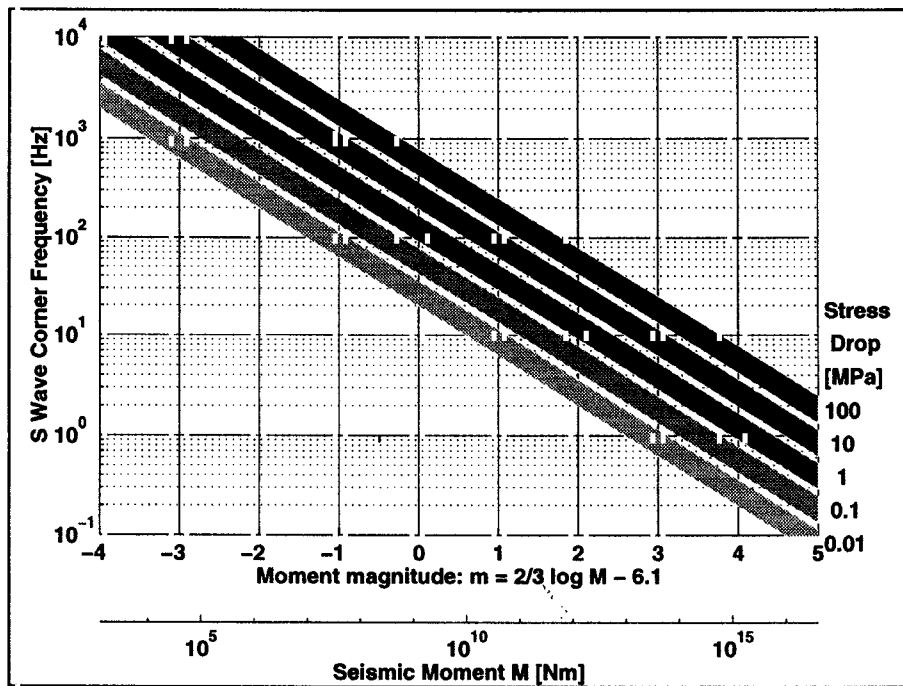


Fig. 1 Expected S-wave corner frequencies, f_o , as a function of seismic moment, M , for a range of stress drops, $\Delta\sigma$. The general relation is given by:

$$f_o = \frac{KV_s^3}{2\pi} \sqrt{\frac{16\Delta\sigma}{7M}}$$

where K is a model dependent term, and V_s is the S wave propagation velocity. A value of $K = 2.34$ from the Brune model is illustrated. The width of each band shows the variation with V_s from 2000m/s, typical of soft rock, to 3700m/s, for hard rock. Although stress drop and moment are independent parameters, very small events are not observed at very high stress requirements, which reduces the high frequency requirements.

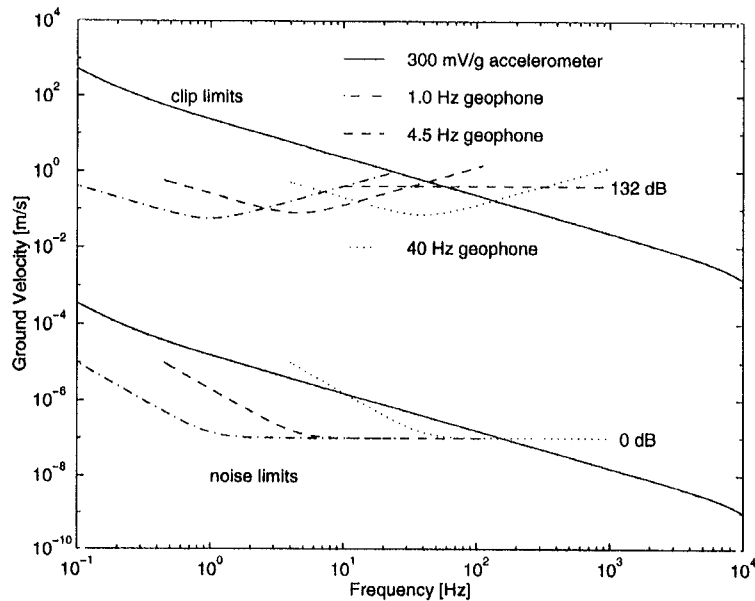


Fig. 2 Sensitivity and dynamic range of sensors commonly used in mine seismic systems. The region between the limits represents the usable range for each instrument. The geophone's greater sensitivity up to several hundred Hz is clearly shown, as is the loss of dynamic range due to displacement clipping below these frequencies. A data acquisition system dynamic range of 132 dB with its quantization noise matching the expected ground noise of 10^{-7} m/s is illustrated.

c. Accurate measurement of very large and/or low stress drop events (corner frequency below 5 Hz in Fig.1) requires specialised earthquake monitoring instruments such as 1 Hz geophones or Force Balance Accelerometers. These are approximately 50 - 100 times more expensive than the 4.5 Hz geophones.

Acquisition System

The data acquisition system should faithfully record and time the output of a network of sensors at a central processing site, including:

- preserving the dynamic range of the signal amplitude, at least 120dB
- dynamically varying the duration of events from 50 ms to 5 s
- using storage and communications efficiently by dynamically altering the sampling rate to match the frequency content of the waveform, by a factor of 25

Application	Minimum system characteristics
Regional mining – monitoring of several operations on a regional basis, larger seismic events, $m_M \geq 0$, over relatively long distances (1 – 30 km)	Low Frequency: (1 Hz - 300 Hz) Sensor density: 5 stations within 5 km of the source Velocity Transducers: (Geophones) Sampling rate: 500 Hz - 4 kHz Event rate: 1 - 100 events per day Communication rate: 1200 b/s Communication method: single twisted pair and/or radio
Mine- or shaft-wide monitoring – from $m_M > -1$ and distances from 300 m to 5 km	Medium frequency: (4.5 Hz - 2 kHz) Sensor density: 5 stations within 1 km of the source Transducers: Geophones/Accelerometers Sampling rate: 10 kHz Event rate: 100 - 1000 events per day Communication rate: 115 kb/s Communication method: dual twisted pair and/or optical fibre
Pillar/remnant monitoring from $m_M > -3$ and distances from 100 m to 1 km	Medium frequency: (3 - 10 kHz) Sensor density: 5 stations within 300 m from the source Transducers: Accelerometers Sampling rate: up to 50 kHz Event rate: 1000 - 10 000 events per day Communication rate: 19200 baud Communication method: copper cable and/or optical fibre

Table 1. Application Scenarios

The central site should have sufficient resources for

- processing the data and making the results available with reasonable immediacy
- archiving of seismic waveform and event data
- computerised interpretation based on space-time quantification and visualization of parameters describing the seismic flow of rock.

Network configuration and sensitivity

Algorithms were developed to plan and evaluate network configurations with regard to location accuracy and sensitivity. It was taken into account that location accuracy is affected by P and/or S arrival time determination errors as well as velocity model errors. Furthermore, it was decided that at least 5 stations are necessary to properly quantify an event.

The planning algorithm is based on the theory of optimal experiment (Kijko and Sciocatti, 1995), where the optimal configuration of n seismic stations is determined from the condition:

$$\min_c \sum_{i=1}^{n_{areas}} w_i \sum_{r=r_{min}}^{r_{max}} \lambda_t \lambda_x \lambda_y \lambda_z \frac{r^{-(1+4b/3)}}{r_{max}^{-4b/3} - r_{min}^{-4b/3}}$$

where c runs over all possible configurations of n seismic stations; w_i

indicates the chances of an event happening in a given seismic area i ($i = 1, \dots, n_{\text{areas}}$);

$\lambda_t, \lambda_x, \lambda_y, \lambda_z$ are the eigenvalues of the matrix $[\mathbf{A}^T \mathbf{A}]^{-1}$; \mathbf{A} is a 4 column partial derivative matrix of theoretical arrival times with respect to the four unknown location parameters t_0, x_0, y_0 and z_0 ; r_{min} is the detectability distance corresponding to the minimum energy of interest; r_{max} is the detectability distance corresponding to the maximum energy of interest and b is the b -value in the Gutenberg-Richter relation.

In planning network configurations, the following need to be taken into account:

- Optimal spatially distributed networks should ensure location error of less than 3% of the average hypocentral distance.
- Sensitivity should be such that the signal to noise ratio of the smallest event to be recorded is at least 10.

The above algorithms have been successfully applied in planning network configurations for 19 South African gold mines and subsequent installations.

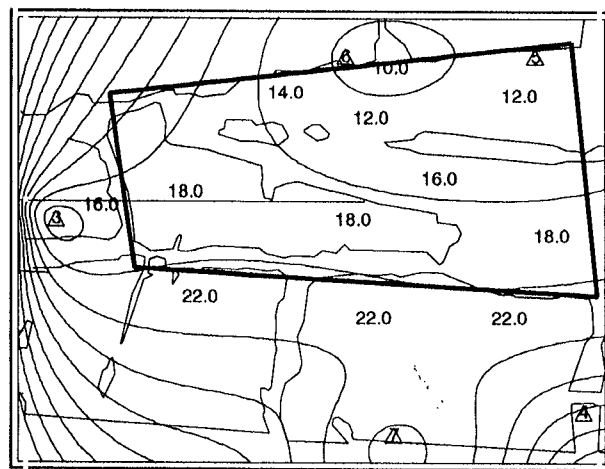


Fig. 3 Expected xyz location error for Postma Dyke area, Western Holdings Mine. The area of interest, delineated by the box, is about 400m x 250 m and shows where the Postma dyke intersects the Arrarat fault.

SEISMOLOGICAL PROCESSING

The following comprehensive suite of seismological algorithms, necessary for routine quantification of seismic sources and, to some degree, for rock mass characterisation, on the basis of data provided by seismic monitoring systems, has been developed and/or tested:

- *P and/or S wave(s) velocity inversion based on clusters of microseismic data*

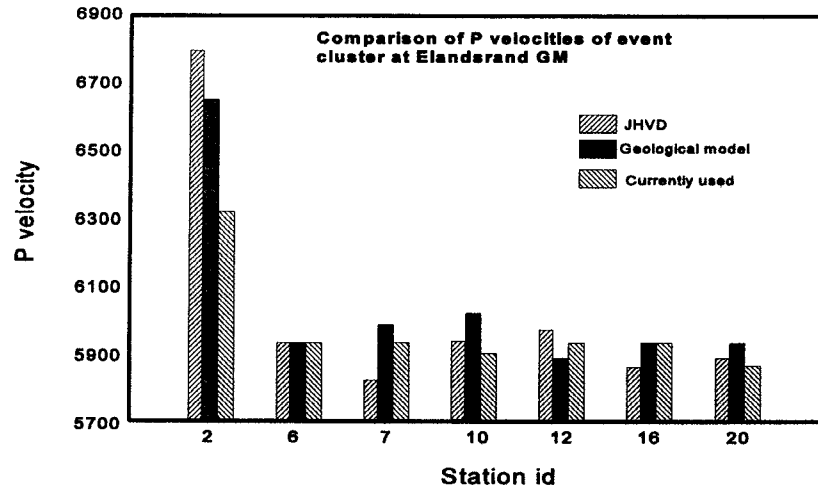


Fig. 4. Results from Joint Hypocentre and Velocity Determination (JHVD) performed on a dataset from Elandsrand Gold Mine. JHVD was used to obtain a P velocity model for different clusters of events, in order to improve routine seismic event location. Cluster size was of the order of 300m \times 200m \times 400m. The figure shows that the inverted velocities correlate well with those calculated using a simple geological model. This method allows for the identification of stations that may need significant changes to the P velocity (see station 2 in this figure).

- *Nonlinear adaptive norm seismic event location method with 3D finite-difference ray tracing based on P and/or S arrivals and/or polarisation data*

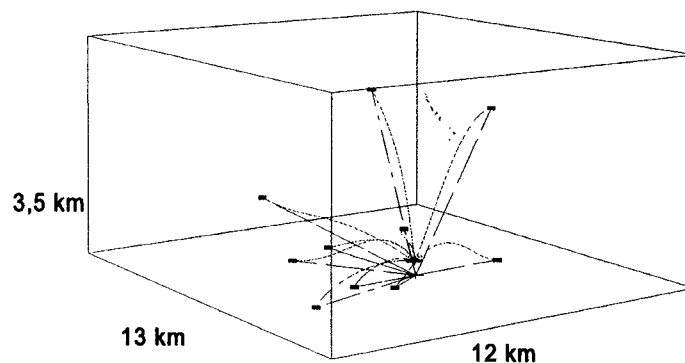


Fig. 6. Event recorded by Vaal Reefs Gold Mine Seismic Network on July 18 1995. Event location by finite-difference raytracing method (+South=81900m, +West=19830m, +Down=2770m), is shown using solid lines, whereas location using straight ray approximation (+South=81945m, +West=19822m, +Down=2948m), is shown in dashed lines. The average hypocentral distance for the location based on raytracing is 4693 m, compared with the average distance for straight ray approximation of 4359 m.

- *3D wavefront construction method which calculates all kinematic and dynamic parameters associated with the wavefields simultaneously.*

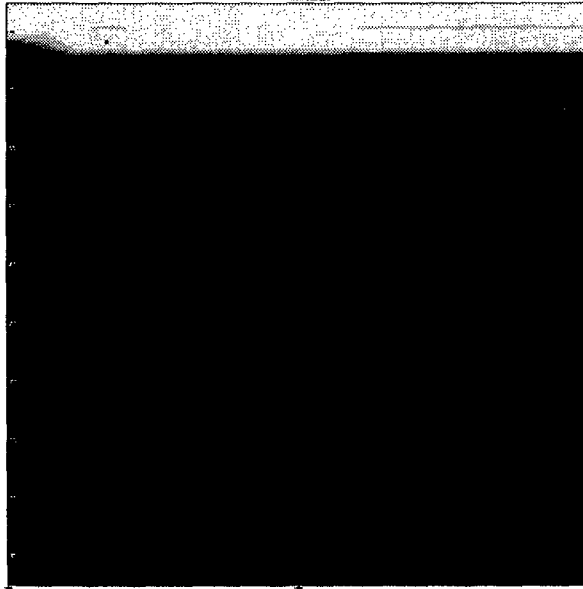


Figure 2 Section of 3D velocity model of one of gold mines in South Africa. Darker color corresponds to higher velocity values. Model is represented by cubic B-splines, using 201x201 points with 10 m spacing. Model box dimension: 2km x 2km. Note the low velocity layer at the top of the model.

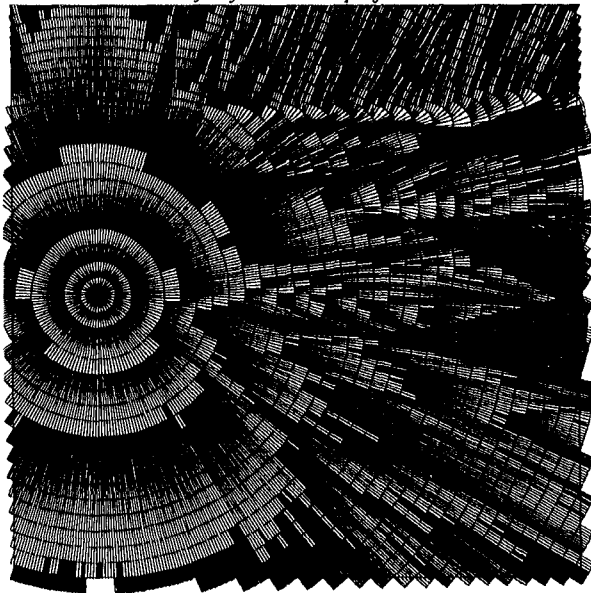


Figure 3. Section through 3D wavefronts distribution for a velocity model shown in Fig. 1. Wavefronts have been calculated using wavefront construction method with 0.01 s increments, $\Delta S_{max} = 10$ m. Numerous caustics are observed. Note head waves generated at transition zones between low and high velocity regions. Transition to the low velocity layer situated at the top of the model is clearly seen.

- *Quality controlled seismic source parameters inversion suitable for automatic processing of large volumes of data*

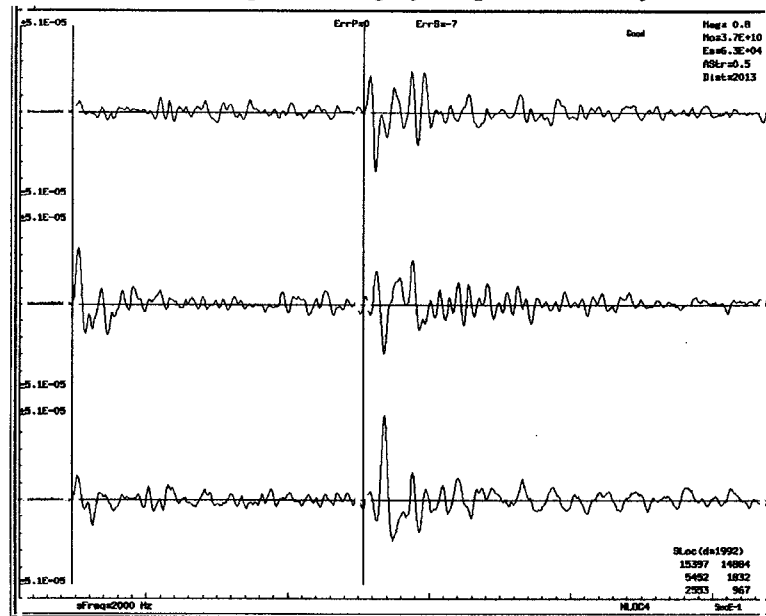


Fig. 8 Three component seismogram of a magnitude 0.8 seismic event recorded by the Welkom Seismic Network with automatically picked P and S arrivals.

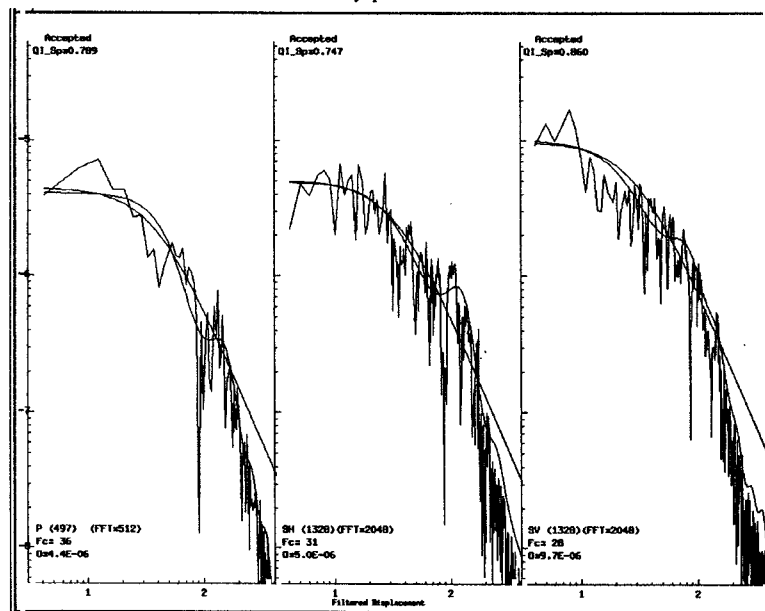


Fig. 9 Results of source parameter estimation for the seismogram shown in Fig. 8. Rapidly changing lines show the ray displacement spectra corrected for instrument response and for Q for P, SV and SH waves respectively. The smooth lines shown are cepstral and fitted Brune model with automatically estimated: spectral level, corner frequency, seismic energy and quality indices.

QUANTIFICATION OF A SEISMIC EVENT

A seismic event can be considered as a sudden inelastic deformation within a given volume of rock that radiates detectable seismic waves. To give some idea of scale, the volume of rock involved in coseismic inelastic deformation (source volume) varies from a fraction of a cubic metre for cracks of about a metre in length, to a fraction of a cubic kilometre for large seismic events. The average strain drop within the source volume varies from 10^{-4} to 10^{-2} . The average velocity of the deformation varies from a few millimetres per second to a few metres per second, generally being slower within softer and less homogeneous rock and at lower differential stress.

Proper quantitative analysis of seismic waveforms can routinely provide reliable information on at least four independent parameters pertaining to the seismic source:

- time of the event, t ;
- location, $X = (x, y, z)$;
- energy radiated from the source of the seismic event, E ; and
- coseismic inelastic deformation at the source called seismic moment, M .

So-called corner frequency f_o (predominant frequency on instrument and Q corrected velocity spectrum) and stress drop, $\Delta\sigma = cMf_o$, where c is constant, are considered strongly model dependent.

Apparent stress

The comparison of radiated seismic energies for seismic events of similar seismic moment provides information about the stress change in the source areas. The ratio of radiated seismic energy to seismic moment multiplied by rigidity, μ , is called apparent stress, σ_A , and is recognised as a model independent measure of the stress change at the seismic source (Wyss and Brune, 1968):

$$\sigma_A = \mu \frac{E}{M}$$

Let us imagine the source of a seismic event associated with a relatively weak geological feature or with a soft patch in the rock mass. Such a source will yield slowly under lower differential stress, producing larger seismic moment and radiating less seismic energy and manifests as a slow or low apparent stress event. The opposite applies to a source associated with a strong geological feature or hard patch in the rock mass, which will manifest as a fast or high apparent stress event.

The apparent stress is proportional to the integral of the square of the velocity spectrum divided by the low-frequency asymptote to the displacement spectrum or, when accelerations are considered, the apparent stress drop depends linearly on the product of the corner, or predominant, frequency and the high-frequency asymptote to the acceleration spectrum. It is then a more reliable and less model-dependent parameter describing the average stress release at the seismic source than the static stress drop $\Delta\sigma$ which depends on corner frequency cubed.

Energy index

The notion of comparing the radiated energies of seismic events of similar moments can be translated into a practical tool called Energy Index (EI) – the ratio of the radiated energy of a given event (E) to the average energy released by events of the same seismic moment in the area of interest ($\bar{E}(M)$) (van Aswegen and Butler 1993):

$$EI = E / \bar{E}(M).$$

Apparent volume

Source volume V – the volume of coseismic inelastic deformation $\Delta\epsilon = \Delta\sigma / \mu$ – can be estimated from $V = M / \Delta\sigma$. Since apparent stress σ_A scales with stress drop, and since there is less model dependence in determining the apparent stress than there is in determining static stress drop, and because, in general $\Delta\sigma \geq 2\sigma_A$, one can define the apparent volume V_A as follows (Mendecki, 1993)

$$V_A = \frac{M}{2\sigma_A} = \frac{M^2}{2\mu E}$$

The apparent volume for a given seismic event scales volume of rock with coseismic inelastic strain of an order of apparent stress over rigidity.

QUANTIFICATION OF SEISMICITY

Mining excavations create considerable stress gradients which the rock mass constantly reduces by means of inelastic deformation in the form of fractures, slip and creep in the surrounding rock – rock flows towards mining excavations or, more precisely, towards local equilibrium, reducing and transferring stresses.

To monitor rock mass response to mining one must be able to quantify continuously in time and space the parameters describing the flow changes in the stress and strain regime. From seismological observations, one can measure only that portion of stress, strain or

rheological property of the rock mass associated with the radiation of seismic waves.

Seismicity can be described by the following four independent parameters:

- average time between events \bar{t}
- average distance, including source sizes, between consecutive events \bar{X}
- sum of seismic energies ΣE
- sum of seismic moments ΣM

From these parameters one can calculate, for a given volume ΔV and time period Δt , the following parameters which describe the physics of seismic flow of rock. (Kostrov and Das, 1988; Mendecki, 1994)

Seismic stress:

$$\sigma_s = \frac{2\mu \Sigma E}{\Sigma M}$$

Seismic stress measures stress changes due to seismicity.

Seismic strain rate:

$$\dot{\epsilon}_s = \frac{\Sigma M}{2\mu \Delta V \Delta t}$$

Seismic strain rate measures the rate of coseismic inelastic deformation.

Seismic stress and seismic strain rate can be treated as tensors provided moment tensor solutions are available for all events considered.

Seismic viscosity:

$$\eta_s = \frac{\sigma_s}{\dot{\epsilon}_s} = \frac{2\mu^2 \Delta V \Delta t \Sigma E}{(\Sigma M)^2}$$

Seismic viscosity is similar to the fluid mechanics concept of turbulent or eddy viscosity. Unlike ordinary or molecular viscosity, turbulent viscosity does not describe the physical properties of the medium but characterises the statistical properties of the flow. Lower seismic viscosity implies easier flow of seismic inelastic deformation or easier stress transfer due to seismicity.

Seismic Relaxation Time and Deborah Number:

$$\tau_s = \frac{\eta_s}{\mu} ; \quad De_s = \frac{\tau_s}{\Delta t}$$

Seismic relaxation time measures the rate of change of seismic stress during seismic flow of rock. It also defines the usefulness of the past data and the predictability of the flow of rock. The lower the relaxation time, the shorter the time span of useful past data and the less predictable the seismic flow of rock. Seismic Deborah number measures the rate of elastic to viscous forces in seismic flow of rock. Seismic Deborah number can be used as a criterium to delineate a volume of rock softened by seismic activity, called soft clusters.

Seismic diffusion:

- for a volume of size L

$$D_s = \frac{L^2}{\tau_s} = \frac{(\Sigma M)^2}{4\mu L \Delta t \Sigma E}$$

- statistical, for a cluster of events

$$d_s = \frac{(\bar{X})^2}{t}$$

Seismic diffusion quantifies the magnitude, direction, velocity and acceleration of the migration of seismic activity and associated transfer of stresses in space and time.

Seismic Schmidt Number:

$$Sc_s = \frac{\eta_s}{\rho d_s} \quad \text{where } \rho \text{ is rock density.}$$

Seismic Schmidt number measures the degree of complexity in space and time (the degree of turbulence) in the seismic flow of rock. Note that seismic Schmidt number encompasses four independent parameters describing seismicity: ΣE , ΣM , X and t .

LIMITS OF PREDICTABILITY

Most phenomena in nature seem to exhibit chaotic behaviour, i.e. they generally are unpredictable over arbitrary large periods of time. The most common example of chaos is turbulence. Since seismicity is nowadays regarded as the turbulent part of the flow of rock, one expects chaos to set in within the context of seismicity. While a decade ago the general attitude towards chaos as a terminology was negativistic, things have changed dramatically lately, as chaos has

become amenable to thorough investigations and, moreover, it denotes the existence of determinism in the data. This means that, despite the fact that a chaotic process is unpredictable over large periods of time, that same process is predictable over a finite temporal range known as its limit of predictability. The discipline that deals with chaotic systems - which we shall be using to compute limits of predictability of various seismic parameters - is the nonlinear dynamics.

There are a number of steps that have to be followed in order to calculate limits of predictability. First of all one needs to prove that the system under study is chaotic. Next one needs to quantify the chaotic behaviour. Finally one can evaluate the limits of predictability on the basis that the stronger the chaotic behaviour the smaller the predictability limit.

The aim of this analysis was to calculate prediction limits for seismic parameters knowing only their time series. In this way, we ensure an objective, model independent way to approach this matter. To assess whether or not chaotic behaviour is encountered, we reconstructed the phase space for each parameter, respectively. The method that achieves this is called embedding; it is aimed at reconstructing the phase space directly from the knowledge of the time series of the seismic parameter under study. A preliminary result is needed: the information link (IL) also known as delay (D) which is in fact the first zero of the autocorrelation function $A(m)$ of the seismic parameter Q :

$$A(m) = \frac{\sum_{i=1}^{N-m} (Q_{i+m} - \bar{Q})(Q_i - \bar{Q})}{\sum_{i=1}^N (Q_i - \bar{Q})^2}; \quad \bar{Q} = \frac{1}{N} \sum_{i=1}^N Q_i$$

where N is the number of events in the time series and Q is a parameter of interest, such as log(Energy), log(Moment), etc. The significance of D is the following: only D consecutive events in the time series are linearly independent in a statistical sense. This helps to further construct the phase space using as orthogonal axis the values Q_i (first axis), Q_{i+D} (second axis), ... $Q_{i+(d-1)D}$ (d -th axis). The procedure stops at a given value (d) which is known as the embedding dimension.

With aid of the correlation integral method, we can further establish the fractal dimension of the distribution of states in the phase space as well as the embedding dimension (d). The correlation integral is defined for a given embedding dimension:

$$C(Q, d) = \frac{2}{(N-D)(N-D+1)} \cdot \sum_{i,j} \Theta(Q - \|Q_i - Q_j\|)$$

where $\|Q_i - Q_j\|$ represents the Euclidian distance between the state "i" and state "j" in the phase space and Θ is the Heaviside function. The slope of the linear portion of the plot $\log C$ vs $\log Q$ gives the fractal dimension d_A of the distribution at a given embedding dimension (d). Finally if the plot d_A vs d flattens at some value of d , that d is the embedding dimension; the corresponding value d_A is the actual fractal dimension of the distribution of states in the phase space (see Fig.10). The flattening is the proof that an attractor exists in the phase space. Moreover, if d_A is rational noninteger, the distribution of states in the phase space constitute a strange attractor, this in fact being strong evidence for the chaotic behaviour of the parameter under study.

All the case studies we investigated so far have indicated chaotic behaviour. The limits of predictability can be estimated if the chaotic behaviour is quantified. This can be done with the aid of the Lyapunov exponent which is a computable measure of the chaotic behaviour of a trajectory in the phase space and expresses the mean exponential rate of divergence of trajectories surrounding it. Its expression is:

$$Ly = \lim_{t \rightarrow \infty} \frac{1}{t} \log_2 \frac{d(\mathbf{x}_0, t)}{d(\mathbf{x}_0, 0)}$$

where $d(\mathbf{x}_0, t)$ is the Euclidian norm of the distance vector between two trajectories that are initially very close to each other. Ly can be computed with the aid of the Wolf algorithm and is an invariant of the dynamics of the trajectories in the phase space, i.e. an objective measure of the degree of chaos.

Once the Lyapunov exponent has been determined, the limits of predictability can be deduced as follows: At present, the total information link the time series of a seismic parameter Q has with the future is D . After an event will have occurred in the future, the information link decreases to $D - Ly$. After the second event will have occurred, the information link decreases to $D - 2Ly$. Finally, there will be an n -th event in the future that will make the information link $D - nLy$ equal or very close to zero. The value

$$n = \frac{D}{Ly}$$

represents the maximum number of events in the future whose parameters can be estimated.

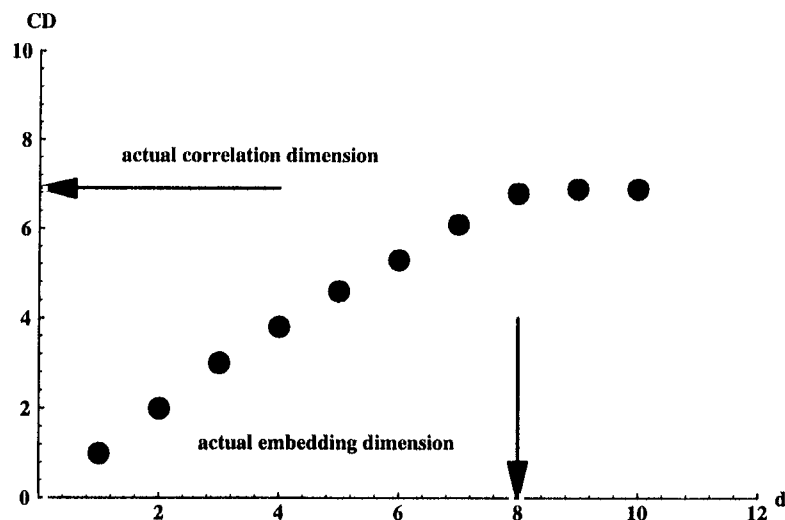


Fig. 10 Generic plot of correlation dimension vs embedding dimension. The flattening point of the plot determines the dimension (d_{min}) of the reconstructed phase space and the dimension d_a of the attractor.

It turned out that these limits are always manageable and range from a couple of hours to about three weeks.

A most important result is that the dynamics of the systems analysed appears to be 8-dimensional. It may be speculated that the underlying physics of seismic rock mass response to mining is 8-dimensional. The remaining problem is to further identify the 8 physical parameters that give rise to this dynamics. The systems studied all exhibit the phenomenon of chaos because of the following reasons:

- a) The existence of attractors has been established.
- b) The dimensionality of the attractors is always fractal.

The occurrence of chaos supports the view which assumes the turbulent nature of the seismic rock mass response to mining (Kagan, 1992; Mendecki, 1995). In terms of considering the apparent volume in calculating the distance between events, it appears that the fractal dimension of the attractor of the distance between events is underestimated if the apparent volume is not taken into account. This is more clearly seen when the number of events is larger. Analysis indicates that the variables x, y, z locations, $\log E$, $\log M$, s_e and s_{ph} are all true reflections of the same underlying physical process which appears to be 8-dimensional. At this stage, we cannot determine the actual eight canonically independent variables which constitute the axes of the phase space. This did not however hinder us in any way in determining the limits of predictability. These limits have been

determined on the basis of the Lyapunov exponent, an invariant of dynamics which quantifies in a statistical way the amount of the existent chaos. It turned out that the limits of predictability are always finite and manageable, ranging from a few hours to about three weeks. It has also been shown that an increase in the predictability limit can be achieved if the monitoring sensitivity at a given area is increased. One can now attempt to estimate the values of the seismic parameters of interest within their limits of predictability. Work in this regard is in progress.

PHENOMENOLOGICAL MODEL AND TIME TO FAILURE

The growth of the deformation processes up to the point of instability is called nucleation. There must be a degree of softening in the system before instability, i.e. breakdown instability within the rock mass will not occur until a quasi-static or quasi-dynamic inelastic deformation has occurred within the critical volume of rock. The volume(s) would be characterised by low seismic Deborah number since stresses are transferred to the area surrounding the nucleation volume. Additionally, it is the nature of rock fracture and friction that the breakdown instability does not occur without some preceding phase of accelerating deformation.

The following qualitative seismic behaviour has frequently been observed at some stage before instability:

- . an increase in the rate of coseismic deformation (accelerations in cumulative apparent volume or drop in seismic viscosity) caused by the increase in the rate of micro seismicity, or, for the same rate, due to the softer nature of individual events.
- . lower seismic stress or Energy Index within and higher outside, or at the interface of, the nucleation zone due to softening in the nucleation volume
- . an increased distance between consecutive events and/or a decrease in time between consecutive events: this would tend to cause an increase in seismic diffusion, its velocity and acceleration

If accelerating deformation coincided with the development of the nucleation zone then, additionally, one would observe a decrease in the average time between events and an increase in the seismic strain rate. This causes an additional increase in diffusion and a decrease in viscosity of the seismic flow of rock resulting in a dramatic decrease in seismic Schmidt number. The following equation captures the main feature of the above model and returns three parameters: C , α and t_f ; t_f is called time at failure and quantifies the potential for instability:

$$\frac{\sum^n V_A}{(\bar{t})_n (\bar{EI})_n \Delta V} = \frac{C}{(t_f - t)^\alpha}$$

where:

n the number of events over which the qualitative behaviour occurs

$\sum^n V_A$ sum of apparent volume over the last n events

$(\bar{t})_n$ average time between seismic events over the last n events

$(\bar{EI})_n$ average energy index over the last n events

ΔV volume of interest, ideally the nucleation volume,

t time at which one estimates time to failure ($t_f - t$)

C, α, t_f parameters to be estimated; t_f is the time at failure

It is expected that the left side of the above equation will sharply increase in value prior to the instability. C is a scaling volume and α indicates the nature of the increase. The closer to the instability, the higher the time derivative that is most informative. For example, close to the instability, strain acceleration is more informative than the strain rate. It is assumed here that there is a smooth transition in the order of the time derivatives of strain that is most informative at any given time and this is assumed to be α .

In the above formalism, an objective way has to be found to delineate the nucleation volume and subsequently a value for n . It should be noted that this analysis is aimed at small, dense seismic networks of pillar/shaft monitoring. In these cases, the actual nucleation volume of an instability can be detected with the aid of seismic Deborah number.

Thus far it has been assumed in the equations that the strain related parameters and the stress related parameters react over the same n events. However, the following may occur: the rate of increase in cumulative apparent volume may occur from a week ahead of the instability whereas the energy index may drop over a period of only hours prior to the instability. Therefore, it has to be considered that the value of n may be variable for different parameters. Using the above approach, seismic potential is quantified by one number (time to failure) which can be used in routine hazard evaluation on mines. As an example of application of the above equation, the following case is presented in Fig.11. The time to failure is approximately 2.5 days for this case.

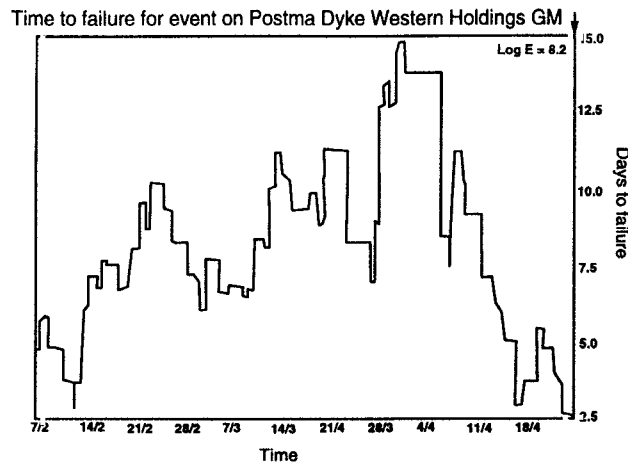


Fig. 11 In this example, the sum of apparent volumes increases, average time between events decreases and median energy index decreases as predicted by the phenomenological model prior to the event of interest. Time to failure steadily drops for 2 weeks prior to the logE=8.2 event. In the 36 hour period preceding the event (11.26 am April 24), the time to failure stayed constant at about 50 hours.

CASE STUDIES AND ROUTINE APPLICATIONS IN SOUTH AFRICAN GOLD MINES.

Ideally the rock mass response to mining should be described in terms of the spatial and temporal variations in stress and strain rate. The above outline for the quantification of seismicity provides a basis for the analysis and interpretation of seismic data to do exactly that.

The first routine application of the quantitative description of seismic events, using at least two physical source parameters rather than one dimensional magnitude, was the identification of areas with above average stress levels. Since 1990, for example, routine plots of apparent stress have been used in the Welkom and the Klerksdorp gold fields to identify 'hot-spots' (e.g. van Aswegen and Butler 1993; van Aswegen and Meijer, 1994); scrutinising contours of weighted EI is presently the daily routine in three major gold mines in the Carltonville area where production staff regularly adapt production planning in response to medium term warnings (Butler, 1995).

With the quantitative description of seismicity, new tools have become available to the rock mechanics practitioners and the identification of places with high strain rates or with high gradients in cumulative strain is enriching the earlier stress based analyses.

Time history analysis for the temporal detection of instabilities is increasingly being used in the production environment (e.g. Amidzic, and Glazer, 1995). A combined success rate of at least 35% is maintained (a successful warning is one which was actually followed

by a significant ($M_m > 2$) seismic event within days).

Four example applications are described below. The first example is a brief consideration of the general characterisation of fault behaviour and stress state. In the second case, it is shown how the initial stress increase and the eventual strain softening of a shaft pillar during its extraction is mirrored by seismic parameters pertaining to stress and strain rate. In the third example, the evolution of the process of bracket pillar failure is examined in terms of the failure of an asperity on the fault. The fourth example is a typical case of an ALARM based on routine time history analysis.

Characterising fault behaviour

Fault stability remains one of the most important rock engineering problems in mines. Numerical modelling for predicting fault behaviour for given mine designs is a common practice, but is limited by a lack of feed-back information to verify input parameters and results (*e.g.* Dennison and van Aswegen, 1993). Seismic parameters pertaining to stress and strain rate may go a long way to overcome these limitations because each event on the fault which was properly recorded yields information about what actually happened.

Fig.12a shows part of the Tanton fault at President Steyn Mine No 4 Shaft with contours of EI based on seismic events which located on the fault surface ($\pm 20\text{m}$) over a period of eighteen months, ending July 1995.

It indicates several areas of relatively high stress along the structure, particularly noteworthy being the concentrations at the lower part of the fault loss area and the area beneath that corner of the shaft pillar closest to the fault. Fig.12b shows contours of seismic Deborah number based on the same data set. Note that low seismic Deborah number and high stress (high EI) are not mutually exclusive - contour highs coincide in some but not all parts of the structure. As applied today, numerical modelling is unable to predict stress/strain behaviour of geological structures in this detail.

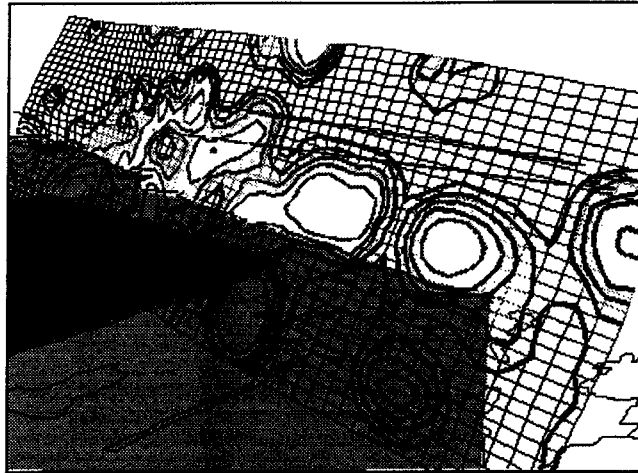


Fig. 12a. A perspective view looking down on the hangingwall side of the Tanton fault (mesh) with contours of E_l based on the source parameters of seismicity within 20m of the fault surface. Grey shading depicts a major Basal reef block on the hangingwall side of the fault, with the shaft pillar in a darker shade. The reef blocks on the footwall side, dipping parallel to the line of sight, show up as straight lines behind the fault surface. The grid spacing on the fault mesh is about 20m.

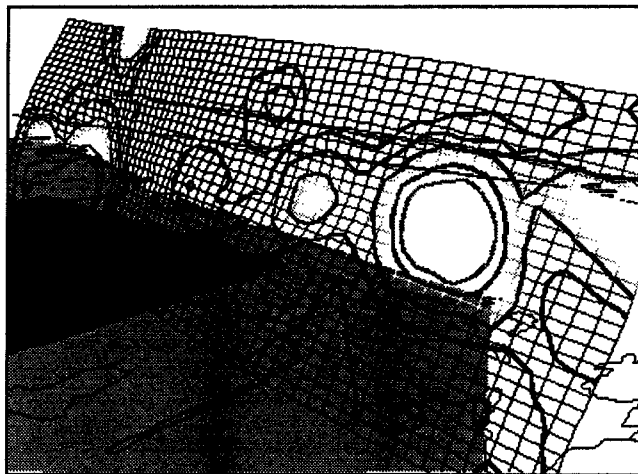


Fig. 12b. Same as Fig.12a but the contours are of inverse seismic Deborah number, thus contour highs indicate high seismic flow.

Shaft pillar extraction

The Western Holdings No. 6 Shaft (WH6#) pillar extraction provided a remarkable mimic of a rock failure test and it serves as a good example case to show the physical meaning of temporal changes in certain seismic parameters, particularly in terms of their value in quantifying the degree of rock mass stability. The mining layout and event distribution over the period 1992 - 1994 are shown in Fig.13.

Seismically, the shaft pillar displayed behaviour similar to that

generally experienced in triaxial rock strength tests, namely an initial period of hardening followed by softening and accelerated deformation. Fig.14 shows this history in terms of cumulative V_A (apparent volume) and moving median EI (energy index). The moving time window here is large (50 days) to smooth out short term fluctuation.

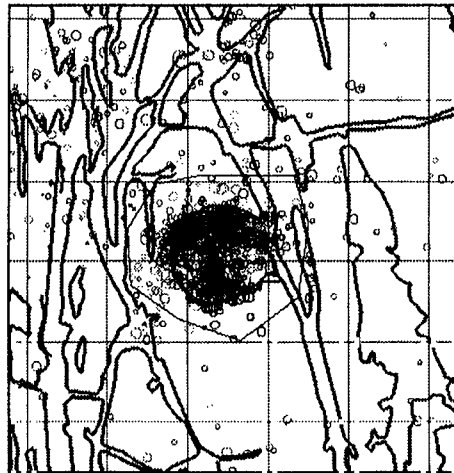


Fig. 13. Distribution of seismic events at and around the Western Holdings No. 6 Shaft (WH6#). The grey lines outline old mine faces; note the circular shape of the shaft pillar. The black lines at the centre show the positions of the pillar mining faces during two stages. The polygon around the shaft was used for time history analysis event selection. The grey scales depict the age of the events starting from May 1992 (light) to September 1994 (dark). The grid spacing is 250 m.

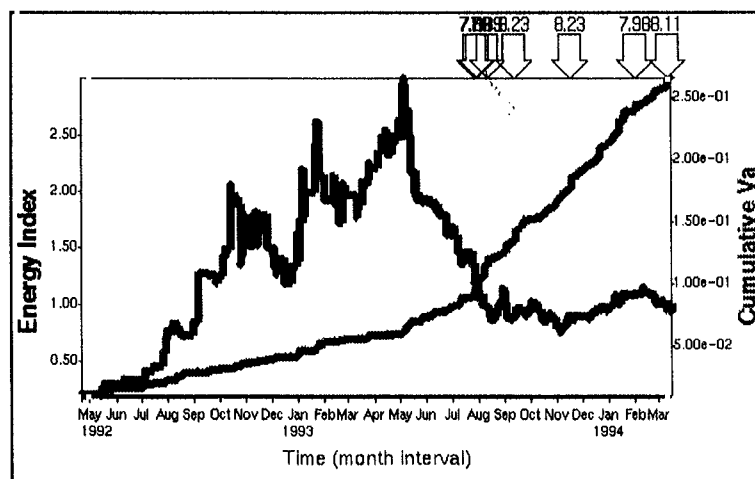


Fig. 14. Time history of ΣV_A and moving median EI for the seismicity associated with the WH6# pillar mining, May 1992 to March 1994. Please note that all seismic events occurred after the drop in EI and during the increased rate in coseismic inelastic deformation.

To imitate a stress/strain curve, Fig.15 is a plot of moving median EI vs. cumulative V_A showing a 'peak strength' followed by weakening and unstable behaviour.

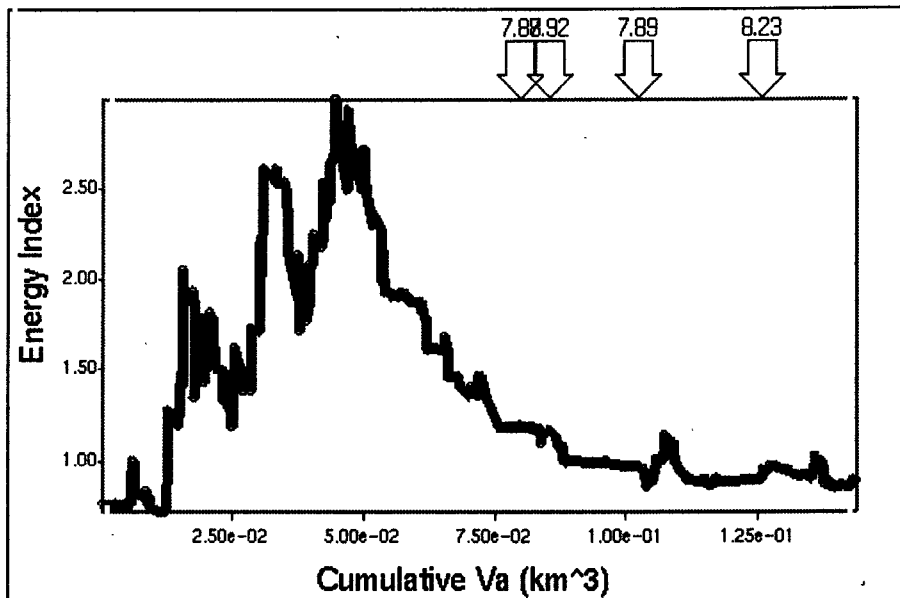


Fig. 15. The same data as shown in Fig.13, plotting moving median EI against ΣV_A , yielding a 'stress-strain' curve. Please note that the larger seismic events occurred during softening of the system.

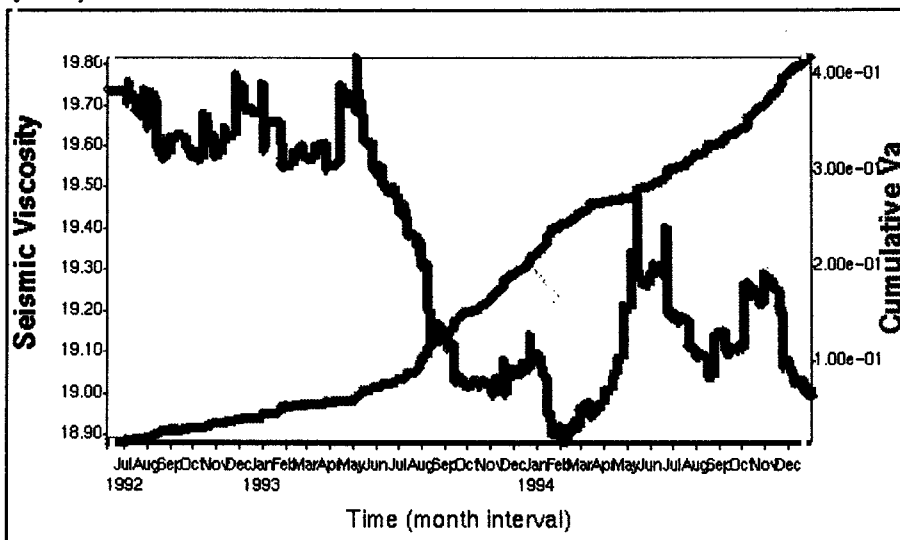


Fig. 16. The variation of seismic viscosity with time during the mining of the WH6# pillar.

In general, the moving time window seismic viscosity decreased at WH6# from the beginning of mining the shaft pillar until the end of July 1993, after which it fluctuated around the lower level, (Fig.16). Similarly, seismic Schmidt number decreased and remained relatively low after the end of July 1993.

To establish the spatial distribution of the stress increase, as indicated by EI and which culminated during May-June 1993, three-dimensional contours of EI based on events during this time period, is shown in Fig.17. In fact, it indicates that stress had increased throughout the volume of interest, as can be seen by the scattered nature of small volumes of high energy index.

Seismic softening and/or accelerated coseismic deformation in the area of interest (Fig.18). were found to be amongst the most successful indicators of unstable rock mass behaviour.

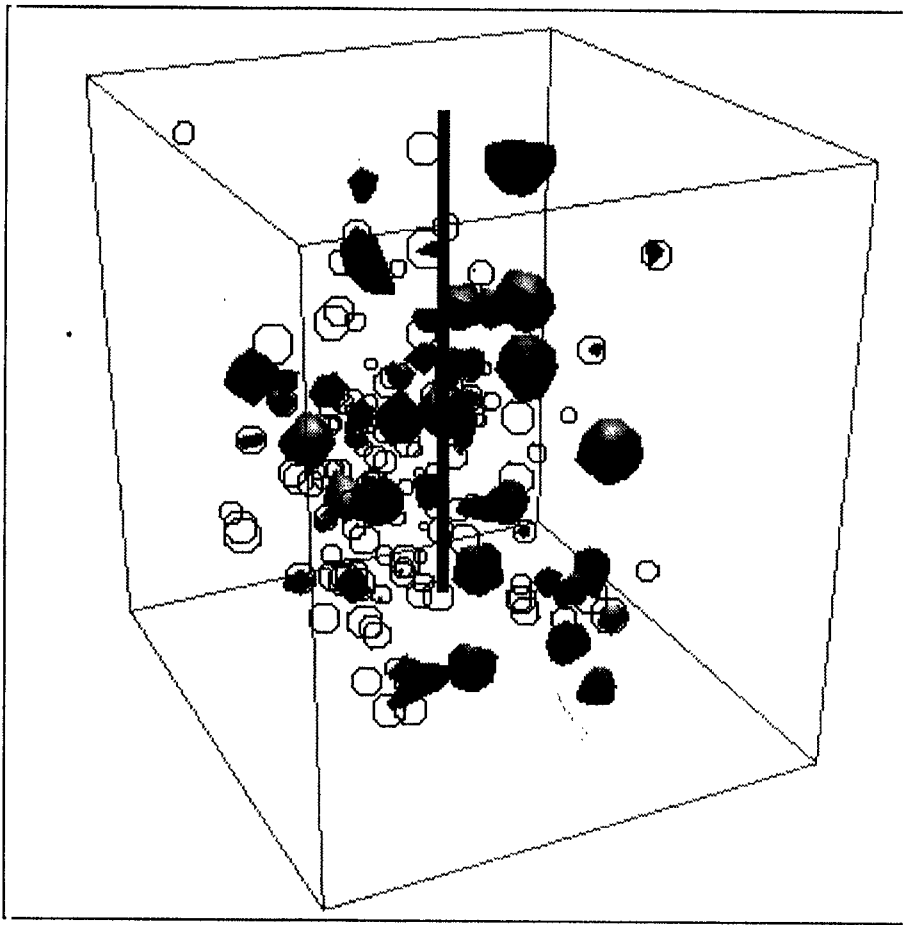


Fig. 17. Iso-surfaces of above average EI with the seismic events around WH6# for the period January to July 1993. Scale varies in this perspective view.

The two strongest seismic events which occurred during the period 1 June 1993 to 1 October 1993 are well predicted by accelerated seismic deformation as indicated by ΣV_A , drop in stress as indicated by moving median EI , increase in seismic diffusion, drop in seismic viscosity and, as a natural consequence of the latter two, a drop or low values of seismic Schmidt number (Fig.19a). Time history analysis of velocity of seismic diffusion is given in Fig.19b. Note the added

information given by decomposing seismic diffusion between the three coordinate directions. In the case of WH6#, the relative values reflect the E-W geometry of the mining faces and probably the activation of a minor, near-vertical fault zone, also E-W trending, which intersects the reef in the shaft pillar, limiting the seismic diffusivity to the YZ (west-down) plane.

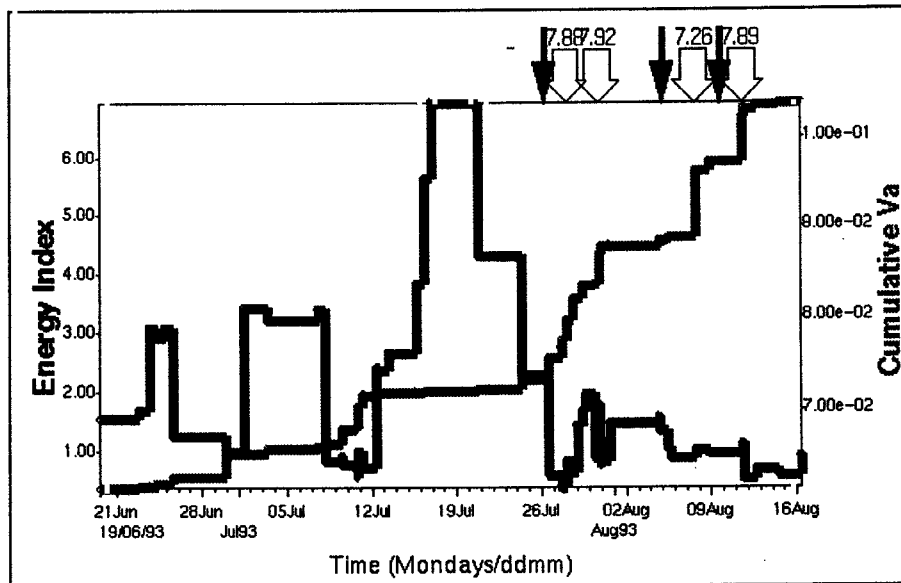


Fig. 18. Time history analysis from WH6# for the period June to August 1993 showing variation in moving average EI, ΣV_a , the timing of the actual warnings issued (black arrows) and the timing of significant seismic events. The figures above the event indicators give their magnitudes in terms of the radiated seismic energy.

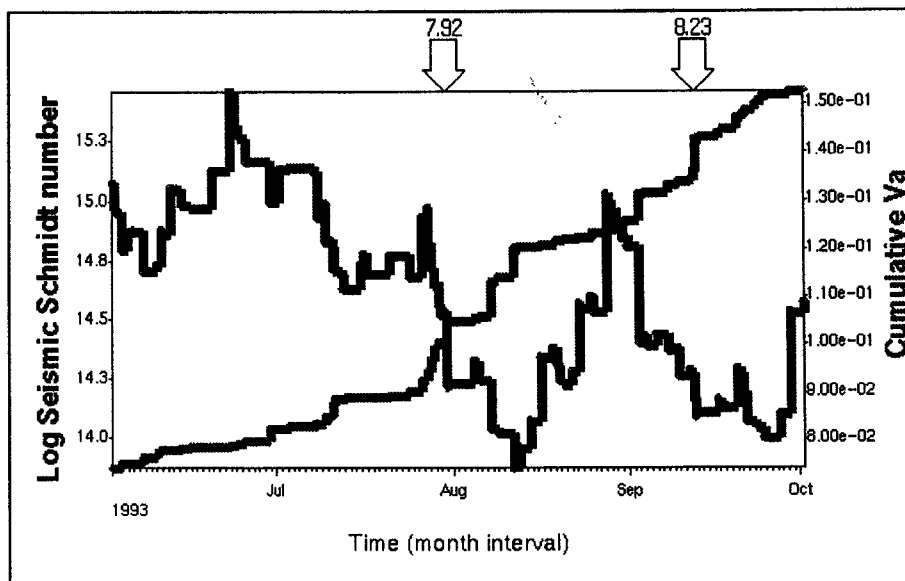


Fig. 19a. The time variation of seismic Schmidt number for the same data set reflected in Fig. 19b.

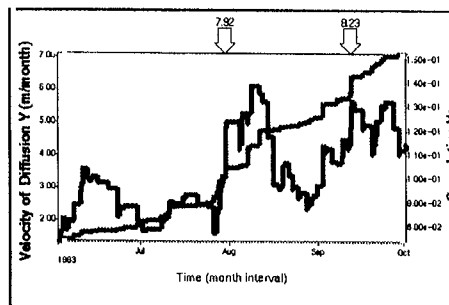
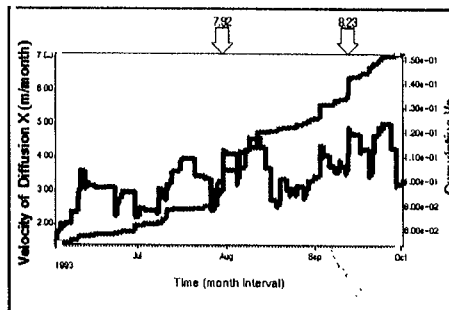
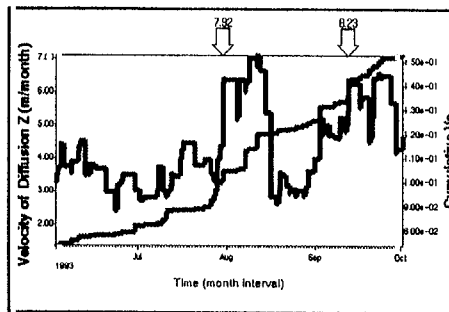
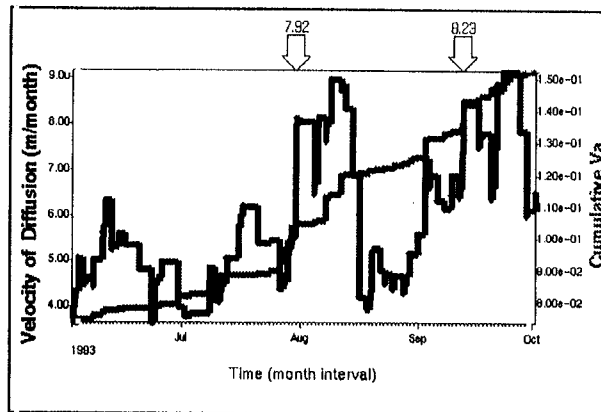


Fig. 19b. The main plot shows the time variation of the velocity of seismic diffusion with respect to two significant seismic events ($\log(E) > 7.9$). The subsequent plots reflect the decomposition of this parameter into the three coordinate directions X (n-s), Y (e-w) and Z (u-d). Note that the seismic diffusion is limited in the north-south direction and is maximum in the vertical direction. (The scale on each of the three smaller plots is the same.)

Predication of the Trough event

The morning of 3 May 1994 the mine seismologist at Western Deep Levels South Mine observed that the routine contour plot of weighted energy index (averaged over four days) indicated an anomalous stress concentration around a large bracket pillar on the Trough structure (referred to as the Trough event). An updated contour plot was produced at mid day. The contours indicated a further increase in stress and a decision was made to evacuate that part of the mine and to keep workers out until the conditions changed. At 18h53 a local magnitude 4 tremor occurred along the Trough structure, followed by several aftershocks in the immediate surroundings. The details of the procedures followed are given in an internal report (Naude 1994). The analysis summarised below is from Mendecki, 1994 and Mayer and Mendecki, 1995.

The Trough structure consists of a west dipping mafic dyke which varies in thickness from 5 to 15 m. The dyke is flanked by faults of small (<20 m) throw. Available data allowed a simplified approximation of the Trough structure geometry as shown in Fig.20.

The precursory behaviour of the Trough structure and environs was studied through spacetime analysis of seismic viscosity and energy index using three dimensional iso-surfaces. The most striking result from the 3D analysis was the recognition of a seismic gap between two lobes of seismic viscosity iso-surfaces, coinciding with the Trough surface. Here, seismic gap is defined as a volume of relatively high seismic viscosity (volume resisting the seismic flow of rock). Such a volume will be characterised by high spatial gradients in seismic stress and seismic strain rates, the gap being slow to deform and accumulating elastic strain. If the gap suddenly fails, a major seismic event may result. This is exactly what happened in the case of the Trough event. The stress history of the last 24 hours may be summarised by two images, the first spanning the period 18h00 on 2 May to 09h46 on 3 May and the second image covering the period 09h46 to 18h50.

During the first period, stress was generally increasing in the seismic gap and along the surrounding part of the Trough structure, as shown by differentially shaded contouring of energy index on the iso-surface of seismic viscosity and additional contour lines on the Trough structure (Fig.21).

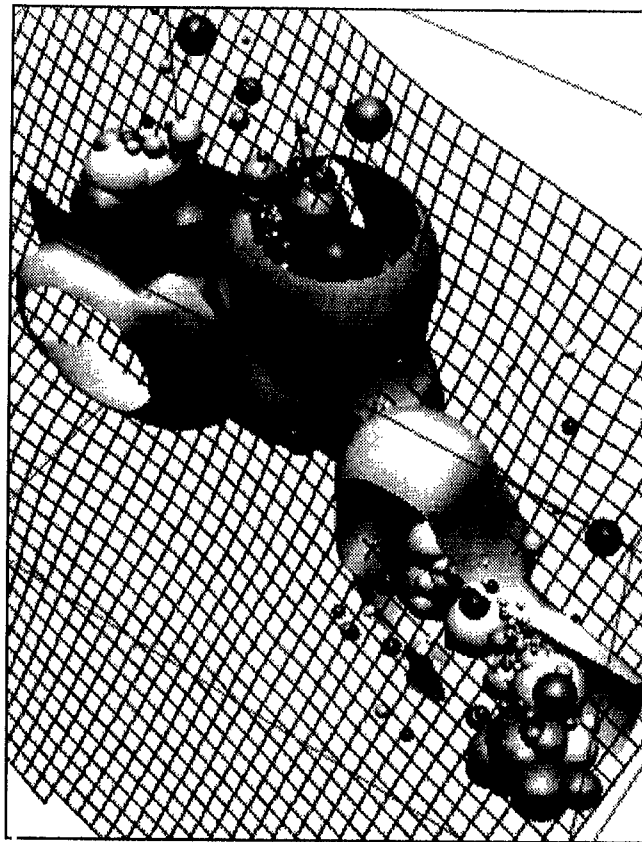


Fig. 20. Seismic events spatially associated with the Trough structure for the period 1/1/94 - 3/5/94. The cutaway iso-surface is of a particular seismic Deborah number.

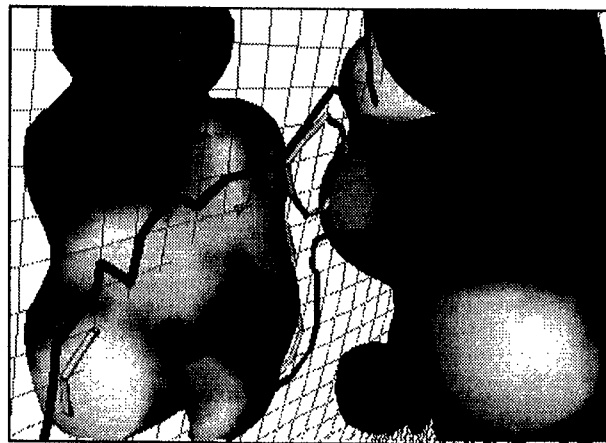


Fig. 21. Iso-surface of seismic viscosity delineating volumes of accelerated seismic flow of rock. A gap is defined where seismic deformation is retarded and it coincides with a particular part of the Trough structure. The iso-surfaces are based on seismic events from 1/1/94 to before the Trough event of 3/5/94. The greyscale shading and contour lines on the fault surface depict variation in EI (the lighter shades reflecting high values) based on seismicity from 18h00 on 25/5/94 to 10h00 on 3/5/94. The mesh lines representing the Trough structure are spaced at 40 m.

During the second period, the stress dropped in the seismic gap reflecting the softening of this part of the rockmass (nucleation volume) where the Trough event occurred (Fig.22).

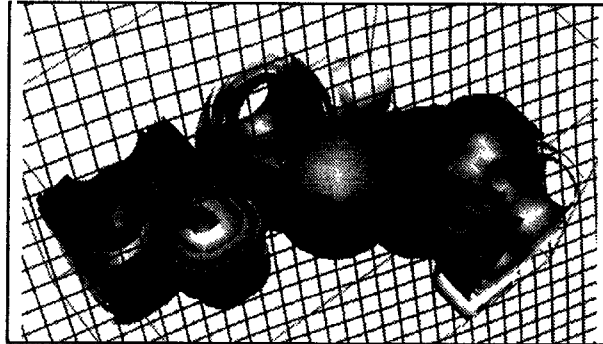


Fig. 22. Similar to Fig.21, showing isosurfaces for different seismic Deborah number values as well as the Trough event (sphere at centre).

A time history analysis of seismic viscosity and seismic diffusion shows that precursory softening and an increase in seismic diffusivity took place a few hours before the Trough event (Fig.23).

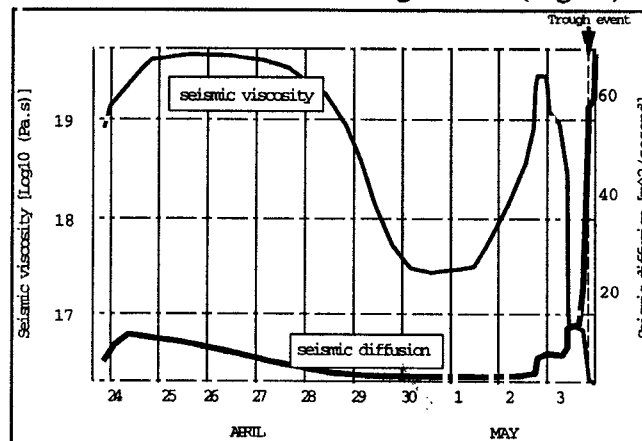


Fig. 23. A time history analysis reflecting the seismic behaviour of the fault/bracket pillar environment during the 10 day period prior to the Trough event.

Routine warnings

Another example case from President Steyn Mine No 4 Shaft is the ALARM issued by the mine seismologist on 10 July 1995 for one of the production areas routinely analysed. Fig.24a is a ΣV_A and moving window EI time history analysis for the area showing the time of the warning and that of a local magnitude 2.5 event. Fig.24b shows that a drop in seismic Schmidt Number also “predicted” the event rather well. To date, more than 60 warnings, based on time history analyses,

have been issued.

This method of stability evaluation is presently applied to at least 50 production sites in the Far West Rand, Klerksdorp and Welkom areas on a daily basis.

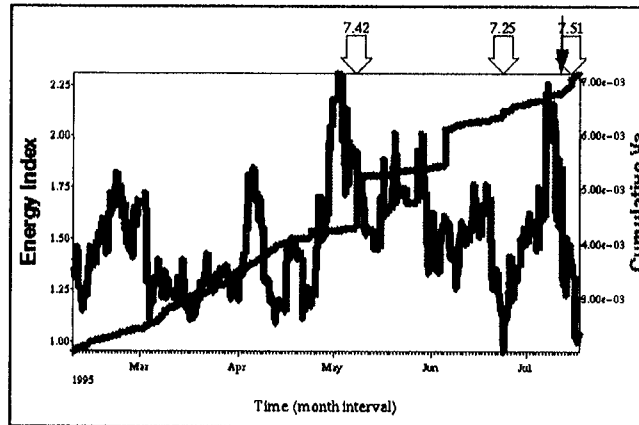


Fig. 24a. Time history analysis for one of the production areas monitored daily at President Steyn Mine No.4 Shaft, showing accelerated seismic strain rate (steepening of ΣV_A curve) and drop in stress (drop in moving window EI) prior to a local magnitude 2.5 event (open arrow). The solid arrow shows the time an actual ALARM was issued.

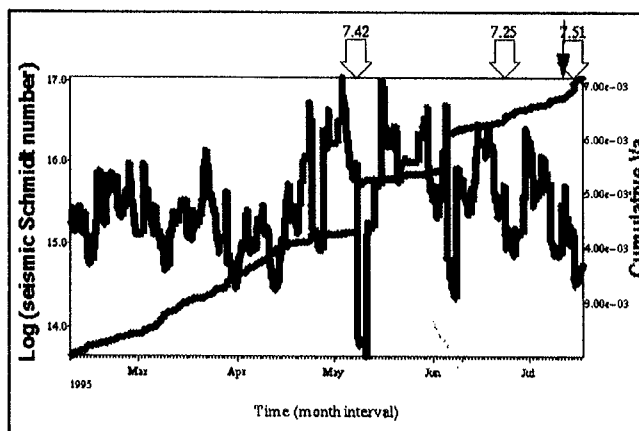


Fig. 24b. Same as Fig.24a, showing moving window $\log(\text{seismic Schmidt number})$.

One aim of the research was to develop methodologies for the short term prediction of unstable rockmass behaviour. While the Trough event presents a good example of the time scale applicable in some of the cases large instabilities, see Fig.23, similar patterns in rockmass behaviour were found in cases where network sensitivity allowed. To illustrate this, two cases are described.

In the first example case a VCR longwall was monitored with a specially enhanced system to yield a sensitivity of moment magnitude -0.8 , i.e. in general, all events of moment magnitude -0.8 and larger were recorded by at least 5 three-component seismic monitoring sites. The seismic record for the area is remarkable because over a 6 month

period nearly 4200 events were recorded of which fewer than 100 (<2.4%) occurred outside the blast time of 2 hours period. Each of the 19 events greater than moment magnitude 1.0 were triggered by blasting. The rock mass behaviour prior to two of these rather small events are considered as examples.

The response to daily blasting is a 'burst' of small seismic events with $\log(EI)$ values which vary by an order of magnitude. The general pattern involves a sudden increase in EI , followed by a decrease (Fig.25). This is, of course, consistent with what is expected: a sudden increase in the stress due to dynamic loading in the rockmass ahead of the advancing mining face, followed by some relaxation. The EI values of the last events reflect the level of stress to which the rock mass settled after the blast.

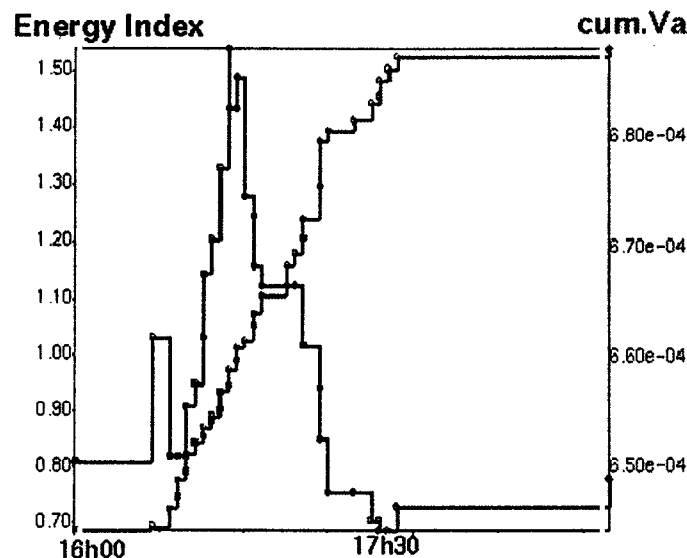


Fig. 25. A typical response to blasting of a longwall at Western Deep Levels South Mine as measured by cumulative V_A and EI . Note the indicated initial rise in stress level and the gradual relaxation.

In the case of the events of interest, this daily final EI value decreases prior to the events (Fig.26a and b). The management of data with such extreme time distribution presents a special problem for stability analysis. The calculation of seismic Schmidt number is highly sensitive to the length of the moving window. By setting this time window at less than 24 hours, 20 hours in this case, the specific effect of the daily blast is quantified. A daily decrease in the value of this parameter is also observed (Fig.26a and b).

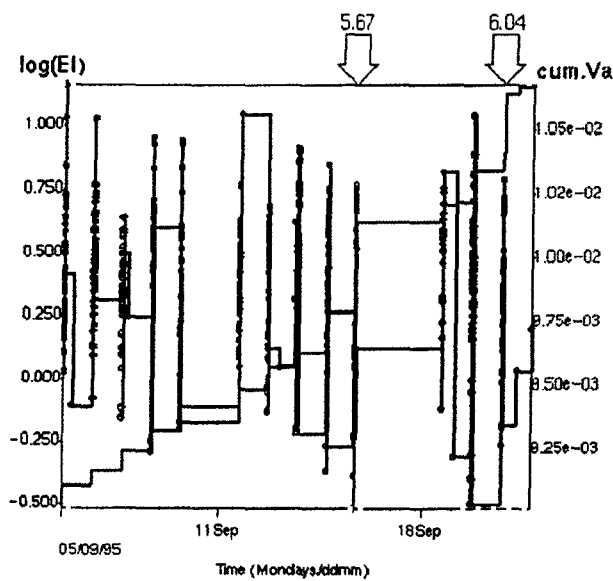


Fig. 26a. Daily response to blasting of a longwall production area at Western Deep Levels South Mine as measured by $\log(EI)$. Note the drop in both parameters prior to larger events.

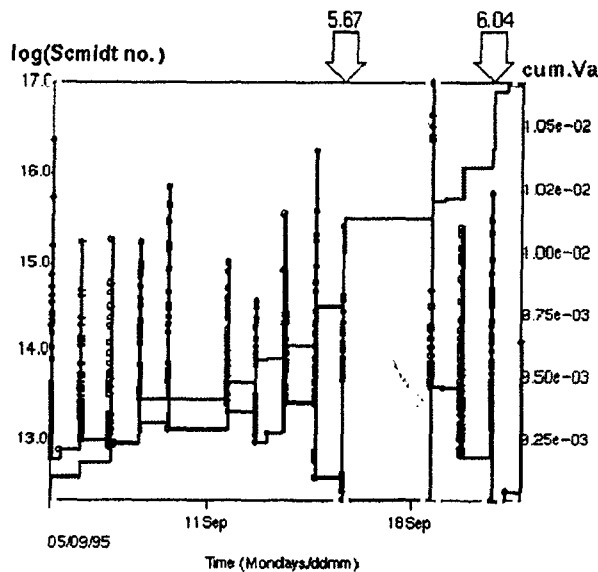


Fig. 26b. Daily response to blasting of a longwall production area at Western Deep Levels South Mine as measured by $\text{Log}(\text{seismic Schmidt number})$. Note the drop in both parameters prior to larger events.

Seismic cover in the area of the second example is equivalent to that of the first case, i.e. network sensitivity down to moment magnitude -0.8. In general, the rock mass responds differently to production blasting since large events tend to occur several hours after blasting. A moment magnitude 1.6 event is well predicted by a combination of seismic Schmidt number and EI (Fig.27a and b). The event occurred near midnight. Comparing the afternoon response to

blasting with that of six days before shows several differences. The range in EI values of blast triggered events is maximum, i.e. the difference between the highest and the lowest values, the seismic Schmidt number is lowest and low values in both EI and seismic Schmidt number are maintained during the post-blasting seismic activity.

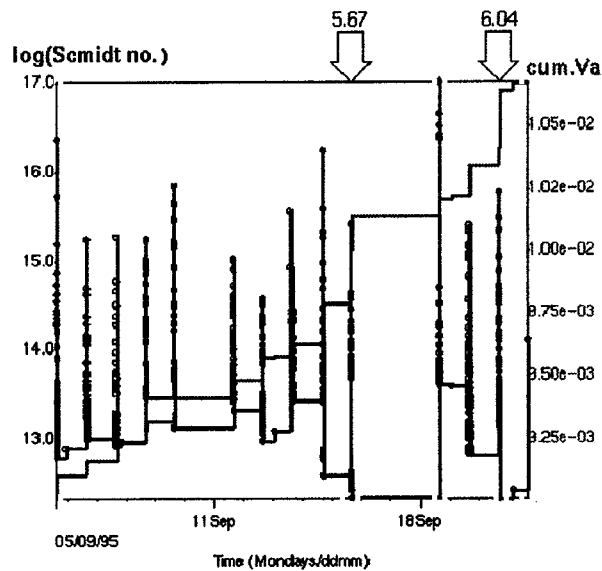


Fig. 27a. Daily response to blasting in a shaft pillar mining area at Welkom as measured by log(EI). Note the drop in both parameters prior to a larger event.

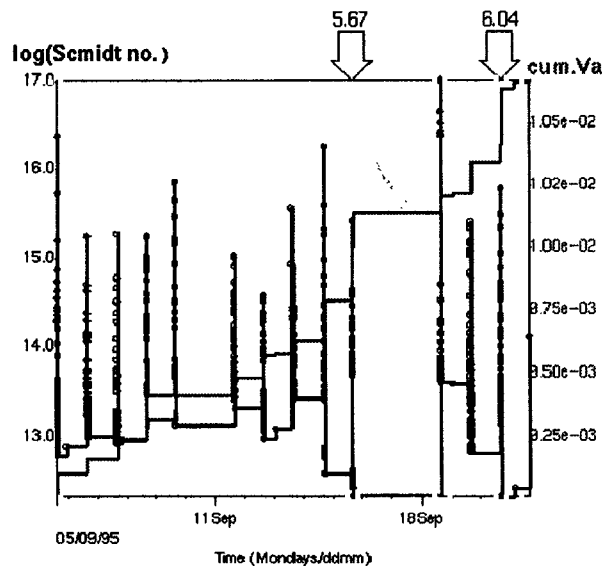


Fig. 27b. Daily response to blasting in a shaft pillar mining area at Welkom as measured by Log(seismic Schmidt number). Note the drop in both parameters prior to a larger event.

NOTES IN CONCLUSION

1. The new, higher standards of seismic data acquisition, seismological processing and interpretation have been defined and technology transferred to the mining industry. It is currently applied on 20 SA gold mines on a routine basis. Fifteen mine seismologists have already been specifically trained for this purpose and are employed in the SA gold mining industry, while several more are in training.

2. A new methodology for the continuous quantification of rock mass response to mining in space and time has been developed and applied. New seismic parameters, i.e. energy index, apparent volume, viscosity, relaxation time, seismic Deborah number, diffusion and seismic Schmidt number, have been defined to quantify the complex nature of seismic flow of rock. The phenomenological model of the nucleation of rock mass instabilities has been developed and tested in hundreds of cases in both forward and back analysis mode. Extremely encouraging is the observation that there seems to be a degree of scale invariance in seismic rock mass behaviour before large and small events. Basic guidelines for seismic data analysis and interpretation for the purpose of early warning of large instabilities have been defined.

The procedure to quantify the potential for instability in terms on "time to failure" has been defined and is currently being transferred to the mining industry for daily use.

3. Using nonlinear dynamics (chaos) theory the predictability of seismic rock mass behaviour has been demonstrated and its limits calculated. In all cases considered, these limits are always manageable and range from a few hours to about three weeks.

4. A success rate of 35% to 60% has been achieved in the forward prediction of larger rock mass instabilities at a few sites where the new methodologies are used in operational mode. The success rate is best where best coverage assures a high sensitivity and data throughput. Reaction to the warnings include improvement of support, the slowing down, or temporary suspension, of production, orderly evacuation (e.g. 5 hours before a magnitude $m_M=4.0$ rockburst a specific part of a mine was evacuated - see *Prediction of the trough event*).

5. It has been shown that the success rate in predicting instabilities depends on the sensitivity and throughput of the seismic monitoring system. There is a need for a research programme on the application of nonlinear dynamics to the prediction of rock mass instabilities and for technologies capable of recording, processing and integrating thousands of seismic events per day to improve the success rate of rockburst prediction.

CHAPTER 1

CHARACTERISTICS OF SEISMIC MONITORING SYSTEMS FOR MINES

This document describes the necessary features of the seismic system so that quantitative seismology may be performed.

A seismic event is considered to be described quantitatively when, apart from its timing and location, at least two independent parameters pertaining to the seismic source, *e.g.* seismic moment and radiated seismic energy; or seismic moment and stress drop, are determined reliably.

The magnitude range of seismic events to be measured determines the types of transducer to be used, which in turn dictates the characteristics of the data acquisition system. The largest events experienced in rockburst prone mines range between local magnitude $m=3$ and $m=5$. The smallest events that are useful in determining the state of the rock in seismically quiet periods have magnitudes between $m=-4$ and $m=-3$ depending on noise levels and other environmental factors. The seismic system must be able to cope with these extremes, even if coverage to the limits is not necessary in all areas.

The medium whereby data is communicated to a central point for analysis and storage has the most influence on the character of a seismic system. Where data must be collected over a large area and results are required immediately, the cost of the communication system can rival that of the acquisition instrumentation and computers. Optical fibre communication, which could profoundly influence the shape of future systems, but is not yet widely available in all mines, is included for completeness.

Finally, physical parameters describing the seismic sources and the rock mass must be extracted from the data and the results analysed and presented in a form useful to mine management.

1.1 TRANSDUCERS

The minimum range of frequencies that must be recorded for meaningful seismological processing is determined from the expected corner frequencies of events occurring in the volume to be monitored. To correctly measure the seismic moment we need frequencies down to at least an octave or 5 spectral points, whichever is lower, below the corner frequency of the largest event to be analysed. To correctly measure the radiated seismic energy we need frequencies at least 5 times above the corner frequency of the smallest event to be analysed. Because of the requirements for the

quantitative description of seismic sources the direction of ground motion must be resolved and all sites should have three orthogonal directional sensors (transverse sensitivity < 5%).

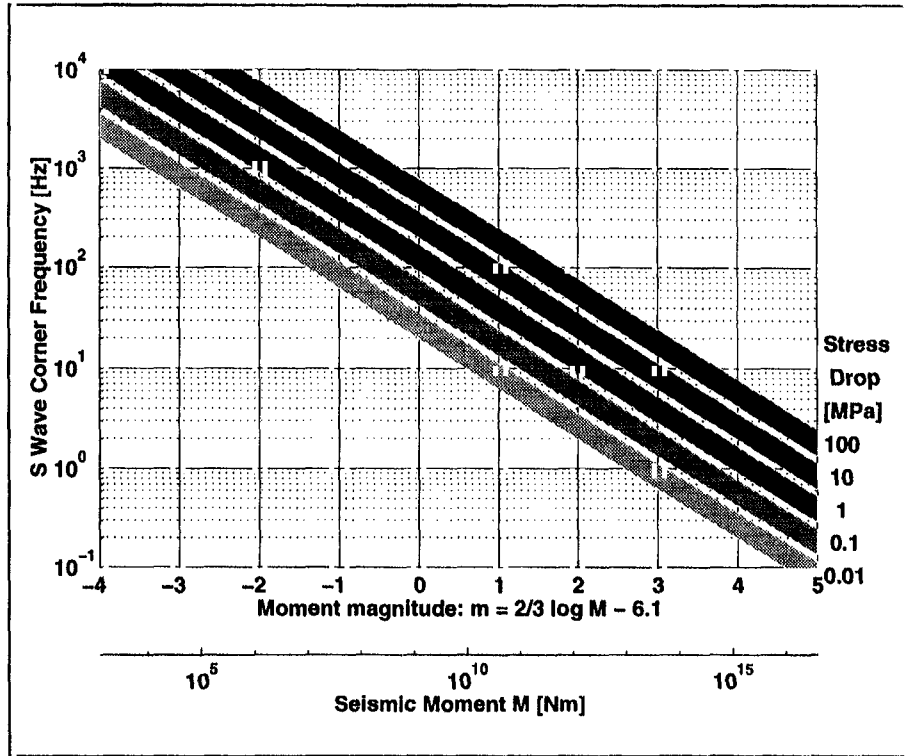


Figure 1.1 Expected S-wave corner frequencies, f_c , as a function of seismic moment, M , for a range of stress drops, $\Delta\sigma$. The general relation is given by:

$$\log M = \log (16/7) + 3 \log (KV_s/2\pi) + \log \Delta\sigma - 3 \log f_c$$

where K is a model dependent term, and V_s is the S wave propagation velocity. A value of $K = 2.34$ from the Brune model is illustrated. The width of each band shows the variation with V_s from 2000m/s, typical of soft rock, to 3400m/s, for hard rock. Although stress drop and moment are independent parameters, very small events are not observed at very high stress drops, which reduces the high frequency requirements.

Fig.1.1 shows the expected S-wave corner frequencies as a function of seismic moment or moment magnitude for a range of stress drops, as indicated by the bold diagonal lines. The data are derived from the Brune model and the width of the lines illustrates the difference between hard and soft rock mines. Although stress drop and moment are independent parameters very small events are not observed at very high stress drops. This lowers the high frequency requirements for the system.

Commonly available transducers have reduced sensitivity below 4.5 Hz, although amplitude correction may allow the signal to be covered down to 2 Hz with reduced dynamic range. In Fig.1.1 this compares to corner frequency of 10 Hz and higher. Lower

frequency transducers tend to be large, specialised earthquake monitoring tools and as such are expensive and difficult to install. A few low frequency installations on a network can increase the confidence placed in measurements of seismic moment of large events.

The attenuation of seismic waves with distance depends on the local geology. Fig. 1.2 illustrates the relationship between measured peak ground velocity and distance from the source for a range of seismic energies as observed in the O.F.S. Goldfield. The data were obtained by fitting a plane to the log of the peak ground velocity measured at each each station as a function of the log of the total radiated seismic energy for the event and the log of the distance of the station from the source. Fifteen thousand events were used in the fitting process. While these particular values only apply to the region where they were measured, they do give an indication as to the range of ground velocities that may be expected.

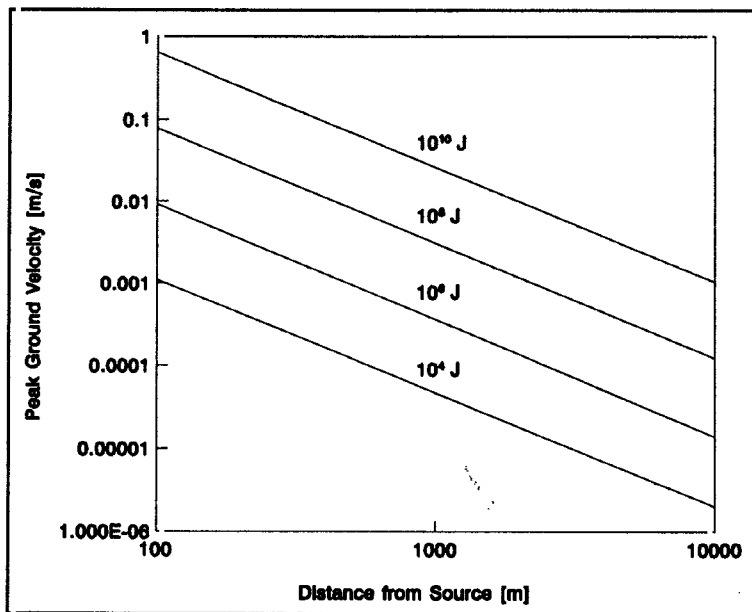


Figure 1.2 Measured peak ground velocities as a function of source distance for events with a range of radiated seismic energies. The lines represent a fit to data from 15000 events recorded in the O.F.S. Goldfield, yielding the relation:

$$\log V = 0.463 \log E - 1.402 \log R + 0.988$$

where V is the measured peak ground velocity at each station, E is the radiated seismic energy of the event and R is the distance of the station from the source.

The range of particle velocities and frequencies that can be

measured with commonly available sensors are illustrated in Fig.1.3. Dynamic range is the ratio of the maximum measurable signal to the noise level, and is expressed in dB, calculated as 20 times the common logarithm of the voltage ratio. Because the geophone is a passive device, the signal conditioning equipment or the intrinsic ground noise effectively sets the noise level. A data acquisition system dynamic range of 132 dB, with a noise floor matching the 10^{-7} m/s environmental noise expected in mines, has thus been superimposed on the geophone response in the figure. This is responsible for the frequency independent noise level and the velocity clipping at intermediate frequencies.

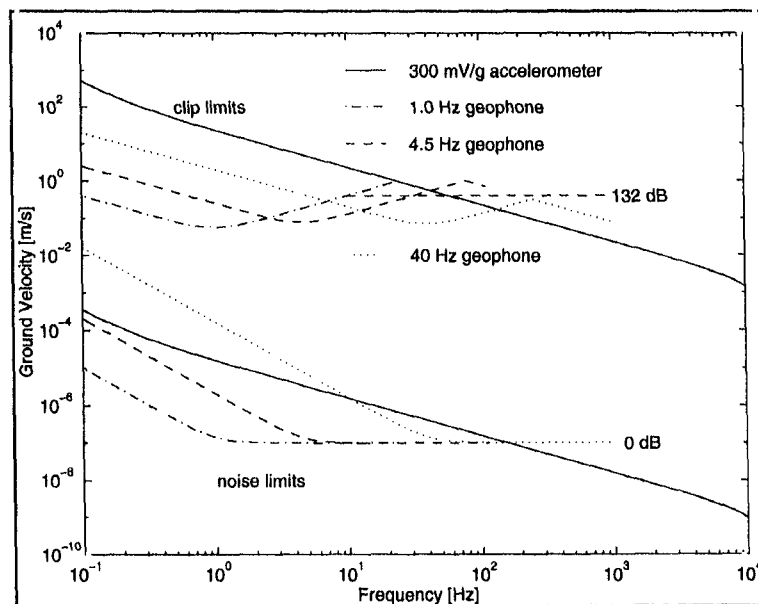


Figure 1.3. Sensitivity and dynamic range of sensors commonly used in mine seismic systems. The region between the limits represents the usable range for each instrument. The geophone's greater sensitivity up to several hundred Hz is clearly shown, as is the loss of dynamic range due to displacement clipping below these frequencies. A data acquisition system dynamic range of 132 dB with its quantization noise matching the expected ground noise of 10^{-7} m/s is superimposed on the geophone data.

Geophones exhibit better sensitivity over the lower frequencies of interest, whereas accelerometers excel at the higher frequencies and can measure without distortion the large amplitude, low frequency strong ground motions of nearby large events.

Geophones

High quality miniature geophones are inexpensive, reliable and

commonly available thanks to extensive use by the oil exploration industry.

Their strong point is their sensitivity over a range of 4 to 500 Hz (typically more than 20 V/m/s when damped) which means that, when used in combination with good amplifiers, the ambient ground noise determines the system noise level of $\sim 10^{-7}$ m/s at the quietest sites in mines. These frequencies also propagate through the rock with little attenuation, so the sensor sites may be fairly widely spaced throughout the mine. The low frequency amplitude and phase responses of a geophone are shown in Fig. 1.3 and Fig. 1.4 respectively. The decreasing sensitivity below 4.5 Hz (the lowest commonly available geophone natural frequency) may generally be corrected down to 2 Hz by suitable processing, since these frequencies are only of interest for large magnitude events which produce correspondingly large amplitude ground motions and the signal to noise ratio is good. Because the output reflects ground velocity, the kinetic energy may be calculated directly, and only one integration is necessary to obtain displacement for the seismic moment. Geophones are inexpensive and relatively easy to install in boreholes long enough to reach intact rock, as long as some care is taken to ensure they are precisely vertical or horizontal (within 2°).

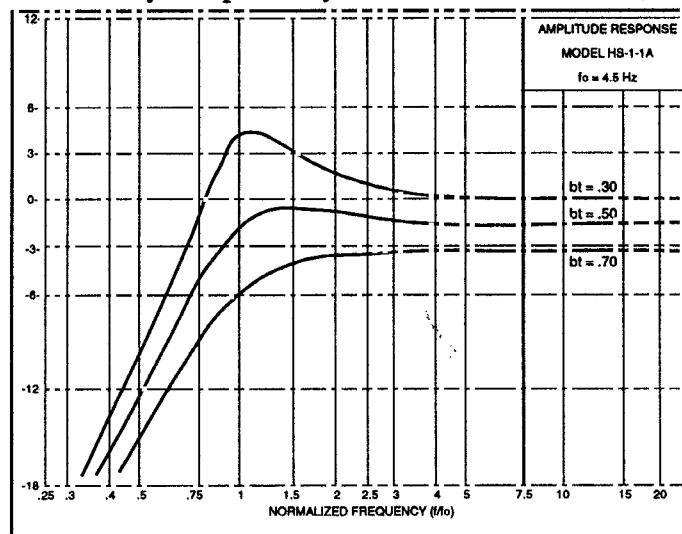


Figure 1.4 Velocity output frequency response of the OYO - GEOSPACE model HS-1 geophone for different values of electrical damping. The general transfer function of a geophone is

$$\frac{s^2}{s^2 + 2 \cdot bt \cdot s + 1}$$

and the steady state frequency response is obtained by setting $s = jf / fo$ where bt is the total damping as a fraction of critical and fo is the undamped natural frequency.

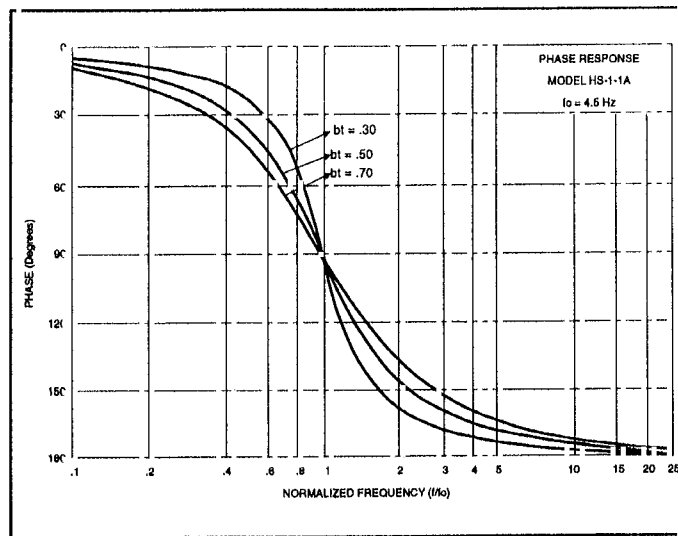


Figure 1.5 Phase output frequency response of the OYO - GEOSPACE model HS-1 geophone for different values of electrical damping.

The weak points of these geophones are distortion and clipping introduced at larger displacements (1 mm to 3 mm) produced by nearby large events, and spurious resonances at frequencies above 150 Hz if driven transversely (in general the ground motions are not constrained to a single direction). Because the geophone output reflects ground velocity, the displacement clipping is not immediately apparent on inspection of the seismograms. The theoretical dynamic range of these sensors is very large, see Table (1.1). As the large events produce low frequencies, we are concerned with the dynamic range at f_0 . This is reduced further in mines by the relatively high ground noise.

Sensor model	Frequency			
	500 Hz [dB]	f_{vmax} [dB]	30Hz [dB]	f_0 [dB]
HS-1	143	158	148	131
SM6	143	160	152	135

Table 1.1 Dynamic range of two geophones at different frequencies. f_{vmax} is the frequency at which the maximum velocity may be measured, allowing for displacement and acceleration limits.

Accelerometers

Where seismic event with corner frequencies above 100 Hz are the

main interest and/or the network is small and dense then accelerometers are the sensors of choice. The sensitivity of a given accelerometer to ground velocity or radiated seismic energy increases with frequency, allowing smaller events to be detected than by a comparable geophone, and without the danger of clipping on large, low corner frequency events. The peak acceleration produced by an event depends more on stress drop than moment and the peak acceleration measured for a given event increases with signal bandwidth. For a dense mine network as envisaged above, piezo-electric accelerometers with built-in amplifiers are used. These instruments have a resonance peak at the high end of the frequency range, see Fig. 1.5. Typically, a device with a resonance at 20 kHz would be used, giving a maximum usable frequency of 10 kHz. Any incident signal at the resonance frequency is amplified mechanically by 30 dB or more, and can lead to clipping, hence the usual choice of such a high value. An insufficiently rigid mounting can cause an apparent downward shift of the resonance frequency into the band of interest.

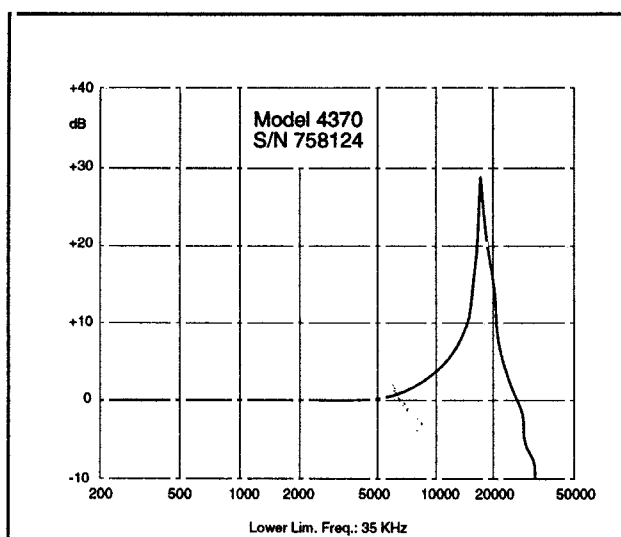


Figure 1.6 Calibration sheet for a B&K 4370 transducer clearly showing the resonance peak at 18 kHz.

The remaining characteristics are largely determined by the internal amplifier. The sensitivity is typically 100 mV/g, the noise level 200 μ g (20 μ V), and the maximum linear signal 50 g (5 V) so the dynamic range required from the acquisition system is less than 120 dB. For comparison with the geophone see Fig.1.2.

The low frequency limit of the amplifier response is typically 3 Hz, although some only roll off below 1 Hz. Frequencies of 3 kHz and above are generally heavily attenuated by the rock. This varies

from site to site, but even in competent Witwatersrand quartzite, source to sensor distances of more than 300 m cause the higher frequency signal to be lost.

Transducer Summary

Geophones provide reasonable coverage down to $m=0$, as shown in Fig. 1.1, provided that there are five stations within 1 km of each event. A dense network is required to compensate for both the geophones' relative insensitivity and the high attenuation of the rock mass to the dominant frequencies of these events. Care must be taken not to accept results from stations near enough to large events to suffer low frequency, large displacement distortion and clipping problems.

Apart from large, low stress drop events, full coverage down to $m_M=-3$ may be provided by a dense network of accelerometers, which have the high frequency sensitivity to reliably detect negative magnitude events and the low frequency insensitivity to measure close, large events. Because of the required density for full coverage, at least five stations within 300m of any expected source area, effectively a separate network is established around each longwall or other working area. Even so, several times more stations will probably be required to cover a given mine with accelerometers than geophones. Table 1.2 illustrates three typical network configurations and introduces the problem of transmission bandwidth.

Lower magnitude limit	-3	0	1
Network Type	Dense accelerometer 5 stations < 300m	Dense geophone 5 stations < 1 km	Regional geophone 5th station > 2 km
Sensor/ anti-aliasing filter	10 kHz	500 Hz	200 Hz
Analogue FM transmission (per component)	100 kHz	5 kHz	1 kHz
Sampling rate	50 kHz	4 kHz	2 kHz
Digital PCM transmission (per 3 components)	5 Mb/s	400 kb/s	200 kb/s

Table 1.2 Typical networks with different sensor densities and direct transmission frequency requirements

Sensor Orientation

There are two aspects to sensor orientation: Firstly, if the lower natural frequency geophones are not installed precisely vertically or horizontally they do not function correctly. Secondly, the true directions of ground motion must be found for each event to be described quantitatively. For these reasons it is advantageous to be able to install sensors accurately with a given orientation, and to be able to estimate the orientation of sensors once installed.

For installation in a borehole, the sensors are usually mounted to a holder or "boat" which is almost as wide as the borehole and much longer than it is wide, so that it closely assumes the orientation of the borehole, which may be determined by surveying. A keyed rod may be used to rotate the boat within the borehole during installation to allow orientation about the borehole as axis. For a vertical hole the handle of the keyed rod may be aligned with a survey mark and the boat assumed to be aligned likewise with a few degrees margin of error. For an off vertical hole some feedback may be obtained as to the orientation of the sensors themselves, either by driving the sensors (if they are geophones) and rotating the boat until a symmetric clipping pattern is obtained, or by including a mercury switch or other tilt sensitive device into the boat. Of course, care must be taken to preserve sensor signal polarity throughout the data acquisition modules.

Once the sensors are operating, any deviation from the assumed orientation may be calculated by comparing the P wave polarization direction with the hypocentral direction for artificial sources or natural events whose locations are known accurately. Given three or more such known locations it is possible to determine a rotation matrix A such that

$$\hat{x}_i = A \hat{y}_i$$

where x_i is the unit direction vector from the sensor to the source for the i th event in standard coordinates determined from the relative source and sensor locations and y_i is the same vector in sensor coordinates determined from the P wave polarization. If the direction of one of the sensor axes is known precisely, the unknown rotation about that axis may be determined from a single event. The rotation matrix A may then be used to transform the ground motion from sensor coordinates into standard coordinates for each sensor and thus contribute to determining the source mechanism for each event.

1.2 DATA TRANSMISSION

The seismic information is generated as a voltage at the outputs of sensors scattered throughout the mine. After an event occurs, the relevant data must be available in processed form on a central computer within a reasonably short time if the system is to be useful. Different methods of transmitting data from the sensors to the central site will be considered, but first the problem of dynamic range must be addressed.

Medium	Low frequency limit	High frequency limit	Distance limit
Filtered telephone line/ Radio voice channel	300 Hz	3000 Hz 1200 bp/s	20 km
Unfiltered telephone line/ instrumentation cable	0 Hz	40 kHz 80 kb/s	5 km (30 dB loss)
Optical fibre (multimode 820 nm)	0 Hz	50 MHz 5 Mb/s	4 km
Optical fibre (multimode 1300 nm)	1 MHz	125 MHz 125 Mb/s	10 km

Table 1.3 Bandwidth of transmission media. The actual analogue bandwidths are given together with the digital bit rates achievable over distances relevant to mine seismic systems.

Table 1.3 details some transmission media and their bandwidth limits at distances useful in mines. These may be compared with direct transmission requirements in Table 1.2.

Resolution and Dynamic Range

The dynamic range of the sensor signal, as noted above, is 120 dB, being the ratio of the maximum useable signal to the noise level. This causes problems for any type of linear electronic processing of the signal, whether amplification, modulation or analogue to digital conversion. By contrast, the resolution required for accurate calculation of the seismological parameters is less than 1% or -40 dB.

It is perhaps worth illustrating this by considering the A/D converter, since this a necessary component of any system. The dynamic range of 120 dB translates into a voltage ratio of 1 million which needs a 20 bit representation. Practical A/D converters, at the sampling rates of interest, output between 8 and 16 bits. A 12 bit converter, for example, divides its input voltage range into 4095

equal-sized intervals and assigns a number to each, thus a voltage near the maximum value is measured with a precision of 0.025%, while a smaller voltage, say 100 A/D units from zero, is measured with 0.5% resolution, and signals smaller than one A/D unit (which are still 250 times larger than the sensor noise level) may be lost completely. This is in contrast to the transducer, which always produces signals with in the order of 1% accuracy, irrespective of the amplitude. Amplifiers and modulators also exhibit limited dynamic range.

Two different approaches may be used to overcome this problem: The first is compression where a non-linear amplifier is used to apply a lower gain to larger signals. Ideally the transfer characteristic would be high linear gain for very small signals where the sensor noise dominates, and logarithmic for larger signals, as this ensures a constant percentage accuracy. To recover the original value for processing, we must be able to calculate the exact gain for each converted value. If we quantify this approach using the sensor specifications above, *i.e.* 120 dB range at 1% accuracy, we find that the output range of the compression stage is reduced to 70 dB, which matches a 12 bit A/D converter. The second approach, gain ranging, is to use several linear amplifiers at different gains on each sensor and pass the output of each via a separate channel to a multi-channel A/D converter. The output of the channel with the largest signal which is within range of the A/D converter is then saved, along with the number of the gain range. To recover the original value for processing, we must look up the gain for the gain number associated with each sample, and multiply this by the converted value. With the same 120 dB input range and 1% accuracy above, we may use a 12 bit A/D converter and gains of x1, x16 and x256 to achieve the same result.

Transmission Methods

Assuming the signals have been reduced to a reasonable amplitude range by one of the above methods, we may now consider different methods of transmission. Properties are summarized in Table 1.4.

Analogue - Base Band: The sensor signal is simply amplified and transmitted to the central site for digitising and recording.

Analogue - Frequency Modulation: The sensor signal is used to vary the frequency of a carrier signal which is transmitted to the central site where the original signal is recovered, for digitising and recording.

Digital - Continuous (Pulse Code Modulation): The signal is digitised at the sensor site and the digital values are transmitted to the central site.

Digital - Store and forward: The signal is digitised at the sensor site and the values are stored temporarily and fed to a trigger algorithm. When a trigger is detected, the central site is informed and the significant data saved for transmission on request to the central site for recording.

The analogue baseband method is generally impractical because of its susceptibility to interference. The cable between the sensor and its associated electronics represents this type of transmission, of course, but even in the most benign environments this distance should be limited to 300 m, and in general, the shorter the better.

The direct digital (PCM) method for mine seismic systems probably still lies somewhere in the future, because it is rare to find a signal channel of sufficient distance-bandwidth product in mines. As the use of optical fibre becomes more common, and the limits for copper twisted pair are pushed out for computer communication, this method will become more viable. Unfortunately, the digital telephone standard of 8 kHz sampling rate and 8-bit compressed samples does not quite match seismic system requirements.

This leaves a choice between analogue FM or digital store and forward transmission. There are cases where the direct link between seismic signal bandwidth and FM transmission bandwidth rules out the use of FM, for example where the 10 kHz accelerometer signal, or even the full 2 kHz geophone signal, must be monitored via a 3 kHz filtered telephone or radio voice channel. In this type of situation the decoupling of signal bandwidth from transmission bandwidth by the store and forward method makes it the only viable proposition.

The advantages of the digital store/forward system are clearly shown in Table 1.4. The flexibility of this system leads to a multiplicity of possible system organisations all utilising the same basic communication method. The common feature of all these systems is that they discard data at the sensor site until triggered, this allows the decoupling between sampling rate and transmission rate. If a site records for 1% of the time, the data rate is decreased by a factor of 100. This compensates for the increase in bandwidth due to digital encoding. In the extreme case the data may be automatically processed at the sensor site, and if successful, only the results transmitted, providing a further factor of 40 data compression.

	Immediate				Delayed
	Analogue		Digital		
	Base Band	Freq. Mod (FM)	Continuous (PCM)	Store/Forward	
Compression [dB]	0 40	0 40	—	—	
Dynamic Range [dB]	60 100	80 120	120+	120+	
Bandwidth [kHz]	2	20	200	3+*	
Multiplexing	No	FDM	TDM	Packet	
Complexity	Low	High	Moderate	High	
Triggering	Central	Central	Remote	Remote	
Timing	Central	Central	Central	Remote/Linked	
Noise Immunity	Low	Moderate	High	High	
Error Detection	Manual	Carrier	Code	Protocol	
Error Correction	No	No	Code	Retransmit	
Base station Acquisition Load	High	High	High	Low	
Manual effort in Calibration	High	Moderate	High	Low	
Fibre Optics	No	Yes	Yes	Yes	
"Duplex" coms	No	No	No	Yes	

*Table 1.4 Characteristics of transmission techniques
Independent of analogue bandwidth*

Triggering and recording must therefore be done at the sensor site, while association and final processing of each event must be performed at the central site. The degree to which processing should be distributed for maximum throughput depends on the communication rate, see Table (1.5). Obtaining the relative timing between stations requires direct transmission.

Transmission rate per station [b/s]	Level of Distributed Processing
> 38400	triggering
≥ 9600	triggering, decimation
≥ 1200	triggering, decimation, full single station seismological processing

Table 1.5 Level of Distributed processing appropriate for different data transmission rates.

1.3 DATA ACQUISITION IN A DISTRIBUTED SYSTEM

For a digital store and forward system with distributed processing as envisaged above, the data acquisition unit provides the essential functions of digitising, triggering, timing, storage and communication for a single triaxial sensor. A calibration pulse may be applied to a geophone, and some processing may be performed on the data before transmission. In addition, slowly varying ("non-seismic") signals may be sampled, and outputs capable of driving alarms at or near the sensor site may be switched whenever seismic or non-seismic inputs exceed preset levels.

Dynamic Range

The problems that seismic signals pose for a data acquisition system relate to the wide variations in amplitude, frequency content and duration from one event to another, coupled with fact that they are transient, *i.e.* the system must adapt itself to the signal instantly as it occurs. The problems of handling 120 dB dynamic range of amplitude are discussed above under data transmission, while duration range is discussed below under triggering.

The frequency content of the signal determines the sampling rate. By Nyquist's theorem, any signal present at higher than half the sampling frequency will appear as a low frequency signal (aliasing) and distort the desired data. An anti-aliasing filter is thus used before sampling. A filter with a very sharp transition between pass and stop bands would allow maximum use to be made of the bandwidth afforded by a given sampling rate. See Fig. 1.6. However, such filters introduce phase distortion into the pass band, visible as overshoot and ringing in the time domain, which needs to be accommodated for seismic processing, see Table (1.6).

Filters with a Bessel characteristic are therefore used, which introduce minimum phase distortion but roll off very gradually, so that a sampling rate of 8 times the highest signal frequency must be used to reduce aliasing to an acceptable -40dB (1%). Geophones with a usable 500 Hz bandwidth thus require sampling at 4 kHz and accelerometers with 10 kHz bandwidth require 80 kHz sampling. In the latter case, the accelerometer resonance is a complicating factor, but signal at the resonance frequency of 20 kHz will not be aliased.

Impulse and steady state attenuation characteristics						
	Poles	Step rise time	Overshoot (%)	Settling Time sec		Stopband dB $f=2f_c$
		0-90% (s)		to 1%	to 0,1%	
		Bessel $f_c=1\text{Hz}$		4	0,5	
	6	0,6	0,6	0,7	1,2	14
Butterworth $f_c=1\text{Hz}$	4	0,6	11	1,0	2,8	24
	6	0,9	14	1,3	3,9	36
Chebyshev $f_c=1\text{Hz}$	4	0,7	18	3,0	5,4	31
	6	1,1	21	5,9	10,4	54

Table (1.6) Time domain performance of anti-aliasing filters.

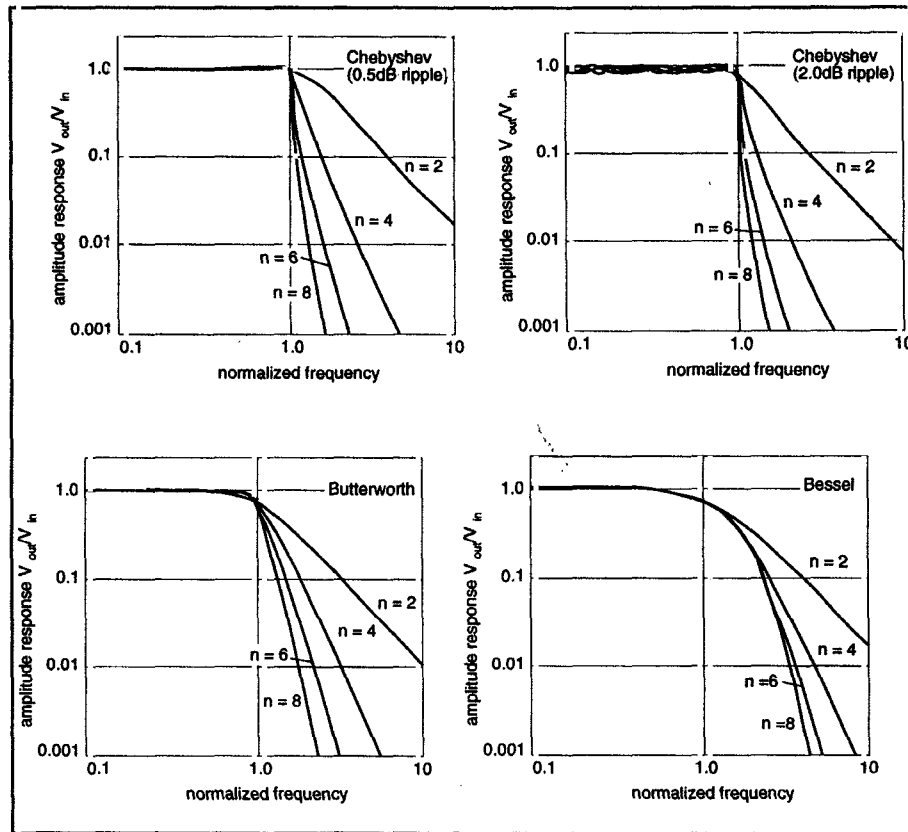


Figure 1.7 Response characteristics of the Chebyshev, Butterworth and Bessel filter showing the effect of the number of poles on the stop band slope.

Once an event has been recorded at a sampling rate of 8 times the highest usable frequency produced by the sensor, the frequency content may be examined and, if the dominant frequency is low enough, the sampling rate may be reduced by decimation to 10 times the dominant frequency of the event. An anti-aliasing digital filter is calculated for the reduced sampling rate, applied to the recorded data, and the result resampled at the reduced rate. This leads to a reduction in storage space, and, if the decimation can be performed at the sensor site, a reduced transmission time.

Triggering and timing

When communication introduces delays, each acquisition unit must trigger and record data independently, then forward the trigger time to the central site for association into an event.

The seismic sensors are monitored continuously and long and short term running averages maintained (LTA and STA). When the ratio of STA/LTA exceeds a certain value on any channel, the acquisition unit triggers and data are recorded until the signal returns to near background level.

The useful range of STA/LTA for triggering is from 2 to 32, depending on the noise characteristics of the site and the sensitivity desired. The lengths of time over which the respective averages are taken should be tailored to the sensor characteristics. This STA/LTA triggering method is sufficient when 3 component sensors are used at the frequencies of interest in mines. Although signals with a ratio of less than 10 between maximum signal and average background noise level do not produce meaningful results when processed, such signals trigger an STA/LTA system reliably.

It is once again important for the sake of conserving storage space and transmission time that the end of the event be recognised, instead of using some fixed maximum size. A small event 200m from the sensor may last only 60ms, whereas a large and/or distant event may sustain the ground motion for several seconds. The processing software requires several hundred samples of pretrigger signal to be recorded for noise evaluation, even after decimation.

The trigger is time-stamped from a local clock which must be synchronised with all units in the network. The clocks are typically stable to better than one part in 10^6 , especially in the stable temperature environment underground, so 100 μ s accuracy may be maintained for 2 minutes, during which time the clocks must be resynchronised. This is achieved by broadcasting an analogue pulse over the normally digital communication lines, thus avoiding any

store and forward delays and synchronising the clocks to the full precision permitted by the available analogue bandwidth.

Event association and communication

Triggers are reported to the central site, which groups together all triggers which could belong to the same event, given their trigger times, sensor locations and P-wave velocities. If enough stations fall into the same group an event is declared and the seismograms are fetched from the outstations and stored for processing. As the communication introduces a delay, the associator waits for a reasonable period before deciding to clear a group with insufficient triggers.

Any form of intercomputer communication may be used, but typically, in mines, voice grade telephone cables are available, which may be used with modems to transfer data via the RS-232 serial ports available on most computers.

In general messages from the central site to the outstations are generated by a single port and broadcast to all stations. When communication is via radio this allows a single transmitter to be used at the central site, and in any case facilitates the broadcast of time synchronisation information. Fault tolerance is obtained by acknowledging receipt of all messages and retransmitting any which are not acknowledged within a reasonable time interval.

A seismogram with a typical length of 2000 samples per channel is transferred to the central site in about 20 seconds at 9600 baud or 2 minutes at 1200 baud. Storage for at least four seismograms should be available in each outstation, so that two seismograms may be held while one is being transmitted and the station continues to scan for triggers. When all buffers are occupied, the one with the lowest maximum amplitude should be cleared if a larger ground motion is detected. Other messages such as trigger reports may be interleaved with blocks of seismogram data.

1.4 CENTRAL CONTROL SITE

The central site processing facility, whether a single multi-tasking computer or a network of computers, must have sufficient resources to continuously acquire, process, analyse and archive seismic data at the rate that events are detected. If there is no prior seismic coverage, the event rate may be estimated by counting events which can be felt on surface and assuming that any such are at least $m=1$,

and multiplying the count by ten for each magnitude below this to which coverage will be established. For example, if 5 events are felt per day, and full coverage will be established down to $m=-1$, then the system should be designed to cope with 500 events per day.

When one of the forms of direct transmission are used, the central site must perform the triggering and recording functions, and for analogue transmission systems, digitising as well. In this case the signal from each sensor component is demodulated if necessary and fed to an A/D converter. The signals may also be passed to a hardware trigger unit which performs the STA/LTA triggering algorithm for each site (see the discussion under distributed system — triggering above). When enough sites trigger within a travel-time window, incoming data is recorded on disk. Some provision must be made for recording pretrigger data, usually this is achieved by reading the inputs continuously and discarding data if a trigger does not subsequently occur. Since all channels are recorded simultaneously there is no problem with establishing the relative timing between samples from different sites.

Events per day	50	150	500
% use of CPU (1 MFlops)	12 %	34 %	115 %
Disk storage for one week's seismograms	100 MB	300 MB	900 MB
Disk storage for three month's events (no seismograms)	50 MB	150 MB	500 MB
% communications bandwidth at 1200 b/s	15 %	45 %	150 %
% communications bandwidth at 9600 b/s	2%	6%	20%

Table 1.7 Computer resource usage for hypothetical networks with different event rates, assuming each event is recorded by 10 stations.

For a distributed digital store and forward system, resources start with serial ports for each incoming data line, and sufficient processing power to service these lines and at least run associator software to capture events and store them to disk.

For more than 100 events per day, some form of automatic processing is essential, as the operator then needs only to verify the automatic result rather than start from scratch. One implementation of automatic processing consumes approximately 10 million floating point operations and 200 KB of memory per three component seismogram. The disk storage requirements are 12 KB per

seismogram and 500 bytes of processed data per station in each event. There should be storage for at least one week's worth of seismograms and several months' worth of events online at one time. Offline storage should be available to archive the systems entire history. Using these guidelines a good estimate may be made of the required computing resources for any seismic monitoring system.

Data analysis and presentation systems vary more widely, depending on the required sophistication, from a personal computer with a pen plotter to a powerful 3D stereo graphics workstation and high resolution colour printer.

CHAPTER 2

CONFIGURATION AND SENSITIVITY OF SEISMIC NETWORKS

2.1 OPTIMUM SPATIAL DISTRIBUTION OF SEISMIC STATIONS

It is well known that accurate location of seismic events is of utmost importance. Most parameters calculated in the study of seismicity has a certain dependence, whether it be weak or strong, on the locations of the events. It is true however, that there is a certain error associated with the observations used to calculate the location of a seismic event. The two main components of this error are arrival time determination errors and velocity model errors. Due to the presence of these errors in the input to the location procedure, there is a certain error associated with the calculated location. In this chapter, it will be shown how to spatially arrange the seismic stations in order to minimize this location error.

Configuration of seismic stations is defined by the number of stations and their spatial distribution. In general, the choice of one or another station configuration should depend upon a certain value related to a given configuration. Then, the best network would be defined by its minimum. The value should depend upon a covariance matrix of the seismic event parameters $\mathbf{x}=(t_0, x_0, y_0, z_0)^T$ where t_0 is origin time and $\mathbf{h}=(x_0, y_0, z_0)^T$ are hypocenter coordinates, and T is the matrix operator that stands for transposition.

The choice of the criterion of optimization depends upon the specific character of the considered problem. The most common is the so-called D -optimum planning, which minimizes the determinant of the covariance matrix of the unknown parameters \mathbf{x} (John and Draper, 1975). The D -criterion is based on the argument that the content of the confidence ellipsoid is proportional to $\sqrt{\det[\mathbf{C}_x]}$, where \mathbf{C}_x is covariance matrix of unknown parameters \mathbf{x} . An obvious optimality criterion therefore is to make this ellipsoid as small as possible by minimizing $\det[\mathbf{C}_x]$. A configuration of seismic stations that minimizes $\det[\mathbf{C}_x]$ is called D -optimal. This criterion has several attractive features. If properties of determinants are used, it is not necessary to calculate the covariance matrix. Assuming that the seismic event parameters \mathbf{x} are estimated by help of any norm within the range between 1 and $+\infty$, the covariance matrix of these parameters, \mathbf{C}_x , with accuracy to the constant, is equal to $(\mathbf{A}^T \mathbf{A})^{-1}$, where \mathbf{A} is the partial-derivative matrix of computed arrival times with respect to \mathbf{x} (Kijko, 1994). Since, by definition, $\det[\mathbf{C}_x]=(\det[\mathbf{C}_x^{-1}])^{-1}$, minimizing $\det[\mathbf{C}_x]$ will maximize $\det[\mathbf{A}^T \mathbf{A}]$, satisfying the D -optimality criterion.

The D -optimization is much more complex when the process (travel times of seismic waves in our case) is described by nonlinear equations and unknown parameters \mathbf{x} are random. In this case the elements of the matrix \mathbf{A} and, equivalently, the covariance matrix \mathbf{C}_x are functions of the *unknown* parameters \mathbf{x}_{TRUE} . Since \mathbf{x}_{TRUE} is not known, the matrix \mathbf{C}_x cannot be calculated and the whole procedure is not applicable. The technique frequently used in such a case is the minimization of the mean value of $\sqrt{\det[\mathbf{C}_x]}$ in the whole domain of the occurrence of seismic events in the given area of seismicity (Kijko, 1977)

$$\text{minimum} \int_{D_h} p_h(\mathbf{h}) \sqrt{\det[\mathbf{C}_x]} d\mathbf{h} \quad (2.1)$$

where D_h is the space domain of the occurrence of seismic events, and $p_h(\mathbf{h})$ is the function describing the space distribution of the event hypocenter coordinates $\mathbf{h}=(x_0, y_0, z_0)^T$. Function $p_h(\mathbf{h})$ indicates what the chances are of an event happening in the vicinity of the point with coordinates \mathbf{h} . In practice $p_h(\mathbf{h})$ can be used to signify the importance of the seismic area relative to other seismic areas in D_h . Not only the probability of event occurrence are taken into account, but also other factors such as the lifespan of mining in that area. In relation (2.1) minimization is performed over all possible configurations of seismic stations.

Thus far it is assumed that all n stations in the network are triggered by an event. This means that for all events the partial derivative matrix \mathbf{A} has the same number of rows and equal to n , if only P-arrival times are used for location; or $2n$, if P and S arrival times are employed in location procedure. Physically this implies occurrence of events with such large energies, that seismic waves are detected by all seismic stations. It is obvious, that such a scenario is not always true. This problem can be addressed integrating (2.1) over range of seismic energy of interest

$$\text{minimum} \int_{D_h} \int_{E_{\min}}^{E_{\max}} p_h(\mathbf{h}) p_E(E) \sqrt{\det[\mathbf{C}_x]} dE d\mathbf{h} \quad (2.2)$$

where $\langle E_{\min}, E_{\max} \rangle$ is the seismic energy range of interest, and $p_E(E)$ is the density probability distribution of energy. In general, it is possible to relate energy of seismic event to some detectability distance r , and often such a relation is approximated by $E=\text{const } r^q$ where q is close to 2.

One should note that now \mathbf{C}_x is also a function of detectability distance r , and thus of seismic event energy, since the number of rows in \mathbf{A} corresponds only to those stations that are within a distance r from the event. Furthermore, following a derivation of seismic energy

distribution by Rikitake (1976), and energy-detectability distance relation $E = \text{const } r^d$, the density probability distribution of detectability distance r can be written as

$$p_r(r) = \frac{-bq}{d \left(r_{\max}^{-bq/d} - r_{\min}^{-bq/d} \right)} r^{-(1+bq/d)} \quad (2.3)$$

where b is the b -value in the Gutenberg-Richter equation relating magnitude m and number of events and d is the d -value in the equation

$$\log E = c + d m \quad (2.4)$$

relating seismic energy release and magnitude m . d is known to be 1.5 and Gutenberg-Richter parameter b is dependant on the specific mine (usually b is in the range from 0.6 to 1.2).

Following the fact that one would typically like to build a network that is optimal for events with energies ranging from E_{\min} to E_{\max} , seismic energy-detectability relation $E = \text{const } r^d$, and density probability distribution (2.3), the criterion for optimal distribution of seismic stations (2.2) takes the final form

$$\text{minimum} \int_{D_h} \int_{r_{\min}}^{r_{\max}} P_h(\mathbf{h}) P_r(r) \sqrt{\det[\mathbf{C}_x]} dr d\mathbf{h} \quad (2.5)$$

In relation (2.5) r_{\min} is the maximum of two distances. The first is the distance from a seismic event to 5th nearest station (it is assumed that 5 stations are needed to properly locate the event), and the second is the distance which is associated with the minimum energy release (E_{\min}) we want to detect. r_{\max} is a detection distance corresponding to the maximum energy release of interest E_{\max} . It should be noted that it must be ensured that $r_{\min} < r_{\max}$.

To clarify this further, consider the following hypothetical example. A certain configuration exists for a certain seismic area. For this area, all events with a certain range of magnitudes $\langle m_{\min}, m_{\max} \rangle$ (or energies) are to be recorded. It is known that an event with magnitude m_{\min} triggers all stations up to 100 m and an event with magnitude m_{\max} triggers all stations up to 5000 m away from the event. Thus, for this event the performance of the configuration is calculated to be:

$$\sum_{r=100}^{5000} \sqrt{\det[\mathbf{C}_x]} \frac{r^{-(1+4b/3)}}{r_{\max}^{-4b/3} - r_{\min}^{-4b/3}} \quad (2.6)$$

However, the configuration is such that the 5th nearest station to the seismic area is 150 m away, the 6th is 300 m away and the 7th station is 1000 m away. If the summation is started from 150 m, then for $r=150, 151, \dots, 299$ 5 stations are used in calculation of matrix A , for $r=300, \dots, 999$ 6 stations are used and for $r=1000, \dots, 5000$ 7 stations are used.

In some practical cases the requirement of the best estimation applies to some sub-sets of unknown parameters only, as e.g. epicenter coordinates. To solve the problem of D -optimal planning for the best estimates of selected parameters, the content of the confidence ellipsoid can be evaluated as the product of the eigenvalues of C_x . This is valid since the eigenvalues form the lengths of the principal axes of the confidence ellipsoid and volume of confidence ellipsoid is proportional to the product of the the eigenvalues of C_x . If we only have a certain subset of parameters of interest, only the associated eigenvalues are used in the forming of the product.

Algorithmically the process can be described as follows:

```

For all possible configurations do
  planning_value = 0
  for all seismic areas
    for  $r_{min}$  to  $r_{max}$  do
      find  $A^T A$ 
      use SVD procedure to find eigenvalues
      of  $(A^T A)^{-1}$ 
      calculate the product of eigenvalues
      planning_value = planning_value +  $\prod_i \lambda_i \cdot \frac{r^{-(1+4b/3)}}{r_{max}^{-4b/3} - r_{min}^{-4b/3}}$ 
    end
  end
end
    
```

The optimal configuration is determined by the minimum (planning_value).

2.2 MAPS OF EXPECTED LOCATION ERROR AND SENSITIVITY

In addition to the described technique, the quality of seismic network configurations can also be evaluated from the maps of expected standard errors of seismic event parameters determination. This is necessary since the procedure described previously generates configurations that are optimal on *average*. Such a configuration is not necessarily optimal for a given event, so evaluation for given scenarios is needed. The maps are based on the calculations of covariance matrix

C_x , when in addition to arrival time errors, uncertainty of seismic velocity model is taken into account. The diagonal elements of the matrix C_x are the variances of the seismic event parameters t_0 , x_0 , y_0 , and z_0 . We define the standard error of the epicenter location to be the radius of a circle, the area of which is equal to that of the ellipsoid of the standard error of the coordinates x_0 and y_0 . The standard error of the epicenter position so defined is described by the formula (Gibowicz and Kijko, 1994)

$$\sigma_{xy} = [\{C_x\}_{22} \{C_x\}_{33} - [\{C_x\}_{23}]^2]^{1/4} \quad (2.7)$$

where $\{C_x\}_{ij}$ is the (i,j) element of the matrix C_x .

These maps would indicate the expected standard error for epicenter determination. Also needed is the expected standard error for the focal depth determination of the event. This error is obtained directly from the covariance matrix and is

$$\sigma_z = [\{C_x\}_{44}]^{1/2} \quad (2.8)$$

Note that these maps of expected standard errors are functions of the magnitude of the events. In other words, if one looks at a certain section of the volume of interest, one first decides on a magnitude m . Therefore the maps of expected standard error would be the answer to the question: if an event with magnitude m has hypocenter \mathbf{h} , in the section looked at, what will the standard error be? Magnitude m can be related (usually empirically) to detectability distance r , given a certain mining area (Butler and Van Aswegen, 1993). All stations within distance r from the hypocenter \mathbf{h} will be used to calculate the expected error in epicenter and focal depth. If there are not at least 5 stations within this distance r we assume that our seismic network cannot "see" an event with magnitude m at point \mathbf{h} .

This leads us to the question: where can our configuration "see" an event with magnitude m ? This forms the basis of the concept of sensitivity of a configuration. As already mentioned, 5 stations are needed to locate an event properly. In actual fact at least three stations are needed, but five is considered minimum for a reliable source calculation. Now one can calculate the distance to the 5th nearest station from the point \mathbf{h} and convert that distance to a magnitude (Butler and Van Aswegen, 1993). This means one can contour these magnitudes. Physically it means that at a certain point \mathbf{h} , an event can be "seen" if it has at least a magnitude that is such that it corresponds

to the distance to the 5th nearest station to h .

However, note that the mere fact that 5 stations recorded an event does not ensure good location error. The five station network may have a very poor geometric configuration - being flat for instance. Therefore one should always study the sensitivity contour and the location error contours together. Ideally one will find a configuration with sensitivity and location errors both being good.

A few examples are now discussed:

Example 1

The scenario of this example is a shaft pillar that is being monitored on one of the deep South African gold mines. The area of interest has a plan view of 650m x 650m. Fig. 2.1 indicates contours of expected errors in focal depth for events with local magnitude 0.0 that occur at a depth of 1921m in the area on and around the shaft pillar. The reef blocks still to be mined out in the shaft pillar is indicated in fig. 2.1. In this example an arrival time determination error of 5ms is assumed and a velocity error of 150m/s. The configuration of seismic stations that has as a result the contours in Fig. 2.1 is very close to the actual configuration currently used in this mine. As can be seen in Fig. 2.1 the expected errors are acceptable, especially in the area of interest, namely the pillar area. On average, the expected error is 54.3m, throughout the area shown in Fig. 2.1.

If one station, namely station 6 (the second most south station), is moved a distance of 66m, then the situation depicted in Fig 2.2 occurs. Clearly there is a strip right through the shaft pillar that has unacceptably high expected error in focal depth - up to 900m! The reason for this bad behaviour is that now the seven stations in the network is close to being on the same plane. This creates a near singularity in the location procedure which then fails to locate the event properly. The point that this example tries to bring accross is that a small change in the spatial configuration may significantly change the location accuracy. Therefore carefull planning is needed before installing a seismic network.

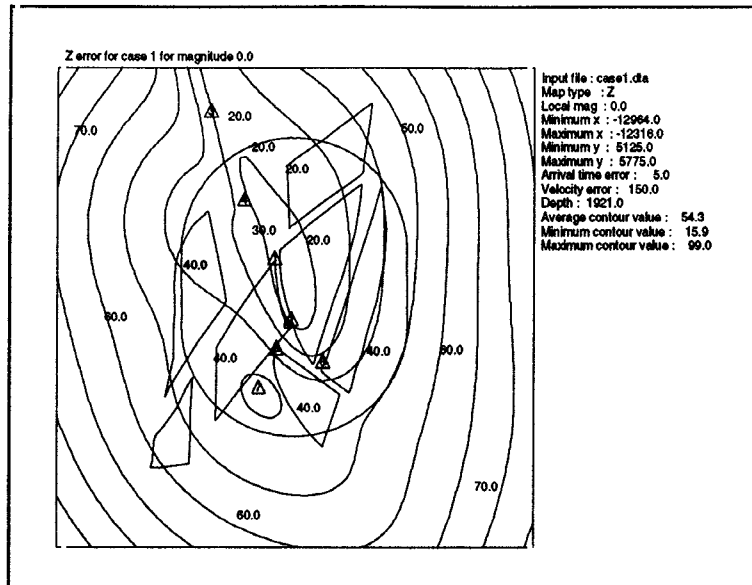


Figure 2.1 Expected errors in focal depth estimation using a seven station seismic network surrounding a shaft pillar in a South African gold mine. The contours show that good focal depth estimation may be expected for events with magnitude 0.0. This figure is a plan view at depth 1921m of a 650m x 650m area.

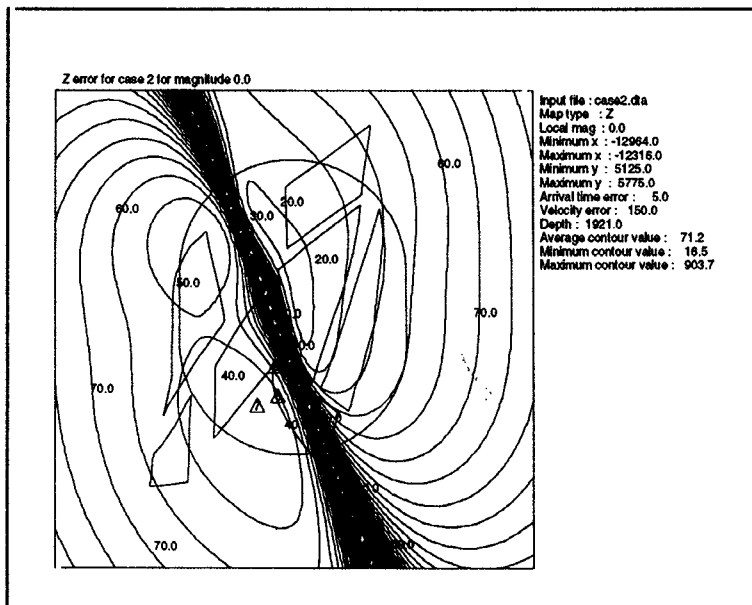


Figure 2.2 Expected errors in focal depth estimation by the same seismic network as in Fig. 2.1, except that one station was moved a distance of 66m. Clearly there is an area right through the shaft pillar in which location will be very unreliable as far as focal depth is concerned.

Example 2. This is a demonstration of a rule of thumb that the area to

be monitored should be surrounded by seismic stations, rather than have the seismic network below, above or beside the area of interest. Fig. 2.3 indicates a plan view of expected errors in focal depth determination of events with local magnitude of 1.2 at a given depth. The area is monitored by a seven station network where all the stations range from 800 m to 2000 m above the level of the map. In this case the average expected error of z coordinate for this 2000 m by 2000 m area is 508 m, which is clearly unacceptable. The lowest expected error is 335 m and the highest 1153 m. Moving only one station (left bottom) 500 m below the level of the map increases performance of the network significantly (Fig. 2.4). Average expected error drops to 81 m with a minimum of 21 m and a maximum of 177 m. The example demonstrates a rule of thumb that it is good to have the area to be monitored surrounded by the seismic network.

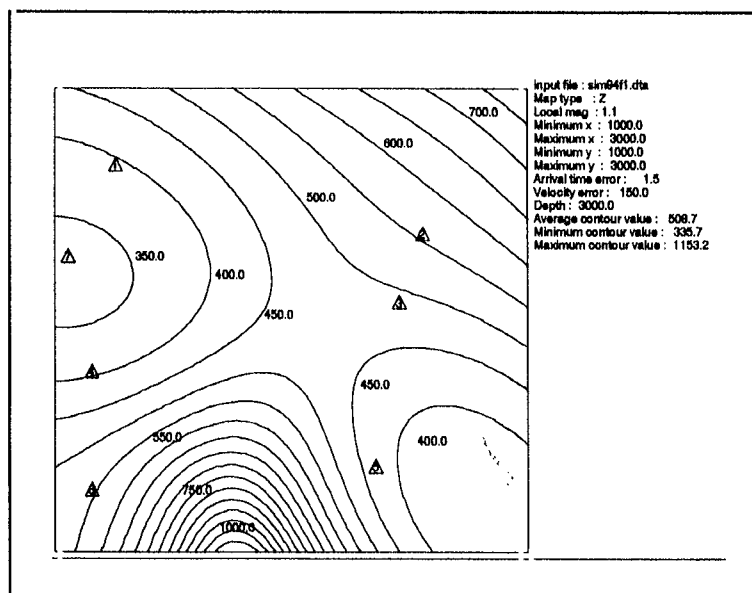


Figure 2.3 Expected errors in focal depth estimation using the seismic network with all stations situated above the plane of the contour map. The area is 2km x 2km and clearly the expected errors are unacceptably large.

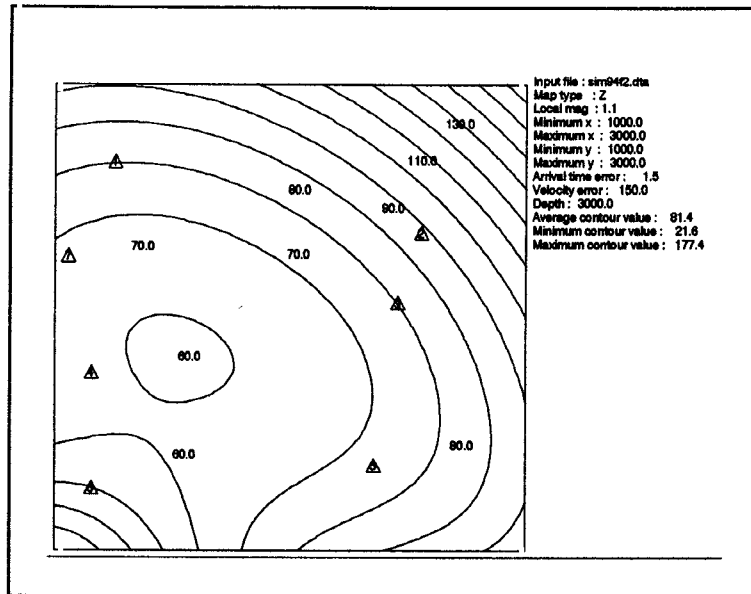


Figure 2.4 Expected errors in focal depth estimation by the seismic network as in Fig. 2.3, except that one station was moved 500 m below the level of the map. The increase in z determination accuracy is significant.

Example 3. Optimal seismic network at actual mine in Canada.

The network had to be optimal for a volume of approximately 1180 m by 1350 m by 350 m deep. It was decided to install a network of 10 stations. There were 16 potential places in which to install these 10 stations giving 8008 possible configurations. The volume of interest was divided into 9 seismic areas that had equal importance. An expected velocity error of 150 m/s and an arrival time error of 1.5 ms was assumed in generation of the contour. A velocity of 5500 m/s for the P wave was assumed throughout the volume of interest. The optimal station configuration was calculated as

$$\text{minimum } \sum_{D_n} \sum_{r_{\min}}^{r_{\max}} p(\mathbf{h}) p(r) f(\mathbf{C}_x) \quad (2.9)$$

where the search was performed over all $\binom{16}{10} = 8008$ possible 10 station configurations and D_n consisted of the 9 seismic areas. It was assumed that $p(\mathbf{h})$ is the same for each seismic area and b , p and d were 0.8, 2, and 1.5 respectively. Function $f(\cdot)$ is the product of the inverses of the singular values of \mathbf{C}_x . In our example we assumed that all 3 coordinates of hypocenter are important to us, so only the subset of 3 corresponding eigenvalues was looked at. Some of the results are shown in the following two figures. Fig. 2.5 indicates the expected epicenter errors σ_{xy} at a depth of 1850 m for events with local magnitude of 0.1. The average expected error was 21 m with

maximum and minimum errors being 65 m and 7 m respectively. The corresponding expected errors in focal depth estimation are contoured in Fig. 2.6. The average error is 15 m; the maximum 43 m and the minimum 4 m. Clearly this network performs very well at this depth (which is approximately in the middle of the volume of interest). Sensitivity contours (Fig 2.7) have shown furthermore that the network can detect events as small as -1.22 magnitude. It should always detect events larger than -0.16.

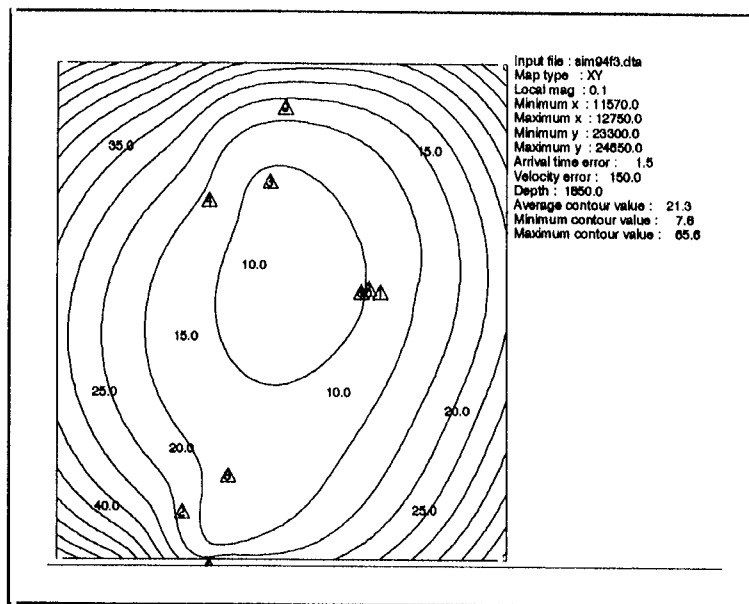


Figure 2.5 Expected errors in epicenter determination at depth 1850 m at Canadian mine using a planned network. The area is 1180m x 1350m and the expected errors are all reasonable.

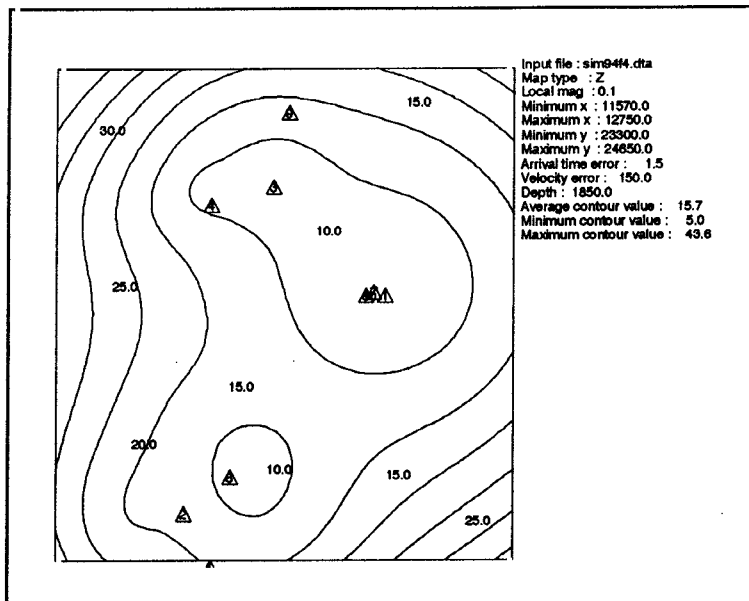


Figure 2.6 Expected errors in focal depth determination at depth 1850 m at Canadian mine using a planned network. The errors in focal depth determination is quite small for this area.

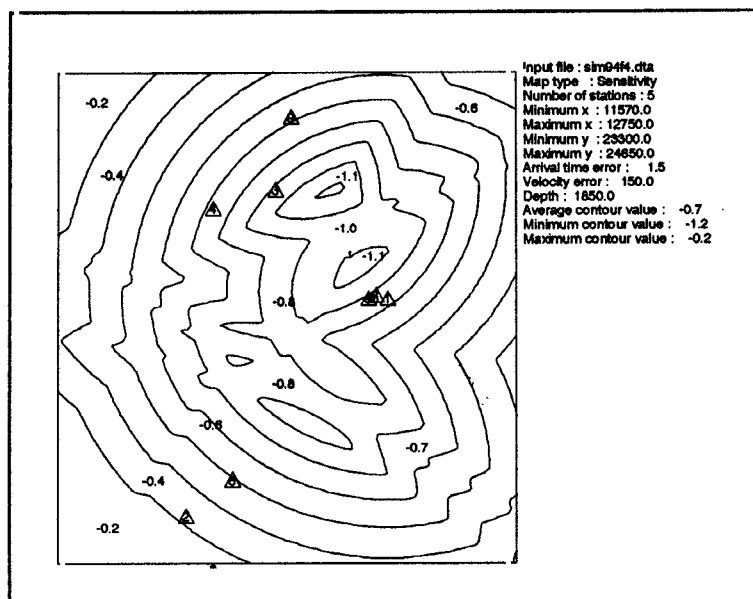


Figure 2.7 Sensitivity contours at depth 1850 m at Canadian mine using a planned network. The network can be seen to be very sensitive, being able to record -1.2 magnitude events in some places.

Example 4. Optimal seismic network at actual mine in South Africa. The volume of interest runs 1950 m in the x direction, 1900 m in the y direction and 2000 m in the z direction. The volume was divided into 6 seismic areas of equal importance. A new 9 station network was

to be installed and there were 20 possible places to position these 9 stations giving a total of $\binom{20}{9} = 167960$ possible configurations.

Again a 150 m/s velocity error and a 1.5 ms arrival time error was assumed. The *P*-wave velocity was assumed to be 6100 m/s. Fig. 2.8 indicates expected epicenter location errors σ_{xy} for events with local magnitude 1.2 and are at a depth of 2500 m. The average expected error was 23 m, the maximum 61 m and the minimum 13 m. Fig. 2.9 denotes the expected error in focal depth estimation with the average being 29 m, the maximum 52 m and the minimum 14 m. Again the planning of the seismic network ensures small location errors. Sensitivity contours (Fig 2.10) show that all event larger than 0.42 will be detected anywhere on the map and in certain places detectable events may have magnitudes as low as -0.26.

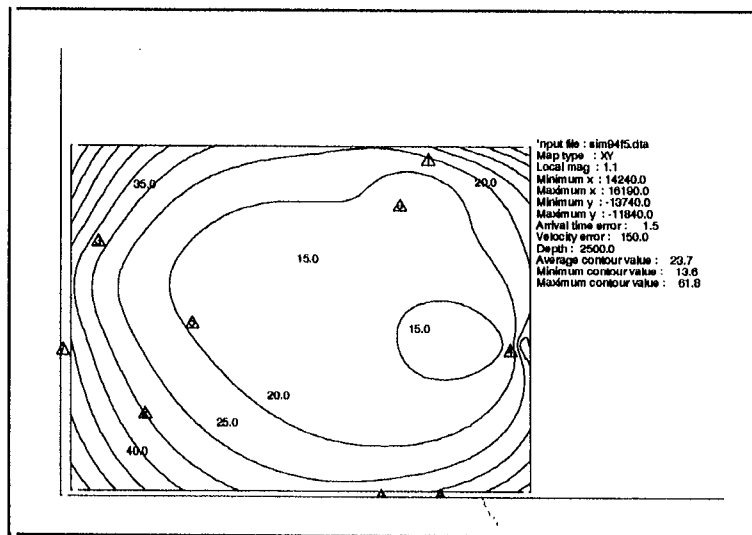


Figure 2.8 Expected errors in epicenter determination at depth 2500 m at South African mine using a planned network. The area is 1950m x 1900m and the expected errors are very low.

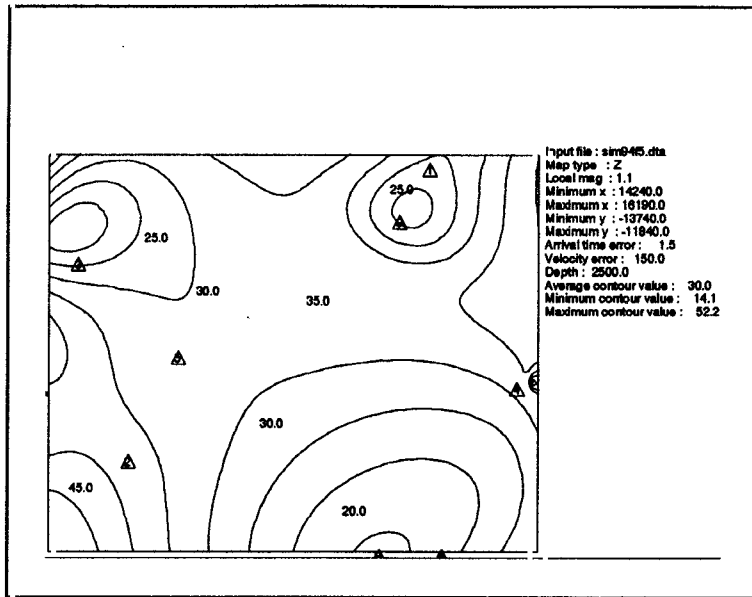


Figure 2.9 Expected errors in focal depth determination at depth 2500 m at South African mine using a planned network. The expected errors in focal depth determination are low.

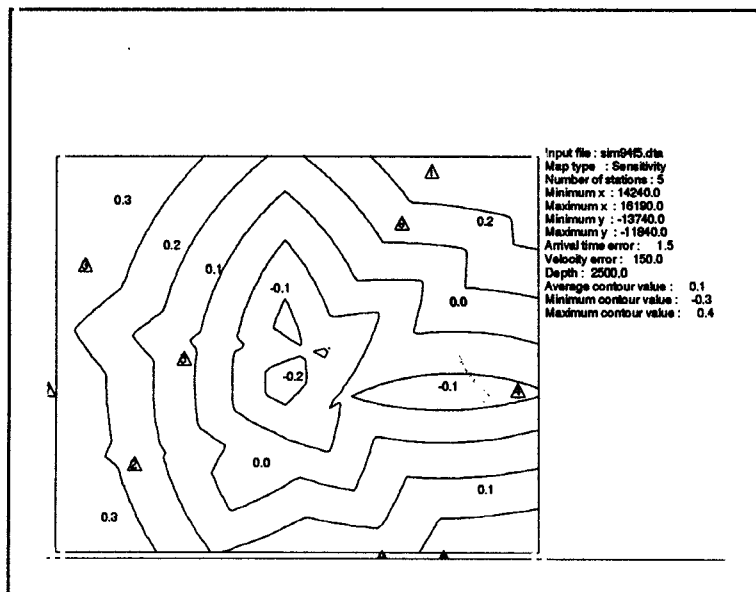


Figure 2.10 Sensitivity contours at depth 2500 m at South African mine using a planned network.

2.3 QUALITY INDEX FOR CONFIGURATION OF SEISMIC STATIONS

At this point, using the procedures discussed in the previous two sections, one can find a satisfactory configuration. However, once it is installed one would still like to field test it for each event that is being recorded - leading one to the concept of quality index for configuration of seismic stations.

If an event is located, one would like to know what the quality of the subnetwork is that located the event. By subnetwork is meant those triggers used in the location of the event. The quality of a given configuration of seismic stations Q_{css} can be estimated as

$$Q_{css} = \frac{27}{\det[\mathbf{C}_x] \left(\frac{n_p}{\sigma_{tp}^2} + \frac{n_s}{\sigma_{ts}^2} \right) \left(\frac{n_p}{V_p^2 \sigma_{tp}^2} + \frac{n_s}{V_s^2 \sigma_{ts}^2} \right)^3} \quad (2.10)$$

In relation (2.10) $\det[\mathbf{C}_x]$ is the determinant of the covariance matrix \mathbf{C}_x and computed at the estimated origin time t_0 and hypocentre x_0, y_0, z_0 . In the discussed case

$$\mathbf{C}_x = (\mathbf{A}^T \mathbf{C}_t^{-1} \mathbf{A})^{-1}$$

where \mathbf{A} is the partial derivative matrix of the theoretical travel times with respect to the seismic event parameters t_0, x_0, y_0 and z_0 . \mathbf{C}_t is the diagonal matrix with expected variances of the arrival time determination and respectively equal to σ_{tp}^2 and σ_{ts}^2 . V_p and V_s are respectively velocities of P and S waves.

CHAPTER 3

LOCATION OF SEISMIC EVENTS AND VELOCITY INVERSION

3.1 LOCATION OF SEISMIC EVENTS

The location of seismic event hypocentre parameters $\mathbf{h} = (x_0, y_0, z_0)^T$ is equivalent to the minimization of the misfit function

$$\Phi(\mathbf{h}) = \sum_{i=1}^n w_i |V_i [t_i - \bar{t} - (T_i - \bar{T})]|^p + \sum_{j=1}^{n_d} w_j |Dis_j|^p \quad (3.1)$$

where:

n – number of arrival times with good quality

w_i – weighting factor derived from the quality index of the arrival time(s) determination at the i th station

V_i – seismic wave velocity to the i th station

t_i – arrival times of P and/or S and/or the differences in S-P at the i th station ($i=1, \dots, n$)

\bar{t} – average observed arrival time

T_i – calculated travel time between the hypocentre and the i th station

\bar{T} – average value of theoretical travel time

n_d – number of stations with quality directions

w_j – weighting factor derived from the quality index of direction.

Dis_j – this distance may be one of two distances: (1) the perpendicular distance from the current estimate of the hypocentre to the direction line from the j th station ($j = 1, \dots, n_d$) or (2) if the z component of the location is questionable it refers to the perpendicular distance from the current hypocentre to the vertical plain through the direction line from the j th station

p – norm equal to 1 or 2

The quality indices for arrival times and directions determination are described below.

The origin time of the seismic event occurrence is estimated from the relation

$$t_0 = \bar{t} - \bar{T} \quad (3.2)$$

The minimization of the misfit function (3.1) is performed by the Nelder-Mead simplex procedure.

To find satisfactory location by the simplex method, one needs to start the iterative procedure from the appropriately chosen starting point. It is recommended to run the iterative process for three different (if available) starting points: a) coordinates of the nearest station, b) average coordinates of the n_d nearest station, c) location based on the direction from the nearest n_d stations. In this case, the best hypocentre location is chosen to be the one for which the value of the misfit function (3.1) is minimal.

The quality of seismic event location can be estimated from

$$QI_LOC = \frac{27}{\det [C_x] \left(\frac{n_p}{\sigma_{t_p}^2} + \frac{n_s}{\sigma_{t_s}^2} \right) \left(\frac{n_p}{V_p^2 \sigma_{t_p}^2} + \frac{n_s}{V_s^2 \sigma_{t_s}^2} \right)^3} \quad (3.3)$$

where $\det[C_x]$ is the determinant of the covariance matrix $C_x = s^2(A^T A)^{-1}$ of seismic event parameters $\mathbf{x} = (t_0, x_0, y_0, z_0)^T$;

\mathbf{A} is the partial derivative matrix of the computed arrival times with respect to seismic event parameters \mathbf{x} and

$$s^2 = \frac{\sum r^2}{(n_p + n_s - 4)}$$

$\sum r^2$ is sum of squared time residuals, and n_p and n_s are respectively number of P and S arrival times. Both $\det[A^T A]$ and $\sum r^2$ are computed at the estimated origin time \hat{t}_0 and hypocentre $\hat{x}_0, \hat{y}_0, \hat{z}_0$. Values σ_{t_p} and σ_{t_s} are respectively standard deviations of P and S arrival times determination, V_p and V_s are respectively velocities of P and S waves.

In some cases, when the distance between the located and the so-called master or reference event is an order of magnitude less than the average hypocentral distance, the relative location technique can be applied (Milev *et al* 1994).

The relative location of seismic events is known also as a "master event" procedure or Arrival Time Difference (ATD) technique. In the ATD procedure, a set of arrival time differences $t_i - t_{Ri}$ ($i=1, \dots, n$) is used. These differences are obtained from n stations which recorded arrival times t_{Ri} generated by a reference event R with known event parameters $(t_{R0}, x_{R0}, y_{R0}, z_{R0})$ and a nearby event with arrival times t_i and unknown parameters (t_0, x_0, y_0, z_0) .

The estimation of (t_0, x_0, y_0, z_0) is equivalent to the minimization of the function

$$\Phi(\delta \mathbf{x}) = \sum_{i=1}^N \left| \delta t_i - \delta t_0 - \frac{\partial T_i}{\partial x_0} \delta x_0 - \frac{\partial T_i}{\partial y_0} \delta y_0 - \frac{\partial T_i}{\partial z_0} \delta z_0 \right|^p \quad (3.4)$$

where $\delta t_i = t_i - t_{Ri}$, T_i are travel times, and $\delta \mathbf{x} = (\delta t_0, \delta x_0, \delta y_0, \delta z_0)^T$ are the unknown adjacents to the reference event parameters \mathbf{x}_R . In most cases $p=2$ which is equivalent to the least squares estimation technique, or $p=1$ if minimization of absolute values of residuals is accepted. The minimization of misfit function (3.4) can be performed by Nelder-Mead simplex procedure. Theoretical travel times do not appear in the misfit function (3.4). Only their partial derivatives with respect to the hypocentral coordinates. When the formula describing the travel time has a form $T_i = d_i / V_i$, the travel time derivatives with respect to the hypocentre coordinates, taken at the reference event hypocentre \mathbf{h}_R are of the form

$$\begin{aligned} \partial T_i / \partial x_0 &= (x_R - x_i) / (d_{Ri} V_i), \\ \partial T_i / \partial y_0 &= (y_R - y_i) / (d_{Ri} V_i), \\ \partial T_i / \partial z_0 &= (z_R - z_i) / (d_{Ri} V_i), \end{aligned} \quad (3.5)$$

where (x_i, y_i, z_i) are the coordinates of the i th station, d_{Ri} is the distance from the reference event to the i th station, and V_i is the average seismic wave velocity between the reference event and the i th station. Taking into account that in (3.5) the velocity V_i can be approximated by an expression $d_{Ri} / (t_{Ri} - t_{R0})$, the ATD location procedure does not require the knowledge of the theoretical travel times and their partial derivatives.

The application of the ATD procedure in mining practice has several advantages. *If the located and reference events are close enough, an order of magnitude less than the average hypocentral distance*, the ATD method is more accurate than the conventional one. The improvement follows from the fact that the ATD approach implicitly removes travel time anomalies which are the main source of the focal parameter errors. The procedure can be used for the location of seismic events regardless of the information available on the absolute location of the reference event. If the reference event location is poorly known, then only a shape of the active area, related to the reference event, can be found. In addition, slight modification of described technique allows for use of ATD procedure when no origin time of the reference event is known (Gibowicz and Kijko, 1994).

3.2 L_1 , ADAPTIVE L_p -NORM AND SIMPLEX MINIMIZATION PROCEDURE

The use of least squares procedures is equivalent to the assumption that the distribution of the arrival time residuals are of Gaussian nature. Jeffreys (1932), who was developing the global travel time tables, first recognized that the time residuals do not follow the Gaussian distribution and occasional large residuals strongly affect the location of earthquakes. The problem of large time residuals is also important for seismic events in mines. An introduction of automatic arrival time detectors, characteristic for modern mining recording systems, increases probability of picking up noise spikes, or confusing P and S arrivals on a particular channel.

To solve this problem, instead of least square misfit function (3.1), the sum of the absolute values of time residuals, known as the L_1 norm, is often introduced. The corresponding misfit function is

$$\Phi(\mathbf{x}) = \sum_{i=1}^n |r_i|, \quad (3.6)$$

where $|\cdot|$ denotes the absolute value. The misfit criterion (3.6) is less sensitive than the L_2 (least squares) norm and tends to decrease the effects of a few large time residuals. But is the L_1 -norm procedure always the best? Does it handle in the best way the problem of arbitrarily erratic data? Possibly some other norm, say L_p where p is not necessary equal to 1, is able to provide a better estimation of unknown parameters. If such a value of p exists, then how to find it?

The following section provides a brief introduction to regression analysis in the presence of arbitrary outliers, and the concept of an optimal value of p -norm determination. The example presents the results of numerical simulation of the seismic event location process, and compares L_1 , L_2 , and adaptive procedures for p -value selection for varying degrees of data contamination.

The L_p -norm estimation problem is defined as follows: find the solution vector \mathbf{x} that minimizes the misfit function (Gonin and Money, 1985a)

$$\Phi_p(\mathbf{x}) = \sum_{i=1}^n |r_i|^p, \quad (3.7)$$

where $1 \leq p < \infty$ and r_i is the i th residual. Minimization of misfit function (3.7) for $1 \leq p \leq 2$ for contaminated data was suggested by Forsythe (1972). When the degree of contamination is moderate to

large, he proposed $p=1.5$ as a compromise. It was already known in the 1960's that the properties of L_p -norm estimators depend critically on the distribution of residuals r_i (Rice and White, 1964; Ekblom and Henriksson, 1969). Harter (1972) was one of the first who related the p -norm value to the kurtosis of the residual distribution. The kurtosis is an inverse measure of the property of sharpness of the frequency distribution peak (Eadie *et al* 1982), and is defined as

$$\beta_2 = \frac{\mu_4}{\mu_2^2} \quad (3.8)$$

where μ_2 and μ_4 are the second and fourth order central moments, respectively. The unbiased estimates of the second and fourth order central sample moments are (Gonin and Money, 1987)

$$\hat{\mu}_2 = \frac{1}{n-1} \sum_{i=1}^n (r_i - \bar{r})^2, \quad (3.9)$$

$$\hat{\mu}_4 = \frac{(n^2 - 2n - 3)}{(n-1)(n-2)(n-3)} \sum_{i=1}^n (r_i - \bar{r})^4 - \frac{3(n-1)(2n-3)}{n(n-2)(n-3)} \hat{\mu}_2^2, \quad (3.10)$$

where \bar{r} is the sample mean of residuals r_i . In Harter's adaptive procedure the sample residual kurtosis $\hat{\beta}_2$ is computed from the provisional regression, which may be, for example, least-squares. If $\hat{\beta}_2 > 3.8$, use the L_1 -norm, if $2.2 < \hat{\beta}_2 < 3.8$, use the L_2 -norm, and if $\hat{\beta}_2 < 2.2$, use the L_∞ (Chebyshev or minimax) norm. If the residuals therefore follow a long-tailed distribution or if outliers are present, there is a high probability that $\hat{\beta}_2$ will exceed 3.8, $p=1$ will be chosen and the outliers will not distort the results. Thus the Harter's procedure provides substantial improvement to the estimation of x in comparison with the least-squares procedure.

However, considerable progress can still be made with regard to Harter's procedure by another empirical relation suggested by Money *et al.* (1982)

$$\hat{p} = 9 / \hat{\beta}_2^2 + 1 \quad (3.11)$$

for $1 \leq \hat{p} < \infty$, and by Sposito *et al.* (1983)

$$\hat{p} = 6 / \hat{\beta}_2^2 \quad (3.12)$$

for $1 \leq \hat{p} \leq 2$. For both these formulas $\hat{\beta}_2 = 3$ implies $\hat{p} = 2$ which is equivalent to the standard least-squares inversion.

A different, theoretically motivated formula is based on the p -order exponential distribution with the probability density function (Turner, 1960)

$$PDF(x) = \frac{p \cdot (0.5)^{1+1/p}}{a \cdot \Gamma(1/p)} \exp \left\{ -0.5 \left| \frac{x-b}{a} \right|^p \right\} \quad (3.13)$$

for $-\infty < x < \infty$, where a and b are the scale and location parameters, respectively, and $\Gamma(\cdot)$ is the gamma function. It can be shown that the k -th central moment of distribution (3.13), for k even valued, is

$$\mu_k = 2^{k/p} a^k \Gamma\left(\frac{k+1}{p}\right) / \Gamma\left(\frac{1}{p}\right), \quad (3.14)$$

and following relation (3.8) the kurtosis β_2 is

$$\beta_2 = \frac{\Gamma(5/p) \Gamma(1/p)}{[\Gamma(3/p)]^2}, \quad (3.15)$$

Formula (3.15) is known as the Box-Tiao relation.

A value for p can be obtained by maximizing the likelihood function over p . Although this approach is theoretically justified, it is not sufficiently practicable. A simple adaptive algorithm is used instead (Gonin and Money, 1985 b; 1987):

- Step 1: Set $i=0$ with $p_i=2$ (i.e., the classical least-squares regression).
- Step 2: Fit the model to the data by minimization of functional (3.7), using the exponent p_i .
- Step 3: From the resulting distribution of residuals r and using formula (3.8), compute the sample kurtosis $\hat{\beta}_2$. Use either formula (3.11) or (3.12) or (3.15) to calculate p_{i+1} .
- Step 4: Repeat steps 2 and 3 until $|p_{i+1} - p_i| < 10^{-4}$.

The above algorithm consists of an inner iteration (minimization of the misfit function (3.7) over the parameters \mathbf{x}) and an outer iteration for the calculation of the exponent p . Despite the fact that the theoretical convergence of the above adaptive scheme has not been proved, it was

found from tests with known p , that the successive p_i 's converge in about 4 iterations (Gonin and Money, 1985 b). The false position root finding method (Press *et al.*, 1989) for p exponent evaluation from the implicit formula was applied.

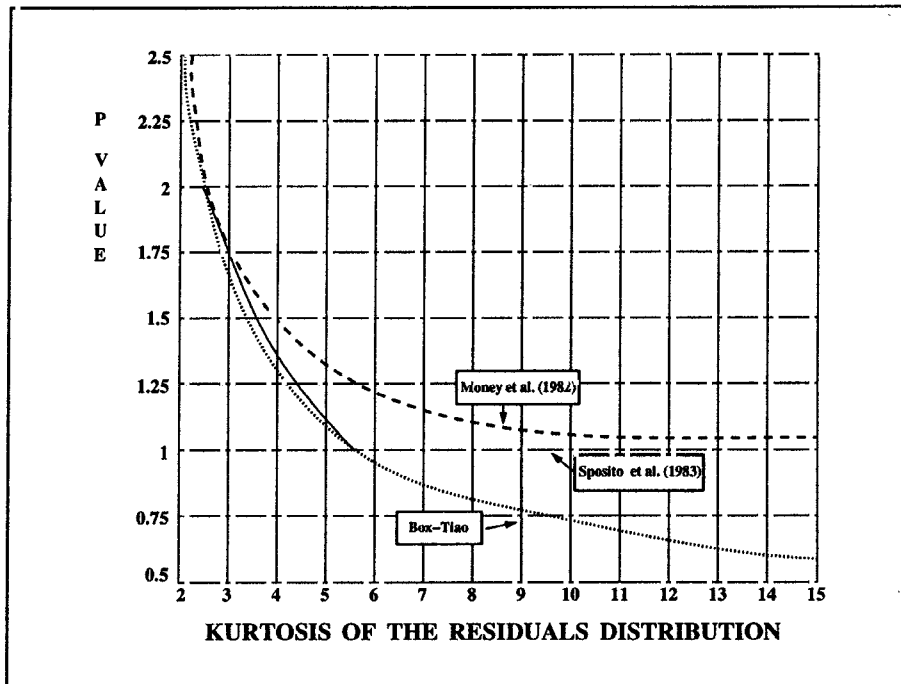


Figure 3.1 Predicted values of the exponent p in the L_p -norm, based on the sample kurtosis of the residual distribution, according to a) formula (3.11) of Money *et al.* (1982), formula (5.12) of Sposito *et al.* (1983) and Box-Tiao formula (5.12) of Gonin and Money (1985a).

Although formulas (3.11), (3.12), and (3.15) predict different values of the norm p (Fig.3.1), these estimators are consistent since the mean square error goes asymptotically to zero (Gonin and Money, 1985b). In case of use of L_1 or in general L_p -norm estimation, the formula (2.16), describing the covariance matrix of the focal parameters \mathbf{x} must be modified. The L_p -norm analogue to the covariance matrix \mathbf{C}_x is given by the formula (Dielman and Pfaffenberger, 1982)

$$\mathbf{C}_x = s^2(\mathbf{A}^T\mathbf{A})^{-1}, \quad (3.16)$$

where s can be approximated by (Cox and Hinkley, 1974)

$$\hat{s} = \frac{r_{(i)} - r_{(j)}}{2(i-j)/n}, \quad (3.17)$$

and $r_{(i)}$ denotes the ordered residuals r_i . Cox and Hinkley (1974) stress that i and j should be symmetric about the index of the median sample

residual and that the difference between i and j should be kept small. Following Gonin and Money (1987) the following formulae for i and j are proposed:

$$i = \left[\frac{n+1}{2} \right] + \nu \text{ and } j = \left[\frac{n+1}{2} \right] - \nu \text{ for } n \text{ odd,}$$

$$i = \left[\frac{n}{2} \right] + \nu \text{ and } j = \left[\frac{n}{2} \right] - \nu \text{ for } n \text{ even,}$$

(3.18)

where $[\cdot]$ indicates the integer portion of the number and ν is an integer chosen to spread i and j symmetrically about the index of the median sample residual. The choice of ν , or the difference, $i-j$, should be kept fairly small, but the choice however, should not cause widely differing values of \hat{s}^2 in a large sample (Dielman and Pfaffenberger, 1982). Additionally, $\hat{r}_{(i)}$ and $\hat{r}_{(j)}$ should not be equal to zero.

For the location of seismic events in mines, the L_1 norm was introduced by Prugger and Gendzwill (1988) and used at Saskatchewan potash mines, Canada, and it is also implemented in the location software used in South Africa (Mendecki, 1990; 1993). The concept of adaptive L_p -norm and its application for location of seismic events was introduced by Kijko (1994). Unfortunately, the location procedures based on the norm different than 2 are rather seldom applied in practice, because of the difficulty involved in the problem formulation in terms of matrix presentation and inversion. The L_p norm based location programs, therefore, are often accomplished by a direct minimization procedure of the misfit functions as the Nelder-Mead simplex subroutine.

The detailed description of the Nelder-Mead simplex subroutine can be found in Himmelblau (1972) and in more recent textbooks on numerical algorithms such as that of Press *et al.* (1989).

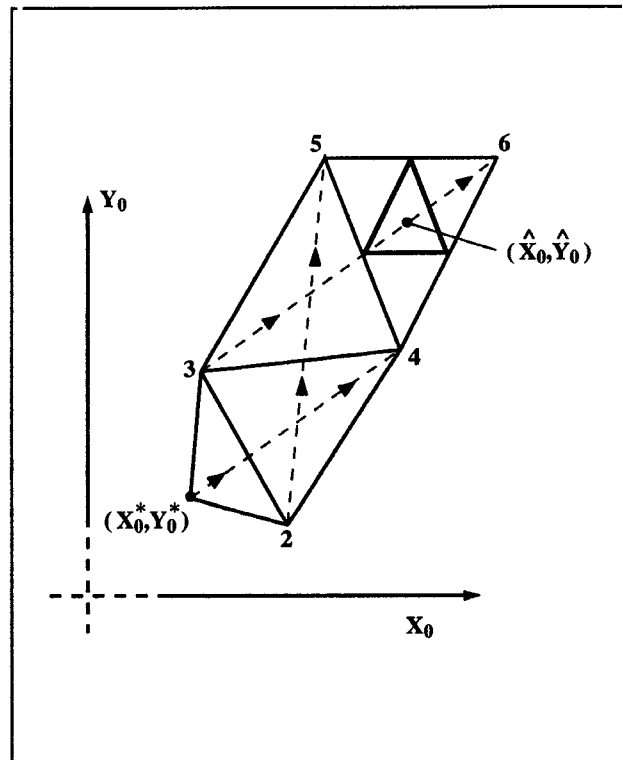


Figure 3.2 Simple illustration of the simplex location algorithm. Starting from a point (\hat{x}_0, \hat{y}_0) , after several successive reflections, the simplex (4,5,6) starts to "collapse" towards the minimum at a point (\hat{x}_0, \hat{y}_0) . (From Rabinowitz and Kulhánek, 1988).

In the brief description of the procedure, the work of Rabinowitz and Kulhánek (1988) is followed. Assume the problem of location contains an evaluation of two parameters only: the epicentre coordinates x_0 and y_0 . Suppose that the minimum of the misfit function $\Phi(x_0, y_0)$ is at the point (\hat{x}_0, \hat{y}_0) and the trial of epicentre is chosen to be at the point (x_0, y_0) (Fig. 3.2). Starting from the point (x_0, y_0) , the algorithm constructs the triangle, having (x_0, y_0) as one of its vertices. Such a triangle in a two dimensional space is called "simplex", and in general, simplex is a figure having one more vertex than the number of dimensions for which it is defined. The misfit function $\Phi(x_0, y_0)$ is evaluated for each of the three vertices, the vertex for which the misfit function attains the highest value is then reflected through the gravity centre of the triangle. If the value of $\Phi(x_0, y_0)$ at the reflected point (say 4 in Fig.3.2) decreases with respect to the initial vertex, then a new simplex is formed by adding vertex 4 and deleting vertex 1. The process is repeated until the reflection fails to produce a vertex with a lower value of Φ . Then the simplex can contract itself and changes the search direction or "collapses" towards the minima according to the termination criterion.

In practice, the simplex iteration stops when the simplex size reaches a predetermined minimum value. Despite the fact that the simplex-based optimization procedure has been known since the early sixties (Spendly and Hest, 1962), only universal use of computers made it an attractive tool. This is especially evident for the problems in which the misfit function exhibits local minima and/or analytical calculation of derivatives is laborious. The modification of the algorithm proposed by Nelder and Mead (1965), the version used in all known seismological applications, has substantially improved the performance capability of the original algorithm. In the Nelder-Mead simplex procedure, the minimization (in general optimization) process is adaptive, causing the simplex to be revised to conform in the best way to the nature of the misfit function. In many cases, the Nelder-Mead simplex optimization procedure is more effective than the Gauss-Newton one: it is derivative free, and it does not require matrix inversions in problems containing ill-conditioned matrices. The procedure can be used for any velocity model and any misfit function. The Nelder-Mead simplex procedure was first introduced for the location of mining events by Prugger and Gendzwill (1988). The same technique is also used for the location of local (Rabinowitz, 1988) and distant earthquakes (Rabinowitz and Kulhánek, 1988). The comparison test of the simplex procedure with the Gauss-Newton procedure and the Thurber (1985) approach (known as a Newton optimization procedure), in which the second order derivatives are included in addition to the first order travel time derivatives, was carried out by Prugger and Gendzwill (1988). The test showed that the Nelder-Mead simplex procedure with a L_1 norm misfit function provided reasonable locations and in most cases was found to be more accurate than either the Newton or the Gauss-Newton procedures.

Despite the fact that direct search optimization methods (such as simplex procedure) are slower than those which operate with derivatives of travel times, the location programs that use the Nelder-Mead algorithm are fast enough and can be used routinely. In general, an application of a misfit function based on the L_1 norm, together with the Nelder-Mead simplex algorithm, is as good or even better than most of the other approaches.

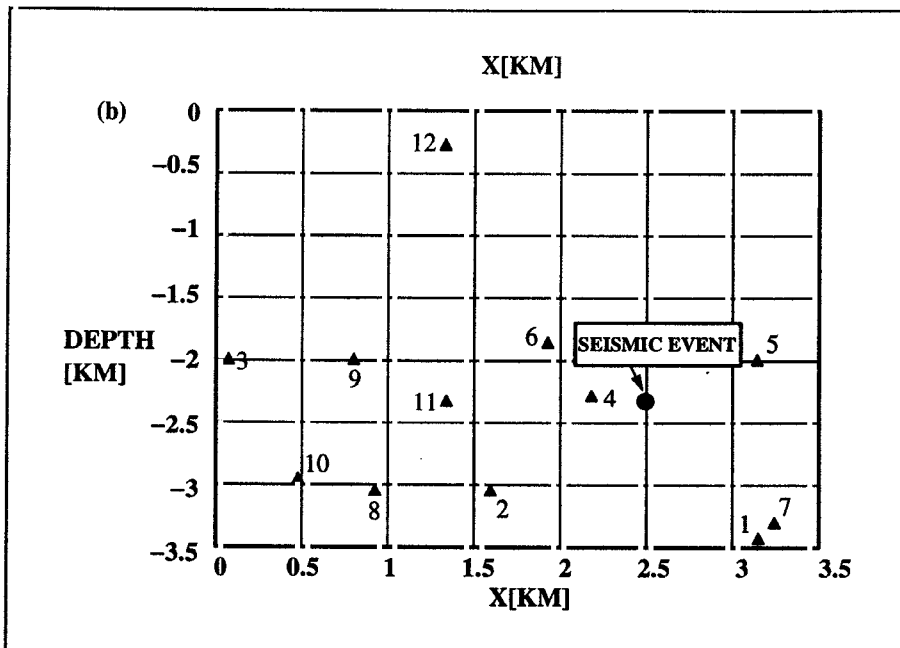


Figure 3.3(a) Horizontal distribution of seismic stations, marked by triangles and numbered from 1 to 12, used to test the concept of the adaptive L_p -norm. The focus of the modelled seismic event is marked by a circle.

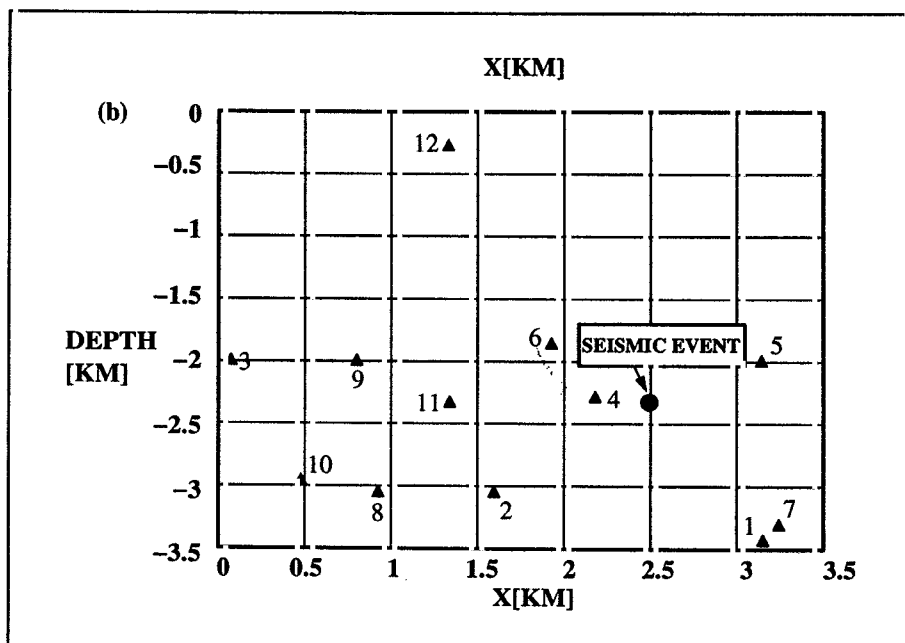


Figure 3.3(b) Vertical distribution of seismic stations, marked by triangles and numbered from 1 to 12, used to test the concept of the adaptive L_p -norm. The focus of the modelled seismic event is marked by a circle.

Example of Application: Numerical simulation of seismic events location in the presence of large arrival time reading errors.

A seismic network similar to that at the Western Deep Levels gold mine in South Africa is shown in Fig.3.3. For a seismic event situated slightly outside the network, the performance of L_1 , L_2 and adaptive L_p -norm seismic event location procedures was tested. Following our notation, the vector of the unknown parameters $\mathbf{x}=(t_0, x_0, y_0, z_0)$, where t_0 is the origin time, (x_0, y_0, z_0) are the hypocentre coordinates, t_i ($i=1, \dots, n$) are the arrival times of P waves and n is number of seismic stations. A half-space crustal model was used, with the P -wave velocity equal to 5925 m/sec. The minimization of misfit function (3.7) was performed by the Nelder-Mead simplex procedure.

Fig.3.4 demonstrates the performance of the L_1 , L_2 and adaptive L_p norms in the presence of one outlying time residual.

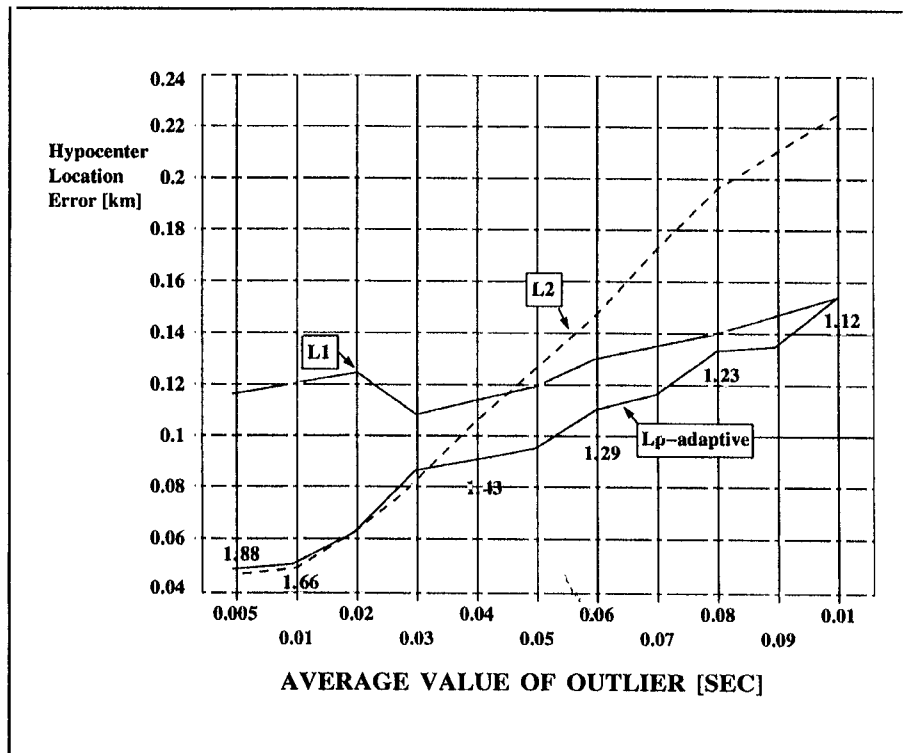


Figure 3.4 Comparison of seismic event location procedures based on the L_1 , L_2 and adaptive L_p norms in the presence of one outlying arrival time in the range of 5 to 100 msec.

For each value of the outlying time residual present at station 1, one thousand seismic events were generated. For each event, P -arrival times recorded by stations 2 to 12 were perturbed by normally distributed random numbers with a standard deviation equal to 5 msec. Fig. 3.4 shows the average error of the hypocentre location computed by employing the L_1 , L_2 and adaptive L_p -norm procedures for outlying residuals in the range from 5 to 100 msec. The optimal values of p -norm were calculated according to formula (3.12), which in general

provides the best estimates of hypocentre coordinates. Our tests showed that the superiority of formula (3.12) over (3.11) is especially significant when outlying residuals are large, while the predominance of relation (3.12) over (3.15) is evident for outliers small and moderate. For large outliers, but with kurtosis still less than 6, formulas (3.12) and (3.15) are essentially the same and both predict values of p close to 1.

The results indicate that up to a certain value of an outlier, the employment of the adaptive L_p -norm provides a substantial improvement over the L_1 -norm; for larger outliers the L_1 and L_p -norm techniques are basically equivalent. When the outlying observations are small, the least-squares technique and the adaptive L_p -norm are essentially the same, and both of them are better than L_1 . As the value of the outlier increases, the least-squares approach becomes progressively less efficient. Finally, the above test indicates that the adaptive L_p -norm approach is always as good as, or better than the L_1 or L_2 norms. Further numerical experiments showed that the superiority of L_p -norm becomes less effective as the number of outlying observations increases, leading to the equivalence of L_1 and L_p -norm procedures.

3.3 VELOCITY INVERSION

In general, information related to the state of the rock volume in a mine that has been traversed by seismic waves can be extracted from two kinds of seismic sources: controlled, artificially generated blasts with known source positions, and induced seismic events with unknown origin times and locations. The first approach is called active tomography and the second is known as passive tomography. This chapter concentrates on the problems of passive tomography which in the case of seismic wave velocity inversion is known under the name of joint hypocentres and velocity determination (JHVD). In contrast to the classical location approach, in which the hypocentre of only one event is located, in this procedure a set of hypocentres and velocity model parameters are jointly determined. This was first formulated for local events by Crosson (1974; 1976 a,b). He used local seismic data to study the velocity model parameters in western Washington. Crosson's approach originally formulated for a one-dimensional structure was extended for three-dimensional velocity inversion by Aki and Lee (1976). Their method was widely applied in various seismic regions of the world. Further references on this subject can be found, for example, in the work of Koch (1985) and Thurber and Aki (1987).

The JHVD procedure under mine conditions was applied by

Mendecki (1981, 1987) and Drzezla and Mendecki (1982 a,b); seismic observations were used to evaluate the focal parameters and velocity anisotropy of the rockmass. In recent applications of the JHVD technique in mines, Jech (1989) used the time difference between P- and S-wave arrivals to relocate seismic events and to improve the velocity model in the Ostrava-Karvina mining district in Czechoslovakia.

3.3.1 Travel Time Equations and Solution

If a seismic event occurs, one of the first interests is its location. Location is a very important aspect since most of the spectral parameters depend very strongly on the coordinates of the event. However, in order to locate the event, one needs to know the velocity structure of the rock between the event and the station along the ray path of the seismic wave. This velocity structure is in fact unknown. Typically, one could just estimate the velocity structure to be a realistic constant velocity and use this to calculate the location of the event. Unfortunately the velocity is not constant, but tends to increase with depth and stress build-up. Geological structures such as dykes, faults and damaged rock may also affect the seismic wave velocity, depending on the wavelength of the wave, its angle to the geological structure and the size of the geological structure.

A certain velocity structure is assumed, for example, a homogeneous rock, so that seismic wave velocities are the same everywhere - which, of course, is not true. Certain assumptions are also made about the way the wave travels through the rock. For instance, assume the wave travels from event to station in a straight line. This assumption is of course only reasonable if the event is not too far away from the station. The initial estimates of the locations are now found using the above mentioned assumptions. Now at this stage one has estimation for location and for velocities as well as a model of how the wave travels through the rock. This can be used to calculate a set of theoretical arrival times - in other words, if the assumptions are correct, the transducer should have received the waves at these theoretical arrival times. In fact, the transducers recorded a different set of arrival times. The difference between these observed and calculated arrival times can be attributed to two main factors. The first is the pick errors. These are intrinsic to the observed times and nothing can be done about them. The pick errors are assumed to be gaussianly distributed with an expected value of 0 and a standard deviation σ_t . Thus, it can be assumed that the picker does not have a bias to pick either too late or too early. The second part that contributes to the difference between observed and calculated arrival times is that the

assumptions are wrong regarding the locations, velocities and travelpaths. A method of finding better locations, as well as velocity model, is to minimize the difference between the observed and calculated arrival times by adapting the current estimate for the sought variables.

The JHVD procedure can be formulated as follows. Consider an example where a network of n_s stations is situated in an area in which n_e seismic events occurred. For simplicity, assume that only the first P -wave arrivals are taken into account, and that each event is recorded by all n_s stations. Additionally, the times t_{ij} ($i=1, \dots, n_e; j=1, \dots, n_s$) are functionally related to the velocity parameters in a known manner. For each seismic event i , the arrival times may be written in a matrix form as

$$\mathbf{t}_i = t_{0i}\mathbf{1} + \mathbf{T}(\mathbf{h}_i, \mathbf{m}) + \boldsymbol{\varepsilon}_i, \quad (3.19)$$

where \mathbf{t}_i , $\mathbf{T}(\mathbf{h}_i, \mathbf{m})$ and $\boldsymbol{\varepsilon}_i$ are n_s dimensional column vectors; \mathbf{t}_i is vector of arrivals times, t_{0i} is the unknown origin time; $\mathbf{T}(\mathbf{h}_i, \mathbf{m})$ is vector of travel times; $\boldsymbol{\varepsilon}_i$ is a vector of time reading errors involved in the determination of arrival times \mathbf{t}_i ; $\mathbf{h}_i = (x_{0i}, y_{0i}, z_{0i})^T$ is a three dimensional column vector of unknown hypocentral coordinates of the i th event; and \mathbf{m} is an unknown n_m dimensional column vector of velocity model parameters.

Assume that each of the time reading errors ε_{ij} ($i=1, \dots, n_e, j=1, \dots, n_s$) have a normal distribution with a mean value equal to zero and the known covariance matrix \mathbf{C}_{ij} . It is also common to assume that there is no correlation between time reading errors at different stations. Then the matrices \mathbf{C}_{ij} become diagonal

$$\{\mathbf{C}_{ij}\}_{jk} = \begin{cases} \sigma_{ij}^2, & j=k, \\ 0, & j \neq k, \end{cases} \quad (3.20)$$

($i=1, \dots, n_e; j, k=1, \dots, n_s$), where σ_{ij}^2 is the variance of arrival time determination from the i th event recorded at the j th station. For convenience, the notation $\mathbf{C}_i = \text{diag}(\mathbf{C}_{i1}, \dots, \mathbf{C}_{in_s})$ is introduced. As the estimation is carried out by a least squares procedure, such values as $\hat{\mathbf{t}}_0$, $\hat{\mathbf{h}}$ and $\hat{\mathbf{m}}$ which minimize the sum of the squared time residuals

$$\Phi(\mathbf{x}, \mathbf{m}) = [\mathbf{t} - \mathbf{t}_0 - \mathbf{T}(\mathbf{h}, \mathbf{m})]^T \mathbf{C}_i^{-1} [\mathbf{t} - \mathbf{t}_0 - \mathbf{T}(\mathbf{h}, \mathbf{m})] \quad (3.21)$$

are taken as an evaluation of the unknown parameters, where \mathbf{x} , \mathbf{t} , \mathbf{t}_0 , \mathbf{h} and $\mathbf{T}(\mathbf{h}, \mathbf{m})$ are multivectors equal to

$$\mathbf{x}_i = \begin{pmatrix} t_{0i} \\ x_{0i} \\ y_{0i} \\ z_{0i} \end{pmatrix}, \mathbf{x} = \begin{pmatrix} \mathbf{x}_1 \\ \vdots \\ \mathbf{x}_{n_e} \end{pmatrix}, \mathbf{t} = \begin{pmatrix} \mathbf{t}_1 \\ \vdots \\ \mathbf{t}_{n_e} \end{pmatrix}, \mathbf{t}_0 = \begin{pmatrix} t_{0i} \mathbf{1} \\ \vdots \\ t_{0n_e} \mathbf{1} \end{pmatrix}, \mathbf{T}(\mathbf{h}, \mathbf{m}) = \begin{pmatrix} \mathbf{T}(\mathbf{h}_1, \mathbf{m}) \\ \vdots \\ \mathbf{T}(\mathbf{h}_{n_e}, \mathbf{m}) \end{pmatrix} \quad (3.22)$$

The travel time functions $\mathbf{T}(\mathbf{h}, \mathbf{m})$ are not linear with respect to the hypocentre coordinates and the velocity model parameters. Therefore a minimization of the misfit function (3.13) can be achieved by iterations only.

The next problem is how to quantify the velocity structure. A method of doing this is to divide the volume up into a 3D grid with n nodes. At each node a velocity is assigned and now calculate a traveltimes field for each event. This is done with a raytracing scheme and they are typically based on finite difference methods. In the next section raytracing will be discussed in more detail. Approximate partial derivatives of traveltimes with respect to the velocity can also be calculated at each gridpoint.

There are two main ways of solving (3.21). Firstly, one can directly minimize the function by using some nonlinear minimization method such as the downhill simplex method by Nelder and Mead. These methods tend, however, to be slow. The function in (3.21) would typically describe an extremely intricate space with lots of local minima. To escape these local minima is not always easy and the starting estimates needs to be very good in most cases. Certain methods exist which guarantee global convergence, such as genetic algorithms, however, these are very computer intensive. The alternative method to minimize (3.21) is to linearize the nonlinear traveltimes and this approach is explained in more detail in the following paragraphs. A Taylor expansion of the first order is made around a starting point. Note that this starting point is significant - if one is too far away from the global minimum the procedure may diverge.

Following the extension of a single event approach to the perturbations of the focal parameters of n_e events and n_m parameters of the velocity model, relation (3.6) takes the form

$$\mathbf{A}_1 \delta \mathbf{x} + \mathbf{A}_2 \delta \mathbf{m} = \mathbf{r}, \quad (3.23)$$

where

$$\mathbf{r} = \mathbf{t} - \mathbf{t}_0 - \mathbf{T}(\mathbf{h}, \mathbf{m}),$$

$$\mathbf{A}_1 = \text{diag} (\mathbf{A}_{11}, \dots, \mathbf{A}_{1n_e})$$

$\bar{\mathbf{h}}$, $\bar{\mathbf{r}}_{0i}$ and $\bar{\mathbf{m}}$ are the first approximation of focal and model parameters and

$$\mathbf{A}_2 = \begin{pmatrix} \mathbf{A}_{21} \\ \vdots \\ \mathbf{A}_{2n_e} \end{pmatrix}. \quad (3.24)$$

The minimization of the sum of time residuals (3.21) is equivalent to the minimization of $(\mathbf{r} - \mathbf{A}_1 \delta \mathbf{x} - \mathbf{A}_2 \delta \mathbf{m})^T \mathbf{C}_t^{-1} (\mathbf{r} - \mathbf{A}_1 \delta \mathbf{x} - \mathbf{A}_2 \delta \mathbf{m})$. Each \mathbf{A}_{1i} is an $(n_s * 4)$ matrix of the i th hypocentre partial derivatives equal to

$$\mathbf{A}_{1i} = \begin{vmatrix} 1, & \frac{\partial T_{i1}}{\partial x_{0i}}, & \frac{\partial T_{i1}}{\partial y_{0i}}, & \frac{\partial T_{i1}}{\partial z_{0i}} \\ \vdots & \vdots & \vdots & \vdots \\ 1, & \frac{\partial T_{in_s}}{\partial x_{0i}}, & \frac{\partial T_{in_s}}{\partial y_{0i}}, & \frac{\partial T_{in_s}}{\partial z_{0i}} \end{vmatrix} \quad (3.25)$$

Each \mathbf{A}_{2i} is an $(n_s * n_m)$ matrix of the partial derivatives of velocity model parameters

$$\{\mathbf{A}_{2i}\}_{kl} = \frac{\partial T_{ik}}{\partial m_l}, \quad (3.26)$$

where $i=1, \dots, n_e$, $k=1, \dots, n_s$, and $l=1, \dots, n_m$.

To give an idea of the size of the linear system in (3.23) consider the following: If there are 100 events and 10 stations that all trigger on each event then \mathbf{A}_1 and \mathbf{A}_2 have 1000 rows, \mathbf{A}_1 has 400 columns and \mathbf{A}_2 has n columns where n is the number of model parameters. (If the volume is divided into a 3D grid then n would be the number of nodes in the grid and this can be a large number.) Clearly the problem can be very large and it is also very sparse. In the above mentioned example for instance, the only nonzero elements in \mathbf{A}_2 would be associated with those nodes in the grid through which the ray front actually passes to get to the specific station. This system also tends to be illconditioned in the sense that a small change to the input arrival times and/or the coefficients in the matrices may mean a very large change in the correction to the sought parameters. The system (3.23) can typically be solved with an iterative least squares method such as LSQR. There are four mechanisms that are usually applied to the

system of equations in order to stabilize them numerically (Gibowicz and Kijko 1994). They are scaling, damping, centring and the use of a priori knowledge. Inverting S-P arrivals eliminates the origin time. As far as the size of the problem is concerned, it can be split into two parts by means of the Spencer Gubbins (1980) formalism. The advantage of this procedure is that the largest matrix to be inverted has dimension n and is thus a function of the number of model parameters and not the number of events.

The least squares estimation of the focal parameters \mathbf{x} and velocity model \mathbf{m} is equivalent to the solution of the system of linear equations

$$\begin{cases} \mathbf{B}_1 \delta \mathbf{x} + \mathbf{E} \delta \mathbf{m} = \mathbf{F}_1, \\ \mathbf{B}_2 \delta \mathbf{x} + \mathbf{E}^T \delta \mathbf{m} = \mathbf{F}_2, \end{cases} \quad (3.27)$$

where $\mathbf{B}_1 = \mathbf{A}_1^T \mathbf{C}_t^{-1} \mathbf{A}_1$, $\mathbf{B}_2 = \mathbf{A}_2^T \mathbf{C}_t^{-1} \mathbf{A}_2$, $\mathbf{E} = \mathbf{A}_1^T \mathbf{C}_t^{-1} \mathbf{A}_2$, $\mathbf{F}_1 = \mathbf{A}_1^T \mathbf{C}_t^{-1} \mathbf{r}$, and $\mathbf{F}_2 = \mathbf{A}_2^T \mathbf{C}_t^{-1} \mathbf{r}$. As already mentioned, due to the non-linearity of the problem, the matrices \mathbf{B}_1 , \mathbf{B}_2 , \mathbf{E} , \mathbf{F}_1 , and \mathbf{F}_2 are functions of the hypocentre coordinates and velocity model, and the problem is solved iteratively.

As mentioned, Spencer and Gubbins (1980) introduced a technique which resolves such problems. A simple rearrangement of (3.27) leads to

$$\begin{aligned} \delta \mathbf{m} &= (\mathbf{B}_2 - \mathbf{E}^T \mathbf{B}_1^{-1} \mathbf{E})^{-1} (\mathbf{F}_2 - \mathbf{E}^T \mathbf{B}_1^{-1} \mathbf{F}_1) \\ \delta \mathbf{x} &= \mathbf{B}_1^{-1} (\mathbf{F}_1 - \mathbf{E} \delta \mathbf{m}) \end{aligned} \quad (3.28)$$

Solution of (3.28) requires the inversion of two matrices: the $(4n_e * 4n_e)$ matrix \mathbf{B}_1 and the $(n_m * n_m)$ matrix $(\mathbf{B}_2 - \mathbf{E}^T \mathbf{B}_1^{-1} \mathbf{E})$. The matrices \mathbf{E} and \mathbf{F}_1 have a block structure

$$\mathbf{E} = \begin{bmatrix} \mathbf{E}_1 \\ \vdots \\ \mathbf{E}_i \\ \vdots \\ \mathbf{E}_n \end{bmatrix}, \quad \mathbf{F}_1 = \begin{bmatrix} \mathbf{F}_{11} \\ \vdots \\ \mathbf{F}_{1i} \\ \vdots \\ \mathbf{F}_{1n} \\ 0 \end{bmatrix}, \quad (3.29)$$

and \mathbf{B}_1 is block diagonal: $\mathbf{B}_1 = \begin{bmatrix} \mathbf{B}_{11} & & & & \\ & \mathbf{B}_{12} & & & \\ & & \ddots & & \\ & & & \ddots & \\ 0 & & & & \mathbf{B}_{1n_e} \end{bmatrix}$,

(3.30)

where for each event i , $\mathbf{E}_i = \mathbf{A}_{1i}^T \mathbf{C}_{ii}^{-1} \mathbf{A}_{2i}$, $\mathbf{F}_{1i} = \mathbf{A}_{1i}^T \mathbf{C}_{ii}^{-1} \mathbf{r}_i$, and $\mathbf{B}_{1i} = \mathbf{A}_{1i}^T \mathbf{C}_{ii}^{-1} \mathbf{A}_{1i}$. Therefore the system of equations (3.28) can be rearranged as follows

$$\delta \mathbf{m} = \left[\sum_{i=1}^{n_e} (\mathbf{B}_{2i} - \mathbf{E}_i^T \mathbf{B}_{1i}^{-1} \mathbf{E}_i) \right]^{-1} \left[\sum_{i=1}^{n_e} (\mathbf{F}_{2i} - \mathbf{E}_i^T \mathbf{B}_{1i}^{-1} \mathbf{F}_{1i}) \right],$$

$$\delta \mathbf{x}_i = \mathbf{B}_{1i}^{-1} (\mathbf{F}_{1i} - \mathbf{E}_i \delta \mathbf{m}), \quad i = 1, \dots, n_e, \quad (3.31)$$

where $\mathbf{B}_{2i} = \mathbf{A}_{2i}^T \mathbf{C}_{ii}^{-1} \mathbf{A}_{2i}$, $\mathbf{F}_{2i} = \mathbf{A}_{2i}^T \mathbf{C}_{ii}^{-1} \mathbf{r}_i$, and $\delta \mathbf{x}_i$ and $\delta \mathbf{m}$ are the correction vectors to the first guess of the i th focal parameters $\tilde{\mathbf{x}}_i$ and velocity model parameters $\tilde{\mathbf{m}}$ respectively. The procedure (3.18) is repeated until some cutoff criteria are met. The solution of the problem requires n_e inversions of the (4*4) matrices \mathbf{B}_{1i} and one inversion of the ($n_m * n_m$) matrix $\sum (\mathbf{B}_{2i} - \mathbf{E}_i^T \mathbf{B}_{1i}^{-1} \mathbf{E}_i)$, where the summation is from $i=1$ to n_e . Without using the concept of Spencer and Gubbins (1980) of the parameter separation and partitioned matrices technique, a straight inversion of the system would normally require operations of the order of $(4n_e + n_m)^3$. The approach described here requires approximately only $4^3 n_e + n_m^3$ operations and limited computer storage.

In order to simplify the problem, it is necessary to quantify the velocity structure differently. If the travel time anomalies from a set of close seismic events are assumed to tend to be strongly correlated and have nearly constant values at the same stations, then it is not necessary to divide the velocity structure in a 3D grid. Rather, an average velocity is assigned to a given station using only those events in the cluster of close events. In other words, the assumption is made that seismic waves from different events in the cluster travel to a given station through more or less the same rockmass. Since the example is applied to a mining environment, the station tends to be fairly close to the events and therefore straightline raypaths are assumed. Thus no raytracing is needed, greatly speeding up calculations. It is necessary to bear in mind that there are now some additional restrictions on the problem. If the cluster of events is too large there exists a physical contradiction: if two events in the cluster are far apart the assumption

that the wave travels through the same rock is no longer valid; conversely, if the cluster is too small increased numerical instability may be found, since the arrival time equations are very similar. This could mean near linear dependencies in the linear system or, equivalently, a space with lots of local minima near the global minimum. In such a case both the linear and nonlinear approach to solve the problem may struggle. For each case study there exists an optimal ratio between average distance from cluster to stations and the size of the cluster. This formulation of the problem can be solved with any one of the approaches as mentioned earlier.

As an example of application of JHVD, using the Spencer Gubbins formalism, data from the Freegold Regional network in Welkom was used. Events were selected from a 1600m x 1600m volume from 1 June 1994 to 23 November 1994. Fig.3.5 shows a plan view of the 30 selected events and the surrounding stations and Fig.3.6 shows the section view. Inversion was performed using the *P* arrivals only, the *S* arrivals only and the *S-P* arrivals. The inverted velocities for 9 of the 15 stations are shown in Fig.3.7. The fifth station (station 22) is a surface site and therefore the velocity is lower than those of the other stations. It can clearly be seen that the inverted *S-P* arrivals generate velocities that correlate well with those obtained if calculated using velocities from the inverted *P* arrivals and from the inverted *S* arrivals. This give a measure of confidence in the calculations.

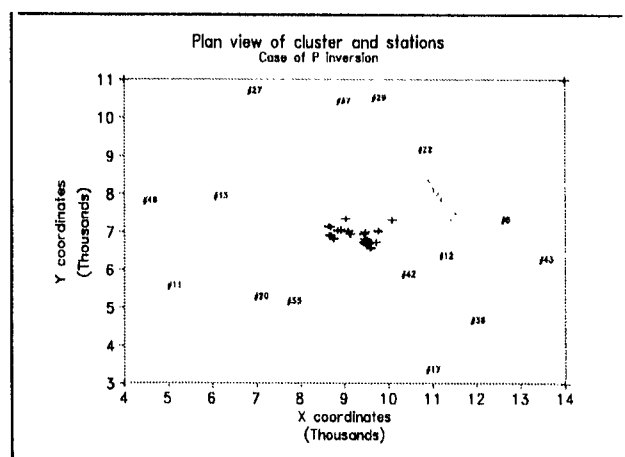


Figure 3.5 Plan view of 30 events selected from the Freegold area.

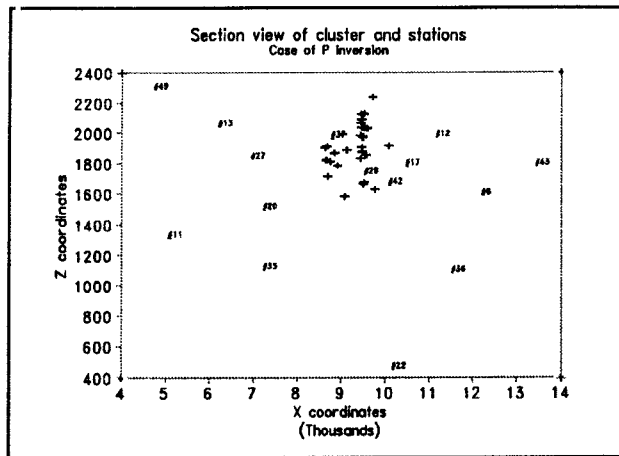


Fig.3.6 Section view of 30 events selected from the Freegold area.

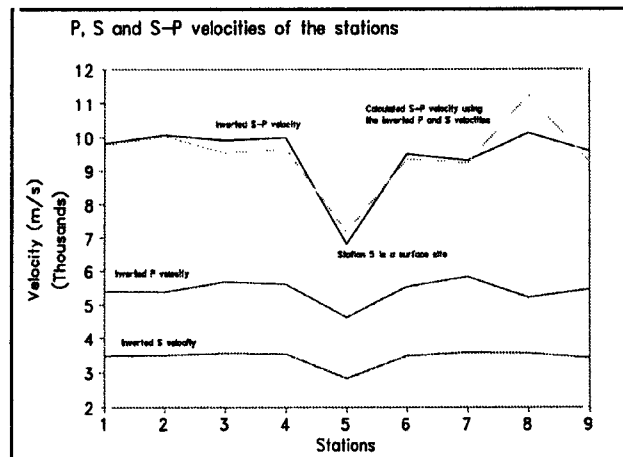


Fig.3.7 Results from JHVD. Notice the good S-P velocity correlation in the inverted and calculated cases. Also notice the lower velocity associated with the surface site.

In another example of application of JHVD, data from the Elandsrand Gold Mine in South Africa was used. JHVD was used on this mine to obtain a P velocity model for different clusters of events, in order to improve location accuracy (Essrich, 1996). Nine clusters of events of approximately 300x200x400 m were chosen and the event locations and velocities were computed using JHVD. To evaluate the results, a simplified geological model of the mine was assumed and P velocities were assigned. The model is shown in Table 3.1.

Using this model, sections were drawn which intersected clusters and stations and average velocities were calculated along straight raypaths. Fig.3.4 shows the comparison between velocities obtained by the model and those obtained employing JHVD for one of the clusters. There is a good correlation between inverted velocities and those predicted by the geological model. JHVD is specifically useful to

identify site which need significant velocity alterations in order to improve location accuracy.

Table 3.1 Elandsrand simplified geological model

Layer	Position	P velocity m/s
Pretoria group (shale & quartzite)	Surface to dolomite (0 - 750)	5000
Dolomite	dip 12° Sth 750 - 2000	6850
Ventersdorp lavas	dip 25° Sth 2000 - 2400	5950
Quartzite	dip 25° Sth 2400 - 3000	6050
Gritty quartzite	dip 15° West 2400 - 2800	5750
Booyesen shale	dip 25° Sth 3000 - 3500	5500

In Fig.3.8, JHVD suggests an increase in P velocity of about 500m/s for station 2 and this is collaborated by the geological model.

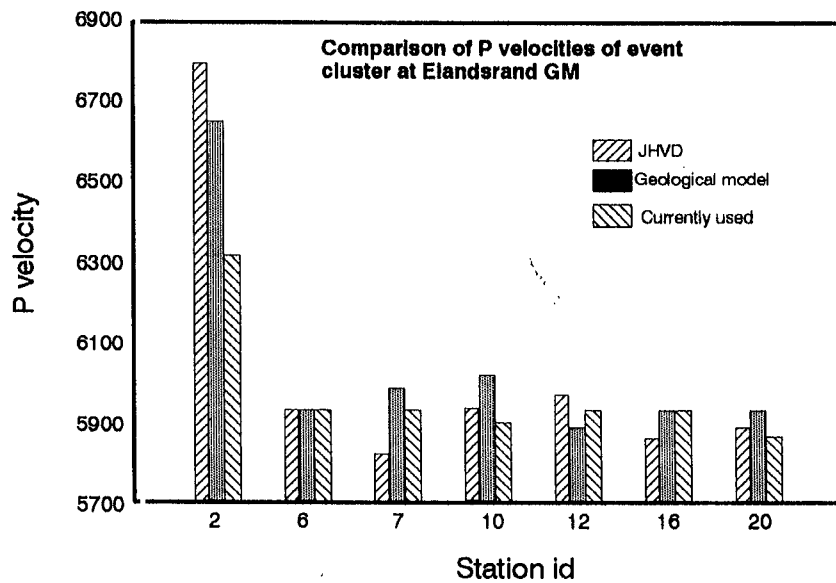


Fig.3.8 Results from Joint Hypocentre and Velocity Determination (JHVD) performed on a dataset from Elandsrand Gold Mine. JHVD was used to obtain a P velocity model for different clusters of events, in order to improve routine seismic event location. Cluster size was of the order of 300mx200mx400m. The figure shows that the inverted velocities correlate well with those calculated using a simple geological model. This method allows for the identification of stations that may need significant changes to the P velocity (see station 2 in this figure).

CHAPTER 4

SEISMIC RAYTRACING

The success rate with the location of seismic events and the inversion of seismic source parameters depends to a great degree on the accuracy of reconstructing the rays seismic waves follow in a given geological medium. In particular, tangents to the seismic rays at the source and at the stations are of importance if routine inversions of seismic moment tensors are to be performed.

Travel times for seismic waves can be calculated in a variety of ways. More complex media require more computationally expensive and tricky schemes to find the transit time, trajectory and associated amplitude and phase shift. If the medium is homogeneous, the path of seismic waves is a straight line connecting source and receiver and the travel path is easy to calculate. In the case when the medium is horizontally layered, the path along which the energy flows may be derived using the invariance of ray parameter. The determination of travel times in media which vary both vertically and laterally requires some sort of raytracing.

All ray tracing procedures could be divided in two steps: kinematic and dynamic raytracing. Kinematic ray tracing includes ray trajectory and traveltimes determination along it, but does not imply any dynamical parameters estimation. Dynamic ray tracing additionally estimates amplitudes, phase shift and a ray-spreading Jacobian. Usually, kinematic ray tracing precedes the dynamic raytracing, but some methods (e.g. wavefront construction methods) estimate both kinematic and dynamic parameters simultaneously. Using the output of dynamic ray tracing, it is possible to compute synthetic seismograms provided that the source function is known.

The basic concept underlying the raytracing is that the seismic energy of infinitely high frequency follows the trajectory determined by the raytracing equations. Physically, these equations describe how the energy continues in the same direction until it is refracted or reflected by velocity variations.

Raytracing methods could be divided into several categories:

- shooting and bending methods,
- point-to-curve methods
- finite difference methods,
- wavefront construction methods.

4.1 Shooting and Bending.

In "shooting" methods of raytracing, a fan of rays is shot from one

point in general direction of other point. The correct path and travel time to connect the two points may then be approached by more accurate guesses for ray path. (e.g. Julian and Gubbins, 1977, Cerveny *et al.* 1977).

"Bending" methods of raytracing start with an initial guess for the ray path. The ray path is then bent by a perturbation method until it satisfies a minimum time criterion. Other names for bending method are: *point-to-point raytracing* or *two-point raytracing*. The problem is then defined by specifying the ray congruence (in terms of source and the list of reflections and mode conversions at all interfaces intersected by the ray) as well as a receiver. The bending methods have been introduced in seismology by Wesson (1971), Chander (1975) and Julian and Gubbins (1977). In the original method of Julian & Gubbins (1977), the most detailed description of which can be found in Pereyra *et al.* (1980), the raytracing equations

$$\frac{d}{ds} \left(\frac{1}{c(\mathbf{r})} \frac{d\mathbf{r}}{ds} \right) - \nabla \left(\frac{1}{c(\mathbf{r})} \right) = 0 \quad (1.1)$$

for a ray r , parameterized by the arc length s , in a velocity field $c(\mathbf{r})$, are approximated by discretizing the ray path into $k + 1$ points ($\mathbf{r}_0, \mathbf{r}_1, \dots, \mathbf{r}_k$) and by using finite differences for the derivatives. The obtained system of equations can then be linearized and solved to find the perturbation that must be applied to some initial guess of the ray in order to reduce the right-hand side of the ray equations to zero. Since the linearized system is approximate, several iterations will usually be sufficient for convergence.

The second type of "bending" methods (Um & Thurber, 1987, Prothero *et al.* 1988) tries to minimize directly the traveltimes as a functional of the ray curve γ .

$$T(\gamma) = \int_{\gamma} \frac{ds}{c} \rightarrow Min \quad (1.2)$$

The advantages of this subgroup of "bending" methods over methods described above are obvious. The precision of the finite-difference approach is restricted by the precision of numerical differentiation, which is inherently more unstable than the numerical integration. The linearization of system of equations described above leads to introducing small errors. Therefore, taking into account the ill-conditioning in the presence of a complicated velocity model, these small errors may prevent the solution from convergence to the desired accuracy, or even cause a divergence.

The difficulties with raytracing using the above described "shooting"

and “bending” methods fall into several categories:

- for strongly varying velocity fields there can be many paths connecting two points of interest and, taking that into account, it is easy to miss the raypath with minimum travel time. This raises the important issue how to generate all the rays in the given congruence which join the source and the given receiver.
- if travelpaths to many points are needed, the computing time necessary for it may render the raytracing impractical.
- even in a smooth medium, there may be a shadow zone, where pairs of points will be connected only by rays that have a very small geometric amplitude because a small change in the takeoff angle results in a large change in the raypath. Shooting methods of raytracing often have trouble finding the correct ray in a shadow zone.

Bending methods do give an answer in shadow zones, however, in both bending and shooting methods, it is possible that the answer is only a local minimum and therefore the global minimum travel time and corresponding ray path remain unknown (Hanyga, 1991).

4.2 Point-to-curve

Most of the problems described above can be overcome by the *point-to-curve raytracing algorithms* (Hanyga, 1991; Hanyga and Pajchel, 1994). These algorithms solve a somewhat relaxed problem: the receiver is not fixed but rather allowed to move along the curve in the model space. The algorithm determines successive receivers and associated rays. The output is a curve in space whose points define the rays as well as the associated receivers. This new problem is well defined as the caustics where the solution curve folds over the receiver curve returning to the receivers already visited along a new solution branch. By adjusting the ray parameters, the ray end point usually marches backward and forward along the receiver curve, thereby visiting the receivers one or several times or not at all and thus generating different arrivals. This technique is based on so-called “continuation methods” (Allgower and Georg, 1990). Continuation methods amount mathematically to solving a system of equations with one more unknown than equations or equivalently forcing the solution to follow implicitly defined curve. All the branches connected into a single curve are successively found, essentially resolving the problem of tracing all the rays at every receiver. Although these methods are

much more powerful than *point-to-point* raytracing methods they are not guaranteed to find all arrivals. This can be attributed to the fact that the implicit curve possibly consists of several disconnected branches. Therefore, after following one branch, it is not certain that there is no other branch and that all arrivals have been found. Caution needs to be exercised to avoid endlessly generating the same arrivals, which may happen if a branch is a closed loop. Another problem which may be encountered is receiver curve definition. Some of the solutions may not be found depending on the actual curve definition and model box size.

Let us now briefly formulate *point-to-curve* algorithm. Rays satisfy the ray differential equations:

$$\begin{aligned} \frac{d\mathbf{x}}{d\sigma} &= \mathbf{p} \\ \frac{d\mathbf{p}}{d\sigma} &= \frac{1}{2} \nabla u^2 \\ \frac{dT}{d\sigma} &= u^2 \end{aligned} \tag{1.3}$$

where \mathbf{x} denotes the ray location, \mathbf{p} the slowness vector, u the slowness (twice continuously differentiable function of \mathbf{x}), T is the cumulative travelttime along the ray, and σ a parameter along the ray defined by the last equation. Let us suppose that a ray in three dimensions is characterized by two ray parameters γ_1 and γ_2 , for instance two initial ray angles in three-dimensional space. Then the ray field is described by $\mathbf{x}(\gamma_1, \gamma_2, \sigma)$ and for a fixed receiver \mathbf{x}^R the *two-point* raytracing problem is given by

$$\mathbf{x}(\gamma_1, \gamma_2, \sigma) - \mathbf{x}^R = 0 \tag{1.4}$$

which is a system of three nonlinear equations with three unknowns γ_1 , γ_2 and σ . Such a system has generally speaking a finite number of isolated solutions which correspond to the finite number of arrivals at the receiver. The main idea behind *point-to-curve* raytracing method is to replace the fixed receiver location \mathbf{x}^R by a receiver curve. Then equation (4.4) can be rewritten as

$$\mathbf{x}(\gamma_1, \gamma_2, \sigma) - \mathbf{x}^R(\lambda) = 0 \tag{1.5}$$

which is a system of three non-linear equations with four unknowns or implicit description of a curve in a four-dimensional space. Explicit definition of that curve can be given by

$$(\gamma_1(s), \gamma_2(s), \sigma(s), \lambda(s)) \tag{1.6}$$

where s is the arclength along the curve. Then the four-dimensional curve whose definition is given by (4.6) represents the solutions of a sequence of *point-to-point* problems. In general, the methods for implicit curve tracing can be divided in two groups: *predictor-corrector* methods and *piecewise-linear* methods. For detailed descriptions of these methods the reader is referred to Allgower and Georg (1990).

Let us now consider example of application of *point-to-curve* raytracing in some model giving rise to caustic. The receiver is located inside the caustic cusp of the source. The model which we will use in following discussion is the MODEL8, described in Hanyga (1988). The model consists of two homogeneous blocks. The rays are contained in the upper block and are reflected without conversion. The propagation speed in the upper block is assumed to be 3.5 km/sec, the density 1.0.

Model box: $-10 \leq x \leq 20, 0 \leq y \leq 20, 0 \leq z \leq 20$;
 Interface: $z = 0.01(x - 10)^3 + 0.05(x - 10)^2 + 5$
 Source: (6, 10, 16)
 Receiver End: (0, 10, 19.5)
 Receiver Line Direction: (1, 0, 0).

The receiver curve has been defined as line passing through the receiver end point with the direction cosines shown above. This is basically the so-called 2.5 D model. Ray distribution found using *point-to-curve* algorithm is shown in Fig. 4.1.

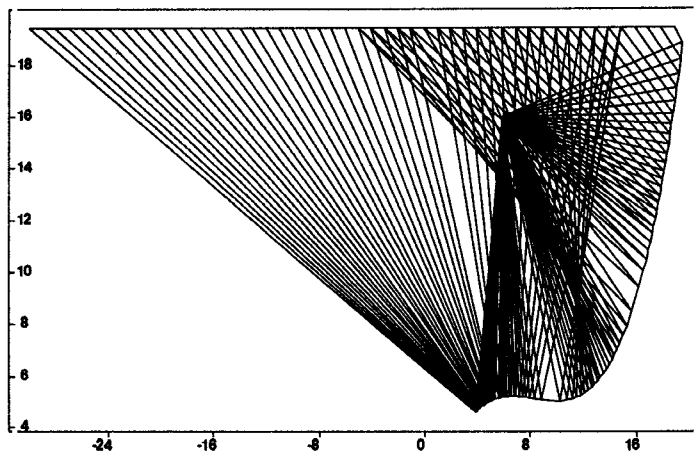


Fig.4.1 Ray distribution for MODEL8 (Hanyga, 1988) calculated for source (6,10,16) and receiver curve defined by the receiver end point (0,10,19.5) and direction cosines (1,0,0) using *point-to-curve* raytracing algorithm. For traveltimes plot, see Fig.4.2.

This example demonstrates the ability of *point-to-curve* algorithms to find multiple solutions - triplications, bifurcation points. Traveltimes

plot for above mentioned model and definition of receiver curve is shown in Fig.4.2. In order to check the stability of the *point-to-curve* raytracing method to different receiver curve definition, we calculated the solutions of the above formulated problem for two different receiver line directions.

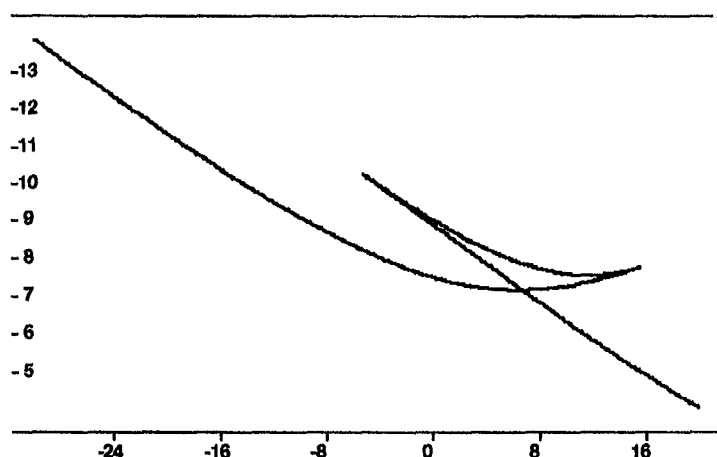


Fig.4.2 Traveltime plot for MODEL8.

In Fig.4.3 the traveltime distribution is shown for receiver line passing through the point (0, 10, 19.5) and making 60 degrees angle with the X axis (direction angles are (60°, 30°, 0°). No triplications are found. Fig.4.4 shows the traveltime plot for receiver line passing through the same receiver end point (0, 10, 19.5) but direction angles now are (30°, 60°, 0°). Triplications are present in the solution. The main reason explaining why the triplications of traveltime curve are not found in Fig.4.3, is the restrictions on receiver curve crossing the greater model boundary. Once the ray curve is outside the greater model boundary (which must be supplied as user defined input) the solution stops. It should be pointed out that in order to overcome that problem the greater model boundary can be defined to change adaptively during the calculation process, correspondingly increasing the computational requirements.

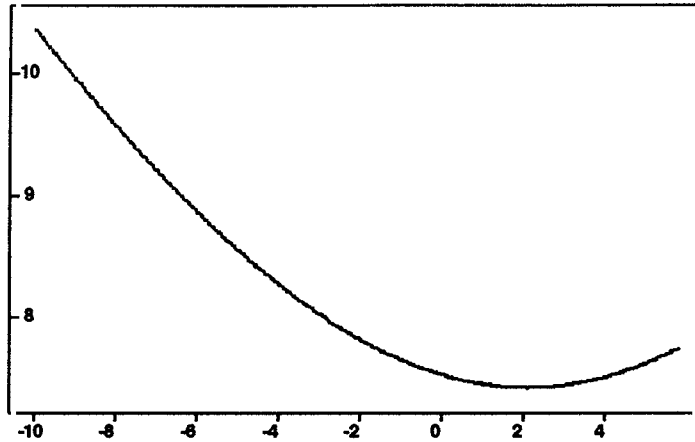


Fig.4.3 Traveltime plot for MODEL8, with receiver line passing through the receiver end point (0,10,19.5) and with direction angles (60°,30°,0°).

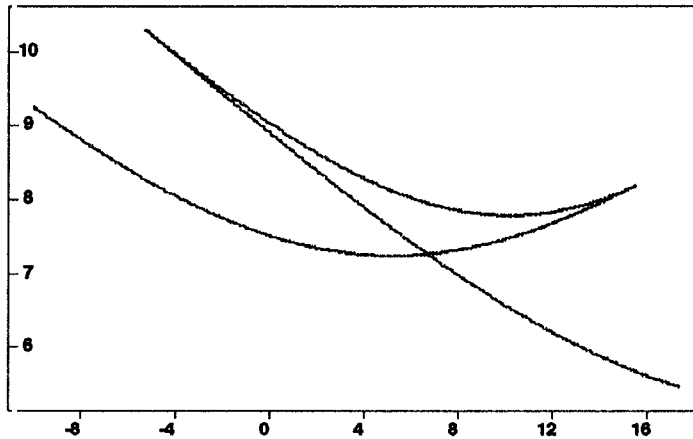


Fig.4.4 Traveltime plot for MODEL8, with receiver line passing through the receiver end point (0,10,19.5) and with direction angles (30°,60°,0°).

4.3 Finite-Difference

Finite difference methods also overcome most of the shortcomings of the shooting and bending methods, but are less accurate.

Vidale (1988) described a finite difference method that extrapolated travel-times away from source. Vidale's algorithm has been initially based on a two dimensional earth model consisting of square cells with nodes positioned at cell corners. Energy is propagated from the source throughout the grid in expanding (square) rings of nodes centred around the source. Let us consider Fig 4.5.

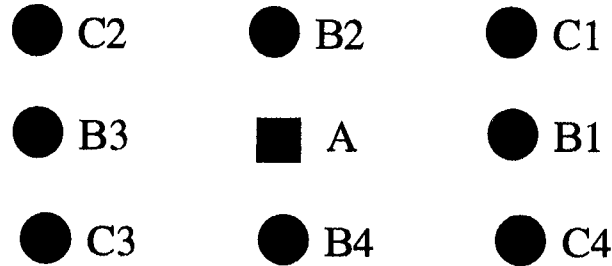


Fig.4.5 The source grid point A and the grid points in the ring surrounding the source point.

The source is assumed to be at grid point A and the timing process is initiated by assigning point A the travel time of zero. Then, through the use of finite difference solution of eikonal equation, all adjacent points can be timed. The four points adjacent to the point A, labelled B1 through B4 in Fig.4.5, can be timed as follows:

$$t_i = \frac{h}{2}(S_{B_i} + S_A) \tag{1.7}$$

where h is the mesh spacing, S_A is the slowness at the point A, and S_{B_i} is the slowness at the grid point B_i being timed. The traveltimes at the four corners are then found by one of two methods, as follows:

a. Plane-wave approximation

$$t_{C1} = t_A + \sqrt{2(hs)^2 - (t_{B2} - t_{B1})^2} \tag{1.8}$$

This equation gives the traveltime to point C1 using the traveltimes from the source to points A, B1 and B2 in a plane-wave approximation. The point A does not need to a source point for this equation to apply.

b. Assuming locally circular wavefronts

The second approach assumes locally circular wavefronts. A circular wavefront can be specified by the three parameters: the x coordinate of the virtual source point $-x_s$; the z coordinate of the virtual source point $-z_s$, and the origin time of the virtual source t_s . The virtual source must lie at the centre of the curvature of the circular wavefronts.

Assuming that the origin of this coordinate system is placed at point A and grid points B1, B2 and C1 have coordinates $(h,0)$, $(0,h)$ and (h,h) respectively, the travel times to points A1, B1 and B2 can be expressed by the following system of equations:

$$\begin{aligned} t_0 &= t_s + S\sqrt{x_s^2 + z_s^2} \\ t_1 &= t_s + S\sqrt{(x_s + h)^2 + z_s^2} \\ t_2 &= t_s + S\sqrt{x_s^2 + (z_s + h)^2} \end{aligned} \quad (1.9)$$

This is a system of three unknowns which can be solved to produce the values of x_s , t_s , z_s , with which t_3 can be calculated as follows:

$$t_1 = t_s + S\sqrt{(x_s + h)^2 + (z_s + h)^2} \quad (1.10)$$

Analysis of accuracy of both solutions has shown that for the wavefronts with very little curvature (4.8) produces the quicker and more accurate answer. For strongly curved wavefronts (4.10) is a better approximation. For optimal accuracy, a "mixed" scheme must be used.

With these schemes to find the traveltimes at the fourth corner of a square, the traveltimes may be found throughout the grid. The order of solution is very important. Firstly, points on the square around the source are timed, then, starting with the minimum traveltime on each side of the initial square, traveltimes are calculated on the next larger square. The solution proceeds the same way until all points in the medium are timed (Fig.4.6). Vidale (1990) later extended his method to the three-dimensional case and proposed a new extrapolation scheme.

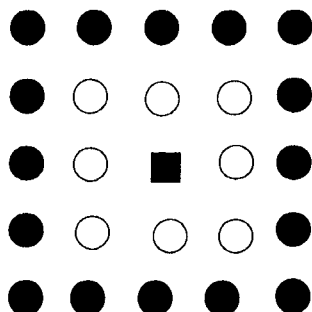


Fig.4.6 Progress of solution of 2D case. The ring of points shown as filled circles are to be timed at this stage. The filled rectangle at the centre of the grid is the source. The hollow circles show the position of the ring timed at the previous stage.

Vidale used an implicit assumption that the traveltimes at a node on a ring can be computed from locally adjacent nodes on the prior inner ring. However, in some cases, when there are large velocity variations of the media, the first arrival energy may actually follow the circuitous route and approach the node from the outer ring. To illustrate that point, consider the two layer model in Fig.4.7, where the source is located in a low velocity layer. The actual arrival at point *D* is the head wave transmitted along the path *A-B-C-D*. However, the expanding square algorithm will time the point *D* before the edge of the square reaches the interface. Therefore, the influence of the high-velocity layer will not be included and will lead to wrong timing of this and many other points.

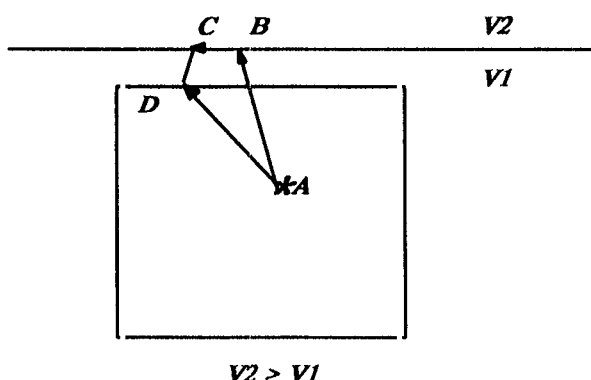


Fig.4.7 A two layer model where infinite-difference scheme by Vidale (1988) will fail to produce the correct solution. A is the source point, D the point to be timed. V_1 and V_2 are the velocities of two layers and $V_2 > V_1$ (Qin et al 1990).

Pure finite-difference methods fail in the velocity field with high contrast and first order discontinuities of arbitrary shapes. An alternative approach proposed by Podvin and Lecomte (1991) appears to be more robust but less accurate. Their method makes use of generalised Huygens principle, which states that wavefronts are envelopes of elementary wavefronts generated by secondary sources. The discretization of the velocity field on a regular grid is not only considered as a mathematical construction, as is done in the pure finite-difference approach, but also as an actual physical representation of the medium. Each elementary grid cell therefore represents an elementary homogeneous piece of the velocity field. The sides and corners of the cells define the location of secondary sources to be used according to Huygens principle. Despite the mentioned loss of accuracy in traveltimes calculations, this method can deal with almost arbitrary complicated first-order discontinuities of the velocity wavefield.

Another alternative approach which avoids that problem, but which requires large computational cost, has been proposed by Qin *et al.* (1992). In this scheme, the solution region progresses outward from an "expanding wavefront" rather than an "expanding square" and therefore honours causality. On every step perimeter the traveltimes array is constructed and sorted in order of increasing traveltimes. Then the solution proceeds, starting with the global minimum traveltimes point, updating the perimeter array until the global minimum traveltimes is found. Therefore, the solution is found along the "expanding wavefront" and causality is preserved, although computational requirements are increased significantly.

All the above described finite difference methods make use of the traditional cell-centred node scheme. An alternative approach has been used by Cao and Greengalgh (1994), which is based on a new corner node velocity model discretization scheme. They have shown that this method offers accuracy advantages. A substantial efficiency improvement is achieved by the incorporation of the wavefront tracking algorithm based on a construction of a minimum traveltimes tree.

A characteristic feature of the finite-difference methods is that they only calculate the traveltimes for the first arrivals at each point on a regular grid. As such, they cannot be, in general, considered as an alternative to other raytracing methods, although they represent interesting complimentary techniques, mainly due to their efficiency, speed, ease of use and their ability to deal with peculiar waves such as headwaves or diffracted waves.

As has been mentioned, the finite difference methods described above provide solutions only for the first arrival traveltimes, which

may be sufficient for some problems, but the first arrivals method can be used to obtain, indirectly, even the later arrivals (Podvin & Lecomte, 1991). A more systematic approach to calculating later arrivals with a modified version of that algorithm has been presented in Podvin (1992).

Once traveltimes are known, rays can be traced back to the source using the direction of the steepest descent from the grid cell closest to the receiver.

The expanding wavefront method of Qin *et al.* (1992) has been applied to a raytracing problem for Vaal Reefs Gold Mine, South Africa. Geological information available consists of basically three layers, where the velocity of the upper layer is 6834m/sec, of the second 6116m/sec and the underlying layer has a velocity of 5779m/sec. Each layer information has been defined in a very sparse grid (1km grid spacing in X direction, 2 km spacing in Y direction). Obviously, initial data could not be used without prior interpolation and model space definition. Each layer's initial grid has been used to interpolate on a fine, uniformly spaced grid with 100 m grid spacing, using B-splines. Perspective mesh plots of each layer's bottom is shown on the left in Fig.4.8. Contour line representation of the same information is shown on the right in Fig.4.8.

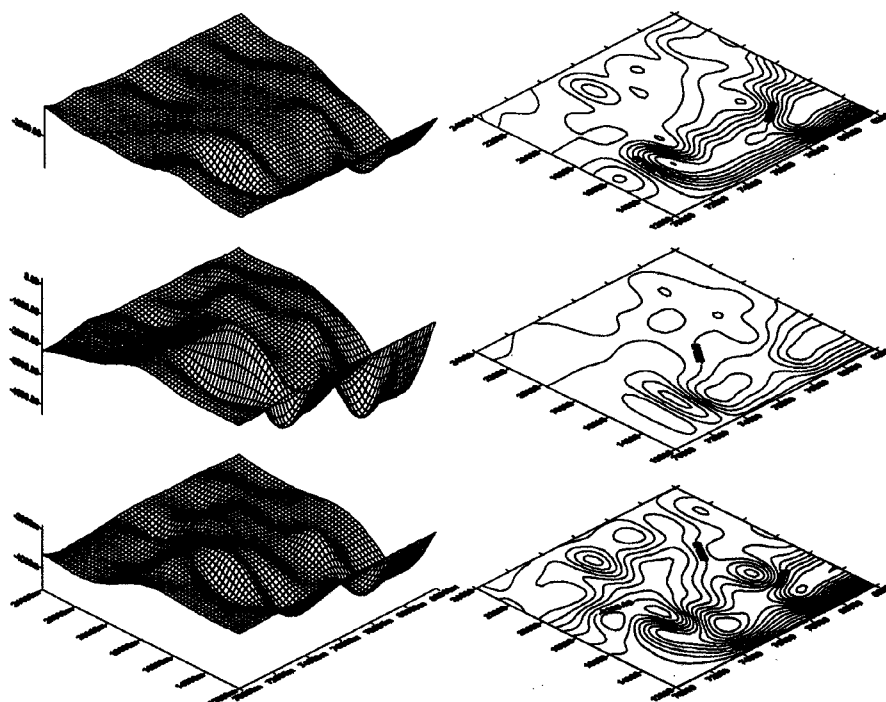


Fig.4.8 Geometry of interfaces for Vaal Reefs Gold Mine Region for $7000m \leq X \leq 82000m$; $12000m \leq Y \leq 24000m$; $0 \leq Z \leq 5000m$ model space represented as a 3D mesh plot. The depth is shown on the left hand axis. The fine mesh grid has been obtained by B-spline interpolation of initial sparse grid.

In each case, the model space used is:

$$\begin{array}{ll} 1200m & \leq X \leq 1700m \\ 7000m & \leq Y \leq 75000m \\ 0m & \leq Z \leq 5000m \end{array}$$

Grid dimensions therefore are 50 by 50 by 50. Source location used was (12500m, 72500m, 4250m). In Fig.4.9 isochron distribution is shown on different model slices by planes parallel to the horizontal plane at various depths: $Z = 0m, 500m, 1000m, 1500m, 2000m, 2500m$, correspondingly. Ray trajectories for different source positions and receivers situated along the model boundaries and in a plane passing through the source and parallel to XZ plane are shown in Fig.4.10. Rays have been smoothed prior to display. Comparing the ray distribution in Fig.4.10, one can see caustics and shadow zones present. Isochrons on slices by planes parallel to YZ plane are shown in Fig.4.11, for $X = 70000m, 71000m, 72000m, 73000m, 74000m, 75000m$ correspondingly.

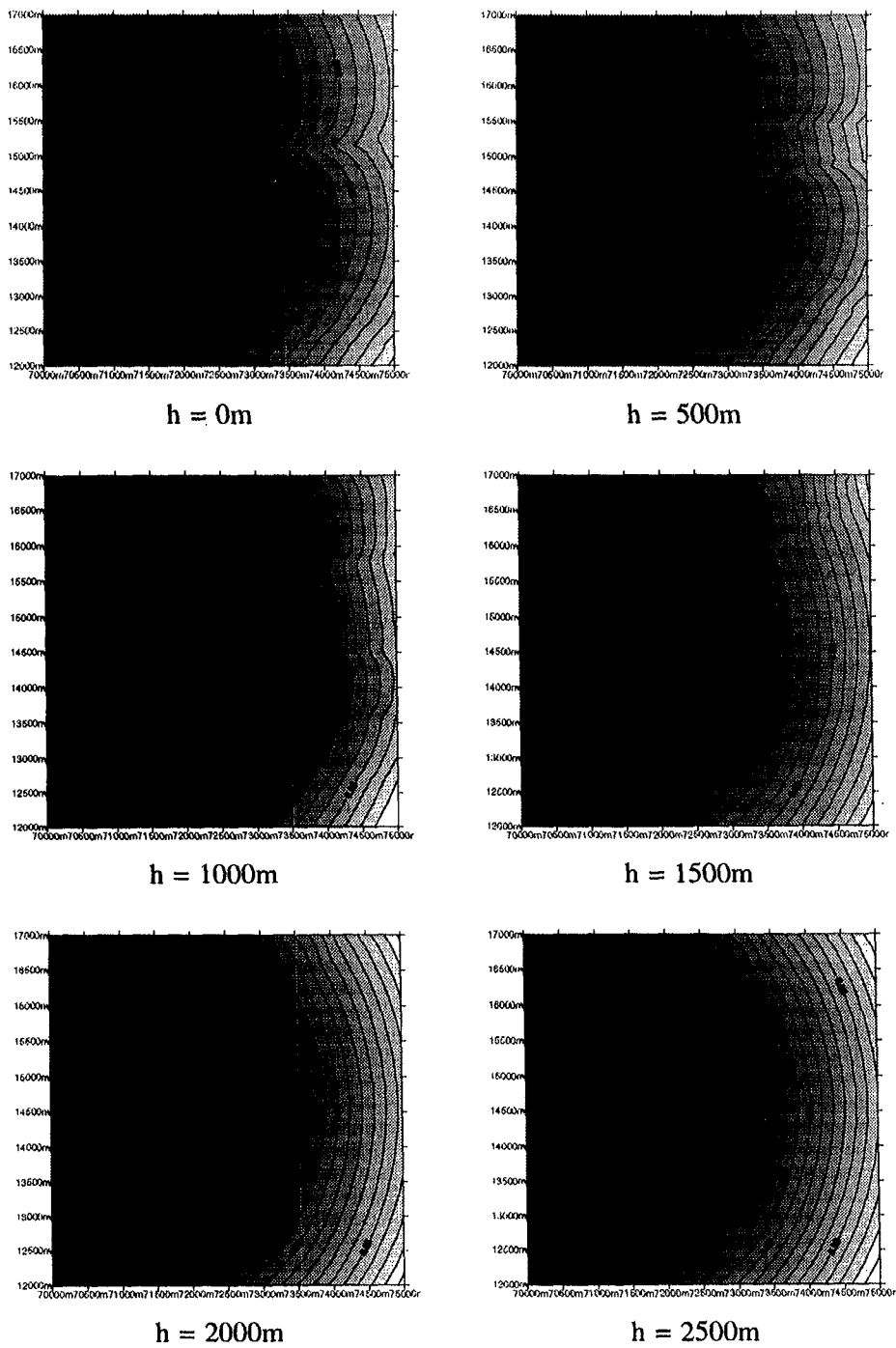
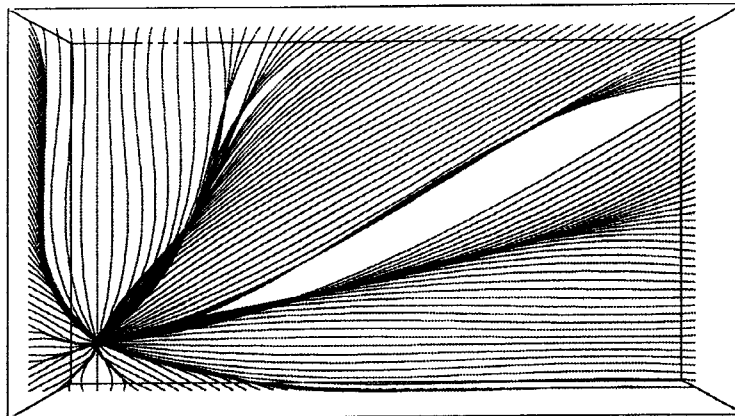
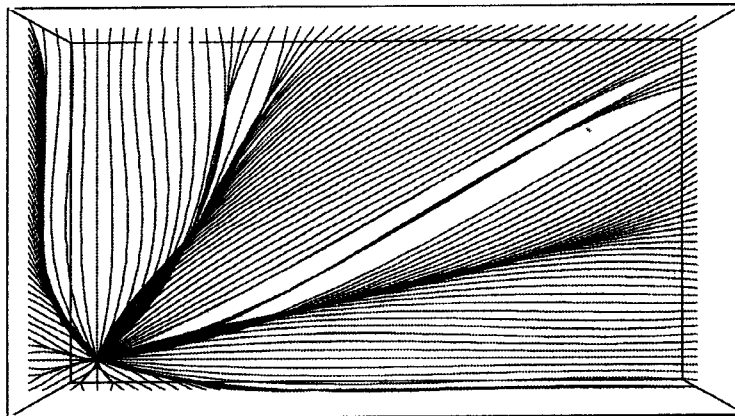


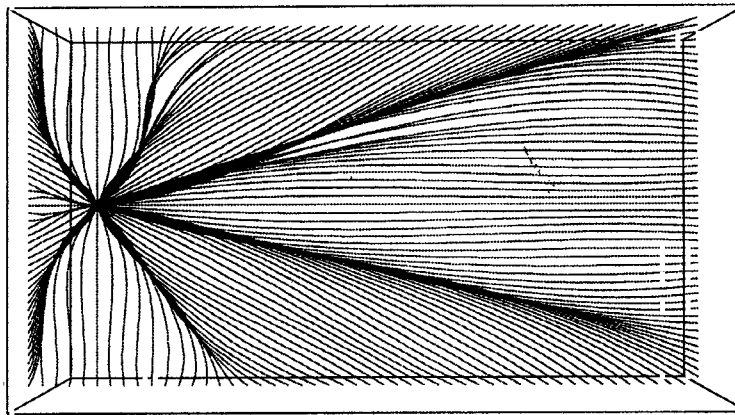
Fig.4.9 Isochrons on slices by planes parallel to XY plane at different depths.



(12500M, 72500M, 4250M)



(12500M, 72500M, 4500M)



(12500M, 72500M, 4500M)

Fig.4.10 Ray plots for receivers situated along the model boundaries and lying in the plane passing through the source and parallel to XZ plane for source locations as indicated. Model space used is $1200m \leq X \leq 1700m$; $70000m \leq Y \leq 75000m$; $0m \leq Z \leq 5000m$. Grid dimension is $50 \times 50 \times 50$. Rays have been smoothed prior to display.

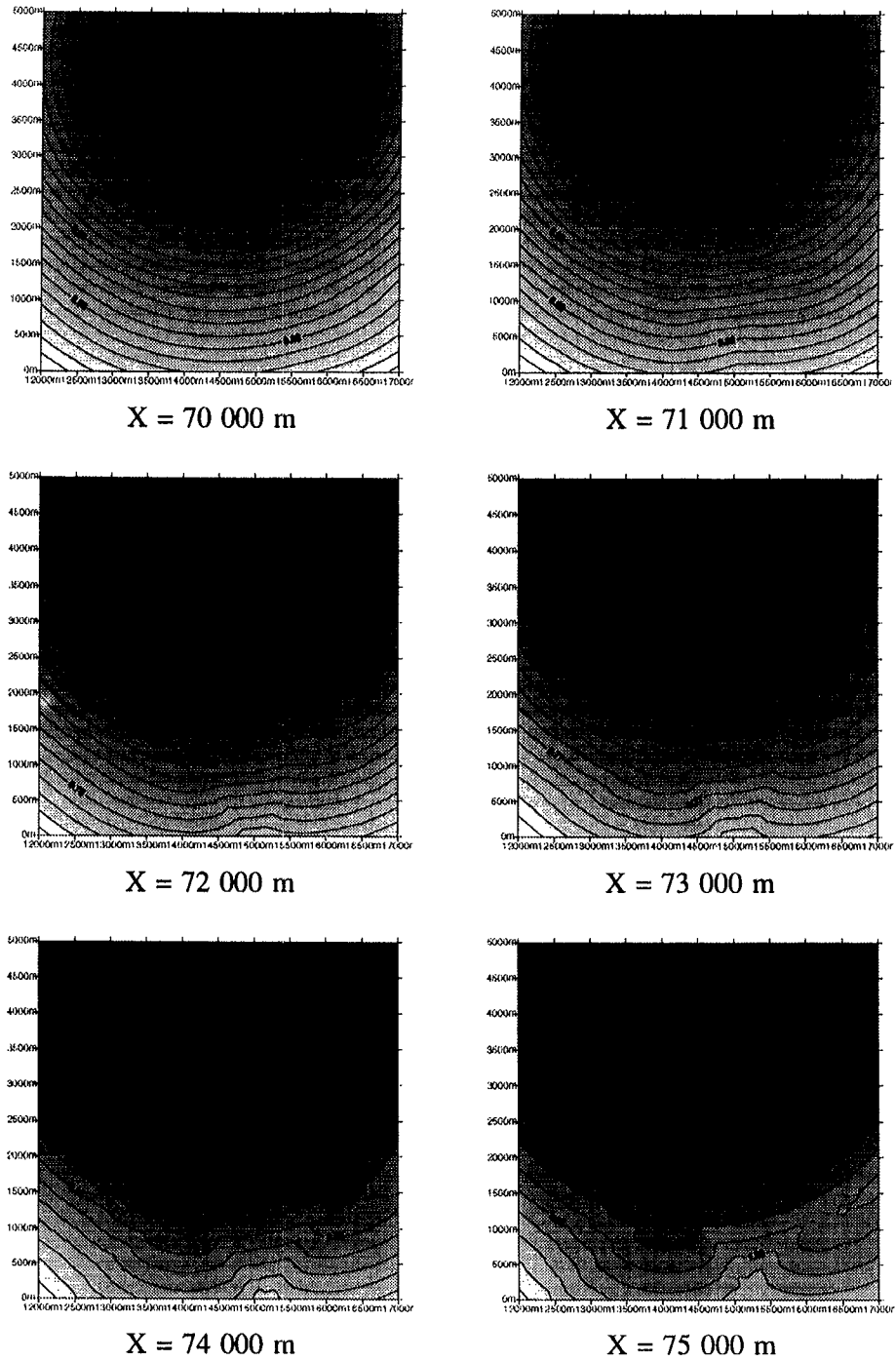


Fig.4.11 Isochrons on slices by planes parallel to YZ plane

4.4 Wavefront Construction Methods

This new group of traveltime and amplitude estimation methods has been pioneered by Vinje *et al.* (1993). These methods are based on ray tracing with the same robustness (in smooth media) as the grid methods; e.g. finite-difference methods, but have the ability to provide the later arrivals and amplitudes. These methods are related to the method of graphical wavefront construction described by Thornburgh (1930) and Riznichenko (1946). The following section briefly outlines the main ideas on which these methods are based. Consider the wavefront shown in Fig.4.12 (Vinje *et al.* 1993). The front is closed and the starting points of this initial wavefront are numbered from 1 to 7. These points will be used as initial positions of rays which will propagate the wavefront from a position at time τ (the position of the wavefront at that time is shown as a solid line) to time $\tau + \Delta\tau$ (dashed line). Different raytracing procedures may be used, but the most straightforward approach is to use the standard Runge-Kutta method or simple Taylor expansion for the purpose of wavefront extrapolation from the old to the new position. In Fig.4.12, the end points of the rays are marked with filled circles. The distance between each new point is calculated and checked against some predefined distance ΔS_{max} . If the distance between two neighbouring points on the wavefront exceeds ΔS_{max} , a new start position of a ray is interpolated on the old wavefront. This is done between points 1 to 7 in Fig.4.12. The following parameters are interpolated (Vinje *et al.* 1992):

- a. start position of the ray,
- b. unit ray tangent vector,
- c. geometric spreading,
- d. amplitude coefficient, and
- e. ray entrance coefficient at the source

In this way, new rays are created between all points on the old wavefront, as shown in Fig.4.12, and the end points of the interpolated rays are marked with hollow circles. In the result of this procedure, a new wavefront is obtained which consists of new points with the distance between the neighbouring points not exceeding the predefined maximum distance ΔS_{max} .

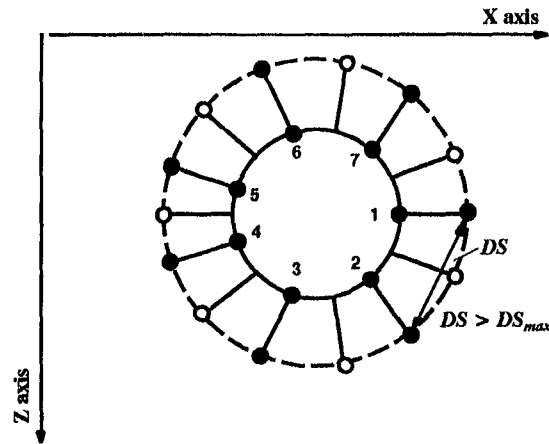


Fig.4.12 Wavefront construction scheme. A new wavefront, dashed line, is constructed from the previous wavefront (solid line). New rays are interpolated between each of the points from 1 to 7 in the old front since DS exceeds DS_{max} Vinje *et al* 1993.

The main advantage of this method is that it is easy to trace not only first arrivals but also almost all others. The method can easily be adopted to simplify and significantly speed up the computation required if only first arrivals are to be traced. It is easy to modify the method to include reflection and transmission at discontinuous interfaces. Whilst conventional raytracing may give no arrivals in areas of large geometrical spreading and it is difficult to cover the entire model space with a bundle of rays from a source point, the above method solves this problem. Vinje *et al.* have shown that this method has very high accuracy compared with finite-difference methods. In a complicated medium, however, there is the problem of undersampling of the ray field at caustics (Lambare *et al.* 1994; Lucio *et al.* 1995). This problem is due to the improper ray sampling criterion, as the ray density has to be controlled in order to ensure accuracy as well as computational efficiency of the algorithm (Lucio *et al.* 1995). The ray density can be controlled at some predefined places like a sequence of flat horizons (Lambare *et al.* 1994). In order to keep the ray density above some minimum level, it is necessary to insert additional rays as the ray field spreads out from the source. An additional ray is created using interpolation on the previous wavefront position and subsequent tracing of the ray.

Several criteria for the ray density control have been suggested, viz: the metric distance between the adjacent rays (Vinje *et al.* 1993); their angular distance (Sun, 1992); and the uniform ray density criteria (Lucio *et al.* 1995). The latter criteria seems to be most accurate and robust, even in regions with strong caustics and multiple arrivals.

Consider now the example of application of the wavefront

construction method to the model consisting of a single isotropic block. The propagation velocity is defined by the following:

$$c(z) = \frac{1}{2} \left(2.5z + 2.5 + \sqrt{(1.5z - 7.5)^2 + 0.1} \right) \quad (1.1)$$

The source position is (0.0, 10.0), the grid size 301 by 301 points with the grid step size equal to 0.1 km, the maximum distance between rays - 0.1 km, and the time increment between successive isochrons is 0.1s. In this model, caustic cusp generated by the velocity variation in the medium is clearly seen. The velocity distribution model, along with its derivatives used in wavefront construction for this model, has been modelled by cubic B-splines. Results of application of this wavefront construction method, shown in Fig.4.13, are in good agreement with the results obtained by extended asymptotic ray theory (Hanyga, 1985).

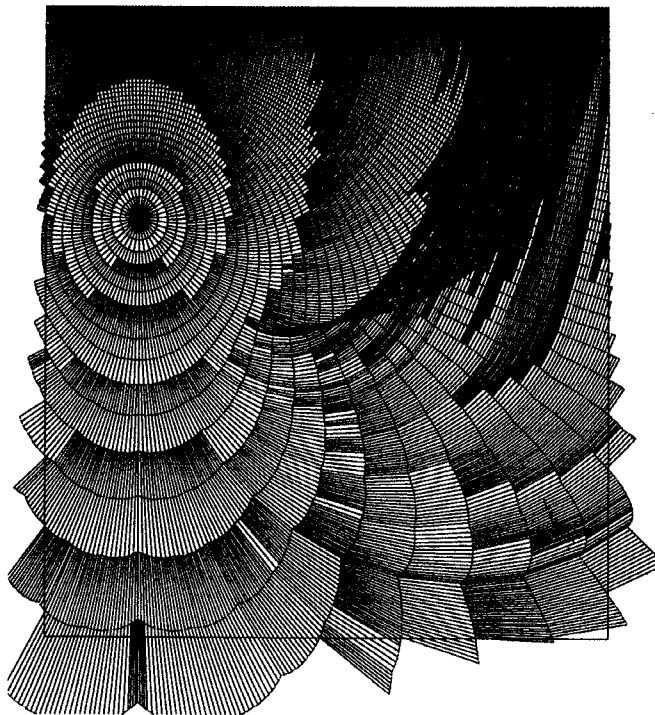


Fig. 4.13 Wavefronts distribution for a velocity model given by Equation (4.11), model dimension 301x301, grid size 0.1, Wavefronts plotted in 0.1s increments. Source position is (0.0,0.0), model box dimension: $-5.0 \leq X \leq 25.0$; $-10.0 \leq Z \leq 20$.

The results of the application of the wavefront construction method to a two-layered model are shown in Fig.4.14. The model size is 201 by 201 points and the grid size 0.01. The velocity in the first layer is 1.5 m/sec, and 1.9 m/sec in the second. The second layer starts at depth 1.1. The velocity distribution is represented by B-splines. The source position is (0.25, 0.75). Head wave generated at the interface are clearly observed.

The velocity model for the cross section of one of the gold mines in South Africa is shown in Fig.4.15. The results of the application of wavefront construction method are shown in Fig.4.16.

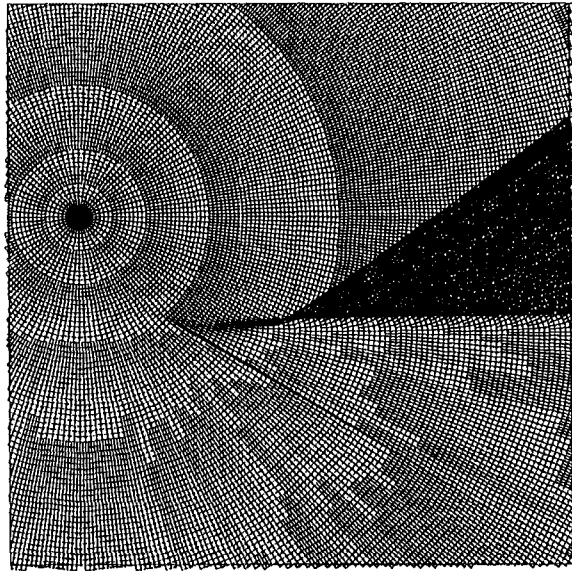


Fig. 4.14 Results of application of wavefront construction method to a two-layered model. Model dimensions $0.0 \leq X \leq 2$; $0.0 \leq Z \leq 2.0$; grid dimensions 201×201 , grid step size 0.01, velocity in upper layer 1.5 m/sec, in lower 1.9 m/sec, source position (0.25, 0.75). The second layer starts at 1.0 depth. Wavefronts calculated with 0.01 increment, $DS_{max} = 0.02$.

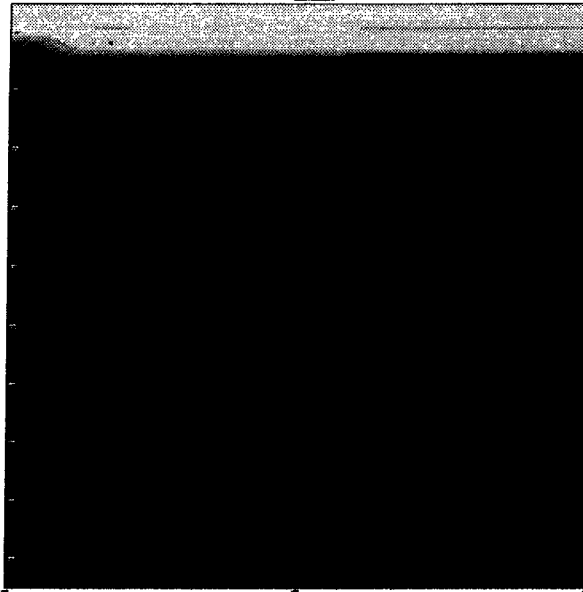


Fig. 4.15 Section of 3D velocity model of one of gold mines in South Africa. Darker color corresponds to higher velocity values. Model is represented by cubic B-splines, using 201x201 points with 10 m spacing. Model box dimension: 2km x 2km. Note the low velocity layer at the top of the model.

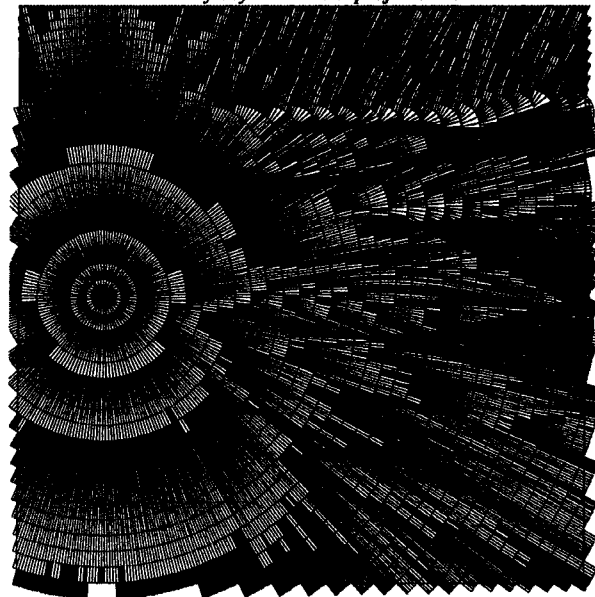


Fig. 4.16. Section through 3D wavefronts distribution for a velocity model shown in Fig. 1. Wavefronts have been calculated using wavefront construction method with 0.01 s increments, $\Delta S_{\max} = 10$ m. Numerous caustics are observed. Note head waves generated at transition zones between low and high velocity regions. Transition to the low velocity layer situated at the top of the model is clearly seen.

The finite-difference methods and methods based on shortest path calculation seem to be the most suitable for hypocentre location. Several methods of finite difference raytracing have been applied to forward problem solution. Vidale & Nelson, (1990) used Vidale's method for traveltime calculation with following grid search to find the global minimum traveltime residual location within the gridded volume. This location method is briefly described below.

Conceptually, this location method is fairly simple. First, the traveltimes to all the discretized grid points in the volume thought to contain earthquake source are computed from the every receiver location. This information, once computed, must be stored for further location. In the second step, for each set of travel times from a particular event, the location that minimizes the travel times residual is considered the best location. Vidale & Nelson (1990) proposed a further refinement by obtaining the location by interpolation within the surrounding 3 by 3 cube of grid points. This cube is resampled to a finer grid measuring 21 by 21 grid points and a higher resolution search is made for the point with the minimum residual. There may be several potential problems to be aware of. First, although the grid search algorithms, like one described above are guaranteed to find the global minima, the true source location may be situated outside the model space. Therefore, it is important to include into the model space definition of the whole area which is thought to possibly contain the earthquake hypocentre. Execution time for that type of location is linearly dependent on number of seismic stations used for location, as well as the grid size. Another type of problem can arise when using such grid search based techniques in models with sharp velocity variations, where the first arrival may be the diffracted waves, which generally have very little energy and thus are difficult to detect on actual seismograms. In order to cope with that problem, the velocity model should be smoothed to avoid the sharp velocity variations. Numerical simulations have shown that traveltimes do not change much with the smoothing of velocity model, but grid methods are more accurate (Whittlinger *et al.*, 1993).

There are several advantages of using finite-difference methods to the location problem. The computations of traveltimes can take into account the fact that the receivers are not situated exactly on grid nodes. Thus, exact station elevation and surface topography can be accounted for, which makes these methods very attractive to mining applications.

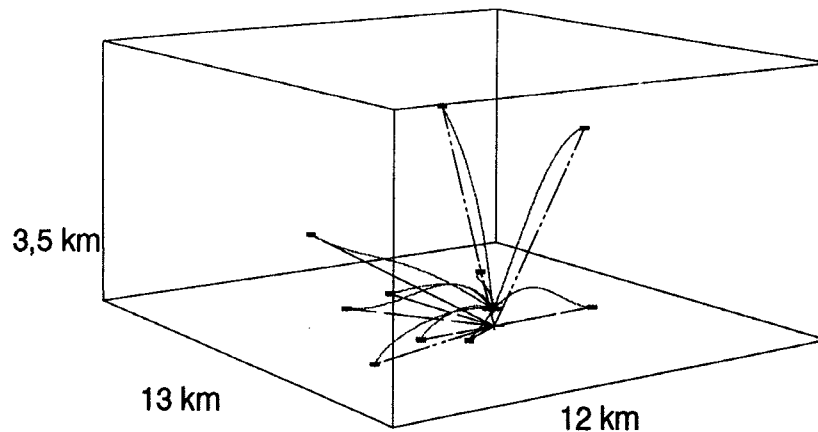


Fig. 4.17 Event recorded by Vaal Reefs Gold Mine Seismic Network on July 18 1995. Event location by finite-difference raytracing method (+South=81900m, +West=19830m, +Down=2770m), is shown using solid lines, whereas location using straight ray approximation (+South=81945m, +West=19822m, +Down=2948m), is shown in dashed lines. The average hypocentral distance for the location based on raytracing is 4693 m, compared with the average distance for straight ray approximation of 4359 m.

In Fig.4.17, the results of application of finite-difference method based on Vidale's (1990) approach are shown for the seismic event recorded by Vaal-Reef Gold Mine Seismic Network on July 18th 1995. Event location by finite-difference raytracing method is shown using solid lines along with the rays connecting the source and receiver locations, whereas the location results obtained using straight ray approximation are shown as dashed lines.

CHAPTER 5

SEISMIC WAVE ATTENUATION AND SITE EFFECT

The attention of seismologists is focused on the understanding of source properties, propagation mechanisms and seismic response due to the local geology. To improve the estimation of seismic source parameters knowledge of the attenuation of a seismic wave is essential.

5.1 ATTENUATION AND SITE EFFECT

The attenuation during the passage of waves through the medium is partly due to inelastic properties and partly due to scattering. The combined effect is expressed in the quality factor of the medium, Q_0 . The quality factor Q_0 is an important parameter for the classification of the rock; for example, a homogeneous rock has a large value of Q_0 , while a fractured rock around a slope has a small value.

In the case in which the site effect is important, an inversion scheme that fits the spectra of mine induced seismic events has been used to determine attenuation. The body wave spectra of seismic events are used to determine individual values of corner frequency for each event, and common Q_0 for all source-receiver paths (Fehler and Phillips, 1991; Humphrey and Anderson, 1992).

The observed spectrum, $Data(f)$ of the seismic wave at a station is controlled by the following product:

$$Data(f) = S(f) \cdot Site(f) \cdot Path(f,R) \quad (5.1)$$

where $S(f)$ is the spectrum at the source, $Site(f)$ is the local site effect, $Path(f,R)$ is the attenuation and the geometric spreading operator, f is the frequency, R is the source - station distance.

The spectrum at the source model is specified by two parameters: the seismic moment, M and the corner frequency, f_0 .

$$S(f) = \frac{R_{\Theta\Phi}}{4\pi\rho V^3} \frac{M}{1+(f/f_0)^2} \quad (5.2)$$

where spectrum at the frequency f , $R_{\Theta\Phi}$ is the radiation pattern, ρ is the density and V is the seismic wave velocity.

As the wave travels along the ray path, the source spectrum will be distorted by the effects of attenuation. The distorted spectrum then takes the form

$$S(f) \cdot Path(f, R) = S(f) \cdot \frac{1}{R} \exp\left(\frac{-\pi fR}{VQ}\right) \quad (5.3)$$

where R is the distance along which the seismic ray travels. The Q depends only on an average source-station property of the medium.

Since a good parametric model of site effect does not exist, the experimental function (non parametric model of the site effect) has to be obtained. The site response function, $Site(f)$, for individual stations is calculated from the average ratio of the observed spectrum, $Data(f)$, to model spectrum, $S(f) \cdot Path(f, R)$

$$Site(f) = \frac{1}{Nsei} \sum_{j=1}^{Nsei} \frac{Data_j(f)}{S_j(f)Path_j(f, R)} \quad (5.4)$$

where $Nseis$ is the number of seismograms taken into account.

In the case where the inversion provides the seismic sources parameters and Q , then estimation of the site effect is straight forward.

In the case when the group of station have similar azimuths to the seismic source, the effects of attenuation may be considered the same for all the events recorded at a selected seismic station. This suggests that a single value of Q may be used as the common quality factor along the ray paths.

The misfit function is defined by

$$\chi^2 = \sum_{j=1}^{Nsei} \sum_{k=1}^{Nfreq} \frac{[\ln(Data_j(f_k)) - \ln(S_j(f_k)Path_j(f_k, R_j))]^2}{\sigma_j^2(f_k)} \quad (5.5)$$

where $Data_j(f_k)$, is the observed velocity spectrum of j th event at f_k frequency, $S_j(f_k)Path_j(f_k, R_j)$ is the model of velocity spectrum of j th event at f_k frequency, $Nsei$ is the number of seismograms being simultaneously inverted and $Nfreq$ is the number of frequencies used in each spectrum. The data variances $\sigma_j^2(f_k)$ are derived from noise samples. The uncertainty of the record spectra is estimated by taking samples of the P-wave coda. The noise samples are shorter than the signal samples and they are corrected for the differing sample duration. The variance for the spectra is determined by the following equation (Boatwright et al., 1991):

$$\sigma^2(f) = \max\left[\frac{N(f) T_y}{Y(f) T_n}, 0.25\right] \quad (5.6)$$

where T_y and T_n are the duration of the data sample and the noise sample respectively.

The spectral model of ground motion is a nonlinear function of

corner frequency, therefore, the data are fitted to the model using a nonlinear inversion, which seeks to minimize the misfit function. The minimum of the misfit function is obtained using an iterative process. Given trial values for the parameters, a procedure has been used which improves the trial solution. The iteration was then repeated until χ^2 stopped decreasing. Quasi Newton methods, a well established algorithm for minimalization, was selected. This method requires the evaluation of the χ^2 function and its derivatives with respect to the parameters. Algorithms using the derivative are somewhat more powerful than those that use only the function. The solution to the inverse problem is the vector:

$$f_{o_1}, f_{o_2}, \dots, f_{o_{N_{seis}}}, Q \quad (5.7)$$

that minimizes the misfit function. In this way we calculated the corner frequency for all N_{seis} stations.

5.2 APPLICATIONS

Firstly, the algorithm was tested with synthetic data. The spectrum of the synthetic seismograms was inverted, assuming that there was no noise. Results were perfect up to six significant digits. The calculation was then repeated for synthetic seismograms perturbed with a noise up to 30%. The resolution dropped to two significant digits in Q_0 and f_0 .

The method has been applied to data from an underground seismic station in the Welkom region. In the first example, inversions were carried out using a set of 11 events, which distances from the station varied from 673m to 2800m.

The initial values of the corner frequencies and seismic moments were obtained from a waveform. The question arises how the estimation of Q_0 depends on its initial value. To address this problem, several tests were performed, with the Q_0 initial value varying from 100 to 500. It seems that the initial value of Q_0 does not affect the results of inversion. Remaining calculations were carried out with the initial value of $Q_0 = 200$

Results of inversion with high frequency decay rate γ equal 2 and 3 are presented in the Table 5.1:

ν	Misfit	Q_0
2	1766	96 +/- 12
3	1754	242 +/- 67

Table 5.1 Inversion for seven seismograms

The observed spectra fit two different seismic source models with the same precision (see the value of Misfit in Table 5.1). In both cases the attenuation is very realistic. The error associated with $Q_0 = 242$ is larger than the first, but still reasonable. Therefore, it is not possible to distinguish between the high frequency decay, γ , of 2 and 3. Seismic source models with the rolloff held constant at $\gamma=1$ and $\gamma=4$ yielded a large misfit function and, moreover, produced unrealistic corner frequencies. The inversion, therefore, will be performed with $\gamma = 2$ (Brune's model).

An inspection of the observed velocity spectra (Fig.5 .1 and 2) shows that the high frequency noise level starts to dominate the spectrum from 500Hz and above (see Fig.5.1) or from 100Hz (see Fig.5.2). The closest seismic events have the high frequency noise only at 700Hz. The high frequency energy is attenuated very rapidly with increasing distance. When the distance between seismic source and a station reaches 1500m, there is no signal above 300Hz. For a distance larger than 2000m a noise starts to dominate spectrum at 100Hz or 150Hz (see Fig.5.2).

To establish the dependence of Q_0 with a distance, seismic events from various distances were processed. Table 5.2 gives the estimated values of Q_0 for increasing distance between station and events. The rows show the range of the distances between three events and a station, the values of Misfit function, the values of Q_0 obtained from the inversion of three records and the maximal frequency of spectra used in the inversion procedure, Freq-max. The Q_0 value systematically increased as more distant events were included into inversion process. Q_0 increases from 64 to 229 with an increase of the distance from 673m to 2800m. The average value of Q_0 is approximately 120.

It was found that the frequency bandwidth has a strong effect on estimation of Q_0 (see Table 5.2: No 6 and 7 and No 9, 10 and 11). If inversion includes seismic events located further than 1500m then the maximum frequency used in inversion should be less than 300 Hz. Therefore, during the inversion process a frequency range has to be modified to match frequency band of data, otherwise all inversions would have to be performed with a minimal value of the high frequency range.

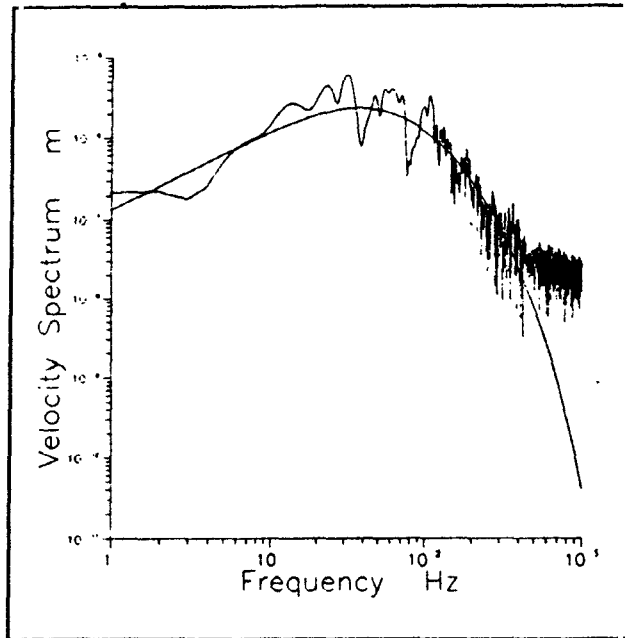


Fig.5.1 The velocity spectrum for the event at distance $R=673m$. The smoothed curve represents the spectral model obtained with $Q_0=64$.

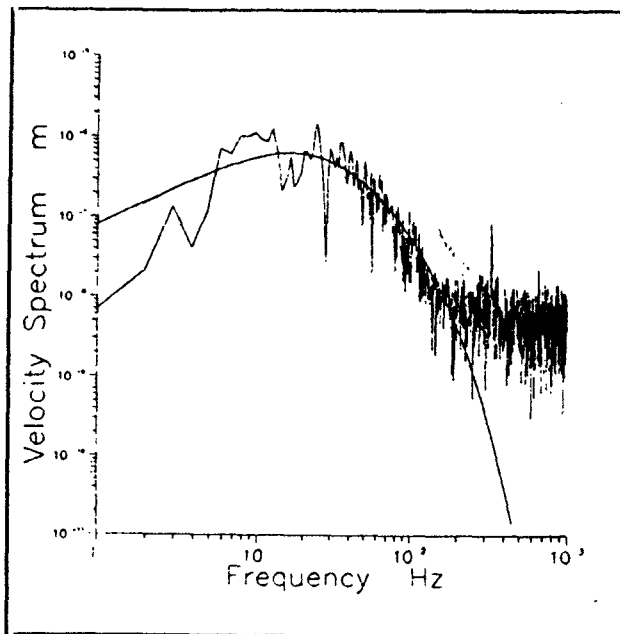


Fig.5.2 The velocity spectrum for the event at distance $R=1951m$. The smoothed curve represents the spectral model obtained with $Q_0=120$.

Rolloff $\gamma = 2$				
No.	Distance Range [m]	Misfit	Q_0	Freq-max [Hz]
1	673-866	737	64+/-9	300
2	717-1068	602	70+/-13	300
3	866-1302	703	99+/-17	300
4	1068-1511	740	107+/-16	300
5	1302-1542	695	109+/-16	300
6	1511-1951	654	103+/-15	300
7	1511-1951	445	88+/-16	200
8	1542-2200	833	132+/-16	300
9	1951-2700	938	210+/-20	300
10	1951-2700	229	125+/-36	100
11	1951-2700	446	110+/-19	200
12	2200-2800	808	229+/-37	300
13	2200-2800	259	120+/-27	100

Table 5.2

How many seismic records have to be inverted in order to obtain stable results? This information is important when performing calculations Q_0 routinely. Several subsets were created to investigate the reliability of estimation of Q_0 . The results indicated that if events are located very close to each other then any three waveforms give similar value of Q_0 . For distances between them larger than 1000m about seven seismograms are needed to obtain stable estimation of Q_0 .

Several calculations of Q_0 were performed with different data sets. Results indicate that Q_0 is a strong function of the local geology. The ray path between an underground seismic event and a surface station can have a quality factor as small as 50. A quality factor range however from 300 to 500 for seismic sources and a station located on the similar depth. If the seismic station and a set of seismic sources are located at a different depth then the quality factor is of the order of 100-200.

The site amplification was estimated for several seismic stations using a different set of seismograms. The intensive testing was

performed at an underground station, where a strong resonance has not been expected. Fig.5.3 shows the site effect obtained from seven seismograms for a frequency range varying from 4.5Hz to 250Hz. Interesting feature is that the error defined as a double variance does not increase with frequency. The similar site effect was obtained for a different data set.

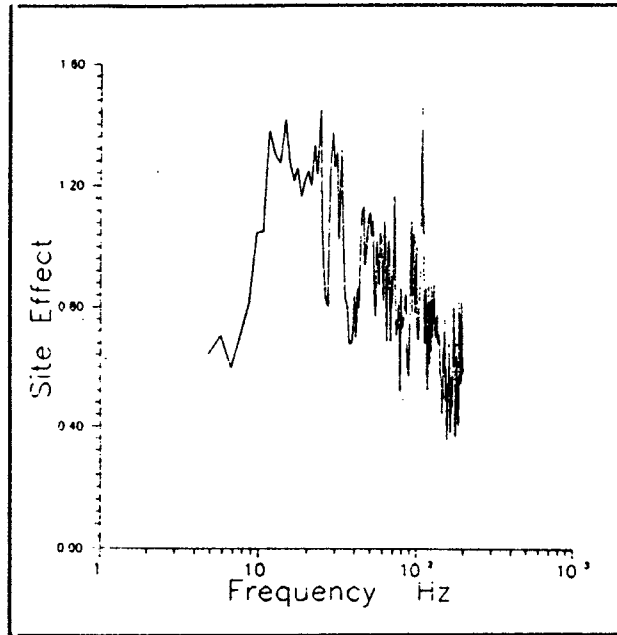


Figure 5.3 Site effect for an underground station.

It is a commonly observed phenomenon that seismic stations placed on loose rock and on bedrock have different amplification. The site effect obtained from a surface station in the Welkom region is dominated by 5 times amplification at a frequency at around 16Hz.

The site effect corrupts an estimation of seismic source parameters and therefore has to be removed from a seismogram before a process of estimation of seismic source parameters will begin.

CHAPTER 6

SOURCE PARAMETERS

The quality controlled seismological processing of three-component waveforms include several steps. They are as follow:

- finding the arrival time of the P- and S-waves and rotation of seismograms
- spectral analysis
- calculation of moment tensor
- calculation of spectral source parameters

6.1 FINDING THE ARRIVAL TIME AND ROTATION OF THE SEISMOGRAM

To find the arrival time of a P-wave it is necessary to remove DC-offset and then to apply a proper P-picker. The use of a short term/long term average picker is recommended. The picker should be tuned to the local conditions, which are determined in this case by signal to noise ratio, *SNR*.

Assuming that the location of the event is known, the azimuth to the epicentre (measured from the north, clock-wise) is also known and the angle of incidence measured from the vertical. Using these values a traditional three-component rotation can be performed to find the radial (longitudinal) component of the P-wave and two transverse components, *SH* and *SV*. The rotation reduces from six (P and S faces for three components) to three (longitudinal P, *SH*, *SV*), the number of wave forms for a given seismic event (e.g. Plesinger *et al.*, 1986).

A more convenient approach is based on polarization analysis of P-wave pulses (Monatalbetti and Kanasievich, 1970; Vidale, 1986). Polarization analysis can be done both in the time and frequency domain. Polarization analysis is made for two polarization windows, one described by a quarter of a dominant period, $T(A_{max})/4$, and the second one by $T(A_{max})/2$. For these two windows a covariance matrices are formed, and their eigenvectors, \mathbf{E}_i , and eigenvalues, λ_i , are computed. The parameter *DPP*, the degree of polarization for a P-wave is calculated as:

$$DPP = 1 - \frac{\lambda_2}{\lambda_1} \quad (6.1)$$

where $\lambda_1 > \lambda_2 > \lambda_3$, and the direction of P-wave is then described by the first eigenvector, \mathbf{E}_1 . To apply some quality measure to obtained results a concept of a quality indices is used. The quality index of the

P pick is

$$QI_{PP} = DPP \cdot SNR(P), \quad (6.2)$$

and the quality index for the P-wave direction is calculated using two polarization windows analysis:

$$QI_{DIR} = DIR(T(A_{max})/4) \cdot DIR(T(A_{max})/2). \quad (6.3)$$

The quality index for P wave, is calculated next, as

$$QI_P = QI_{PP} \cdot QI_{DIR}. \quad (6.4)$$

In a similar manner, two quality indices for SH and for SV waves are calculated:

$$\begin{aligned} QI_{SH} &= DPS \cdot SNR(SH) \cdot DEF, \\ QI_{SV} &= DPS \cdot SNR(SV) \cdot DEF, \end{aligned} \quad (6.5)$$

where DPS is the degree of polarization for S waves and DEF is the angle of deflection, measured as a difference between the expected direction of S waves (which is assumed to be perpendicular to P wave direction) and that found from the rotation. The degree of polarization of S waves is defined by:

$$DPP = \frac{\left(\frac{1-\lambda_2}{\lambda_1}\right) + \left(\frac{1-\lambda_3}{\lambda_1}\right) + \left(\frac{\lambda_2}{\lambda_1} - \frac{\lambda_3}{\lambda_1}\right)}{2\left(1 + \frac{\lambda_2}{\lambda_1} - \frac{\lambda_3}{\lambda_1}\right)} \quad (6.6)$$

The quality index for S waves is formulated as

$$QI_S = DPS \cdot DEF \cdot SNR(SH) \cdot SNR(SV).$$

Finally, the quality index of rotation is:

$$QI_{ROT} = QI_P \cdot QI_S.$$

All quality indices are normalized to take value between 0 and 1. The DPS value can be used to build a S-wave picker. If F_1 is a deflection angle, $F_2 = DPS$, F_3 is energy S / energy P, F_4 energy S / energy of initial pulse on P wave, and F_5 is SNR on SH and SV , then S-picker is formulated as the value:

$$S\text{-picker} = F_1 \cdot F_2 \cdot F_3 \cdot F_4 \cdot F_5 \quad (6.7)$$

also normalized to (0,1). S-wave arrival time is detected, if S-picker value is higher than some threshold, chosen for the given local conditions.

6.2 SPECTRAL ANALYSIS

The proper calculation of Fourier spectrum is very important for subsequent calculation of the source spectral parameters. Let $DS(f)$ be the displacement spectrum, $VS(f)$ the velocity spectrum, and $AS(f)$ the acceleration spectrum. For spectral parameter calculation the displacement spectrum must be evaluated, which can be easily calculated from the $VS(f)$ and $AS(f)$, because :

$$DS(f) = \frac{VS(f)}{(2\pi f)} = \frac{AS(f)}{(2\pi f)^2} \quad (6.8)$$

For the purposes of mining seismology, the use of ten cycles for P wave and 15 cycles for SH and SV wave, as a time window for Fourier analysis is recommended. After choosing the proper time window, the data needs to be filtered, using some band pass Butterworth filter (4-pole filter seems to be adequate for this). The lower frequency band is specified by the lowest frequency of the sensor, and the highest frequency band is recommended to be not greater than one fifth of the sampling frequency. This requirement means that a very high sampling frequency is needed to properly record a seismic event with a low magnitude. The result of filtering should be tapered by a taper window to avoid spectral energy leakage. Several windows are available, such as Hamming or Hanning windows. The Hanning tapers are defined as follows:

$$u(t) = \begin{cases} \frac{1}{2} + \cos \frac{2\pi t}{T} & \text{for } |t| \leq \frac{T}{2} \\ 0 & \text{for } |t| > \frac{T}{2} \end{cases} \quad (6.9)$$

and its Fourier transform is:

$$U(f) = \frac{T}{2} \text{sinc}(fT) + \frac{T}{4} [\text{sinc}(fT+1) + \text{sinc}(fT-1)] \quad (6.10)$$

where sinus cardinal $\text{sinc } x = \sin(\pi x)/(\pi x)$.

The Hamming taper is described by:

$$u(t) = \begin{cases} 0.54 + 0.46 \cos \frac{2\pi t}{T} & \text{for } |t| \leq \frac{T}{2} \\ 0 & \text{for } |t| > \frac{T}{2} \end{cases} \quad (6.11)$$

and its Fourier transform is:

$$U(f) = 0.54 T \operatorname{sinc}(fT) + 0.23[\operatorname{sinc}(fT+1) + \operatorname{sinc}(fT-1)] \quad (6.12)$$

The best results, for the broad frequency band, can be obtained by using multitaper window technique. After applying a taper to filtered data, Fast Fourier Transform is calculated, and the result is subsequently corrected (in the frequency domain) by seismic channel magnification and on attenuation. An attenuation correction function in frequency domain can be expressed as:

$$AC = \exp \frac{\pi fR}{(Q + Q_0 f) V} \quad (6.13)$$

where R is the distance between the source and the recording side, Q_0 is equal 0 if no information on $Q(f)$ is available, otherwise Q_0 is an initial value of attenuation from $Q(f)$. Q can be evaluated during inversion procedure, in which Q is one of parameters to be calculated. $Q(f)$ should be known from the results of recordings of coda waves for different regions of the mine. The spectrum calculated above described the way spectra should be smoothed for further use by, for example, cepstral filtering. The cepstrum $C(q)$ is an inverse FFT of the spectrum natural logarithm:

$$C(q) = \operatorname{FFT}^{-1} \ln(DS(f)) \quad (6.14)$$

The filtering corresponds to cepstrum zeroing after m zero crossing. The filtered displacement spectrum FDS, now is expressed as follows

$$FDS(f) = \exp (FFT(C_T(q))).$$

where $CT(q)$ is the truncated cepstrum, set to zero after m zero-crossings. The number m usually takes value 3, 4 or 5. For a given real spectrum of the waveforms it is necessary to estimate spectral model of displacement spectrum, $MDS(f)$, to be able to use

standard Brune model for calculation of spectral source parameters, see Fig.6.1.

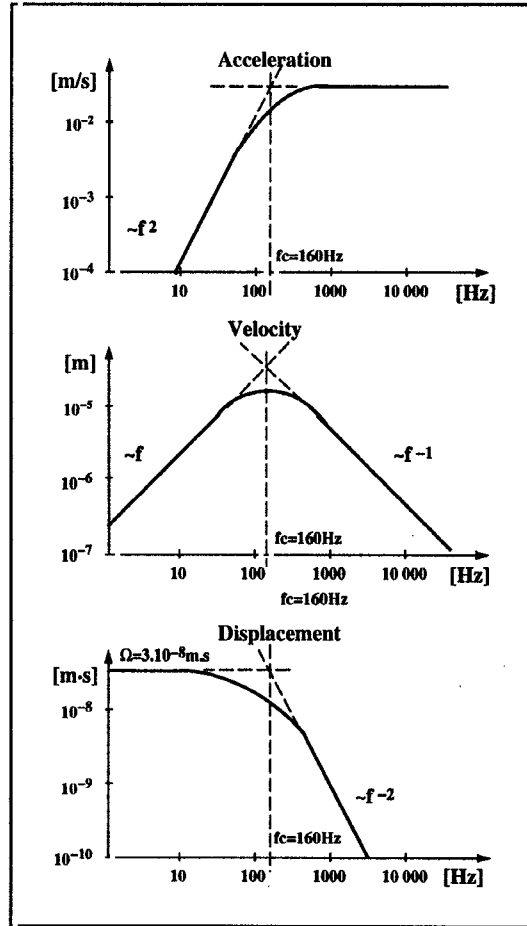


Figure 6.1 Theoretical spectra for Brune model

The simplest and the most frequently used spectral model is that described by the low-frequency level Ω_0 and the corner frequency f_0 , above which the spectrum is assumed to fall off as a power of frequency (Aki, 1967; Brune, 1970, 1971). The model displacement spectrum $MDS(f)$ for a given seismic station is expressed as follows:

$$MDS(f) = \frac{\Omega_0}{\left(1 + \left(\frac{f}{f_0}\right)^n\right)} \exp\left(-\frac{\pi f R}{QV}\right) \quad (6.15)$$

The model parameters, Ω_0 , f_0 , and Q can be found by iterative linear inversion of spectral data (Del Pezzo *et al.*, 1987, Scherbaum, 1990). For nonlinear procedures it is possible to use for example an optimization procedure, such as down-hill simplex method. As a starting point for Ω_0 usually an average from first 5 spectral points is

taken. Starting value for f_0 is that one found from dominant period of P and S waves. The starting value for Q is an initial value for $Q(f)$. Additionally, a number of constraints is usually applied during the inversion procedure. They are as follows: the corner frequency f_0 must be smaller than the upper cutoff and greater than the lower cutoff of frequency, and:

$$\begin{aligned} 0.25 f_{(SH)} < f_{(p)} < 2.5 f_{(SH)} \\ 0.5 f_{(SH)} < f_{(SV)} < 2 f_{(SH)} \end{aligned}$$

It is generally accepted that $Q_p/Q_s = (3/4)(V_p/V_s)$, and that for the Poisson ratio $0.25 Q_p = (9/4) Q_s$. In the case of mine events one can assume, that

$$\begin{aligned} 0.2 Q_p < Q_{SH} < Q_p \\ 0.5 Q_{SH} < Q_{SV} < 2 Q_{SH} \end{aligned}$$

The fitting function can have the form:

$$SPECT(\Omega, f_0, Q) = \min_f \sum \| wf(f) \cdot (FDS(f) - MDS(f)) \|^p$$

where $wf(f)$ is the weighting function proportional to the signal-to-noise ratio. Here $p=1$ for the first norm (L_1), or $p=2$ for the second norm (L_2). The process of finding the best fit is repeated for different m and the best fit is finally accepted.

The integral of the velocity power spectrum, $IVPS$, multiplied by the density ρ and wave velocity V , gives the energy flux of a plane wave, ϵ :

$$\epsilon = \rho \cdot V \cdot IVPS,$$

where:

$$IVPS = \int_{f_1}^{f_2} FVS^2(f) df \tag{6.16}$$

The three spectral parameters, Ω_0 , f_0 , and ϵ are calculated separately for P and S waves. The corner frequency for S waves is the averaged value corner frequencies for SH and SV , and Q_0 is geometrical average of these for SH and SV $\Omega_0 = \sqrt{\Omega_0 SH + \Omega_0 SV}$. The energy flux ϵ is the sum of energy fluxes for SH and SV . In this case, when the SV -wave spectrum is distorted and not acceptable, then the low-frequency level for SH is multiplied by $\sqrt{2}$ to represent Ω_0 for S-wave, and the corner frequency f_0 for the SH -wave is accepted as that for S-wave, and energy flux ϵ multiplied by 2 is accepted as the energy flux for S wave. If the SH spectrum is not acceptable, no

spectral parameters for S waves are determined. If the S wave spectrum is rejected, then no spectral parameters from P waves are considered and data recorded by the given station are not taking into account for the given event.

$$\begin{aligned}
 QL_{\Omega_0} &= 1 - \frac{SD(\Omega_0)}{\Omega_0} \\
 QL_{f_c} &= 1 - \frac{SD(f_c)}{f_c}
 \end{aligned}
 \tag{6.17}$$

The quality index for the low-frequency level Ω_0 is calculated as follows:

$$QL_{\Omega_0} = 1 - \frac{\sum_{f_1}^{f_{01}} \|FDS_i - MDS_i\|^p}{\sum_{f_1}^{f_{01}} |FDS_i| + |MDS_i|}$$

$$QL_{f_0} = 1 - \frac{\sum_{f_{01}}^{f_{02}} \|FDS_i - MDS_i\|^p}{\sum_{f_{01}}^{f_{02}} |FDS_i| + |MDS_i|}$$

where $f_{01} = (f_1 + f_0)/2$ and $f_{02} = (f_0 + f_2)/2$.

Standard deviation

Standard deviations of the spectral parameters $\mathbf{x} = (\Omega, f_0, Q)$ $SD(f_0)$ and $SD(Q)$ are equal to the square roots of respective diagonal elements of the covariance matrix \mathbf{C}_x .

$$\begin{aligned}
 SD(\Omega) &= \sqrt{\{\mathbf{C}_x\}_{11}} \\
 SD(f_0) &= \sqrt{\{\mathbf{C}_x\}_{22}} \\
 SD(Q) &= \sqrt{\{\mathbf{C}_x\}_{33}}
 \end{aligned}
 \tag{6.18}$$

where matrix \mathbf{C}_x is equal to

$$\mathbf{C}_x = s^2 \mathbf{A}^T \mathbf{A}.
 \tag{6.19}$$

In equation below, \mathbf{A} is $(n_f \times 3)$ a matrix of partial derivatives

$$\begin{aligned} \{\mathbf{A}\}_{i1} &= \frac{\partial MDS(f_i)}{\partial \Omega} \\ \{\mathbf{A}\}_{i2} &= \frac{\partial MDS(f_i)}{\partial f_0} \\ \{\mathbf{A}\}_{i3} &= \frac{\partial MDS(f_i)}{\partial Q} \end{aligned} \quad (6.20)$$

calculated at the point of estimated parameters $(\hat{\Omega}, \hat{f}_0, \hat{Q})$ and frequency f_i ($i=1, \dots, n_f$) where n_f is number of analyzed frequencies. The model of displacement spectrum $MDS(f)$ is approximated by the function

$$MDS(f) = \exp\left[\frac{R\pi f}{(Q + Q_0 f)V}\right] \cdot \frac{\Omega}{1 + \left(\frac{f}{f_0}\right)^\omega} \quad (6.21)$$

where R is hypocentral distance, V is seismic wave velocity, and Q_0 and ω are constants.

If the estimation of spectral parameters $\mathbf{x}=(\Omega, f_0, Q)$ is performed by help of a least squares procedure (L_2 norm), the value of s^2 is

calculated according to the formula $\sum_{i=1}^{n_f} r_i^2 / (n_f - 3)$, where r_i are

differences between observed and estimated displacement spectrum $MDS(f_i)$ calculated at the frequency f_i . Quality indices are then calculated from the formula

$$QL_{f_c} = 1 - \frac{SD(f_c)}{f_c} \quad (6.22)$$

Fig.6.2 shows waveforms of a seismic event of magnitude $m_M=0.8$, recorded by the Welkom seismic network.

Fig.6.3 shows instrument and Q corrected P, SH and SV spectra, the same spectra after cepstral filtering and Brune's model fit with automatically calculated source parameters.

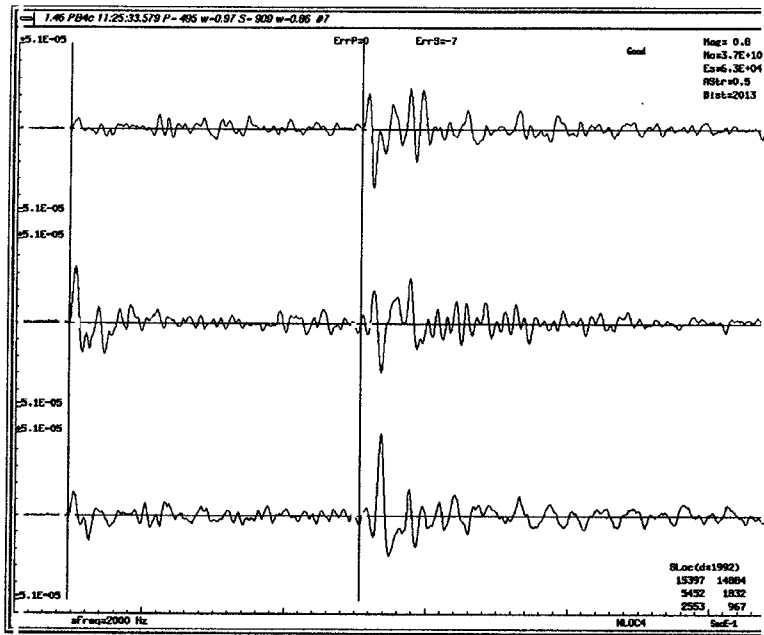


Fig. 6.2 Three component seismogram of a magnitude 0.8 seismic event recorded by the Welkom Seismic Network with automatically picked P and S arrivals.

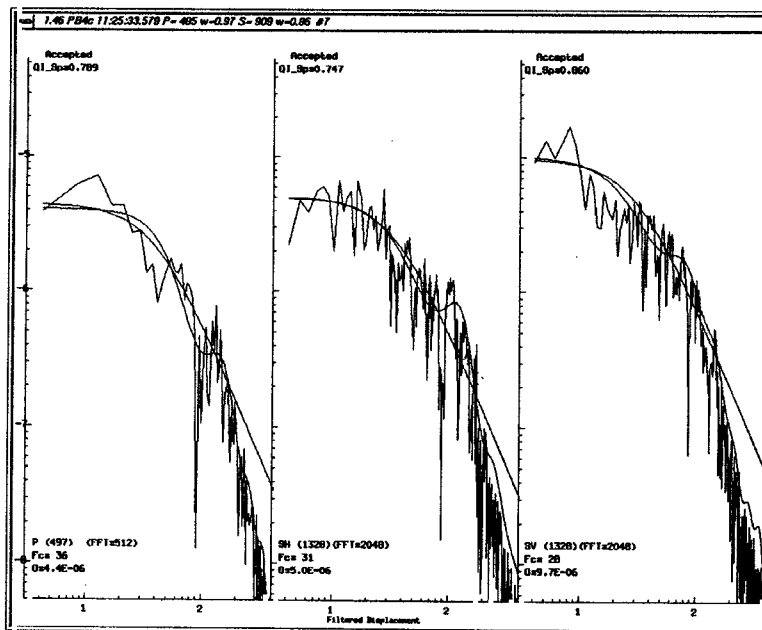


Fig. 6.3 Results of source parameter estimation for the seismogram shown in Fig.6.2. Rapidly changing lines show the ray displacement spectra corrected for instrument response for P, SV and SH waves respectively. The smooth lines shown are smoothed by cepstral smoothing and fitted Brune model spectra with automatically estimated corner frequency and quality estimates.

6.3 MOMENT TENSOR

Elements of moment tensor represent magnitude of forces acting in the seismic source.

Moment tensor, M , in three dimensional space is described by a matrix in Cartesian system of coordinates. Due to involvement of only internal forces in energy radiation from the seismic source, the matrix representing moment tensor is symmetric, so $M_{ij} = M_{ji}$. The eigenvalues of the isotropic part of the moment tensor describe the forces responsible for the volume changes in the source and the deviatoric part of the moment tensor can be decomposed in several ways. The most frequently used decompositions of the deviatoric part is into three double couples, or into a combination of the double couples and so called Compensated Linear Vector Dipoles, *CLVD* (Ben Menahem and Singh, 1981).

The radiated displacement created by the source can be described as the product of the moment tensor and the convolution (in time domain) of the source-time function with (the spatial derivative of the Green function represents the generalized double couples acting in the seismic source, and can be used to calculate seismic waves from the model source, for which components of the moment tensor are equal to 1 on the main diagonal, and zero otherwise, and also the source time function is a delta function). Frequently, the source-time function is usually considered to be a delta-function.

It is recommended to use the frequency domain and calculate the component M_{ij} in two steps. The first step involves only the data from four station. The equation which is used in frequency domain during the first step is as follows:

$$\Omega_{wk} = G_{kij} M_{ij} \quad (6.23)$$

where ik are the weights equal to the normalized values of the quality index QI_MTS .

This quality index is described as follows:

$$QI_MTS = QI_Q_0 \cdot QI_DIR \cdot \cos(\Delta_i) \quad (6.24)$$

where QI_Q_0 is the quality index for the low-frequency level Q_0 from P, *SH* or *SV* waves at a given station, QI_DIR is the quality index for the P-wave direction found from the polarization analysis, and Δ_i is the difference between the angle of incidence found from P-wave polarization and the calculated geometry from the source location. The only accepted amplitudes Q_0 are those with QI_MTS not smaller than 0.5. Besides the observed polarities of the P waves (at least 4), the

polarities of two best S waves of the alternative signs are taken for the first stage moment tensor calculation. The best solution out of the four, in terms of L_1 norm (the smallest sum of residuals), is then accepted as the initial solution for the second stage of the moment tensor calculation. In the above equation the Green function can be replaced by the radiation pattern of the point source (Aki and Richards, 1980), and the solution for M_{ij} can be found by the nonlinear simplex optimization method. As mentioned above, the moment tensor can be decomposed into the isotropic part M_v , and two deviatoric components, M_{DC} - pure double couple, and M_{CLVD} - Compensated Linear Vector Dipole.

The three components are as follows:

$$\begin{aligned}
 M_v &= m_v \begin{bmatrix} 1 & 0 & 0 \\ 0 & 1 & 0 \\ 0 & 0 & 1 \end{bmatrix} \\
 M_{CLVD} &= m_{CLVD} \begin{bmatrix} 0 & 0 & 0 \\ 0 & -1 & 0 \\ 0 & 0 & -1 \end{bmatrix} \\
 M_{CLVD} &= m_{CLVD} \begin{bmatrix} -1 & 0 & 0 \\ 0 & -1 & 0 \\ 0 & 0 & 2 \end{bmatrix}
 \end{aligned} \tag{6.25}$$

The graphical presentation of the radiation patterns of P-waves, corresponding to the given moment tensor is usually displayed on an equal-area lower-hemisphere projection which demonstrates the areas corresponding to compressional P-wave first motion and the area of dilatational first motion. The areas are separated by nodal lines, on which the amplitude of P-waves vanishes.

6.4 SPECTRAL SOURCE PARAMETERS

Seismic source parameters are calculated separately for P and S waves on the basis of spectral parameters: the low frequency spectral level Ω_o , the corner frequency f_o , and the energy flux ϵ .

For small seismic events, as in the case of mining tremors, the moment tensor can be calculated from spectral parameters:

$$M_o = \frac{4\pi\rho c R \Omega_o}{F_c} \tag{6.26}$$

where ρ_v is the density of source material before seismic events, c is either P-wave or S-wave velocity at the source, R is the distance between source and the receiver, F_c accounts for the radiation pattern of either P or S waves. If the radiation pattern is not known, then an averaged value is used.; for P-waves $F_c = 0.52$, and for S-waves $F_c = 0.63$. If the receiver is on the free surface, than the M_0 should be divided by half for SH waves, and by proper value, depending on the angle of incidence, for P and SV waves. A free-surface correction is not needed if the receiver is underground.

The seismic moment for S waves is calculated as a geometrical average of moment tensors for SH waves (M_{SH}) and for SV waves (M_{SV}):

$$M_s = \sqrt{M_{SH}^2 + M_{SV}^2}$$

The whole seismic moment is assumed to be the arithmetic average of these P wave (M_p) and S wave (M_s):

$$M = \frac{(M_p + M_s)}{2}$$

The magnitude scale is also used to describe the strength of a seismic event. According to Hanks and Kanamori (1979), magnitude M can be calculated using scalar moment as follows:

$$M = 2/3 \log M_0 - 6.0,$$

where M_0 is in N·m.

Seismic energy radiated from the seismic source represents only elastic energy. It is assumed that seismic energy consists only one half of the total energy radiated, which, according to Boatwright and Fletcher (1984), neglecting the surface effect, is

$$E_C = 4\pi\rho c \langle F_c \rangle^2 \frac{\sum_n I_{cn} R_n^2}{\sum_n F_{cn}^2} \quad (6.27)$$

where the summation index runs over the measurements of the energy flux ε at n stations. The factor $\sum_n F_{cn}^2 / 4\pi \langle F_c \rangle^2$ is the radiation pattern coefficient appropriate to the sampling of the data corresponding to the distribution of the take-off angles. If the local mechanism is not known, this factor becomes equal to the number of measurements

divided by 4π .

The whole seismic energy E is composed of three components which are separately calculated for the P, SH and SV waves:

$$E = E_p + E_{SH} + E_{SV}$$

Estimation of the source dimension heavily depends on the model. Usually a circular dislocation is assumed as a geometrical model of the source. The radius of a such fault is inversely proportional to the corner frequency f_o of either P or S wave:

$$r_o = \frac{K_c \beta_o}{2\pi f_c} \quad (6.28)$$

For the simplest source of Brune (1970,1971), represented by a circular dislocation with instantaneous stress release, the constant $K_c = 2.34$. For a quasi-dynamic model of the circular fault of Madariaga (1976), K_c for P-waves is assumed to be equal to 2.01, and for S-waves equal to 1.32. β_o is the S-wave velocities at the seismic source area.

Several different estimates of stress release in seismic source exists. Dynamic stress drop and apparent stress are discussed briefly.

The dynamic stress drop (also called effective stress drop) is a difference between the initial stress and the kinetic friction level on the fault area (Brune, 1970, 1971) and can be calculated from the seismic data:

$$\Delta\sigma = \frac{7}{16} \frac{M_o}{r_o} \quad (6.29)$$

For most mine tremors it is a value within the range from 0.01 10 MPa.

The apparent stress is calculated on the base of radiated seismic energy E and seismic moment, M_o , and has been proposed as a measure of the global stress release (*e.g.* Kanamori *et al.*, 1993; Mendecki, 1993). The apparent stress is (Wyss and Brune, 1968)

$$\sigma_a = \frac{\mu E}{M_o} \quad (6.30)$$

where μ is the shear modulus of the source material.

If the moment tensor is known, then for given seismic stations the apparent stress is calculated as follows:

$$\sigma_A = \frac{G(E_p + E_{SH} + E_{SV})}{\|M_V^T + M_{DC}^T + M_{CLVD}^T\|_E}$$

otherwise

$$\sigma_A = \frac{G(E_p + E_{SH} + E_{SV})}{\frac{1}{2}[M_p + (M_{SH}^2 + M_{SV}^2)^{\frac{1}{2}}]}$$

Seismic moment and stress drop allows the calculation of source volume V , which is interpreted as the region with the largest inelastic shear strain drop:

$$V = \frac{\|M_V^T + M_{DC}^T + M_{CLVD}^T\|_E}{\Delta\sigma}$$

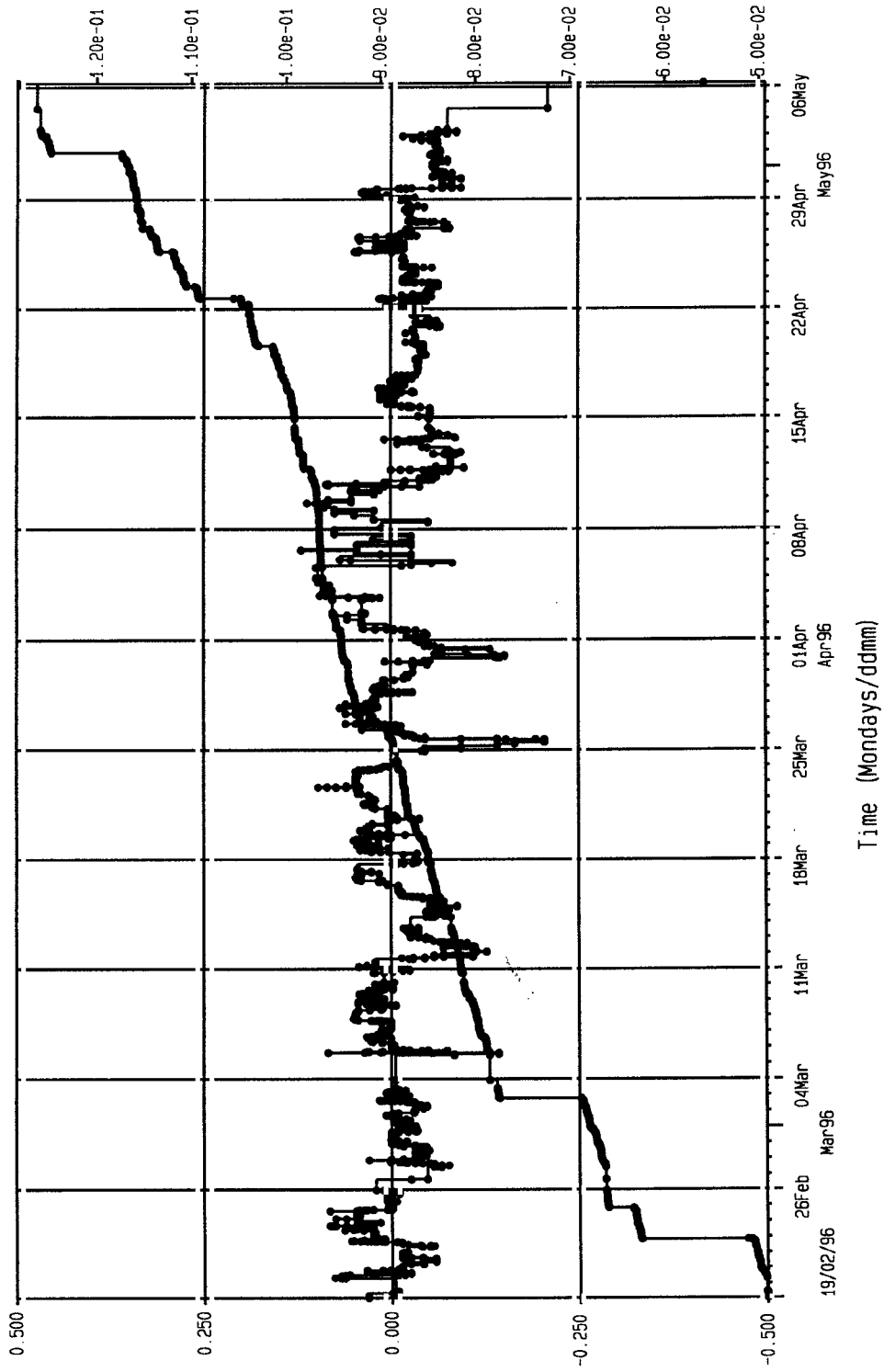
otherwise

$$V = \frac{\frac{1}{2}[M_p + (M_{SH}^2 + M_{SV}^2)^{\frac{1}{2}}]}{\Delta\sigma}$$

May 6 11:41 1996 --ISS 4di time history interpretation (Thist)-- <FREEGOLD>

Log10 (EI)

Apparent Volume (Km³)



Hints and information for ISS 4di...

Axis: Time (Mondays/ddmm) Data is from wh2pillar.ply
 BL_RED: Log10 (EI) A in energy-moment relation: 1.849
 Processing: median filtered B in energy-moment relation: -13.421
 BL_BLUE: Apparent Volume (Km³) Indicators: log10 Energy > 6.00
 Processing: cumulated Window: 002 days 00 hrs 01 mins or 5 Samples

Min. Time: Jan 9 22:43 1995 +NS 7180.1 to 7797.9
 Max. Time: May 6 06:21 1996 +EM 4734.2 to 5493.9
 Sites: 2 - 17 +VERT 748.2 to 4898.6
 N events: 3164 filter: no filter

Chapter 7

STATISTICAL ANALYSIS OF SEISMICITY

7.1 GUTENBERG - RICHTER RELATION

The classical description of seismic activity is based on the seismic activity rate λ , equal to number of events with magnitudes greater than or equal to a defined magnitude level m_{\min} during a specified time period T ; the parameter b in the Gutenberg-Richter relation; and sometimes, the maximum regional magnitude m_{\max} . The Gutenberg-Richter relation takes the form:

$$\log n = a - bm, \quad (7.1)$$

where n is the number of earthquakes with magnitude m , and a and b are parameters. It should be noted that often, instead of magnitude m , log of seismic moment M or log of seismic event energy E is used. In general, the relation (7.1) may be interpreted either as being a cumulative relationship, if n is the number of events with magnitude equal or larger than m in a given time interval (then by definition $\lambda=n$), or as being a density law, if n is the number of events in a certain small magnitude interval around the value of m . The parameter a is a measure of the level of seismicity, whereas the parameter b , which is typically close to 1, describes the ratio between small and large events in a given interval of time.

Procedures for Assessment of Parameter b .

Several efficient statistical procedures for the evaluation of parameter b are available. Probably the best known is the maximum likelihood estimator of b or equivalently $\hat{\beta}$, where $\beta=b\ln(10)$, introduced by Aki (1965) and Utsu (1965) and equal to

$$\hat{\beta} = \frac{1}{\bar{m} - m_{\min}} \quad (7.2)$$

where the sample mean magnitude $\bar{m} = \Sigma m_i/N$, m_{\min} is the threshold of completeness defined as a magnitude above which all N events occurred are reported. The determination of m_{\min} relies on the magnitude distribution (7.1). In most cases, the minimum magnitude of completeness of a data set is determined by plotting cumulative number of events as a function of magnitude. These plots are then fitted with straight lines and m_{\min} is the level at which the data fall below the lines.

Formula (7.2) was derived under the assumption that magnitudes of seismic events are independent, continuous random variables, unlimited from the top, and following Gutenberg-Richter relation (7.1).

From the central limit theorem it follows that for sufficiently large N , $\hat{\beta}$ is approximately normally distributed about its mean value equal to (7.2) with the standard deviation equal to

$$\hat{\sigma}_{\beta} = \hat{\beta} / \sqrt{N} \quad (7.3)$$

The standard deviation of $\hat{\beta}$ is obtained by dividing $\hat{\sigma}_{\beta}$ by $\ln(10)$. For an estimate of time varying seismic hazard and, for prediction of impending seismic events, the approximation of σ_{β} obtained for a time dependent β is more useful. Shi and Bolt (1982) showed that for slow temporal changes of β and large samples N , the standard deviation of $\hat{\beta}$ is

$$\hat{\sigma}_{\beta} = \hat{\beta}^2 \left\{ \sum_{i=1}^N (\bar{m} - m_i)^2 / [N(N-1)] \right\}^{1/2} \quad (7.4)$$

Despite very successful application of formula (7.2) in great number of studies, the Aki-Utsu approach has significant shortcomings, such as the assumption that magnitudes are unbounded from the top.

The maximum likelihood estimate of β for continuous magnitudes between m_{\min} and its upper limit m_{\max} is the solution of the following equation (Page, 1968; Cosentino *et al.*, 1977)

$$\frac{1}{\beta} = \bar{m} - m_{\min} + \frac{(m_{\max} - m_{\min}) \exp[-\beta(m_{\max} - m_{\min})]}{1 - \exp[-\beta(m_{\max} - m_{\min})]} \quad (7.5)$$

which can be obtained only by recursive solutions. Nevertheless, a simple approximation of β is possible. Following relations (7.2), with accuracy to the second term of the Taylor expansion of (7.5), the $\hat{\beta}$ value corrected for presence of m_{\max} becomes (Gibowicz and Kijko, 1994)

$$\hat{\beta} = \hat{\beta}_0 (1 - \kappa_{\max}) \quad (7.6)$$

where

$$\kappa_{\max} = \hat{\beta}_0 \frac{(m_{\max} - m_{\min}) \exp[-\hat{\beta}_0 (m_{\max} - m_{\min})]}{1 - \exp[-\hat{\beta}_0 (m_{\max} - m_{\min})]} \quad (7.7)$$

and $\hat{\beta}_0$ is the Aki-Utsu estimator (7.2).

Procedures for Assessment of Seismic Activity Rate λ

The simplest formula for assessing the seismic activity rate λ , follows from its definition:

$$\lambda = N/T, \quad (7.8)$$

where N is the total number of events with magnitudes greater than or equal to the threshold of completeness m_{\min} , and T is the span of the event catalog. Assuming that the occurrence of seismic events in time follows a Poisson distribution, the approximate standard deviation of λ is equal to $\lambda^{1/2}$.

Procedures for Assessment of m_{\max}

At present there is no generally accepted method to estimate the maximum magnitude m_{\max} . Three statistical procedures for the evaluation of m_{\max} , in which a crucial role is played by the maximum observed magnitude X_{\max} are described.

Method I. When quick results are required without going into sophisticated analysis, the following rule (Robson and Whitlock, 1964) would apply to evaluate m_{\max} from a data set of $X_1 \leq X_2 \leq \dots \leq X_{n-1} \leq X_{\max}$

$$\hat{m}_{\max} = X_{\max} + (X_{\max} - X_{n-1}) \quad (7.9)$$

where \hat{m}_{\max} is estimation of m_{\max} , and X_{\max} and X_{n-1} are the largest and the second largest magnitude observed in the region.

Method II. In this approach the condition for the evaluation of m_{\max} is based on some properties of the end point estimator of a uniform distribution. Following Gibowicz and Kijko (1994), the estimation of maximum magnitude m_{\max} is equal to

$$\hat{m}_{\max} = -\frac{1}{\beta} \ln \left\{ \exp(-\beta m_{\min}) - [\exp(-\beta x_{\max})] \frac{\lambda T + 1}{\lambda T} \right\} \quad (7.10)$$

where λ is the activity rate, and T is the span of the catalog.

Method III. In this approach the evaluation of m_{\max} is obtained from the condition

$$X_{\max} = \text{EXPECTED}(X_{\max} | T) \quad (7.11)$$

that the largest observed magnitude X_{\max} is equal to $\text{EXPECTED}(X_{\max} | T)$, which is the largest *expected* magnitude in the span T of the catalog. The formula for $\text{EXPECTED}(X_{\max} | T)$ is given by (Kijko and Sellevoll, 1989)

$$\begin{aligned} \text{EXPECTED}(X_{\max} | T) = & \quad (7.12) \\ m_{\max} - \frac{E_1(Tz_2) - E_1(Tz_1)}{\beta \exp(-Tz_2)} - m_{\min} \exp(-\lambda T) \end{aligned}$$

where $z_1 = -\lambda A_1 / (A_2 - A_1)$, $z_2 = -\lambda A_2 / (A_2 - A_1)$, $A_1 = \exp(-\beta m_{\min})$, $A_2 = \exp(-\beta m_{\max})$, and $E_1(\cdot)$ denotes an exponential integral function which can be approximated as (Abramowitz and Stegun, 1970)

$$E_1(x) = \frac{1}{x} \exp(-x) \frac{x^2 + a_1 x + a_2}{x^2 + b_1 x + b_2} \quad (7.13)$$

where $a_1 = 2.334733$, $a_2 = 0.250621$, $b_1 = 3.330657$, and $b_2 = 1.681534$.

The described procedures for estimating Gutenberg-Richter distribution parameters b , λ and m_{\max} have been demonstrated on seismic data from the Far West Rand (FWR) mining area in South Africa. The catalog was compiled from the Geological Survey of South Africa Bulletins. The data covers the time period between January 1972 and December 1991 and is complete from a threshold magnitude of $M_L = 2.8$. The maximum observed magnitude X_{\max} for the catalog is $M_L = 4.8$.

From the catalog, $\hat{\lambda}$ ($m=2.8$) is known to be 8.48 ± 0.18 events per month and $\hat{\beta}$ is 2.50 ± 0.06 ($\hat{b} = 1.06 \pm 0.02$). Method I, for evaluation of m_{\max} , is the most rudimentary procedure and gives an \hat{m}_{\max} of 5.0 for the FWR. The more sophisticated methods II and III both give the same \hat{m}_{\max} of 4.83 ± 0.32 .

7.2 INTEGRATED VOLUME OF GROUND MOTION

The volume of ground motion (VGM) (Mendecki, 1985) is a single number that integrates the probabilities of seismic events occurring at different magnitudes described by the Gutenberg-Richter relation (7.1), and the relation between magnitude, distance, and peak ground velocity, over the magnitude range of interest. The resulting

VGM is equal to the total rock mass volume affected by peak velocities not smaller than a certain critical velocity v over a period of time T ,

$$VGM(m_0, v) = Av^c \lambda T \beta / B \frac{\exp(-Bm_0) - \exp(BX_{\max})}{\exp(-\beta m_{\min}) - \exp(\beta m_{\max})} \quad (7.14)$$

where m_0 is the minimum magnitude of a seismic event considered to be important from a damage point of view, X_{\max} is maximum observed magnitude during the time interval T , $A = 4\pi/3 \exp(-3a_3/a_2)$, $B = \beta + 3a_1/a_2$, $C = 3/a_2$. Values a_1 , a_2 , and a_3 are parameters in the formula

$$\ln v = a_1 m + a_2 \ln R + a_3, \quad (7.15)$$

which relates the peak ground velocity v with magnitude m and hypocenter distance R . Fig. 7.1 illustrates the results from an assessment of the VGM variations in the FWR mining area between January 1985 and December 1991.

From a damage point of view the values of magnitude and peak particle velocity considered to be important are 1.0 and 100 mm/sec, respectively. Fig. 7.1 shows the activity rate λ in events per month for $m_{\min}=2.8$, the estimated Gutenberg-Richter \hat{b} value, X_{\max} , and the variations in VGM. This figure serves as an illustration of the information that is integrated together to obtain the potential VGM. Note, in this example, that the large variation in the \hat{b} value between 1986 and 1989 has a significant influence on the VGM, despite the drop in activity rate and X_{\max} .

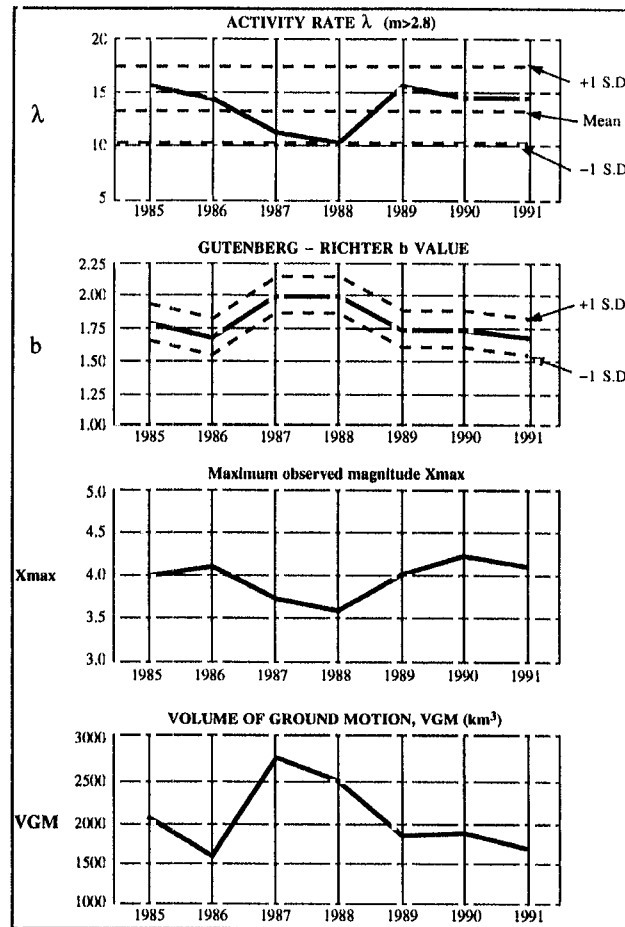


Figure 7.1 Illustration of the VGM and the hazard parameters used in the VGM calculation

7.3 SPACE-TIME CLUSTERING OF SEISMICITY

This paragraph introduces a methodology which finds clusters of anomalous seismicity which may lead to the occurrence of a significant seismic event.

The formulation of the clustering process is conceptually close to the single-link cluster analysis first adapted to seismology by Frohlich and Davis (1990). The difference in the approach used here is the incorporation of a moving time window which is reminiscent of Matsumura (1984) procedure. Seismic events are placed into a moving time window of some specified length. For each new event that comes into the window, links are calculated between this most recent event and all the events in the window. The link distance is both a space and time and is defined as

$$STD_{ij} = \sqrt{d_{ij}^2 + c^2(\Delta t_{ij})^2} \quad (7.16)$$

where d_{ij} is space distance between events i and j . Alternatively, d_{ij} can be replaced by $d_{ij}(r_i + r_j)$, where r_i and r_j are radii of an equivalent spherical source e.g. $r = \frac{3}{4\pi} \sqrt[3]{V_A}$, Δt_{ij} is time difference, and c is a time-distance conversion parameter. Although the units of STD_{ij} are meters or kilometers, this is not simple distance but includes both space and time separation. If a link distance STD_{ij} is found to be less than the maximum link length STD_{max} , the two events in question are linked together. At some stage in the clustering process, an event from one cluster may link to an event belonging to another cluster. The algorithm will merge the two clusters together. Occasionally two clusters should physically be linked together, however no events occurred near enough to each other for a link to be formed. This situation can arise from using a time window which is too small. Such a problem is easily amended by periodically testing distances between cluster centroids. If cluster centroids drift near enough to each other, the algorithm will merge them into one.

The choice of the time window length is therefore one of the most important considerations. If the selected window length is too small, clusters may have no events in the window at some point in time. Such a situation would effectively terminate the clustering procedure. If the window length is too large, many links must be calculated for each new event causing the algorithm to become unnecessarily slow. The average activity rate for the mine must be studied to decide on an appropriate window length. From our experience the window should have at least 25 events at any time.

In addition to the time window length, the method requires the specification of two parameters, the "cutoff distance" STD_{max} , and time-distance conversion factor c . A value c is chosen such that two simultaneous events separated by a distance $d/\Delta t$ in average are as likely to be related to each other as two events with identical locations occurring at time T apart. In practice, c factor is determined as a mean value of $d/\Delta t$ ratio for all events in the catalogue.

For each cluster, a number of parameters are monitored so that the seismicity can be characterized. The mean X, Y, and Z along with variances of the coordinates are stored so that the shape of the ellipsoid can be determined via the covariance matrix. The physical cluster volume holds one standard deviation of event locations with respect to the cluster centroid. The minimum, maximum, and cumulative energy, moment, apparent stress, and

apparent volume are continuously updated within the clusters. Parameters such as b -slope, activity rate, and the probability of occurrence of a strong event can be determined at any time. Also, the volume of the ellipse relates how concentrated the events are in the area.

The ability of the space-time clustering analysis algorithm to detect anomalous clusters of seismicity is demonstrated in Fig. 7.6. This figure shows the clusters of seismicity one of Gold mine in South Africa for a one year period. A moving time window of 10 days was used with a maximum space-time distance $STD_{max}=250$ m. The level of completeness for the data was energy $10^{4.5}J$. Without any knowledge of the mining the space-time clustering algorithm was able to detect seven clusters of seismicity in the mine. Four of them are demonstrated of Fig. 7.2. The maximum distance between "centres" of the clusters did not exceed 1800m.

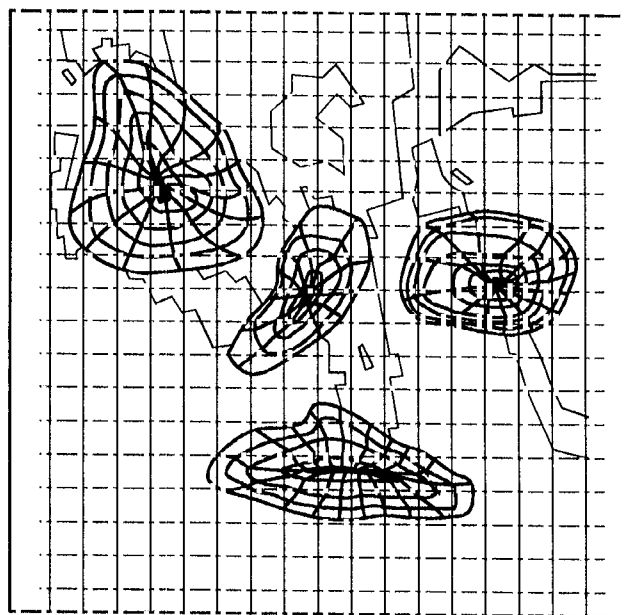


Figure 7.2 Four of seven identified clusters of seismic events at an analyzed gold mine in South Africa

7.4 PROBABILITY MODEL FOR SEISMIC EVENT OCCURRENCE BASED ON TEMPORAL VARIATIONS OF STRESS-STRAIN RELEASE

Among various methods to evaluate the probability of strong seismic event occurrence in mines, those employing the temporal variations of seismic activity parameters, especially expressed as

Gutenberg - Richter parameters a and b , has been particularly widely applied. Time variations of these coefficients during seismic event sequences indicate that they depend on the rheology and structure of the rock and therefore can be considered as parameters describing the capability to release accumulated stress energy. Despite often successful applications of the above approach in different mining environments (e.g. Brady, 1977; Gibowicz, 1979; Brink, 1990; Lasocki, 1993), the approach has a weak point: it can not be clearly explained based on, or derived from, current understanding of fracture processes of the rock.

Bearing these limitations in mind, Mendecki (1993, 1994) proposed an alternative approach: direct monitoring of stress-strain release. Fig. 8.22 in Chapter 8 presents a typical stress-strain diagram of a rock sample. After passing through the elastic and strain-hardening regimes, the material softens, and further increments of strain are associated with the drop of the stress. The deformation is considered to be unstable when the inner product of any infinitesimal change of stress and strain is negative. Details about this and detail description of the whole concept can be found in Chapter 8.

Following this concept, the development of the potential instability can be identified through the monitoring of the rates of change of stress and inelastic strain. Although the seismic waveforms do not provide direct information about the absolute stress, but only about the stress drop at the source, a number of seismological studies and numerous underground observations suggest that in all calculations stress σ can be replaced by apparent stress σ_A . In addition, in our analysis as a measure of strain ϵ , apparent volume V_A defined by formula (7.13) is used.

Following the approach, the development of the potential instability can be identified through the monitoring of the rates of the change of stress and inelastic strain, where stress is replaced by apparent stress and strain by cumulative apparent volume.

It is obvious, that the above model of rock rupture and instability is very simplified. It must be conceded, that at present there is no comprehensive theory of rock fracture, from which even basic relations can be derived from fundamental physical laws (Kagan, 1994). The seismic event occurrence is characterized by high degree of randomness, hence it has to be investigated by stochastic procedures.

In this paragraph the statistical procedure which makes it possible to predict strong seismic event and express it in terms of probability is described, where as input information, stress and strain release is used. In the following section the logistic

distribution, as a tool for estimation of probability of strong seismic event occurrence, is described. In the final section example of prediction of strong seismic events based on the application of above approach in one of South African deep gold mines is presented.

Some alternative applications of logistic distribution in probability assessment of earthquake occurrence in southern California and Hokkaido-Tohoku region, Japan, are described respectively by Niazi and Mortgat (1983) and Kuge and Honkura (1986).

Logistic Distribution: A Model for Probability of Strong Seismic Event Occurrence

Suppose that in the region under consideration one is able to identify the area of instability, or equivalently, the place where the strong seismic event will occur. Following previous experience (Kijko *et al.*, 1993), such an area can be localized by detection of space-time clustering of seismicity. If such an area is properly localized, the relationship between seismic stress- strain release and seismic event occurrence may be used, and the logistic distribution is expected to provide an exceptionally effective tool for future prediction of such a strong events.

Suppose that for a specified time window ΔT (let us call it *prediction window*) one has an observation y which is related to the occurrence of a seismic event with energy E , equal or exceeding a specified level of energy E_0 . It is clear that y can take one of two possible forms. Without loss of generality we may code the two possible values of y by 1 (if occurrence of seismic event with $E \geq E_0$ took place) and 0 (in case of absence of such a event), and write

$$\begin{cases} \text{Probability } (y = 1) = p, \\ \text{Probability } (y = 0) = 1 - p. \end{cases} \quad (7.17)$$

Assume that each prediction window ΔT is preceded by so-called *parameter window* T and each ΔT is always selected immediately ahead of its parameter window T . Let, for each prediction window ΔT_i , binary observations y_i and set of q variables $\mathbf{x}_i = (x_{i1}, \dots, x_{iq})^T$ from the parameter window T_i be available; $i=1, \dots, n$, and n stands for number of analyzed prediction windows. The elements of vector \mathbf{x}_i are respective values related to the seismic stress and strain release within parameter window T_i . The problem is to a develop procedure for *assessing* the probability p of seismic event occurrence within specified time window ΔT , and with energy $E \geq E_0$, based on seismic

stress-strain observations \mathbf{x} in preceding time window T .

In the study, the assessment of relation between probability $Probability(y=1)=p$ and variables \mathbf{x} is attempted by use of the logistic distribution. Following Cox and Snell (1989), the cumulative distribution function of the logistic distribution has the form

$$p = \frac{\exp(\Theta^T \mathbf{x})}{1 + \exp(\Theta^T \mathbf{x})}, \quad (7.18)$$

where according to the new notation \mathbf{x} is $m=q+1$ dimensional column vector of observed independent variables $\mathbf{x}=(x_0, x_1, \dots, x_q)^T$, $x_0=1$, and Θ is a $(m \times 1)$ column vector of unknown distribution parameters $\Theta=(\theta_0, \theta_1, \dots, \theta_q)^T$. The new notation was introduced in order to make it possible to write relation (7.18) in very compact way.

Parameters Estimation

Unknown parameters Θ must be determined somehow, so that one can use formula (7.18) to estimate the probability of a seismic event occurrence p , given an observation vector \mathbf{x} . For this purpose, based on the records of past seismic event occurrence y_1, \dots, y_n , and variables describing stress-strain release $\mathbf{x}_1, \dots, \mathbf{x}_n$, the maximum likelihood estimation technique (Eadie *et al.*, 1971) can be applied. The maximum likelihood estimate of the parameters Θ is that value of $\hat{\Theta}$ for which the likelihood function $L(\mathbf{x}_1, y_1, \dots, \mathbf{x}_n, y_n | \Theta)$ has its maximum, given the particular stress-strain release $\mathbf{x}_1, \dots, \mathbf{x}_n$, and seismic response y_1, \dots, y_n . The likelihood function $L(\mathbf{x}_1, y_1, \dots, \mathbf{x}_n, y_n | \Theta)$ is (Cox and Snell, 1989)

$$L(\mathbf{x}_1, y_1, \dots, \mathbf{x}_n, y_n | \Theta) = \frac{\exp\left(\sum_{j=0}^q \theta_j t_j\right)}{\prod_{i=1}^n (1 + \exp(\Theta^T \mathbf{x}_i))} \quad (7.19)$$

$$\text{where } t_j = \sum_{i=1}^n x_{ij} y_i.$$

The predictive capability of the logistic distribution (7.18) in strong seismic event prediction was tested during the mining of a

pillar in one of South Africa deep gold mines. The extraction of the pillar started in March 1992 and finished in May 1994. During that period more than 2000 seismic events were recorded in the energy range 10^3 to 10^9 J.

The assessment of strong seismic event occurrence probabilities is based on two types of vector \mathbf{x} . In the first case the independent variables \mathbf{x} are selected as $\mathbf{x}=(1,x_1)^T$ where x_1 is equal to the average value of $d\sigma/d\epsilon$ within parameter window T . In the second case $\mathbf{x}=(1,x_1,x_2)$, where x_1 and x_2 are respectively average values of stress $\bar{\sigma}$ and strain rate $\dot{\epsilon}$ within parameter window T .

Applications of the above formalism for the first case with vector \mathbf{x} selection ($x_1=d\sigma/d\epsilon$) are shown in Fig.7.3 and 7.4.

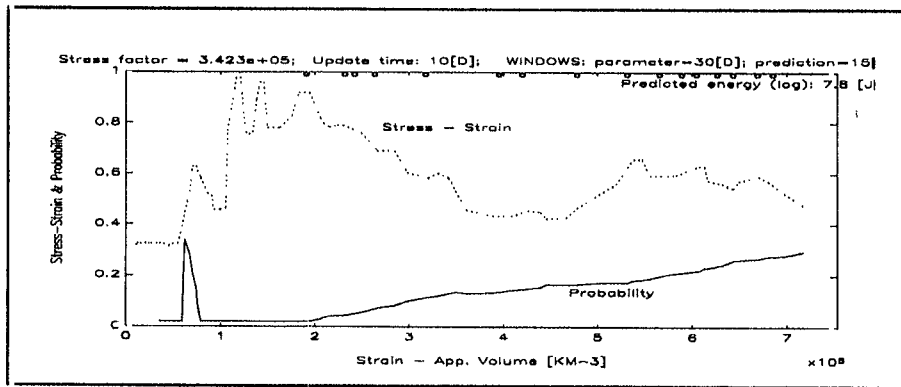


Fig. 7.3. Probability of the occurrence of seismic events with the energy $E \geq 10^{7.9}$ J within time interval $\Delta T=15$ days, during the mining of the pillar in deep gold mine, South Africa. Assessment of probabilities (solid line) is based on temporal variations of $d\sigma/d\epsilon$ value within time window 30 days. Smoothed stress-strain curve is shown by dashed line.

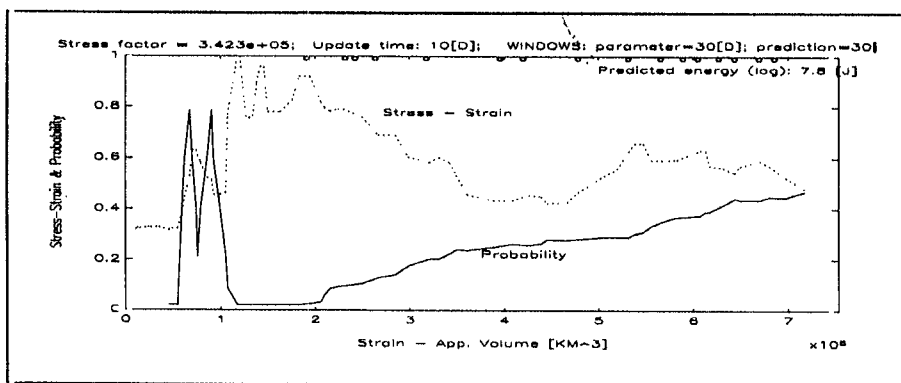


Fig. 7.4. Probability of the occurrence of seismic events with the energy $E \geq 10^{7.9}$ J within time interval $\Delta T=30$ days, during the mining of the pillar in deep gold mine, South Africa. Assessment of probabilities (solid line) is based on temporal variations of $d\sigma/d\epsilon$ value within time window 30 days. Smoothed stress-strain curve is shown by dashed line.

The catalog of seismic events was divided into successive 30 days parameter windows ($T=30$), and each window was treated as a

single x_1 observation. Dependent variables y are equal to 1, if during the prediction window ΔT (following immediately ahead of parameter window T), at least one event with energy $E \geq E_0 = 10^{7.8}$ J took place. If such an event did not occur, $y=0$ was assumed. The computer program for assessment of seismic event occurrence probabilities fully simulates adaptive learning as time flows. Initially, probabilities (7.18) were estimated when two sets of observations (x,y) from two sets of parameter-prediction windows were available. Then with the flow of time, their values are successively updated. Probabilities were calculated for prediction window $\Delta T=15$ (Fig. 7.3), and $\Delta T=30$ days (Fig. 7.3). The predictive power of the model is low (peaks in probability curves when no events occurred), when observations (x,y) from only a first few windows are available. The predictive power of the procedure increases as time flows and more observations are used for estimation of parameters Θ . Comparison of Fig. 7.3 and 7.4 clearly shows the role of length of prediction window. As one might expect, increase of prediction window from $\Delta T=15$ (Fig. 7.3) to $\Delta T=30$ days (Fig. 7.4), results in increase of estimated probabilities. In both figures it is also clearly demonstrated, that all largest seismic events during mining of the pillar occurred within the softening phase which corresponds to the decrease of stress-strain curve.

The second case, where assessment of probability of seismic event occurrence is based on stress and strain rate $[x=(1, \dot{\sigma}, \dot{\epsilon})^T]$, is demonstrated on Fig. 7.5 and 7.6. In both figures, in addition to the plot of probability as a function of time, stress and strain release curves are included. Again, it is clearly shown that the predictive power of the procedure increases as time flows and more observations are used for parameters Θ estimation. The example clearly demonstrates that all the largest seismic events occurred within the softening phase which corresponds to the decrease of stress and increase of strain rate.

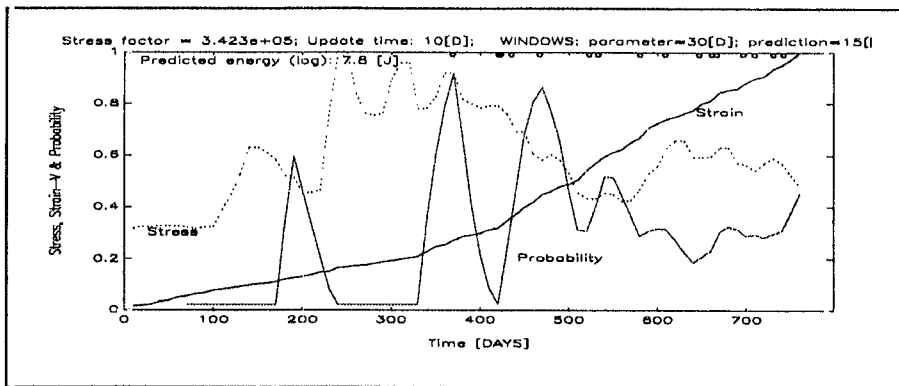


Fig. 7.5. Probability of the occurrence of seismic events with the energy $E \geq 10^{7.9}$ J within time interval $\Delta T = 15$ days, during the mining of the pillar in deep gold mine, South Africa. Assessment of probabilities (solid line) is based on temporal variations of σ and strain rate $\dot{\epsilon}$ within time window 30 days. Smoothed stress and strain curves are shown by dashed lines.

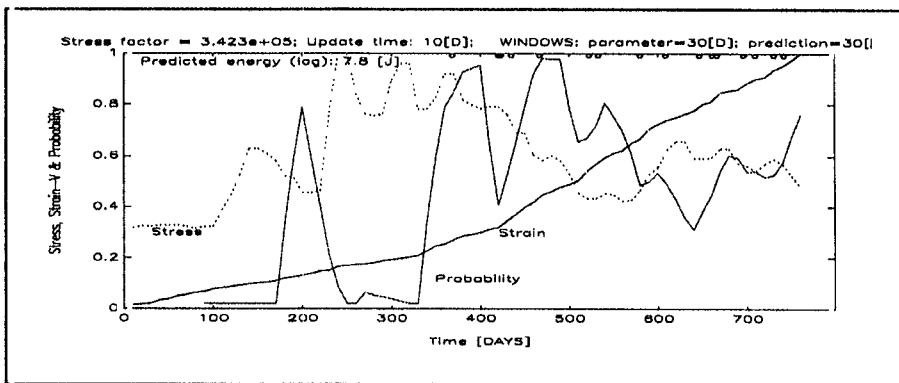


Fig. 7.6. Probability of the occurrence of seismic events with the energy $E \geq 10^{7.9}$ J within time interval $\Delta T = 30$ days, during the mining of the pillar in deep gold mine, South Africa. Assessment of probabilities is based on temporal variations of stress σ and strain rate $\dot{\epsilon}$ within time window 30 days. Smoothed stress and strain curves are shown by dashed lines.

Conclusions

The aim of this paragraph was to show that the combination of logistic distribution and stress-strain release can be successfully applied for assessment of probability of strong seismic event occurrence in mines. Successful assessment of such probabilities also proves the correctness of our basic assumptions: (a) apparent stress can be used as an indicator of the level of the local stress, and (b) cumulative apparent volume provides insight into rate of coseismic deformation.

Also it is important, that such σ_A and V_A can be estimated apart from any model of the source, and are based only on two

standard characteristics calculated for each seismic event: seismic moment M and seismic energy E .

7.5 PROBABILITY MODEL FOR SEISMIC EVENT OCCURRENCE BASED ON FRACTAL FORMALISM

Essentially, there are two alternative approaches to describe the complexity of the space time distribution of seismicity generated by the rupture process. The first consists of the development of physical models based on the fracture mechanics of the rock. An example of such approach was described in previous section. The second approach, (that will be used here), is based on stochastic models, which describe most of the observed statistical features of seismic event occurrence. Different techniques can be used, and one of them is based on the concept of fractals, introduced and extensively discussed in geoscience context by Mandelbrot (1989).

The fractal approach is used to characterize sets that exhibit irregularity regardless of the scale at which the set is examined. The formal definition of a fractal distribution is given by the relation (Mandelbrot 1982).

$$N_i = \frac{c}{x_i^D}, \quad (7.20)$$

where N_i is the number of objects with linear dimension x_i ; D is the fractal dimension and c is a constant. It seems to be a general principle that all processes close to a certain critical stage generate power law distributions such as (7.20). A fractal approach to natural earthquake occurrence has been applied in a large number of recent studies and it has been shown that seismicity has fractal nature with respect to time and size. For example, Kagan and Knopoff (1980 a,b, 1981) and Sadowskiy *et al* (1984) have shown that earthquake fault zones have three dimensional structure with a fractal distribution in size. Aki (1981) hypothesized that there is a fractal relation between the b value from the Gutenberg Richter frequency magnitude relation and the fractal dimension D . According to Aki (1981) $D = 3b/c$ where c is the constant of the log of seismic moment versus magnitude relation. According to Kanamori and Anderson (1975) c is close to 1.5. Therefore $D = 2b$. The seismic energy released by earthquakes also shows a fractal nature. Bebbington *et al* (1990) have pointed out that Soviet seismologists, for many years, have classified seismic events directly on the energy basis using an empirical energy frequency power law distribution such as (7.20) where D is within range 0.4 to 0.8. The

fractal nature of the temporal distribution of seismicity has been demonstrated by Kagan and Knopoff (1978, 1981) and Smalley *et al* (1987). These fractal structures in space, time and size are observed not only in the seismicity of earthquakes, but have also been verified in microfracturing experiments on rock samples. For a summary of results and general discussion see Korvin (1992) and Kagan (1994).

The aim of this paragraph is to determine whether a temporal variation in fractal dimension associated with time and size distribution of seismic events in mines may be used for prediction of strong mining induced seismic events. For this purpose a fractal based stochastic model of seismicity, which by using a power law takes into account the time dependency between successive events, was developed. It is also shown how such a model can be used in mines for continuous evaluation of seismic event occurrence probability within a specified time interval.

7.5.1 Building the Model

Before constructing our model of seismicity a few assumptions must be made.

Firstly it is known that some time after the occurrence of a major seismic event, the aftershock activity (if any) dies off and background seismicity exceeds the aftershock activity. Similarly, some time before the occurrence of a major seismic event, the foreshock activity (if any) may exceed background seismicity. Foreshocks, aftershocks and the major event together form a cluster of events with strong interdependence in time and space. When looking at a seismic catalog, the cluster is defined as a set of events in the same volume of rock, each of which occurred within a time t_c from at least one of its neighbours in time. The event in such a set with the largest seismic moment is assumed to be the major event. The determination of the critical time parameter t_c is not an easy task. For extensive discussion on this matter see the recent paper by Molchan and Dmitrieva (1992).

Secondly, it is assumed that the clusters (or equivalently, the main events) follow a Poissonian distribution in time. Therefore clusters of events are statistically independent although individual events within the same cluster are mutually dependent.

Thirdly it is assumed that such a time interdependency within a cluster is described by a fractal based relation.

The fourth assumption is that there is no principal physical difference between events within a cluster. Thus, following Kagan

and Knopoff (1981) and Kagan (1991 a) it is assumed that all seismic events, regardless of whether they are main events or not, have the same distribution of their size. In this study the size of an event is described by two independently determined parameters: seismic energy and seismic moment. Such a compound description of event size is similar to that described by Nava (1994).

Lastly, it is assumed that the correlation between occurrence times and size of seismic events is negligible. This was confirmed by Wu *et al* (1994). As a result, our analysis of seismic data is simplified significantly by separation of the seismic event size distribution and calculating its parameters independently from the remaining parameters of the model.

Extensive and detailed discussion on the applicability and limitations of some of the above assumptions, as well as alternative models, can be found in the set of papers by Kagan and Knopoff (1980b, 1981, 1987a,b), Kagan (1991a), Ogata (1988, 1994) and Vere Jones (1994). Examples of empirical two dimensional distributions of seismic event size parameters (seismic energy and seismic moment) observed in some of the deep gold mines in South Africa can be found in Mendecki (1993) and van Aswegen and Butler (1993).

The clue to the quantitative evaluation of future seismic activity is the conditional intensity function $\Lambda(T,E,M)$. This is the activity rate of events with energy $E \geq E_c$ and seismic moment $M \geq M_c$ given the past information on seismicity $d_k = (t_k, E_k, M_k)$, $k = 1, \dots, n$ and n is the number of events. It is assumed that all n observed events are complete from energy level E_c and seismic moment M_c . The concept of conditional intensity function for the description of point processes was developed in the early 1970's and it is known that such a function characterizes a point process completely (eg Rubin 1972, Liptzer and Shiraev 1978). Among the first who applied the conditional intensity function in analysis of seismic event catalogues was Hawkes and Adamopoulos (1973), Ogata and Akaike (1982) and Vere Jones and Ozuki (1982).

In our model seismicity is described by the function $\Lambda(T,E,M)$ which consists of the sum of three parts: part one describes the main events, part two the aftershocks and part three describes the foreshocks.

Main events

The number of main events of interest in T is equal to the activity rate of main events multiplied by the probability that it will have energy $E \geq E_c$ and seismic moment $M \geq M_c$. This can be written as

$$\lambda \cdot P_{EM}(E, M)$$

Aftershocks

Following our model the number of aftershocks of interest in a given cluster i is equal to the number of aftershocks associated with cluster i , multiplied by the probability that the event will have energy $E \geq E_c$ and moment $M \geq M_c$, multiplied by the probability that it occurs at time t away from the occurrence of the previous aftershock. In the case of the first aftershock, t is relative to the main event. This can be written as $v(E_p, M_i) \cdot P_{EM}(E, M) \cdot P_i(t)$ where E_i and M_i is the energy and seismic moment of the main event respectively. Note

that following assumption four, the size distribution $P_{EM}(E, M)$ is the same for main events and aftershocks and that aftershocks are linked to the main event via $v(E_p, M_i)$.

Foreshocks

Finally it is assumed that the number of foreshocks of interest in a given cluster i is equal to the number of foreshocks associated with cluster i , multiplied by the probability that it will have energy $E \geq E_c$ and moment $M \geq M_c$, multiplied by the probability that it occurs at time t away from the occurrence of the previous foreshock (in the case of the first foreshock this time dependency does not exist).

This can be written as $\delta_i \cdot P_{EM}(E, M) \cdot P_i(t)$ for foreshocks that are not the first foreshock in the cluster. Since foreshocks that occur first are not time dependent on preceding events, the number of them is equal to the activity rate first foreshocks ϵ multiplied by the probability that it has energy $E \geq E_c$ and moment $M \geq M_c$. This can be written as $\epsilon P_{EM}(E, M)$. Note that δ_i is the total number of foreshocks associated with cluster i that are not first foreshocks.

Finally one can write:

$$\Lambda(T, E, M) = \lambda P_{EM}(E, M) + \epsilon P_{EM}(E, M) + \sum_{i=1}^{M_e} \delta_i P_{EM}(E, M) P_i(t) + \sum_{i=1}^{M_e} v(E_p, M_i) P_{EM}(E, M) P_i(t) \quad (7.21)$$

where M_e is the number of main events in T .

7.5.2 Fractal Based Parameterization of the Model

In order to make use of the conditional intensity function $\Lambda(T, E, M)$

further, the parameterization of $P_{EM}(E, M)$, $v(E, M)$, δ_i and of $P_i(t)$ has to be performed. Firstly the parameterization of $P_{EM}(E, M)$ is considered. The size of a seismic event (in the sense of its strength) is usually expressed by one parameter only, which is seismic event magnitude. In recent years, more and more often Richter's magnitude is replaced by seismic moment or seismic moment magnitude M_w , introduced by Kanamori (1977). Occasionally, size of seismic events is described by released seismic energy.

The distributions of seismic moment M (or seismic energy E) is usually assumed to follow a Pareto distribution which is an appropriate transformation of the Gutenberg-Richter frequency-magnitude and $\log(M)$ (or $\log(E)$) versus magnitude relation

$$P_M(M) = \frac{\beta M_c^\beta}{M^{\beta+1}}, \quad (7.22)$$

for $M_c \leq M < \infty$. M_c is the threshold of completeness and $\beta = b/c$ where b is a Gutenberg Richter parameter and c is 1.5 (Kanamori and Anderson, 1975). Requirements of finiteness of seismic moment or seismic energy (Knopoff and Kagan 1977) implies that the power law distribution (7.22) must be modified. Usually, this is done by introduction of an upper limit on the distribution, which in the case of seismic moment is described by maximum moment M_x (Anderson 1979, Molnar 1979) and E_x in the case of seismic energy.

Since some advanced seismic recording systems used in mines (as ISS for example) allows for independent estimation of seismic moment and seismic energy, the two dimensional model of seismic size is used in this work. As a first approximation it is assumed that E and M follow a bivariate power law distribution (Johnson and Kotz 1972) which takes the following form:

$$P_{EM}(E, M) = \frac{\beta(\beta+1)}{E_o M_o} \left(\frac{E}{E_o} + \frac{M}{M_o} - 1 \right)^{-\beta-2}, \quad (7.23)$$

where $E_o \geq E_c$, $M_o \geq M_c$ and $\beta > 0$. Note that this distribution assumes β to be the same for both energy and moment. It is also assumed E_c and M_c are known and that the catalog contains all events which occurred with energies $E \geq E_c$ and $M \geq M_c$.

Introduction of a maximum value of seismic moment M_x and seismic energy E_x is needed to fulfil the requirement of finiteness of these two parameters. This is equivalent to truncation of distribution (7.23) from the top. After simple calculations required by proper renormalization, the probability density function (7.23) takes the form

$$P_{EM}(E, M) = C \left(\frac{E}{E_o} + \frac{M}{M_o} - 1 \right)^{-\beta-2}, \quad (7.24)$$

where $E_c \leq E_o \leq E \leq E_x$, $M_c \leq M_o \leq M \leq M_x$ and

$$C = \frac{\beta(\beta + 1)}{E_o M_o} \left[1 - \left(\frac{E_x}{E_o} \right)^{-\beta} - \left(\frac{M_x}{M_o} \right)^{-\beta} + \left(\frac{E_x}{E_o} + \frac{M_x}{M_o} - 1 \right)^{-\beta} \right]^{-1}. \quad (7.25)$$

It should be noted that the power law distribution (7.25) is not the only distribution type that can be used to describe the size distribution of seismic events. For example, according Vere Jones (1977), Main and Burton (1984) and Kagan (1991b), the best one dimensional candidate fulfilling the requirement of the finiteness of seismic moment or seismic energy is the gamma distribution

$$P_{EM}(M) = \text{const} \frac{e^{-M/M_x}}{M^{\beta+1}}, \quad (7.26)$$

where $M_c \leq M \leq \infty$. M_x is a parameter that controls the distribution in the upper ranges of M and const is a normalizing coefficient. The form of (7.26) originates from maximum entropy reasoning (Eadie *et al* 1982) and is the natural outcome of a stochastic critical branching model (Vere Jones 1976). For small and moderate seismic events, (9.26) behaves as a power law distribution. For very strong events it fulfils the requirements of finiteness of energy or seismic moment. Now one has parameterized the event size distribution using five parameters (E_o , E_x , M_o , M_x , β). It is assumed E_c and M_c are given. Kagan (1991b) hypothesize that β is close to $1/2$.

Let us consider the parameterization of the function

describing the after- and foreshock occurrence δ_i , $v(E_i, M_i)$ and $P_i(t_i)$. Following Kagan (1991a) one assumes that $v(E_i, M_i)$ is of the form,

$$v(E_i, M_i) = v M_i^\gamma, \quad (7.27)$$

where $v \geq 0$ and $\gamma > 0$. Physically, this means that the larger the main event (in terms of moment), the more aftershocks it should have. Since the relationship between the number of foreshocks and the size of the main event is unknown, one assumes $\delta_i = \delta$. Another reason one cannot make the number of foreshocks dependant on the main event, is that the main event occurs later in time than the foreshocks. This formalism assumes that only the past and not the future influences the present.

The time probability density function is assumed to be

fractal and of the form

$$P_i(t) = \frac{-\alpha t^{-\alpha-1}}{t_x^{-\alpha} - t_o^{-\alpha}}, \quad (7.28)$$

where $\alpha > -1$ and not equal to 0, t_o is the "deadtime" and t_x is the maximum allowable time interval between two successive events in a cluster. Physically t_o means that if an event occurs, the preceding event is at least a time t_o into the past.

Together with the activity rates λ and ϵ there are thirteen parameters $\theta = (\lambda, \beta, \gamma, \nu, \alpha, \epsilon, \delta, E_o, M_o, t_o, E_x, M_x, t_x)$ that describe the process of seismicity in our model. The next step will be to find values for these parameters.

7.5.3 Parameters Estimation

As an evaluation method for the parameters θ , the maximum likelihood procedure is chosen. The maximum likelihood estimate of θ is the value of the parameter vector θ which minimizes the logarithm of the likelihood function. For n seismic events each with origin time, energy and seismic moment equal to $d_k = (t_k, E_k, M_k)$, where

$k = 1, \dots, n$, and occurring in period $[0, T]$, the log-likelihood function is (Cox 1975)

$$\ln L(d_1, \dots, d_n | \theta) = \quad (7.29)$$

$$\int_0^T \int_{E_o, M_o}^{E_x, M_x} \ln \Lambda(t, E, M | \theta) dN(t, E, M) - \int_0^T \int_{E_o, M_o}^{E_x, M_x} \ln \Lambda(t, E, M | \theta) dM dt.$$

In formula (7.29) $\Lambda(t, E, M | \theta)$ is the parameterized conditional intensity function (7.21), given values for θ and $N(t, E, M)$ is a 3D Dirac delta function. The log-likelihood (LLF) must now be calculated.

The first term of the right hand side of (7.29) can be written as the sum of n elements:

$$\sum_{k=1}^n \ln \phi_k$$

where

$$\phi_k = \begin{cases} \lambda P_{EM}(E_p, M_j), & \text{if } k \text{ is the } i\text{th main event} \\ \epsilon P_{EM}(E_p, M_j), & \text{if } k \text{ is the } i\text{th first foreshock} \\ \delta_i P_{EM}(E_p, M_j) P_i(t_j), & \text{if } k \text{ is } j\text{th foreshock of } i\text{th cluster, } j > 1 \\ \nu (E_p, M_j) P_{EM}(E_p, M_j) P_i(t_j), & \text{if } k \text{ is } j\text{th aftershock of } i\text{th cluster.} \end{cases} \quad (7.30)$$

Now following (7.29):

$$LLF = \sum_{k=1}^n \ln \phi_k - \sum_{i=0}^{m_e} \int_{t_0}^{t_{i+1}} \lambda dt - m_e t_o - \int_0^T \epsilon dt - \int_0^T \sum_{i=1}^{m_e} \delta_i P_i(t) dt - \int_0^T \sum_{i=1}^{m_e} v (E_p M_i) P_i(t) dt, \quad (7.31)$$

where t_{i+1} is the occurrence time of the $i + 1$ th main event taken relative to the occurrence time of the i th main event and t_1 is taken relative to the start of the catalog and $t_{m_e+1} = T$. After further transformations

$$LLF = \sum_{k=1}^n \ln \phi_k - \lambda T + \lambda m_e t_o - m_e t_o - \sum_{i=0}^{ffs} \int_{t_0}^{t_{i+1}} \epsilon dt - ffs t_o - \int_0^T \sum_{i=1}^{m_e} \delta_i P_i(t) dt - \int_0^T \sum_{i=1}^{m_e} v (E_p M_i) P_i(t) dt, \quad (7.32)$$

where t_{i+1} is the occurrence time of the $i + 1$ th first foreshock taken relative to the occurrence time of the i th first foreshock. Also t_1 is taken relative to the start of the catalog and $t_{ffs+1} = T$ and ffs is the number of first foreshocks.

Following further transformation

$$LLF = \sum_{k=1}^n \ln \phi_k - \lambda T + \lambda m_e t_o - m_e t_o - \epsilon T + \epsilon ffs t_o - ffs t_o - \int_0^T \sum_{i=1}^{m_e} \delta_i P_i(t) dt - \sum_{i=1}^{m_e} \left[v M_i^{\gamma} \sum_{j=1}^{a_i} \int_{t_0}^{t_j} P_i(t) dt - a_i t_o \right] - T_A, \quad (7.33)$$

where a_i is the number of aftershocks associated with cluster i , t_j is occurrence time of aftershock j in cluster i taken relative to the occurrence time of the $j - 1$ th aftershock. If $j - 1$ is zero then the occurrence time of the main event is used. T_A is the time associated with those parts between the last aftershock of the previous cluster and the next main event. Now

$$LLF = \sum_{k=1}^n \ln \phi_k - \lambda T + \lambda m_e t_o - m_e t_o - \epsilon T + \epsilon ffs t_o - ffs t_o - \int_0^T \sum_{i=1}^{m_e} \delta_i P_i(t) dt - \sum_{i=1}^{m_e} \left[v M_i^{\gamma} \sum_{j=1}^{a_i} \frac{t_j^{-\alpha} - t_o^{-\alpha}}{t_j^{-\alpha} - t_o^{-\alpha}} \right] - n_a t_o - T_A, \quad (7.34)$$

where n_a is total number of aftershocks, and

$$LLF = \sum_{k=1}^n \ln \phi_k - \lambda T + \lambda m_e t_o - m_e t_o - \epsilon T + \epsilon ffs t_o - ffs t_o \quad (7.35)$$

$$- \sum_{i=1}^{m_c} \left[\delta \sum_{j=1}^{f_i} \frac{t_{j+1}^{-\alpha} - t_o^{-\alpha}}{t_x^{-\alpha} - t_o^{-\alpha}} \right] - f_s t_o - T_f - \sum_{i=1}^{m_a} \left[\nu M_i^{\gamma} \sum_{j=1}^{a_i} \frac{t_{j+1}^{-\alpha} - t_o^{-\alpha}}{t_x^{-\alpha} - t_o^{-\alpha}} \right] - n_a t_o - T_A,$$

where f_i is the number of foreshocks (the first one excluded) associated with cluster i , t_{j+1} is the occurrence time of the i th main event, f_s is the total number of non first foreshocks and T_f is the time associated with those parts between the previous main shock and the next non first foreshock.

Finally LLF is

$$\sum_{i=1}^{m_c} \ln \left[\lambda C \left(\frac{E_i}{E_o} + \frac{M_i}{M_o} - 1 \right)^{-\beta-2} \right] + \sum_{i=1}^{ffs} \ln \left[\epsilon C \left(\frac{E_i}{E_o} + \frac{M_i}{M_o} - 1 \right)^{-\beta-2} \right] + \quad (7.36)$$

$$\sum_{i=1}^{fs} \ln \left[\delta C \left(\frac{E_i}{E_o} + \frac{M_i}{M_o} - 1 \right)^{-\beta-2} (-\alpha t_i^{-\alpha-1} (t_x^{-\alpha} - t_o^{-\alpha})^{-1}) \right] +$$

$$\sum_{i=1}^{n_a} \ln \left[\nu M_i^{\gamma} C \left(\frac{E_i}{E_o} + \frac{M_i}{M_o} - 1 \right)^{-\beta-2} (-\alpha t_i^{-\alpha-1} (t_x^{-\alpha} - t_o^{-\alpha})^{-1}) \right] -$$

$$\lambda (T - m_e t_o) - \epsilon (T - ffs t_o) - \sum_{i=1}^{m_o} \delta \sum_{j=1}^{f_i} \frac{t_{j+1}^{-\alpha} - t_o^{-\alpha}}{t_x^{-\alpha} - t_o^{-\alpha}} -$$

$$\sum_{i=1}^{m_c} \nu M_i^{\gamma} \sum_{j=1}^{a_i} \frac{t_{j+1}^{-\alpha} - t_o^{-\alpha}}{t_x^{-\alpha} - t_o^{-\alpha}} - T_c,$$

where T_c is some constant. Firstly, the truncation parameters E_o , M_o , t_o , E_x , M_x and t_x are estimated. E_o and M_o are estimated as the lowest observed energy and moment respectively, from the start of the catalog to the current time. Following Kijko and Funk (1994), M_x and E_x are estimated by $2M_{max} - M_{max-1}$ and $2E_{max} - E_{max-1}$ respectively, where M_{max} and E_{max} are the highest observed moment and energy from the start of the catalog until the current time and M_{max-1} and E_{max-1} are the second highest observed moment and energy.

In Kagan's (1991a) model of seismic flow:

$$t_o = kM^{\frac{1}{3}}$$

where k is a constant and M is the moment of the previous event. Such a scaling procedure ensures different values of coda duration

for events with different seismic moments. The value of k is usually set in such a way that:

$$kM_c^{\frac{1}{3}}$$

is approximately equal to the coda duration of an event with threshold seismic moment M_c . Another way to approximate t_o is to set it equal to the minimum time difference between two successive events. If the catalog is long enough, this estimate will approach the t_o associated with M_c . The value of t_x may be estimated as the length of the catalog.

The seven parameters $\lambda, \epsilon, \beta, \delta, \nu, \chi, \gamma, \alpha$ are now estimated. This is done by equating the relevant derivative of the *LLF* to zero. From condition:

$$\frac{\partial LLF}{\partial \lambda} = 0$$

one obtains

$$\lambda = \frac{m_e}{T - m_e t_o} \tag{7.37}$$

Similarly, from $\frac{\partial LLF}{\partial \epsilon} = 0$ we have

$$\epsilon = \frac{ffs}{T - ffs t_o} \tag{7.38}$$

and from the condition $\frac{\partial LLF}{\partial \beta} = 0$ it follows that

$$\sum_{i=1}^n \frac{\partial C}{\partial \beta} - \sum_{i=1}^n \ln \left(\frac{E_i}{E_o} + \frac{M_i}{M_o} - 1 \right) = 0, \tag{7.39}$$

where n is total number of events and $\partial C / \partial \beta$ is

$$\left\{ \left[1 - \left(\frac{E_x}{E_o} \right)^{-\beta} - \left(\frac{M_x}{M_o} \right)^{-\beta} + \left(\frac{E_x}{E_o} + \frac{M_x}{M_o} - 1 \right)^{-\beta} \right] \left[\frac{2\beta + 1}{E_o M_o} \right] - \left[\frac{\beta(\beta + 1)}{E_o M_o} \right] \right. \\ \left. \left[\left(\frac{E_x}{E_o} \right)^{-\beta} \ln \left(\frac{E_x}{E_o} \right) + \left(\frac{M_x}{M_o} \right)^{-\beta} \ln \left(\frac{M_x}{M_o} \right) - m \left(\frac{E_x}{E_o} + \frac{M_x}{M_o} - 1 \right) \left(\frac{E_x}{E_o} + \frac{M_x}{M_o} - 1 \right)^{-\beta} \right] \right\} / \\ \left[1 - \left(\frac{E_x}{E_o} \right)^{-\beta} - \left(\frac{M_x}{M_o} \right)^{-\beta} + \left(\frac{E_x}{E_o} + \frac{M_x}{M_o} - 1 \right)^{-\beta} \right]^2 \tag{7.40}$$

The value of β can be found from relation (7.39) and (7.40) using for instance the bisection method with starting value around 0.5.

From condition $\frac{\partial LLF}{\partial \delta} = 0$ it follows that

$$\delta = \frac{f_s(t_x^{-\alpha} - t_o^{-\alpha})}{\sum_{i=1}^{m_e} \sum_{j=i}^{f_i} [t_{j+1}^{-\alpha} - t_o^{-\alpha}]} \quad (7.41)$$

In the same way, from $\frac{\partial LLF}{\partial v} = 0$ one obtains

$$v = \frac{n_a (t_x^{-\alpha} - t_o^{-\alpha})}{\sum_{i=1}^{m_e} M_i^\gamma \sum_{j=i}^{a_i} [t_j^{-\alpha} - t_o^{-\alpha}]} \quad (7.42)$$

Similarly from condition $\frac{\partial LLF}{\partial \gamma} = 0$ and substituting v from (7.42)

$$\frac{\sum_{i=1}^{n_a} \ln M_{j(i)}}{n_a} - \frac{\sum_{i=1}^{m_e} M_i^\gamma \ln M_i \sum_{j=i}^{a_i} (t_j^{-\alpha} - t_o^{-\alpha})}{\sum_{i=1}^{m_e} M_i^\gamma \sum_{j=i}^{a_i} (t_j^{-\alpha} - t_o^{-\alpha})} = 0 \quad (7.43)$$

Finally, from the condition $\frac{\partial LLF}{\partial \alpha} = 0$, and substitution of v and δ , one has

$$\begin{aligned} \frac{f_s}{\sum_{i=1}^{f_s} \ln t_i} - \frac{f_s}{\sum_{i=1}^{f_s} \ln t_i} \frac{1}{\alpha} + \frac{f_s}{\sum_{i=1}^{f_s}} \frac{(t_x^{-\alpha} \ln t_x - t_o^{-\alpha} \ln t_o)}{(t_x^{-\alpha} - t_o^{-\alpha})} - \\ \frac{n_a}{\sum_{i=1}^{n_a} \ln t_i} + \frac{n_a}{\sum_{i=1}^{n_a}} \frac{1}{\alpha} + \frac{n_a}{\sum_{i=1}^{n_a}} \frac{(t_x^{-\alpha} \ln t_x - t_o^{-\alpha} \ln t_o)}{(t_x^{-\alpha} - t_o^{-\alpha})} \end{aligned} \quad (7.44)$$

$$\frac{f_s \sum_{i=1}^{m_e} \sum_{j=1}^{f_i} (t_x^{-\alpha} - t_o^{-\alpha})(t_o^{-\alpha} \ln t_o - t_{j+1}^{-\alpha} \ln t_{j+1}) - (t_{j+1}^{-\alpha} - t_o^{-\alpha})(t_o^{-\alpha} \ln t_o - t_x^{-\alpha} \ln t_x)}{(t_x^{-\alpha} - t_o^{-\alpha}) \sum_{i=1}^{m_e} \sum_{j=1}^{f_i} (t_{j+1}^{-\alpha} - t_o^{-\alpha})}$$

$$\frac{n_a \sum_{i=1}^{m_e} M_i^\gamma \sum_{j=1}^{a_i} (t_x^{-\alpha} - t_o^{-\alpha})(t_o^{-\alpha} \ln t_o - t_j^{-\alpha} \ln t_{j+1}) - (t_j^{-\alpha} - t_o^{-\alpha})(t_o^{-\alpha} \ln t_o - t_x^{-\alpha} \ln t_x)}{(t_x^{-\alpha} - t_o^{-\alpha}) \sum_{i=1}^{m_e} M_i^\gamma \sum_{j=1}^{a_i} (t_j^{-\alpha} - t_o^{-\alpha})}$$

Relations (7.43) and (7.44) are two nonlinear equations in two unknowns. This can be solved using Newton's method for example. Inserting values for α and γ in (7.41) and (7.42) will render values of ν and δ .

7.5.4 Probability Assessment

At this stage we have described the process using function Λ and we have found estimates of the parameters θ . One would now like to extrapolate the statistical properties of Λ in order to predict seismic events in the future. So one would like to have a formula to express the probability that an event with energy larger than E^* and moment larger than M^* will occur in the next time period Δt . A formula by Ogata (1994) says that the probability that an event occurs in time interval $(T, T + \Delta t)$ with energy within range (E_o, E) and seismic moment within range (M_o, M) is,

$$P[(T, T + \Delta t); (E_o, E); (M_o, M)] = 1 - e^{-\int_T^{T+\Delta t} \int_{E_o}^E \int_{M_o}^M \Lambda(t, E, M) dM dE dt} \quad (7.45)$$

where T is the time of the last event occurrence. If this procedure is applied within a moving time window, this probability is time dependant through the time dependancy of its parameters θ . Relation (7.45) must now be adapted to our own purpose. Let us first calculate:

$$\int_T^{T+\Delta t} \int_{E_o}^{E^*} \int_{M_o}^{M^*} \Lambda dM dE dt ,$$

which after some transformations can be expressed as: $f(E^*, M^*) \cdot g(T, T + \Delta t)$, where

$$f(E^*, M^*) = \frac{CE_oM_o}{\beta(\beta+1)} \left[\left(\frac{E^*}{E_o} + \frac{M^*}{M_o} - 1 \right)^{-\beta} - \left(\frac{M^*}{M_o} \right)^{-\beta} - \left(\frac{E^*}{E_o} \right)^{-\beta} + 1 \right] \quad (7.46)$$

and

$$g(T, T + \Delta T) = \left[\lambda \Delta t + \epsilon \Delta t + \delta \frac{((T + \Delta t)^{-\alpha} - T^{-\alpha})}{(t_x^{-\alpha} - t_o^{-\alpha})} + \frac{\nu M_i^\gamma ((T + \Delta t)^{-\alpha} - T^{-\alpha})}{(t_x^{-\alpha} - t_o^{-\alpha})} \right] \quad (7.47)$$

Now let t_n be the time of the last event occurrence, t_i the current time and Δt the period for which a prediction must be made. Now according to (7.45) and (7.46) the probability of seismic event occurrence in the range of energy (E, E_x) and seismic moment (M, M_x) , relative to the current time t_i is

$$1 - e^{-[f(E_x, M_x) - f(E, M_x)] g(t_i + \Delta t)} \quad (7.48)$$

According to the assumption t_c is an external time parameter that defines the cluster - if two events occur within a time t_c from each other, they belong to the same cluster otherwise they do not. If $t_i - t_n > t_c$ it means the next event to occur must be part of the next cluster. If this is the case the next event must be the first event of the next cluster, making it either a first foreshock or a main event. Since no other events in that cluster exist yet, the event cannot be an aftershock or a foreshock other than the first one. In this case $g(t_p, t_i + \Delta t)$ takes the form

$$\lambda \Delta t + \epsilon \Delta t \quad (7.49)$$

If $t_i + \Delta t - t_n < t_c$ then the next event to occur must be part of the current cluster. In this case it cannot be a first foreshock and if the current largest moment in the cluster is smaller than the moment of interest M^* , then it can not be an aftershock either. So now $g(t_p, t_i + \Delta t)$ takes the form

$$\lambda \Delta t + \frac{\delta \left((t_i + \Delta t)^{-\alpha} - t_i^{-\alpha} \right)}{t_x^{-\alpha} - t_o^{-\alpha}} \quad \text{if } M_i = M^* \quad (7.50)$$

and

$$\lambda \Delta t + (\delta + \nu M_i^\gamma) \frac{\left((t_i + \Delta t)^{-\alpha} - t_i^{-\alpha} \right)}{t_x^{-\alpha} - t_o^{-\alpha}}, \quad \text{if } M_i \geq M^*$$

The last situation that may occur is that $t_i + \Delta t - t_n > t_c > t_i - t_n$ in which case the next event to occur may be part of the same cluster or not. In this case $g(t_p, t_i + \Delta t)$ is,

$$\lambda \Delta t + \epsilon (t_i + \Delta t - t_n - t_o) + \frac{\delta \left((t_n + t_o)^{-\alpha} - t_o^{-\alpha} \right)}{t_x^{-\alpha} - t_o^{-\alpha}} \quad \text{if } M_i < M^* \quad (7.51)$$

and

$$\lambda \Delta t + \epsilon (t_i + \Delta t - t_n - t_o) + (\delta + \nu M_i^\gamma) \frac{\left((t_n + t_o)^{-\alpha} - t_o^{-\alpha} \right)}{\left(t_x^{-\alpha} - t_o^{-\alpha} \right)} \quad \text{if } M_i \geq M^*$$

The predictive capability of strong seismic events of the above formalism was tested in the following example. Events with energy larger than $5.5 \times 10^6 \text{J}$ are predicted for a 10 day period in an area surrounding a stope of one of the deep gold mines in South Africa. The catalog spans 153 days and 292 events in the relevant area were selected. The following actual events exceeded an energy of $5.5 \times 10^6 \text{J}$:

<u>No</u>	<u>Time (d)</u>	<u>Energy (10⁶J)</u>
1	0.000 000	11.800
2	3.732 639	27.900
3	43.817 361	5.540
4	46.568 056	6.580
5	47.652 083	9.780
6	56.825 000	5.800
7	67.923 611	9.470
8	69.690 278	7.140
9	73.561 806	5.530
10	104.687 500	55.400
11	144.415 972	49.500
12	145.728 472	64.200

These events will be used to test the prediction. The parameters discussed in the previous sections were estimated using data from a 20 day moving parameter window (the history). This parameter window moved in steps of 12 hours and it was assumed that if our event is closer than 1 hour to the preceding event, it belonged to the same cluster.

In Fig.7.6 one can see that probabilities between time 20 and 38 tend to go down and there were no events larger than $5.5 \times 10^6 \text{J}$ in this period. Then in the 11 day period from day 38 to 49 there is sharp increase in probability and 3 events (no's 3,4 and 5) occurred in this period. After the occurrence of event 5, the probability does not drop drastically as one would have expected. Instead makes a slight dip and then increases again, though at slightly slower rate. Obviously the series of events 3 to 5 was not enough to relieve the hazard in this area. Only when event 6 (day: 56.8) occurs, does the probability go down. This downward trend continues for 8 days until day 65, in which time no events larger than $5.5 \times 10^6 \text{J}$ occur. From day 65 to 84 there is short term fluctuation in probability but on average it stays at more or less the same level. In this period 3 events (no's 7,8 and 9) occurs. Around day 84 the probability drops drastically, probably due to an event of $1.08 \times 10^6 \text{J}$ on day 83.6. The decrease continues until day 92 during which time no events larger than $5.5 \times 10^6 \text{J}$ occur. From day 92 to day 99 there is a sharp increase in probability and in this time 7 events will energy larger than 10^6J occur before the probability flattens off! It stays at the same level for about 6 days, and then a large event (event 10 with energy $55.44 \times 10^6 \text{J}$) occurs. This event is somewhat unexpected, given the flattening of the probability curve, but it must be taken into account that the probability has been steadily rising since day

92 (for 12 days in other words). Even now the probability continues to rise until day 110 when apparently a smallish event ($1.26 \times 10^6 \text{J}$) breaks the upward trend in probability. The probability now decreases on average until day 128. During this time no event with energy larger than $5.5 \times 10^6 \text{J}$ occur. For the next 16 days the probability steadily rises until two extremely large events (no 11 with $49.5 \times 10^6 \text{J}$ and no 12 with $64.2 \times 10^6 \text{J}$) occur on days 144 and 145.

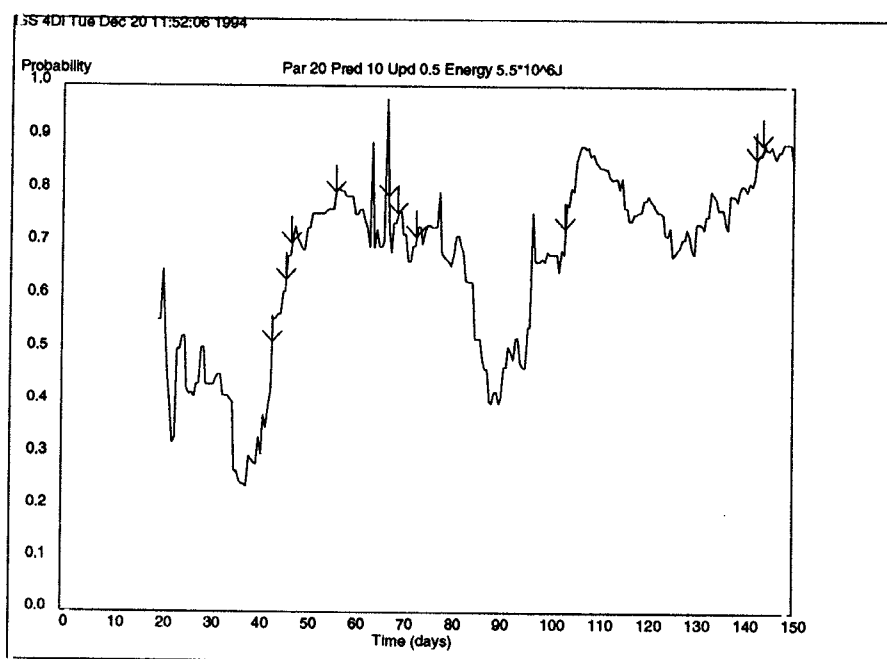


Figure 7.6 Plot of probability of seismic events in the next ten days, using a 20 day history, versus time. The events predicted are those with energy at least $5.5 \times 10^6 \text{J}$. The data was obtained from one of the deep gold mines in South Africa.

On the whole it seems that the probabilities are fairly good representations of the actual event occurrences.

However, the following points need some consideration.

1. One might have to consider an alternative formalism (eg Markov chains) that allows one to have events depend on future events as well as past events. If this were the case, then one would be able to link the number of foreshocks to the main shock size as is physically the case.
2. Since we are in a mining environment, the conditional intensity function Λ should be adapted to take into account the blasting. In blasting periods

other parameters would control the seismicity than is the case out of blasting periods.

3. The formalism can be rewritten in such a way, so that a priori knowledge of the thresholds of completeness is not needed. Further study may show that this may improve results.
4. In this theory, one assumes to be working in a small enough volume so that events within a time cluster is also within a space cluster. It would be possible to extend the formalism so that the spatial variables can be added to the time and size and also be parameterized accordingly.
5. Some form of reliability associated with the estimated probabilities of event occurrence should be incorporated.
6. For a given θ and Λ one must find ways to suggest optimal external parameter choice. These would include time t_c , length of parameter window, length of prediction window and the period of the calculation. Some ideas are given by Molchan and Kagan (1992) and Pepke *et al* (1994).

7.6 CORRELATION BETWEEN SEISMICITY IN ADJACENT MINING AREAS

In this paragraph a simple technique is demonstrated which makes it possible to find out whether seismic activities in different mining areas (seismic clusters) depend on each other.

The concept of interaction between natural seismicity at different areas is not new. This problem was studied by several authors and different approaches are known (*e.g.* Chiaruttini, *et al.*, 1980; Båth, 1984 a,b; Mantovani *et al.*, 1987; Mucciarelli *et al.*, 1988; Alberto *et al.*, 1989). The problem of the interaction between seismicity at different areas became especially interesting after clear evidence that the Landers, California earthquake, June 28, 1992 ($M_w=7.3$), triggered increased seismicity out to distances of several hundred kilometers (*e.g.* Anderson *et al.*, 1992, 1993; Michael, 1992; Reasenber *et al.*, 1992; Hill *et al.*, 1993).

Interaction between seismicity at different excavated areas

was also observed in mines. A simple trial to quantify such a phenomenon is described by Kijko (1980). Clear evidence of interaction of seismicity of different mining areas at Western Deep Levels Mine, South Africa, was recently demonstrated by Butler (1994).

In this paragraph, following an approach introduced by Båth (1984a, b), a simple technique is applied which makes it possible to find out whether seismic activity in different mining areas depend on each other. If such dependence is found to exist, then the degree of mutual interaction is also estimated.

The interaction is tested through the calculation of cross-correlation functions $CC_{\tau}(\lambda_i, \lambda_j)$ and $CC_{\tau}(E_i, E_j)$. Function $CC_{\tau}(\lambda_i, \lambda_j)$ is the cross-correlation between seismic activity rates λ_i, λ_j and $CC_{\tau}(E_i, E_j)$ is the cross-correlation between seismic energies E_i, E_j released by each pair (i, j) of clusters, $i < j, i, j = 1, \dots, 4$, and τ is mutual time shift. The cross-correlation function of two time series measures the similarity between them as a function of a relative time shift. The normalized cross-correlation function of two discrete time series $\{x\} = \{x_0, \dots, x_n\}$ and $\{y\} = \{y_0, \dots, y_n\}$ is defined as (e.g. Dimri, 1992)

$$CC_{\tau}(x, y) = \frac{1}{(n-s)\sigma_x \sigma_y} \sum_{k=0}^{n-s} (x_k - \bar{x})(y_{k+s} - \bar{y}), \quad (7.52)$$

where time shift $\tau = s \cdot \Delta t$, Δt is sampling rate, s is an integer, x, y , and σ_x, σ_y are averages and standard deviations of time series $\{x\}$ and $\{y\}$ respectively. The value of CC_{τ} is always in between $\langle -1, 1 \rangle$. If it is +1, the time series $\{x\}$ and $\{y\}$ have a perfect positive linear relationship. If CC_{τ} is equal to -1, $\{x\}$ and $\{y\}$ are linearly related but in the opposite way. If there exists no relationship between $\{x\}$ and $\{y\}$, then the value of CC_{τ} is 0. Intermediate values indicate partial relationships.

An example of assessment of interaction between clusters of seismicity at different mining areas is presented below. Data used in the present analysis are the same as in the previous paragraph and covers the time period of one year. Altogether, 20024 seismic events were taken into account with seismic energy equal to or greater than 10^4 J. Before calculating cross-correlation functions, the raw data was cumulated into $\Delta t = 3$ weeks time intervals. The cross-correlation functions of activity rate and logarithm of released seismic energy, between each pair of four clusters was analyzed. An illustration of such a analysis for two from four space-time clusters of seismicity are presented at Fig. 7.7 and 7.8. The minimum and

maximum distance between "centers" of clusters was equal to 0.62 and 1.78 km respectively. Already visual scanning of activity rates and energy release of these two clusters reveals a high resemblance between the respective curves Fig. 7.8. Not only the major features, but also several synchronous details can be seen in each two sets of respective time series.

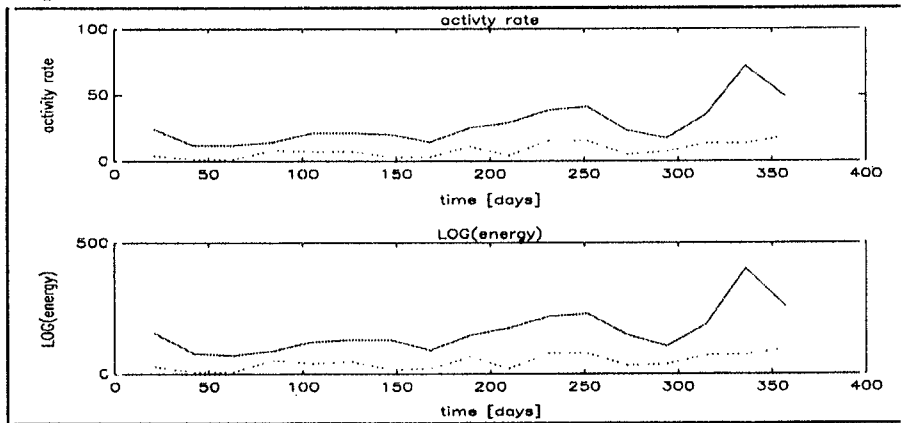


Figure 7.7 Number of seismic events (upper plot) and logarithm of seismic energy released (lower plot) in 3 week intervals, for two clusters from Fig.7.6, for the period January — December 1992.

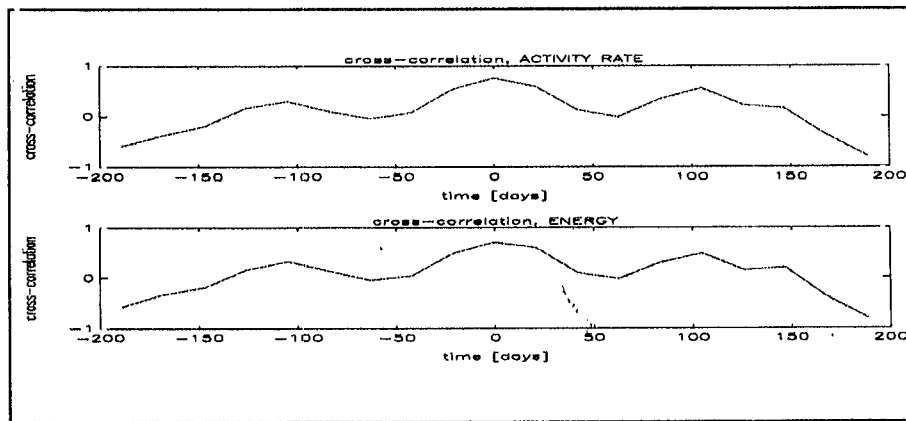


Figure 7.8 The cross-correlation functions of activity rates and released seismic energy for two clusters from Fig. 7.6.

The individual maxima of cross-correlation functions of activity rate and logarithm of released seismic energy, between each pair of four clusters is displayed in Table 7.1. As follows from that table, maxima of cross-correlations of seismic activities, reach values from 0.65 to 0.89 and respective cross-correlations of seismic energy release varies between 0.69 and 0.91. With only one exception (clusters #1 and #4), the maxima occur at $\tau=0$ time lag. It is interesting to note that when the data are cumulated into one week intervals, the maxima of the cross-correlation functions remain

close to $\tau=0$.

		ACTIVITY RATE correlation			
		1	2	3	4
SEISMIC ENERGY RELEASE correlation	1		0.82	0.89	0.77
	2	0.79		0.87	0.64
	3	0.91	0.88		0.75
	4	0.79	0.69	0.77	

Table 7.1 Maximum cross-correlation coefficients of activity rates (upper triangular matrix and seismic energy released (lower triangular) for 6 possible pairs of 4 clusters.

An unexpected result is that the simple technique, used for evaluation of cluster interaction, would also show a decrease of interaction with the distance between clusters. This is in fact the case (Fig. 7.9). Correlation coefficients for six distances are plotted on this figure as a function of distance from a reference cluster. This result shows decreasing interaction and is encouraging since intuitively one would expect this.

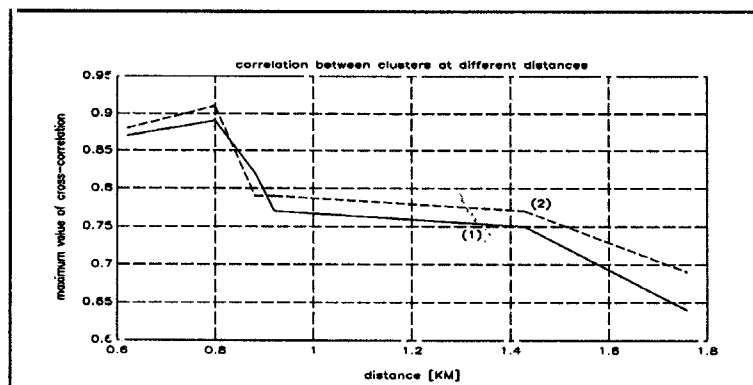


Figure 9.9 Correlation coefficients of activity rates (1) and released seismic energy (2) as a function of distance from a reference cluster.

The results of the performed analysis may be summarized as follows: (1) there is a clear correlation between seismic activities and seismic energy release in detected clusters; (2) the degree of interaction between clusters decreases as distance increases.

Mining engineers have suspected for some time now that seismicity at active faces is affected by induced seismicity at other

mining faces in some cases at significant distances apart. The results from this paragraph support this and further indicate that the degree of interaction is indeed a function of distance. One must therefore consider fairly large regions of activity around the zone of interest when performing back or forward analyses. The result also suggests that triggering mechanisms may be more complex than was previously suspected.

7.7 SIGNIFICANCE OF DIFFERENCE

7.7.1 Two Random Variables

Given two values of a observational value a statistical analysis should be done to determine if they differ significantly. For each value the average, its standard deviation and the number of observations must be known. The significance of difference, SID, can be estimated from the probability that any random value will fall into the interval bounded by the two average values

$$SID(x_1, x_2) = \frac{1}{\sqrt{2\pi} SD(x_{12})} \int_{\min(x_1, x_2)}^{\max(x_1, x_2)} \exp \left[\frac{(x - x_{12})^2}{2[SD(x_{12})]^2} \right] dx \quad (7.53)$$

where

x_1, x_2 – average values to be compared

n_1, n_2 – number of observations

$$x_{12} = \frac{n_1 x_1 + n_2 x_2}{n_1 + n_2}$$

$$SD(x_{12}) = \sqrt{\frac{(n_1 - 1) [SD(x_1)]^2 + (n_2 - 1) [SD(x_2)]^2}{n_1 + n_2 - 1}}$$

7.7.2 Difference in Relation to Average

Given a value of a certain observed parameter x , a statistical evaluation should be done to determine how significantly x deviates from its average value \bar{x} . One of the simplest ways to estimate the significance of difference between x and \bar{x} is the determination of the probability that any random value will fall in the interval $|x - \bar{x}|$. Assuming that the random variable x follows a normal distribution with an average value \bar{x} and standard deviation SD , such a

probability is defined as:

$$SD(x, \bar{x}) = \frac{\sqrt{2}}{\sqrt{\pi}SD} \int_{\bar{x}}^{\bar{x}+\Delta} \exp\left[\frac{-(x-\bar{x})^2}{2SD^2}\right] \quad (7.54)$$

where: $\Delta = |x-\bar{x}|$

CHAPTER 8

LIMITS OF PREDICTABILITY

Nonlinearity and chaos are common features of many systems in nature, (Gutzwiller, 1991; Radu, 1995) though this has been acknowledged largely only during the past two decades. The phenomenon, which goes under the name "chaos", is an intrinsic feature of dynamics and comprises the large sensitivity to initial conditions of the evolution of a nonlinear dynamical system. In practice, it may happen that the response of a physical system varies greatly when small changes occur in the environment containing the physical system. This type of behaviour is regarded as chaotic.

Special methods and techniques have emerged from the study of these systems that exhibit the phenomenon of chaos (Heiss, 1995). Their main merit is that they can sometimes offer alternative avenues to the traditional approach which consists of solving exactly the relevant equations of motion. Moreover, in the absence of a self-consistent model describing the dynamics of the process under study, it is not possible to gain any insight into the problem without the aid of more refined techniques. It is accepted that the occurrence of seismic events cannot currently be modelled with easy-to-use analytic equations. A study of the physics of seismicity is therefore expected to rely mostly on accurate data interpreted with the aid of nonlinear dynamics.

The seismic flow of rock is regarded as a highly complex process, intermittent in space and time, that provides for the occurrence of turbulence (Mendecki, 1995). In turn, turbulence is commonly associated with chaotic behaviour (Radu, 1995). It therefore appears that it is sensible enough to assume chaos may set in within the dynamics underlying the seismic flow of rock. In real systems, chaos and order coexist. By order we mean structures exhibiting a high degree of spatio-temporal regularity. Chaos and order both arise from the same type of nonlinear laws (Gutzwiller, 1991) and are often inseparable.

In order to make predictions about the occurrence of rockmass instabilities that may develop during the mining process, we need to manipulate the novel features of chaos theory. There is a connection between chaotic behaviour and instability. A system that is completely random but non-chaotic, has a very stable configuration that may persist even in the presence of external perturbations. On the other hand, a system that is ordered may become unstable in the presence of external forces as its entropy has the opportunity to increase. The coupling between a regular system and external perturbations is in general nonlinear and leads to chaotic behaviour. Rockmass subjected

to external conditions (e.g. mining) is regarded as a nonlinear dissipative system far from equilibrium. In such a system, instability is the uncertainty about the path to be followed by the system in its phase space, a concept to which we turn next.

8.1 Phase Space

When a nonlinear-type analysis is performed, the main object of study is the system's "phase space". The phase space of a physical system is the set of all possible states that the system can have. That collection of states can be spanned by a number of canonically independent variables (Gutzwiller, 1991). To render the notion of phase space clearer, we illustrate below the simple case of the one dimensional harmonic oscillator. This physical system is described by the following energy conservation relation:

$$E = \frac{m\omega^2}{2} x^2 + \frac{p^2}{2m} \quad (8.1)$$

where x is the position coordinate, $p = m\dot{x}$ is the momentum coordinate, m is the mass of the oscillator, ω is the oscillation frequency and E is the energy of the oscillations. The variables that will span the phase space are x and p . If we represent the above equation in the system's phase space we get an ellipse. All the possible states of the system (harmonic oscillator) lie on that particular ellipse (see Fig.8.1). This configuration corresponds to a perfectly stable kind of motion.

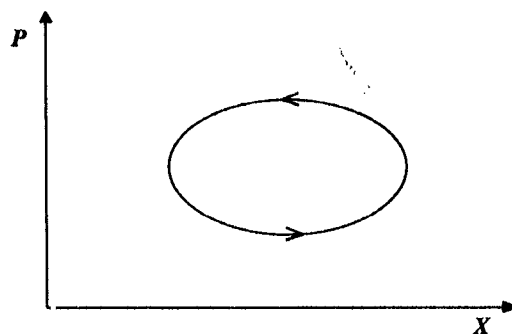


Fig.8.1 Phase-space configuration of the harmonic oscillator.

We can construct phase space configurations for any physical system. Such configurations are, for instance, in use in the study of instability and failure modes in geomaterials (Mroz, 1985). If we denote by u the displacement at a typical point of interest, then the plane (u, \dot{u}) (where \dot{u} is the rate of change in displacement) will

constitute the phase space of that particular material point. If consecutive points in the phase-space are joined, one arrives at a curve along which the dynamics of the process evolves with time. We have generated analytically three deformation modes which we present for illustration together with the corresponding stress-strain diagrams, respectively. The first case is a "stable mode" deformation where the displacement varies according to the equation:

$$u(t) = \frac{t^2}{t^2 + 1} \cdot \sin(3t) \quad (8.2)$$

where t is the time. The resulting phase space (u, \dot{u}) is a curve which tends towards a limiting cycle as shown in Fig.8.2.a. The corresponding strain-stress diagram can be derived according to the following discussion: strain (ϵ) is proportional to u while stress (σ) is proportional to the applied force which in turn is proportional to \ddot{u} , \ddot{u} being the acceleration of the point of interest. We show in Fig.8.2.A the strain-stress diagram that corresponds to this stable deformation mode.

In the case of a cyclic unstable mode of deformation that can be modelled with the formula:

$$u(t) = t^2 \sin(9t), \quad (8.3)$$

the corresponding phase space consists of a spiral that diverges as time increases. This is illustrated in Fig.8.2.b. In Fig.8.2.B we display the strain-stress diagram that corresponds to this type of deformation.

Finally, we consider the burst which can be described by:

$$u(t) = \frac{(t^7 + t)}{10} \quad (8.4)$$

which leads to an almost sudden increase with time. The phase space diagram is a monotonous curve that diverges as time increases. The strain-stress diagram however indicates a very sharp drop in the stress as soon as the softening regime is entered. Fig.8.2.c and Fig.8.2C show these features.

From the analysis of the above deformation modes we notice that the first situation is the most stable while the burst is least stable. The conclusion is that the more phase space a trajectory can explore within a certain time, the more unstable the corresponding deformation is.

The dimension of the phase space is determined by the number of degrees of freedom. If x_1, x_2, \dots, x_n and p_1, p_2, \dots, p_n are the canonical parameters that fully describe the dynamics of the system under study,

then the dimension of the phase space is $2N$. As time evolves, the state of the system moves along a trajectory in the phase space. States that happen to be on a closed boundary at a given time remain on a closed curve at any time in the future.

If two nearby trajectories tend to diverge exponentially from each other, that behaviour is termed "chaotic". The onset of chaos is in general a consequence of the nonlinear coupling (Radu, 1995; Heiss, 1995) that takes place between the canonical variables. Such a coupling is frequently seen in the differential equations that usually relate the canonical variables to each other. Rock mass response to mining is a complex process that qualifies as a good example. The coupling between a regular system and external forces is seen, for instance, when a rock cavity is subjected to the external stress of the surrounding rockmass. A number of quantitative measures have been introduced to quantify the degree of chaos in a given system. The most commonly used one is the "Lyapunov exponent" (Gutzwiller, 1991) which measures the average exponential divergence rate of nearby trajectories.

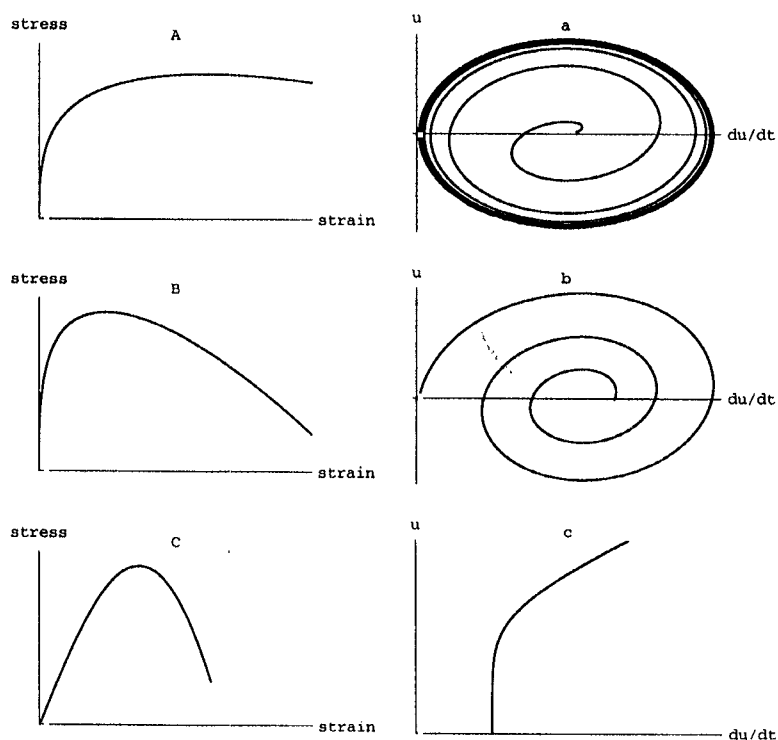


Fig.8.2 Trajectories in phase space for plastic deformations.

In conservative systems - where the total energy of the system remains constant - the volume of the phase space is constant. The "flow" of the trajectories winds around a toroidal shape which does

not deform in time (see Fig.8.3). With increasing chaotic behaviour the tori may break down and disintegrate, yet the volume of the phase space stays the same. A completely different situation is encountered in the case of dissipative systems which are kept far from thermodynamic equilibrium by mass and energy exchange with the environment. There, as the energy dissipates, the dynamics tends to vanish or reach a steady state.

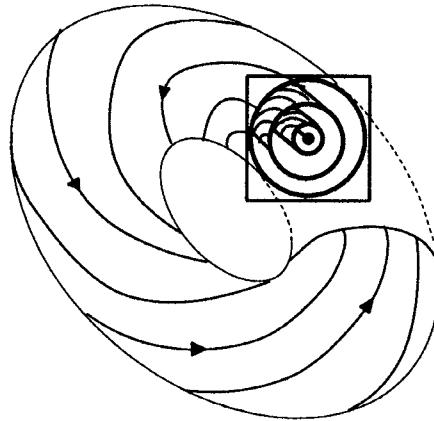


Fig.8.3 Invariant tori in the 3-dimensional surface of constant energy.

This is seen in the phase space as a continuous contraction of the volume. Moreover, the trajectories are gradually “attracted” to and “captured” by an attractor. An attractor is a submanifold of the phase space (e.g. a point, a closed curve, etc) towards which all the trajectories tend to settle. If the dissipative system is also chaotic, the attractor usually has a fractal dimension and is called “strange attractor”. In such a case, to study the dynamics of the system, it suffices to only investigate the attractor. Fig.8.4 illustrates the Lorenz attractor which is used in weather and climate studies. There, we clearly distinguish two limit cycles (the attractor itself) surrounded by basins of attractions. A basin of attraction is the neighbourhood surrounding the attractor within which any trajectory will eventually “sink”. In general, dissipative systems need not contract all volumes in the phase space, some sets may expand their volume with time, but such submanifolds do not contain attractors.

Making predictions about the physical parameters of the system under study amounts to estimating the evolution of the states in the corresponding phase space. As the seismic flow of rock is “par excellence” dissipative, we will need to identify and investigate the relevant attractors that may be encountered in the phase space. Recall that the complexity of a real system is measured by the dimension of the attractor describing its asymptotic motion. Using nonlinear techniques the basin of each attractor can be divided into subsets of

given levels of predictability (e.g. low, moderate, high, etc). The ultimate aim is to map present states of the system into the future, based on knowledge about the time history of the system. Depending on the local level of predictability on the attractor - which in fact results from the computation of Lyapunov exponents - one can evaluate prediction functions that will interpolate into the future various seismic parameters such as apparent volume, energy index, seismic viscosity, etc. Although the technique does not lead to exact solutions, it can supply good estimates.

8.2 Reconstruction of the Phase Space From Seismic Data

In the chapter entitled Quantitative Seismology and Rock Mass Stability, a number of seismic parameters which quantify rock mass stability, such as seismic moment, seismic energy, energy index, were introduced. To completely reveal the dynamics behind rock mass instability, the phase space needs to be constructed. Although the seismic parameters should be considered as phase variables, it is not known whether they are all independent and canonical. Moreover, their number may also be smaller than the minimum number of independent physical variables that "fully" span the phase space. A solution to this apparent inconvenience is to avoid the direct study of the physical phase space. Instead, an analogous space is being introduced - the embedded phase space. The embedded phase space aims at reconstructing the original phase space - which, for some reason, is not possible to construct directly. If a, b, c, d, \dots are the parameters that completely describe the dynamics of the system and their time series are known, one would be able to construct the "real" phase space. However, since the parameters a, b, c, d, \dots are related to each other by "the same dynamics", a theorem by Takens (1984) ensures that it is sufficient to use only one physical variable to "simulate" the actual phase space. The method that achieves this is called "embedding". An attractor that exists in the "real" phase space will be seen in the "embedded" phase space as well. The difference between the two attractors, "real" and "embedded", can be recovered by smooth transformations. This means that a thorough knowledge about the "embedded" attractor is equivalent with understanding the behaviour of the trajectories on the "real" attractor.

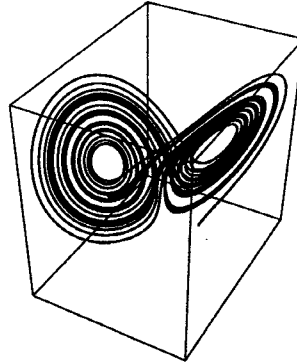


Fig.8.4 Illustration of the Lorenz attractor.

In the embedding of the phase space a given physical parameter is chosen, such as the seismic moment, M . The time series of the seismic moment is denoted by M_i . The “embedded” phase space is then constructed by using as orthogonal axes the vectors $(M_i, M_{i+D}, M_{i+2D}, \dots, M_{i+(d-1)D})$, where d is the dimension of the “embedded” phase space and D is the so-called delay lag. Notice that since the attractor is a submanifold of the “real” phase space, it is not necessary to use a value of d equal to the dimension of the “real” phase space. However, d should be sufficiently large to embed the attractor that needs to be studied. The delay D is chosen as the first zero of the linear autocorrelation function (Abarbanel, 1990) defined by:

$$C(m) = \frac{\sum_{i=1}^{N-m} (M_i - \bar{M})(M_{i+m} - \bar{M})}{\sum_{i=1}^N (M_i - \bar{M})^2} \quad (8.5)$$

where:

$$\bar{M} = \frac{1}{N} \cdot \sum_{i=1}^N M_i$$

In Fig.8.5 a cut (Poincaré map) through the embedded phase space of $\log M$, using data from the mine PIPILLAR (President Brand Mine), is shown. The appearance of an attractor, with its basin of attraction (lower density of points), can be clearly discerned.

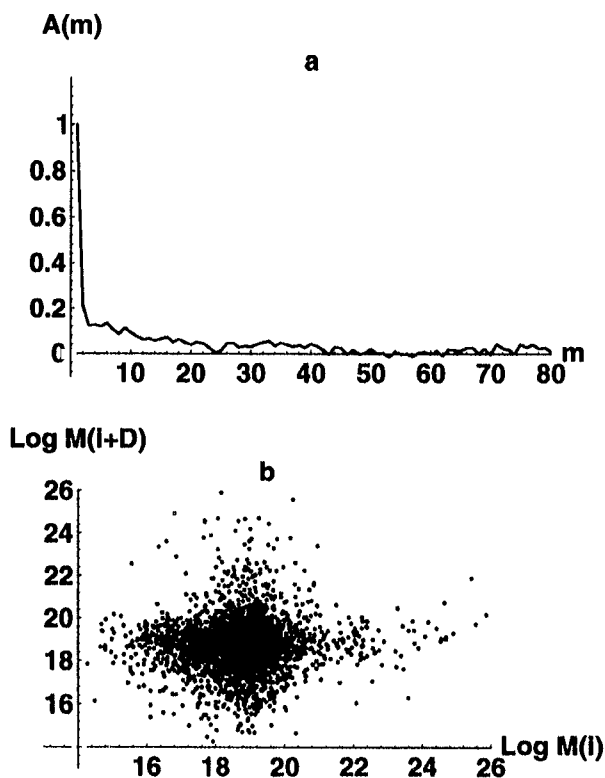


Fig.8.5 (a) Autocorrelation function of the logM and (b) Poincaré map of the logM attractor as at PIPILLAR area.

8.3 Fractal Correlation Dimension

As already mentioned, the dynamics of chaotic systems that are dissipative exhibits “strange” attractors, i.e. attractors whose dimensions are fractal. There are various methods that are used to calculate the dimension of an attractor. In seismological studies, the most popular one calculates the correlation integral (Eneva, 1996) which is defined as:

$$C(r) = \frac{2}{(N-D+1)(N-D)} \cdot \sum_{ij} \Theta(r - \|\mathbf{r}_i - \mathbf{r}_j\|) \quad (8.6)$$

where $\Theta(x)$ is the Heaviside function, i.e. $\Theta(x) = 1$ if $x > 0$ and $\Theta(x) = 0$ otherwise. \mathbf{r}_i and \mathbf{r}_j are the physical coordinates of any two points of a discrete version of the attractor and $\|\mathbf{r}_i - \mathbf{r}_j\|$ is the distance between the points i and j , given by the equation:

$$\|\mathbf{r}_i - \mathbf{r}_j\| = \sqrt{\sum_{k=1}^d (r_{i+(k-1)D} - r_{j+(k-1)D})^2} \quad (8.7)$$

where D is the lag (delay) corresponding to the parameter r and d is the embedding dimension. The parameter r can be, for instance, location (x, y, z) , $\log E$, $\log M$, time between consecutive events, etc.

In the case of a fractal, the correlation integral scales as:

$$C(r) \propto r^{d_a} \quad (8.8)$$

where d_a is the dimension of the fractal. For a given embedding dimension d , the fractal correlation dimension can be estimated as the slope of the linear portion of the plot $\log C(r)$ vs $\log r$, which generically looks like in Fig.8.6. As r increases, $C(r)$ reaches its maximum value (i.e. 1) as the distances $\|\mathbf{r}_i - \mathbf{r}_j\|$ can never be larger than some r_{max} .

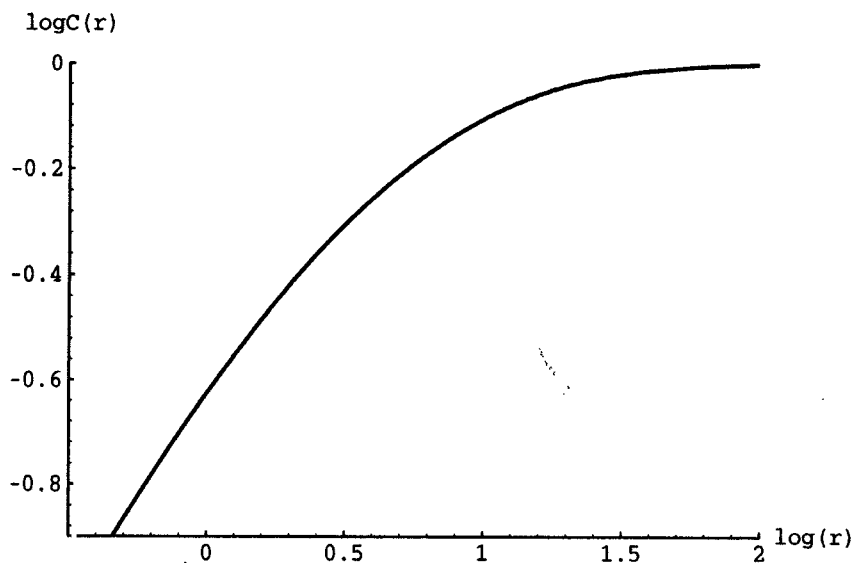


Fig.8.6 Generic plot of $\log C(r)$ vs $\log r$. The slope of the linear portion represents the correlation dimension.

Finally, plotting d_a vs d , one may establish the minimum embedding dimension which “fully” embeds the attractor. This is very important as an improper embedding of the attractor may lead to severe errors when estimates about the future behaviour of a physical parameter of interest are made. Generically, the plot d_a vs d looks like in Fig.8.7.

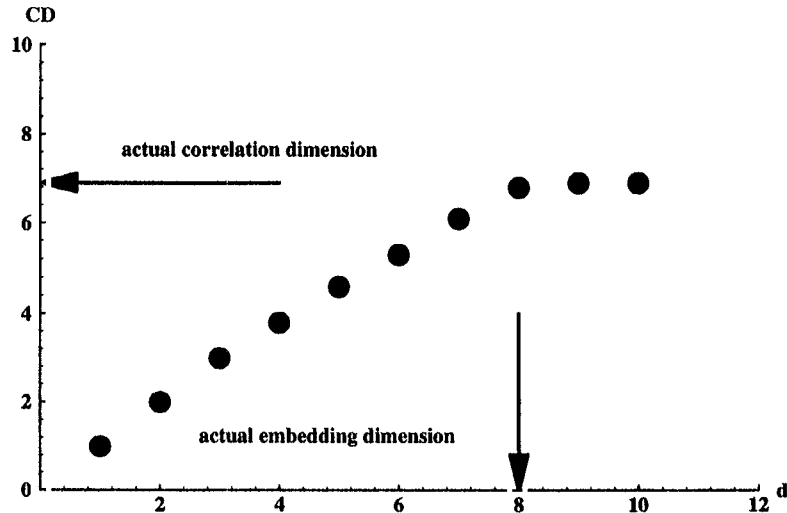


Fig.8.7 Generic plot of correlation dimension vs embedding dimension. The flattening point of the plot determines the dimension (d_{min}) of the reconstructed phase space and the dimension d_u of the attractor.

When d reaches a certain value d_{min} , the fractal correlation dimension d_u no longer increases. At that point (d_{min}) a number of results are established: the fractal dimension of the attractor is the value of d_u corresponding to d_{min} . Moreover, if d_u is fractional, there is chaos in the system, as strange attractors - attractors of fractal dimension - can be exhibited by chaotic systems only. Finally, the value d_{min} denotes the “proper” embedding dimension necessary to reconstruct the phase space and to make accurate estimates of physical parameters of interest.

8.4 Numerical Results

Clusters of seismic events from the mines Western Holdings Postma (WHPST), P1PILLAR and President Brand 2-East (PB2EAST) have been investigated in connection with possible chaotic behaviour. In Table 8.1, below, we summarise the main features of these areas.

Table 8.1 Features of interest in the investigated areas.

	Area: WHPST	Area: P1PILLAR	Area: PB2EAST
Parameter	Delay lag	Delay lag	Delay lag
log(Moment)	171	43	9

log(Energy)	171	43	9
x location	26	23	22
y location	47	12	25
z location	72	8	32
s_e	25	20	22
s_{ph}	25	20	22
Δt	136	31	11

A few comments are in order at this stage. First of all, as mentioned in the previous chapter, we distinguish between two kinds of distance between seismic events: the distance between the spatial location of the events (s_e) and the distance between the events taking into account the source size (s_{ph}). The relation between the two distances is:

$$s_{ph} = s_e + r_i + r_j \quad (8.9)$$

where r_i and r_j are the radii of the apparent volumes of the events “ i ” and “ j ” respectively. From the results shown above, it appears that the number of linearly dependent events is the same whether s_{ph} or s_e is used as input for the autocorrelation function. However, the spatial correlation range is always longer in the case when s_{ph} is used. Finally, the fact that $\log E$ and $\log M$ give rise to the same number of linearly dependent events enhances the assumption that there is a simple relation connecting the two physical parameters.

The results of the analysis of fractal correlation dimension are presented in terms of plots of fractal correlation dimension d_a vs embedding dimension d . The value of d where such a plot flattens is denoted as the embedding dimension d_{min} corresponding to the parameter under study. The fractal dimension of the respective parameter is interrelated to d_{min} . In Fig.8.8a-h, WHPOST, Fig.8.9a-h, P1PILLAR and Fig.8.10a-h, PB2EAST show such plots for the three areas under study.

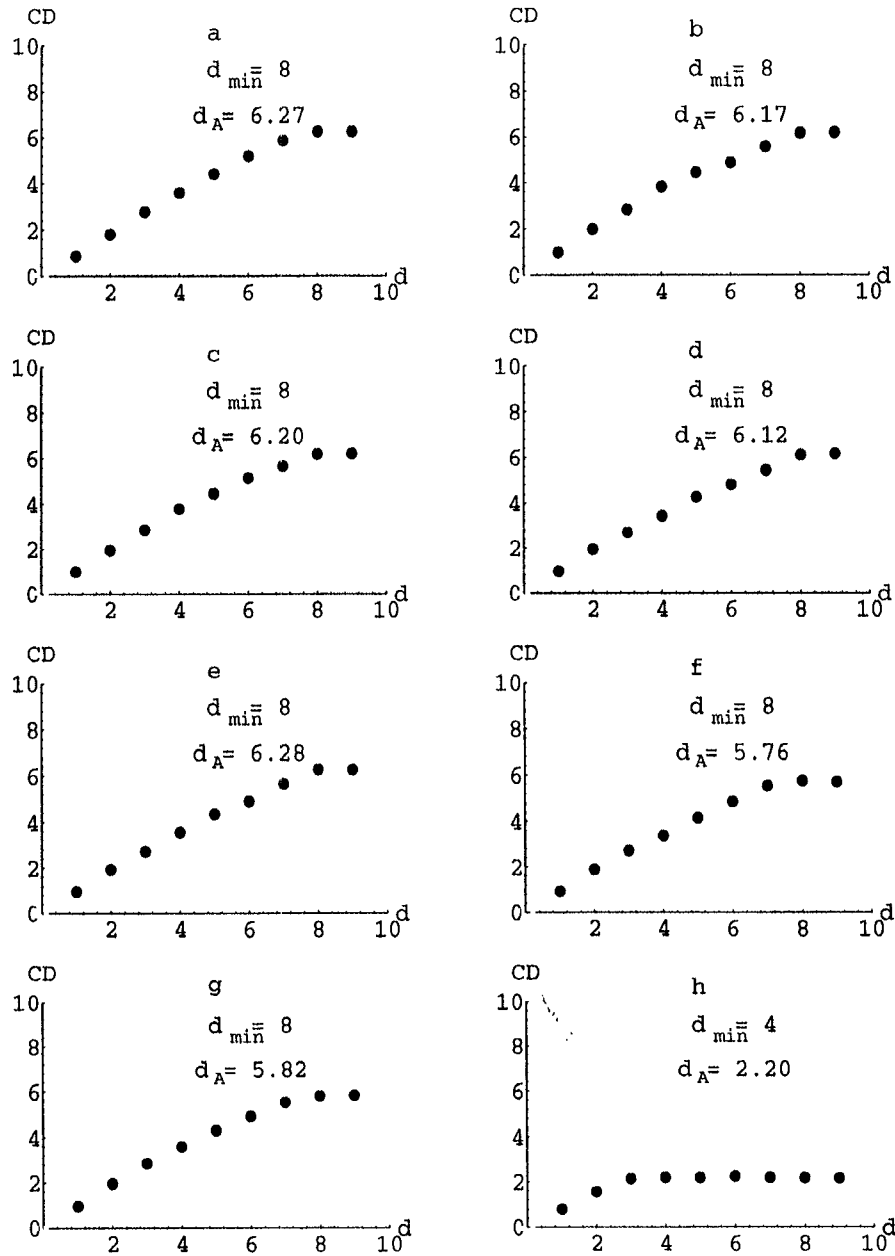


Fig. 8.8 Correlation dimension analysis for the area WHPOST, where:
 a. $\log E$
 b. $\log M$
 c. x location
 d. y location
 e. z location
 f. distance between locations of consecutive events
 g. distance between locations of consecutive events including the source size
 h. time between consecutive events

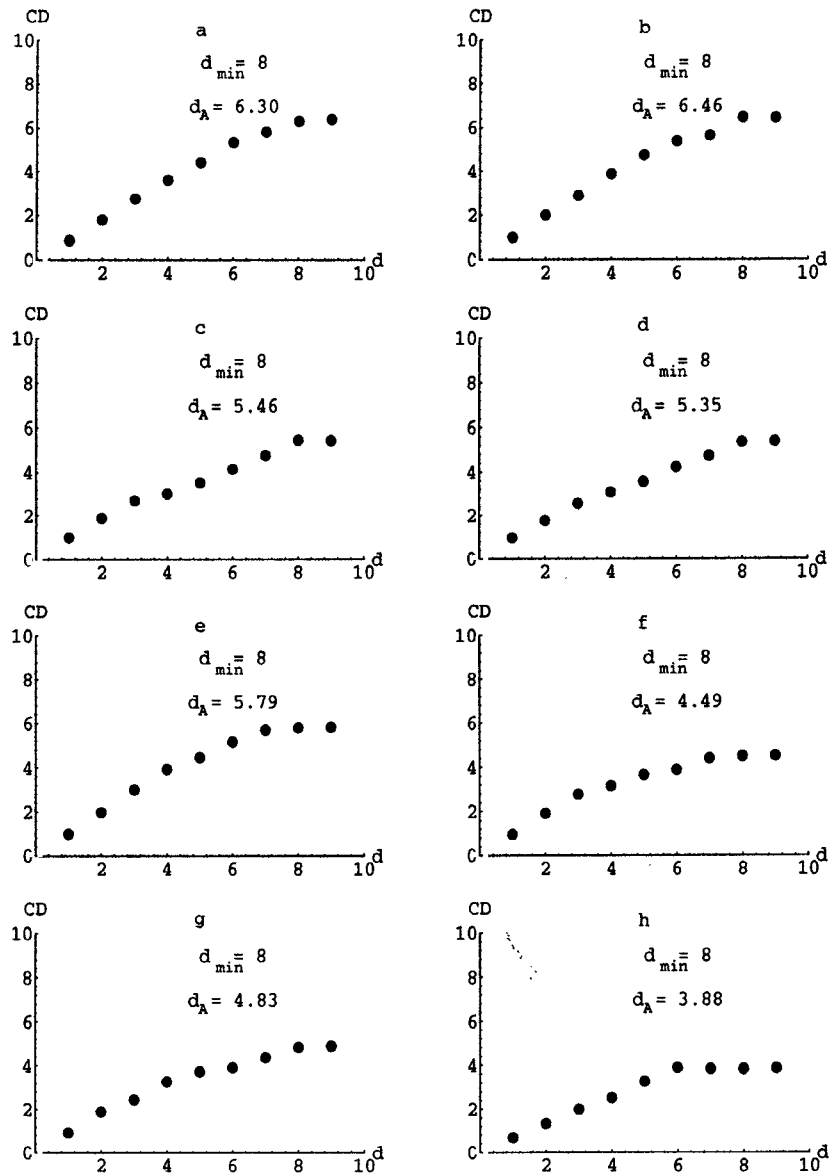


Fig. 8.9 Correlation dimension analysis for the area P1PILLAR where:
a. $\log E$
b. $\log M$
c. x location
d. y location
e. z location
f. distance between locations of consecutive events
g. distance between locations of consecutive events including the source size
h. time between consecutive events

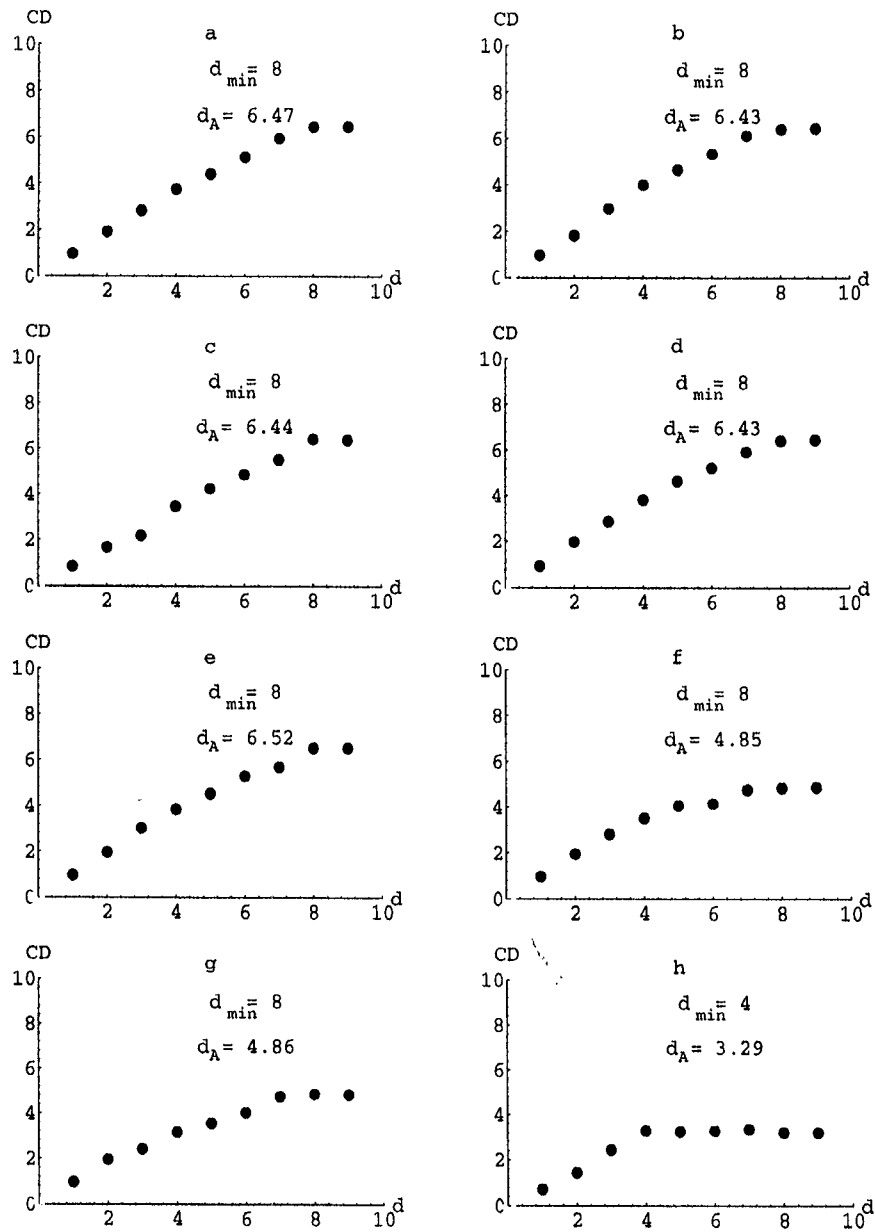


Fig. 8.10 Correlation dimension analysis for the area PB2EAST, where:
 a. $\log E$
 b. $\log M$
 c. x location
 d. y location
 e. z location
 f. distance between locations of consecutive events
 g. distance between locations of consecutive events including the source size
 h. time between consecutive events

8.5 Lyapunov Exponent and Limits of Predictability

The phase space of a chaotic system contains regions of stochasticity where a description of the motion in terms of analytic formulae is not possible. The alternative to such a situation is to treat the motion in a more statistical sense. Instead of calculating individual orbits, one may seek to determine the evolution of certain average quantities that describe the degree of disorder. There are various ways to describe the motion in a stochastic region using terms like ergodicity, mixing, K-systems, Lyapunov exponents, etc.

We seek to evaluate the chaotic behaviour of time series of seismic parameters by calculating Lyapunov exponents. Lyapunov exponents are a computable measure of the chaotic behaviour of a trajectory and express the mean exponential rate of divergence of trajectories surrounding it.

Let us assume that we have managed to reconstruct the phase space of a seismic parameter by embedding its times series. We denote by P the dimension of such a phase space. Next, we consider a trajectory in this P -dimensional phase space and a nearby trajectory with initial conditions \mathbf{x}_0 and $\mathbf{x}_0 + \Delta\mathbf{x}_0$ respectively. These trajectories evolve with time, yielding the tangent vector $\Delta\mathbf{x}(\mathbf{x}_0, t)$ having the Euclidian norm $d(\mathbf{x}_0, t) = \|\Delta\mathbf{x}(\mathbf{x}_0, t)\|$.

The time evolution for $\Delta\mathbf{x}$ in the case of time series can be found using the Wolf algorithm (Wolf, 1985). Finally, we introduce the mean exponential rate of divergence of two initially close trajectories:

$$Ly(\mathbf{x}_0, \Delta\mathbf{x}) = \lim_{t \rightarrow \infty} \frac{1}{t} \log_2 \frac{d(\mathbf{x}_0, t)}{d(\mathbf{x}_0, 0)} \quad (8.10)$$

$d(\mathbf{x}_0, 0) \rightarrow 0$

It can be shown that Ly exists and is finite (Liebermann and Liechenberg, 1988). Furthermore, there is a P -dimensional basis of $\Delta\mathbf{x}$, such that for any $\Delta\mathbf{x}$, Ly takes on one of the P values Ly_i which are the Lyapunov characteristic exponents. Moreover, the Lyapunov exponents are independent of the choice of metric for the phase space. These exponents are all zero for integrable systems (no divergence of trajectories) and at least one is finite for chaotic systems (divergence of trajectories) and indicates how unpredictable and incomputable a time series is. In the case of finite time series, as it is the case in practical applications, formula (8.13) can only be applied for the range of time one has taken the measurements over. This leads us to define the so-called "local Lyapunov exponent" (LLE).

$$LLE = Ly(\mathbf{x}_0, \Delta\mathbf{x}) = \lim_{d(\mathbf{x}_0, 0) \rightarrow 0} \frac{1}{t} \log_2 \frac{d(\mathbf{x}_0, t)}{d(\mathbf{x}_0, 0)} \quad (8.11)$$

The LLE can now be used to quantify the minimum predictability limit. With the aid of the Wolf algorithm we can determine for a time series the maximum local Lyapunov exponent (LLE_{max}) out of all LLE s that characterise the chaotic behaviour in the respective P-dimensional phase space. LLE_{max} represents the maximum amount of information lost by the time series during two consecutive event occurrences. The amount of information is quantified by the lag D corresponding to the respective parameter: the last event in the time series has a linear information link up to the next D events in the future. However, this amount reduces to $D-LLE_{max}$ after the first event in the future will occur, then to $D-2LLE_{max}$ after the second event will occur, etc. If n is the number of events in the future after which $D-nLLE_{max}$ becomes zero, we denote n as the maximum number of events that we can predict based on the “present” knowledge of our time series. This number is given by:

$$n = \text{Int} \left[\frac{D}{LLE_{max}} \right] \quad (8.12)$$

where $\text{Int}[q]$ represents the integer part of the quantity q .

The temporal limit of predictability can now be constructed in the following manner. Let t_1 be the time elapsed from the occurrence of event 1 to event n in the time series, t_2 be time that passed between event 2 and event $n+1$, ..., and t_{N-n+1} be the time consumed between event $N-n-1$ and N . The averaging over t_1, t_2, \dots, t_n has a result the correlation time of the time series (t_c) under study, according to the parameter that yielded the Lyapunov exponent LLE_{max} :

$$t_c(n) = \frac{\sum_{i=1}^{N-n+1} t_i}{N-n+1} \quad (8.13)$$

The expression (8.18) represents the minimum limit of predictability of the parameter analysed.

The Lyapunov exponents and corresponding limits of predictability calculated for various seismic parameters at P1PILLAR and PB2EAST areas are illustrated in Table 8.2.

The value of the Lyapunov exponent does not depend on the sensitivity by which an area is monitored, as such quantities (Lyapunov exponents) are invariants of the dynamics underlying the time series under study. In this regard, we have performed tests in which we filtered the time series of different parameters at a given

area in terms of magnitude. While the Lyapunov exponent stayed the same at all levels of magnitude where we could perform the embedding analysis, the predictability limit increased with lower magnitude, as shown in Table 8.3. This indicates that larger sensitivity leads to larger limit of predictability for seismic parameters. Hence, we stress that nonlinear dynamics techniques are applicable only to areas with increased sensitivity.

Table 8.2 Limits of predictability

Parameter	Area: WHPOST		Area: P1PILLAR		Area: PB2EAST	
	LLE_{max}	Min. limit of predictability	LLE_{max}	Min. limit of predictability	LLE_{max}	Min. limit of predictability
log(Moment)	1.03	24.9 days	1.13	22.2 hrs	1.02	8.3 Hrs
log(Energy)	1.00	25.6 days	1.12	22.2 hrs	0.97	8.3 Hrs
x location	1.14	3.1 days	1.21	11.3 hrs	1.05	20.8 Hrs
y location	1.09	6.7 days	1.07	6.5 hrs	1.03	23.0 Hrs
z location	1.20	9.3 days	1.07	13.6 hrs	0.88	1.43 days
Distance between locations of consecutive events	1.21	2.8 days	1.45	8.3 hrs	1.22	17.2 Hrs
Distance between locations of consecutive events including source size	1.21	2.8 days	1.43	8.3 hrs	1.30	16.3 Hrs
Time between consecutive events	2.67	7.9 days	3.51	5.4 hrs	2.87	3.8 Hrs
Average minimum limit of predictability:		10.3 days		12.3 hrs		16.5 Hrs

LLE_{max} - Maximum Lyapunov Exponent

Table 8.3 PIPILLAR area limits of predictability for various sensitivities.

Area: PIPILLAR

Period of Monitoring: 30 September 1995 to 29 December 1995.

Parameter: log(Moment)

Minimum recorded magnitude	Minimum limit of predictability
-2.3	22.26 hours
-1.6	16.70 hours
-1.3	12.05 hours
-1.0	8.45 hours

To summarise, we stress that a most important result is that the dynamics of the systems analysed appears to be 8-dimensional. It may be speculated that the underlying physics of seismic rock mass response to mining is 8-dimensional. The remaining problem is to further identify the 8 physical parameters that give rise to this dynamics. The systems studied all exhibit the phenomenon of chaos because of the following reasons:

- a) The existence of attractors has been established.
- b) The dimensionality of the attractors is always fractal.

The occurrence of chaos supports the view which assumes the turbulent nature of the seismic rock mass response to mining (Kagan, 1992; Mendecki, 1995). In terms of considering the apparent volume in calculating the distance between events, notice that, although the number of linearly dependent events does not depend on whether one uses s_e or s_{ph} , it appears that the fractal dimension of the attractor of the distance between events is underestimated if the apparent volume is not taken into account. This is more clearly seen when the number of events is larger, as at PIPILLAR. Analysis indicates that the variables x, y, z locations, $\log E$, $\log M$, s_e and s_{ph} are all true reflections of the same underlying physical process which appears to be 8-dimensional. At this stage, we cannot determine the actual eight canonically independent variables which constitute the axes of the phase space. This did not however hinder us in any way in determining the limits of predictability.

These limits have been determined on the basis of the Lyapunov exponent, an invariant of dynamics which quantifies in a statistical way the amount of the existent chaos. It turned out that the limits of predictability are always finite and manageable, ranging from a few

hours to about three weeks. It has also been shown that an increase in the predictability limit can be achieved if the monitoring sensitivity at a given area is increased. One can now attempt to estimate the values of the seismic parameters of interest within their limits of predictability. Work in this regard is in progress.

CHAPTER 9

QUANTITATIVE SEISMOLOGY AND ROCK MASS STABILITY

9.1 SEISMIC MOMENT, SOURCE SIZE AND STRESS DROP

The most general description of the processes at the seismic source V is by the distribution of forces or moments equivalent to the inelastic deformation. One can describe the inelastic processes at the source as the stress-free change of size and shape of an elastic body without alteration of the elastic properties of the region (Bachus, Mulcahy 1976a,b). If change in size and shape can be expressed as a change in strain $\Delta\epsilon_{kl}$, then the equivalent stress change (or change in moment per unit volume) can be given by

$$m_{ij} = c_{ijkl} \Delta\epsilon_{kl} = \Delta\sigma_{ij}, \quad (9.1)$$

where c_{ijkl} are elastic constants and m_{ij} is called the seismic moment density tensor or inelastic stress or stress glut $\Delta\sigma_{ij}$. Therefore, the stress glut represents the internal stress necessary to cancel the strain produced by the internal inelastic process, that is; to restore the source to its original shape and size (see Fig.9.1).

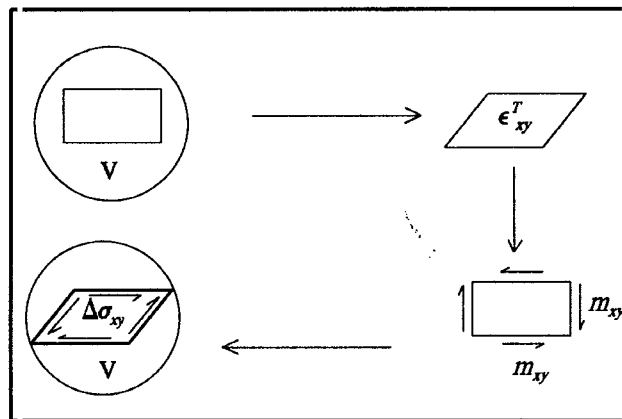


Figure 9.1. The concept of inelastic stress or stress glut. The rectangular element in the unstressed configuration (top left) undergoes a spontaneous change in strain. If it were not surrounded by the rest of the body, it would take the deformed shape shown on the top right. The seismic moment, inelastic stress, or stress glut is the stress that is needed to bring it back to its initial rectangular shape (bottom right). Finally, if the element is reinserted into the unstressed body and the stresses are allowed to readjust a final state of stress is obtained. This is the stress change (stress drop or increase) created by the inelastic strain ϵ^T (after Madariaga 1983).

The stress glut is not exactly the stress drop — the difference between the initial equilibrium stress and the final equilibrium stress. The stress drop is not limited to the source volume but stress glut $\Delta\sigma_{ij}$ vanishes outside V .

The total moment integrated over the source volume is the seismic moment tensor. For long waves compared to the source size, the whole volume V can be considered to be a system of couples located at, say, the centre of V , and the moment tensor components are

$$M_{ij} = \int_V c_{ijkl} \Delta\epsilon_{kl} dV = \int_V \Delta\sigma_{ij} dV. \quad (9.2)$$

The moment tensor measures the inelastic deformation at the source during the seismic event and its value at the end of the source process measures the permanent inelastic strain produced by the event.

If one interprets the source volume V as the region with the largest inelastic shear strain drop $\Delta\epsilon$ (of the order of stress drop $\Delta\sigma$ over rigidity G), the seismic moment may then be defined as the product of the estimated stress glut (drop) and source volume (Madariaga, 1979)

$$M = G \Delta\epsilon V = \Delta\sigma V \rightarrow V = \frac{M}{\Delta\sigma}, \quad (9.3)$$

and stress glut (drop), $\Delta\sigma = M/V$, is then defined as a spatial density of the seismic moment.

The seismic moment of the idealised planar source is usually defined

$$M = G\bar{u}A \quad (9.4)$$

where \bar{u} is an average displacement (slip) over the source area A .

Seismic moment tensor can be decomposed into isotropic (volume change) and deviatoric components M_V and M_D providing an additional insight into the nature of coseismic strain drop

$$M = M_V + M_D \quad (9.5)$$

The eigenvalues and corresponding eigenvectors of M_D describe the magnitude and orientation, respectively, of the principal moment axes (neglecting gravity) acting at the source. These principal moment axes are uniquely determined by moment tensor inversion. Principal moment orientation data can provide sufficient information to find the best stress tensor (Michael, 1987).

A simple shear dislocation source can have nonzero isotropic

components if the source surface is irregular or imbedded in an anisotropic material (Backus and Mulcahy, 1976b.)

The deviatoric component is usually decomposed into a double-couple (DC), describing the shear component of the seismic source, and into a compensated linear vector dipole (CLVD)

$$M_D = M_{DC} + M_{CLVD} \quad (9.6)$$

This decomposition however is non-unique. The name CLVD is not very fortunate either since the DC component itself is also equivalent to two linear vector dipoles aligned to the principal axes.

The possible physical realizations of the CLVD are:

- a sudden change of shear modulus in the presence of an axial strain, from which the effect of volume change is removed (Knopoff and Randall, 1970)
- tensile failure of rock in the presence of high pressure fluids (Julian and Sypkin, 1985)
- complexity of the seismic source (Fröhlich *et al.*, 1989).

Figures 9.2 and 9.3 show results of moment tensor inversions for two seismic events associated with two underground prefracturing blasts:

blast 1: 6 boreholes approximately 16m long, 25kg of emulsion per hole, delayed initiation

blast 2: 2 boreholes each 23m long, 125kg of emulsion per hole, simultaneous initiation.

In both cases seismic events of almost identical scalar seismic moment have been recorded by a number of 3 component digital seismic stations. Seismic moment tensor inversion and its decomposition however show a considerable difference in the nature of the co-seismic strain drop:

	M_V	M_{DC}	M_{CLVD}	$V=M/\Delta\sigma$
event 1:	-0.02	0.36	0.39	$2.4 \cdot 10^5 \text{ m}^3$
event 2:	-0.14	0.53	0.28	$0.8 \cdot 10^5 \text{ m}^3$

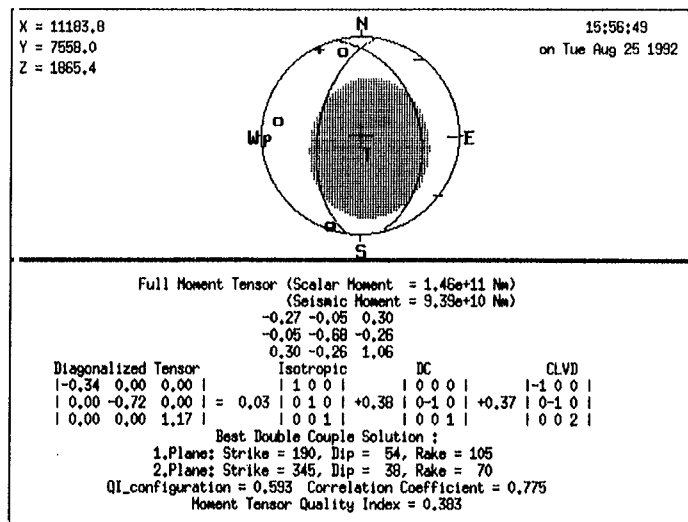


Figure 9.2. Results of the moment tensor inversion and the decomposition of the seismic event associated with blasts No.1: 6 boreholes approximately 16m long, 25kg of emulsion per hole, delayed initiation. Static stress drop estimated from 9 three-component seismic stations, $\Delta\sigma = 2.82 \text{ E5 Pa}$

Amplitudes of recorded ground motions, Fig.9.4, confirm that the larger the non-double couple component, the slower (or sweeter - Fröhlich, 1993) is the event and the weaker the ground motions (McGarr, 1993). Although 100kg less explosives were used, blast 1 should be considered more successful than blast 2 since it induced an inelastic deformation in a softer manner and over a larger volume.

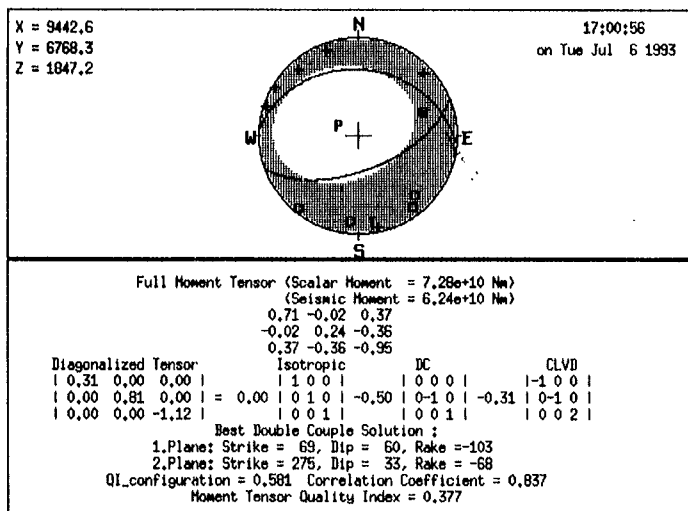


Figure 9.3. Results of the moment tensor inversion and the decomposition of the seismic event associated with blast No.2: 2 boreholes each 23m long, 125kg of emulsion per hole, simultaneous initiation. Static stress drop estimated from 12 three-component seismic stations, $\Delta\sigma = 1.41 \text{ E6 Pa}$

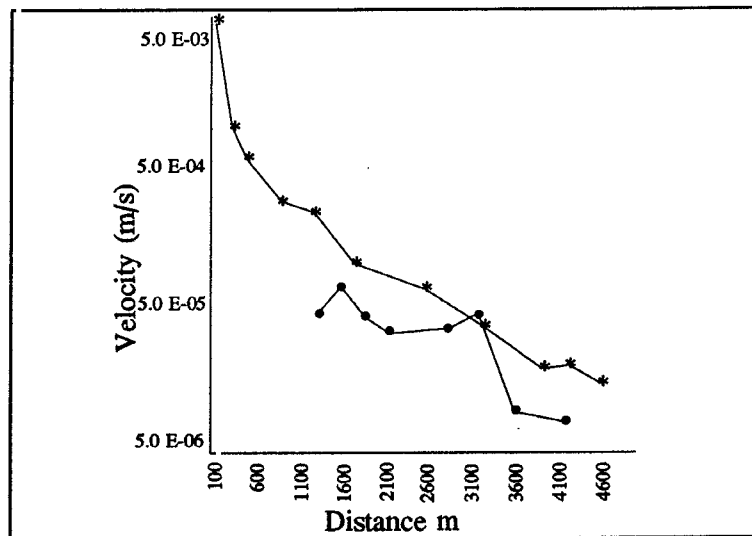


Figure 8.4. Amplitudes of recorded ground motions versus distance for two seismic events associated with underground blasts.

- blast 1: 6 boreholes approximately 16m long, 25kg of emulsion per hole, delayed initiation
- * blast 2: 2 boreholes each 23m long, 125kg of emulsion per hole, simultaneous initiation.

One can show that the seismic moment M is proportional to the integral of the far-field displacement pulse of the seismic radiation. This property is frequently used to determine seismic moment from body wave observations in the time or in the frequency domain.

Since radiation from a seismic source is of finite duration Δt_{cs} , the spectrum of the far-field displacement has a finite width $\Delta \omega$, where $\Delta t_{cs} \cdot \Delta \omega \approx \pi$ and $\omega = 2\pi f$. Seismologists estimate the spectral width from the intersection of a constant low-frequency trend and a high-frequency asymptote of the attenuation corrected spectrum and call this intersection the corner frequency f_o , see Fig.9.5. The source dimension r and stress drop $\Delta \sigma$ relate to the corner frequency as follows

$$r = c_1 f_o^{-1} \quad (9.7)$$

$$\Delta \sigma = c_2 M f_o^3, \quad c_1, c_2 \text{ constants} \quad (9.8)$$

Fig.9.5 presents a model of instrument and attenuation corrected far-field S-wave acceleration, velocity and displacement spectra of a seismic event of moment-magnitude $m_M = 0.5$.

Estimation of stress drop from waveforms is a strongly model dependant technique but it may provide reasonable estimates and a fair comparison between different sources from the same region recorded

by the same seismic system.

Seismic moments of events recorded at distances close to the source can be grossly overestimated when calculated using far field point source models.

Heterogeneities within the rock mass produce complexity of the radiated pulse shapes. It was found (*e.g.* Madariaga, 1979) that for multiple or complex sources the seismic moment is smaller than for simple planar sources of the same area and stress drop. A simple interpretation of this result is that the unbroken sections of the source reduces overall distortion at the source region reducing seismic moment. The stress drop of these complex events, estimated by the usual circular source formula are only a fraction of the actual stress drop on the broken section of the source. The actual and estimated stress drops are in the ratio of the total source size to the size of a typical subevent.

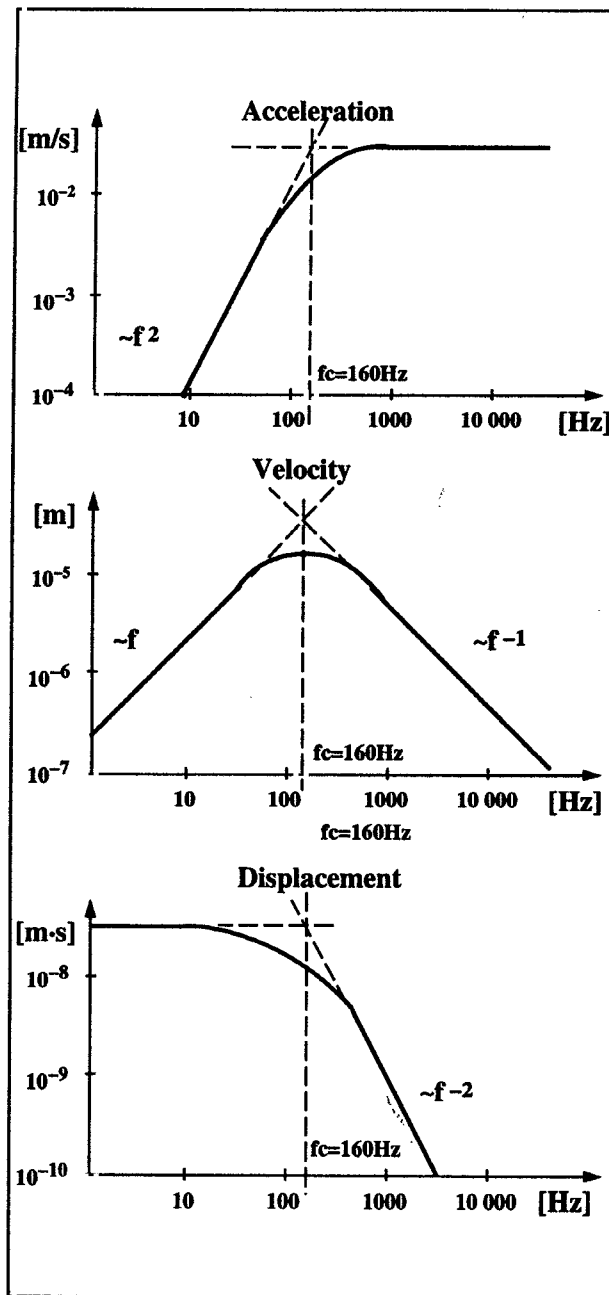


Figure 9.5 Models of instrument and attenuation corrected far-field S-wave acceleration, velocity and displacement spectra of a seismic event of moment-magnitude $m_M = 0.5$, where: S-wave velocity = 3500 m/s, rock density = 2700 kg/m³, distance = 100 m, seismic moment = 7.10^9 Nm , $m_M = 2/3 \log M - 6.1 = 0.5$, f_1, f_2 - bandwidth of the seismic system

9.2 SEISMIC ENERGY

The energy release during fracture and frictional sliding is due to the transformation of elastic strain into inelastic strain. This transformation may occur at different rates ranging from slow creep-like events to very fast dynamic seismic events with an average velocity of deformation at the source of up to a few metres per second. Slow type events have a long time duration at the source and thus radiate predominantly lower frequency waves, as opposed to dynamic sources of the same size. Since excitation of seismic energy can be represented in terms of temporal derivatives of the source function one may infer that a slower source process implies less seismic radiation. In terms of fracture mechanics, the slower the rupture velocity, the less energy is radiated; the quasi-static rupture would radiate practically no energy.

To assess the physical sources of radiated energy let us consider the formula for seismic energy for the single fracture-type source, expressed in terms of source parameters (Kostrov, 1974; Rudnicki and Freund, 1981).

$$E = -2\gamma_{eff} A^{+1/2} \int_A (\sigma_{ij}^0 - \sigma_{ij}^1) u_i n_j dA + \int_0^{\Delta t_{cs}} dt \int_{A(t)} \dot{\sigma}_{ij} u_i n_j dA \quad (9.9)$$

where:

- γ_{eff} - effective surface energy that includes the total loss of mechanical energy, in particular inelastic work, and heat flow from the fracture edge (Irwin, 1948).
- A - fracture area with the displacement u_i
- $\sigma_{ij}^0 - \sigma_{ij}^1$ - the difference between the final (at the end of the event) and initial stress
- n_j - unit vector normal to the fracture plane
- Δt_{cs} - source duration
- $\dot{\sigma}_{ij}$ - traction rate.

From dimensional analysis it follows that the last two terms in (9.9) vary with the fracture area as $A^{3/2}$, whereas the fracture work, $2\gamma_{eff} A$, is proportional to A (Kostrov and Das, 1988). Thus, the relative contribution of the fracture work to seismic energy decreases with an increase in the size of the fracture. Consequently for sufficiently small fractures the first term may almost cancel the second term suppressing the acoustic emission so that "silent" fracture would occur.

The second term in equation (9.9) is determined by the static quantities - stress drop and final slip. The last term, containing the traction rate, strongly depends on how the fracture propagates and

correlates with slip. The faster the oscillations of stress the greater their contribution to the radiated energy due to the presence of the time derivative of stress. The energy due to radiation of high frequency waves during accelerating and decelerating rupture is called radiational friction. It usually occurs when the moving zone of slip pulse reaches regions of differing resistance to deformation. If traction rate and slip are uncorrelated the third term will vanish. There is ample evidence that real rupture propagates in a discontinuous fashion, controlled by the strength and distribution of barriers and asperities. It is unclear however what such incoherent rupture contributes to the total radiated energy.

The equation (9.9) shows that it is impossible to obtain an unambiguous expression for radiated energy only in terms of changes from the initial equilibrium state of the medium to the final equilibrium.

In the far-field the P and S-wave contributions to the total radiated-energy are proportional to the integral of the square of the P and S velocity spectrum. For a reasonable signal to noise ratio in the bandwidth of frequencies available on both sides of the corner frequency the determination of that integral from waveforms recorded by seismic networks is fairly objective.

The high frequency component of seismic radiation needs to be recorded by the seismic system if a meaningful insight into the stress regime at the source region is to be gained.

9.3 APPARENT STRESS AND ENERGY INDEX

Apparent strain is the ratio of seismic energy E over seismic moment M and when multiplied by rigidity G is called apparent stress σ_A , and recognised as a model independent measure of the dynamic stress release in the source region

$$\sigma_A = \xi \bar{\sigma} = G \frac{E}{M} = \frac{E}{\Delta \epsilon V}, \quad (9.10)$$

where ξ is so-called seismic efficiency and $\bar{\sigma}$ is average or effective stress which is equal to half the sum of the initial and final stress, before and after the event (Wyss and Brune, 1968, 1971); $\Delta \epsilon$ and V are the coseismic strain drop and the source volume respectively.

The apparent stress is proportional to the integral of the square of the velocity spectrum divided by the low-frequency asymptote to the displacement spectrum or, when the acceleration spectrum is considered, the apparent stress depends linearly on the product of the

corner frequency and the high-frequency asymptote to the acceleration spectrum, see Fig.9.5. It is then a far more reliable and model independent parameter describing an average stress release at the source than corner frequency cubed dependant static stress drop, see equation (9.8).

Although the seismic waveforms do not have direct information about the absolute stress (for a bit of hope in inferring absolute stress from seismic radiation see Spudich, 1992), but merely about the dynamic stress drop at the source, a number of seismological studies and numerous underground observations suggest that a reliable estimate of stress drop, or preferably the apparent stress, can be used as an indicator of the local level of stress. Gibowicz et al. (1990) consider apparent stress an independent parameter of stress release in the case when P and S wave contribution to the seismic energy is included. Mendecki (1993) showed an example where apparent stress associated with seismic events of magnitudes between 1.3 and 1.5 varies from 0.2 to 40 bars, being generally higher at greater depth and within less faulted rock. McGarr (1994) states that if seismic efficiency $\xi \leq 0.06$ – which is an average value deduced from laboratory stick-slip experiments – then measurements of apparent stress can be used to infer the absolute level of deviatoric stress at the hypocentre. In general, the apparent stress expresses the amount of radiated seismic energy per unit volume of inelastic coseismic deformation.

Let us imagine the source of a seismic event associated with a relatively weak geological feature or with a soft patch in the rock mass. Such a source will yield slowly under lower differential stress producing larger seismic moment and radiating less seismic energy - low apparent stress event. The opposite applies to a source associated with a strong geological feature or hard patch in the rock mass - high apparent stress event.

In the case of a so-called complex event or multiple events, the rapid deformation process at the initial source can push the stresses in the adjacent volume to a level much higher than could normally be maintained by the rock, producing higher apparent stress sub-event(s) that need not be an indication of a generally high ambient stress prior to the event. Although the estimate of apparent stress does not depend on the rupture complexity (Hanks and Thatcher, 1972), the complexity of the event should be tested before meaningful interpretation in terms of stress can be given.

Since radiated seismic energy broadly increases with increasing moment, to gain insight into the stress regime one would need to compare the radiated seismic energies associated with seismic events of a similar seismic moment (or moment-magnitude).

Fig.9.6 shows the apparent stress associated with seismic events of

similar moment-magnitude, between 0.8 and 1.0, in the Welkom area. One can observe considerably higher values of apparent stress associated with seismic events in area A, where mining of small pillars takes place approximately 300m deeper than scattered mining of larger blocks in area B. The ratio of the largest to the smallest apparent stress in Fig.9.11 is well over 100.

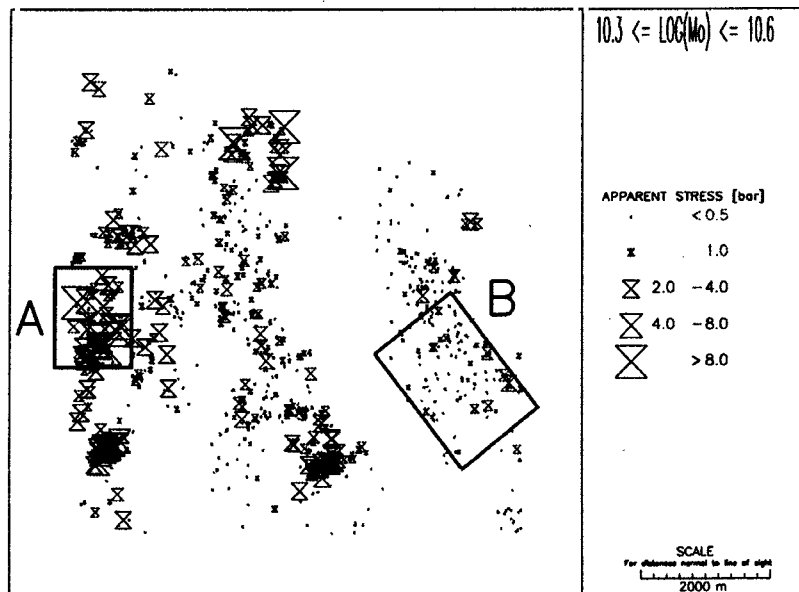
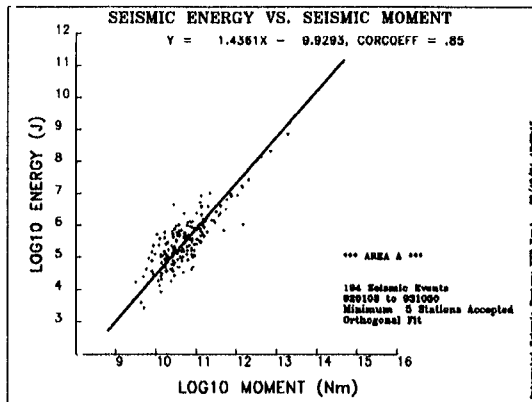
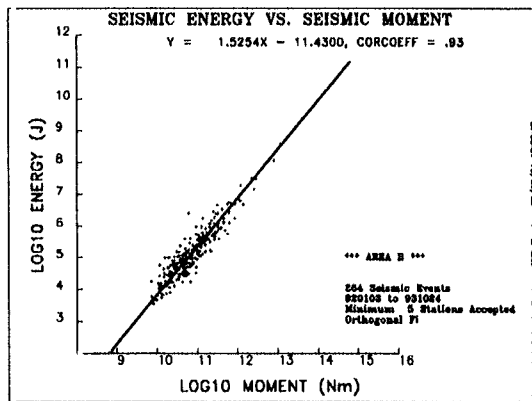


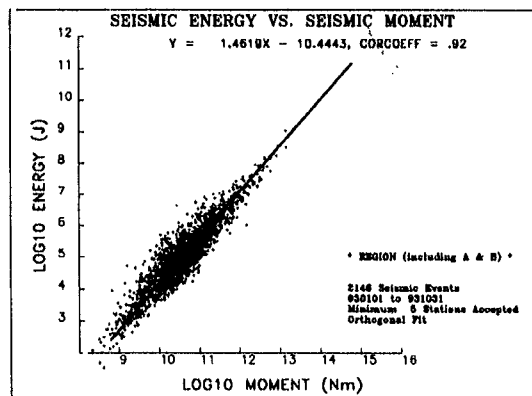
Figure 9.6. Apparent stress of seismic events within the restricted magnitude range of 0.8 to 1.0 in the Welkom area, RSA, for the period 1 January to 31 October 1993. A (~1850m) and B (~1550m) indicate examples of areas (and depth below surface) of consistently high (box A) and consistently low (box B) apparent stress



Area A



Area B



Whole Region

Figure 9.7. Seismic moments and radiated seismic energies of events associated with the two areas A and B and the whole region in Fig.9.6. Please note higher energies (3.5 times on average) for the same seismic moments associated with the deeper mining in area A. The greater scatter in the case of A could be explained by greater inhomogeneities brought about by the presence of faults.

Fig.9.7 shows log energy vs. log moment plots for seismic events for the *entire* magnitude range that occurred in the areas A and B and the whole region shown in Fig.9.6 (*restricted* magnitude range).

The notion of comparing the radiated energies (or apparent stresses or stress drops) of seismic events of similar seismic moments can conveniently be translated into a practical tool called Energy Index (van Aswegen and Butler, 1993). Energy Index (EI) of the j th event is the ratio of the radiated seismic energy of that event to the average energy radiated by events of this same seismic moment in the area of interest (see Fig 9.8):

$$EI_j = \frac{E_j}{\bar{E}(M_j)} \quad (9.11)$$

where $\log \bar{E} = c5 \log M_j + c6$, $c5$, $c6$ are constants.

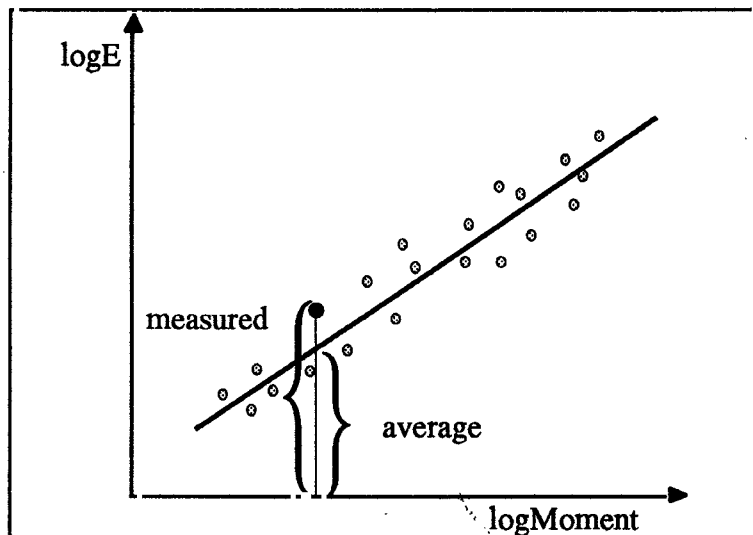


Figure 9.8 Energy index concept: $EI = E/(\text{average } E \text{ for given moment } M \text{ in a given area})$

An average energy index for seismic events occurring within the volume ΔV and time interval $t_2 - t_1$ is then

$$EI(\Delta V, t_2 - t_1) = \frac{\sum_{j=1}^{n(t_2, t_1)} EI_j}{n(t_2, t_1)} \quad (9.12)$$

where $n(t_2, t_1)$ is the number of events for a given ΔV and $t_2 - t_1$.

Fig.9.9 shows contours of energy index over the whole region, as at Fig.9.6, for the entire data set shown in Fig.9.7 – Whole Region. One can see general agreement between areas of high apparent stress

in Fig.9.6 and high values of energy index contours in Fig.9.9.

Energy index, when applied properly, provides information about the stress level and the rate of change of stress in the area.

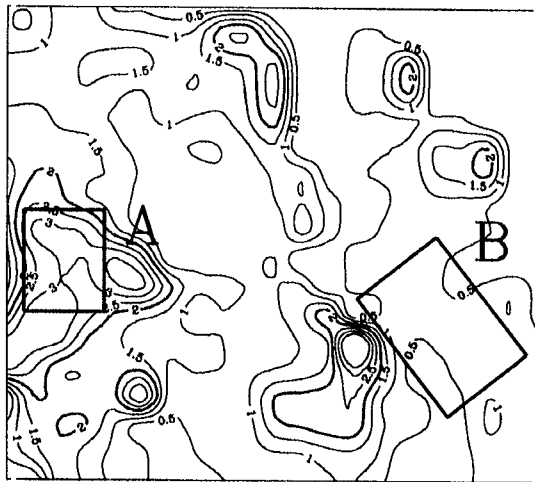


Figure 9.9 Contours of energy index of all 2146 events (see Fig. 8.7, Whole Region) which occurred between 1 January and 31 October 1993, in the area shown in Fig. 9.6. The thicker the line the higher the energy index.

9.4 SOURCE VOLUME, CLUSTERING OF SOURCES AND SEISMIC DAMAGE

Apparent Volume

The strain drop produced by the event can be localized in a zone that is narrow in comparison with the length of the radiated seismic waves. In many cases, seismic events that occur close to the underground excavations exhibit a volume rather than a planar character, with many zones of permanent deformation and complex geometry accompanied by a local volume change (Teisseyre, 1980a, 1980b, Ortlepp, 1984). Fig.9.10 shows a few examples of possible displacement patterns at the seismic source.

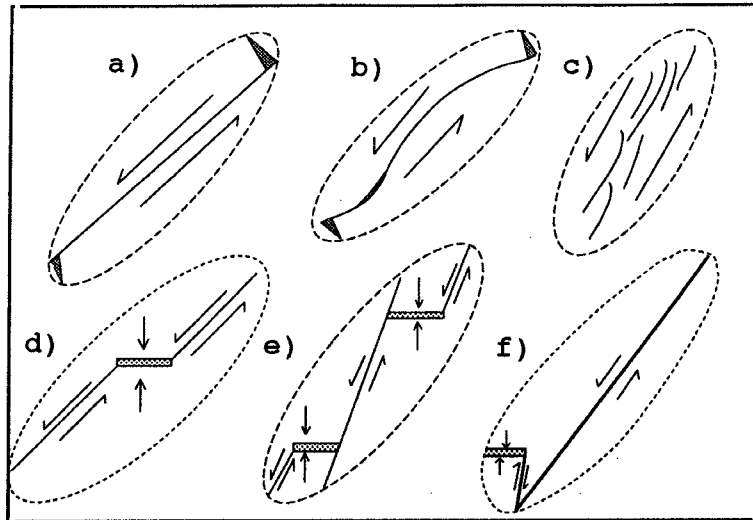


Figure 9.10 Example of displacement patterns at the seismic source:

- a) simple shear and two tensiles
- b) shear over nonplanar fault, dilation and two tensiles
- c) multiple shears
- d) two fault related shears and implosion associated with slope closure
- e) multiple shears and slope related implosions
- f) fault related shear, implosion associated with slope closure and shear along newly created discontinuity

Source volume V – the volume of coseismic inelastic deformation $\Delta\epsilon = \Delta\sigma / G$ can be estimated from $V = M / \Delta\sigma$. Since apparent stress σ_A scales with stress glut (drop), and since there is less model dependence in determining the apparent stress than there is in determining corner frequency cubed dependant static stress drop, and because, in general $\Delta\sigma \geq 2\sigma_A$, one can define the apparent volume V_A as follows (Mendecki, 1993)

$$V_A = \frac{M}{2\sigma_A} = \frac{M^2}{2GE} \quad (9.13)$$

The apparent volume for a given seismic event scales volume of rock with coseismic inelastic strain of an order of apparent stress over rigidity.

Apparent volume, like apparent stress, depends on seismic moment and radiated seismic energy, and, because of its scalar nature, can easily be manipulated in the form of cumulative or contour plots etc., providing insight into the rate and the distribution of coseismic deformation and/or stress transfer in the rock mass.

Fig.9.11 shows the correlation of cumulative apparent volume of seismic events associated with the Ararat fault in the Welkom area and creep being measured on this fault over a period of three and a half

months (see also van Aswegen and Butler, 1993). It confirms the notion of a positive correlation between coseismic and aseismic deformation.

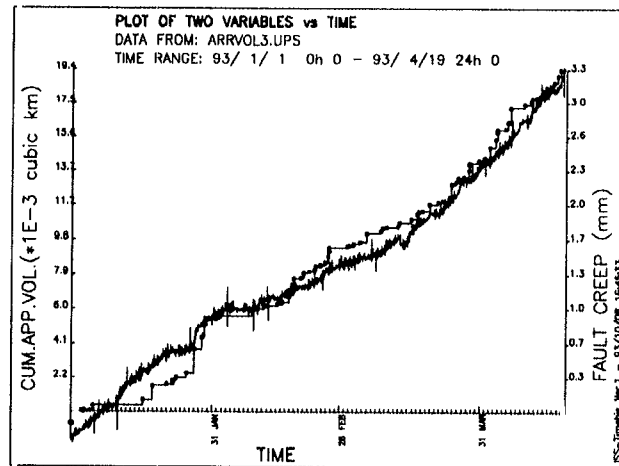


Figure 9.11. Plot of cumulative apparent volume of events around the fault (dotted line) with superimposed, measured fault creep (darker, noisy line).

Apparent volume, or source volume, gains sensitivity to the inelastic coseismic deformation from its two dimensional description of the seismic source, namely, by seismic moment and seismic energy or by seismic moment and stress drop.

Fig.9.12 shows cumulative plots of radiated seismic energy, seismic moment and apparent volume versus time for the area surrounding the source of a large seismic event of energy $E=2 \cdot 10^{10}$ J. There is no precursory behaviour on cumulative energy or cumulative moment plots both being one dimensional descriptions of the source. One can however see a dramatic increase in a gradient of the cumulative apparent volume for the last three months before the event.

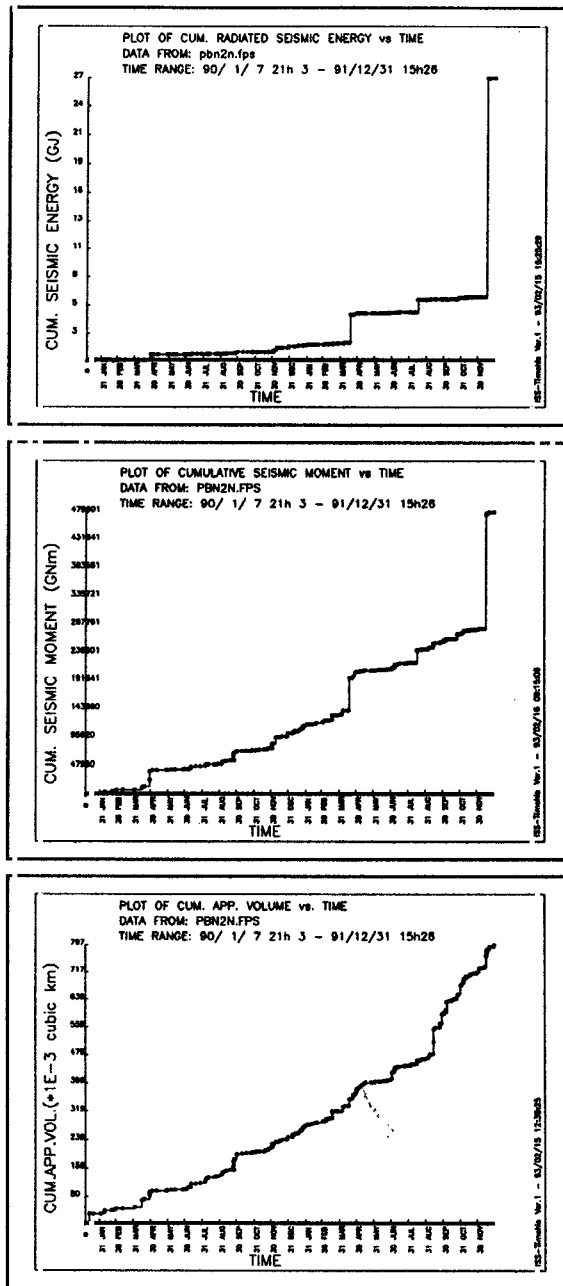


Figure 9.12. Cumulative plots of radiated seismic energy, seismic moment and apparent volume versus time for the area surrounding the source of a seismic event of energy $E=2 \times 10^{10} \text{ J}$. Note an increase in the gradient in the cumulative apparent volume plot for the last three months prior to the major event (after Mendecki, 1993).

Clustering of Seismic Sources in Space

The two parameter description of seismic sources, namely seismic moment and stress drop or seismic moment and radiated energy, can be used to describe the clustering of seismic sources in space.

The clustering of sources of two seismic events can be quantified by :

$$CSS_2 = \frac{r_1 + r_2}{d_{12}} \tag{9.14}$$

where:

r_1 and r_2 are the radii of an equivalent spherical source
 d_{12} is the distance between the locations of these events:

$$r = \sqrt[3]{3V/(4\pi)}$$

where V is the source volume or the apparent volume of the event.

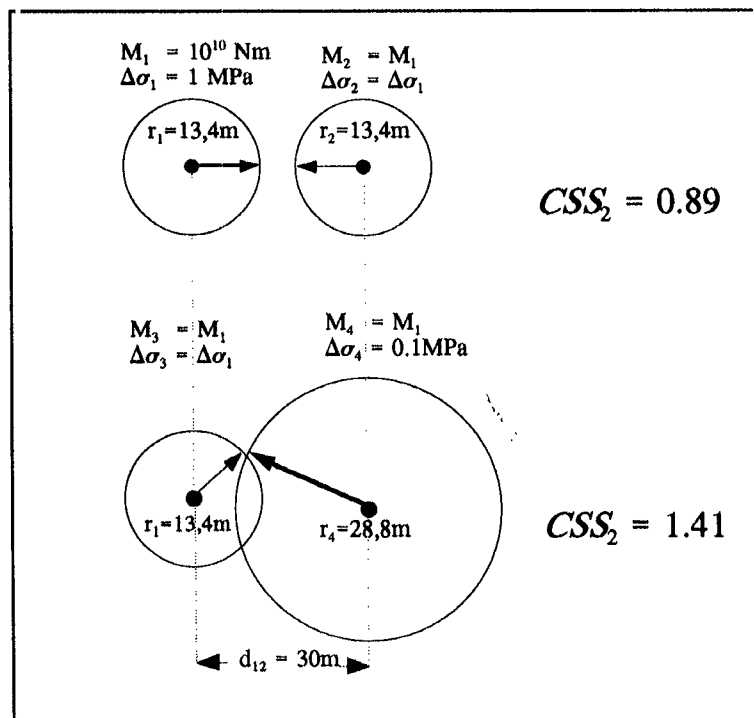


Figure 9.13 An example of clustering of equivalent spherical sources of two pairs of seismic events. Moment-magnitude of all four events is $m_M = 0.6$

The clustering of n seismic sources can then be described as

$$CSS = \frac{\sum_{i < j}^n (r_i + r_j)}{\sum_{i < j}^n d_{ij}} \quad (9.15)$$

where $\sum_{i < j}^n$ covers all combinations of pairs within the population of n seismic events, $n > 1$

Seismic Damage

The damage of materials is the progressive physical process by which they break. At the macroscale, the source of the seismic event, being a volume of suddenly created inelastic deformation, could be considered as a damage within the rock mass.

Cumulative damage due to the number of seismic events could be defined as the ratio of total volume of coseismic inelastic deformation, measured by the source volume or by the apparent volume, to the volume of interest

$$D_c = \frac{\sum V_A}{\Delta V} \quad (9.16)$$

United or effective damage could then be defined as the ratio of united volume of coseismic inelastic deformation to the volume of interest,

$$D_u = \frac{UV_A}{\Delta V}, \quad (9.17)$$

where UV_A is united apparent volume, *i.e.* the union of apparent volume for a number of seismic events, where overlapping volumes of coseismic deformation are taken into account only once.

The clustering of seismic damage, CSD, within a given volume of rock ΔV can be described by the ratio:

$$CSD = \frac{D_c - D_u}{D_c} = \frac{\sum V_A - UV_A}{\sum V_A} \quad (9.18)$$

The clustering of seismic damage varies between zero and one. CSD is zero where there is no overlapping volume between seismic events and is equal to one in the case where an infinite number of seismic

events of identical volume each occurred in the same place. Table 9.1 demonstrates the concept.

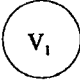
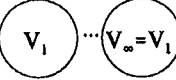


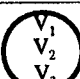
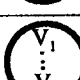
Case	No of Events	D _c	D _U	CSD
	1	V ₁	V ₁	0
	∞	V ₁ +V ₂ + ... = ∞	V ₁ +V ₂ +...= ∞	$1 - \frac{U V_A}{\sum V_A} = 1 - 1 = 0$
 V ₂ =½V ₁	2	V ₁ +V ₂ = $\frac{3}{2}$ V ₁	V ₁	1/3
 V ₂ =V ₁	2	V ₁ +V ₂ = 2V ₁	V ₁	1/2
 V ₂ =V ₁ V ₃ =V ₁	3	V ₁ +V ₂ +V ₃ = 3V ₁	V ₁	2/3
	∞	V ₁ +V ₂ + ... = ∞	V ₁	$1 - \frac{U V_A}{\sum V_A} = 1 - 0 = 1$

Table 9.1 Cumulative, united and clustering of seismic damage for a different idealised configuration of seismic events.

9.5 SEISMIC STRAIN AND SEISMIC STRESS

An average seismic strain tensor within the volume ΔV and over the time t₂ - t₁ = Δt is proportional to the sum of the seismic moments of all events which occurred in this volume during Δt (Kostrov, 1974; Jackson and McKenzie, 1988)

$$\epsilon_s (\Delta V, \Delta t) = \frac{\sum_{t_1}^{t_2} M}{2G \Delta V} \tag{9.19}$$

The average seismic strain rate then is

$$\dot{\epsilon}_s (\Delta V, \Delta t) = \frac{\sum_{t_1}^{t_2} M}{2G \Delta V \Delta t} \tag{9.20}$$

An average seismic stress can be defined as

$$\sigma_s(\Delta V, \Delta t) = \frac{\int_{t_1}^{t_2} \Sigma E}{\dot{\epsilon}_s \Delta V \Delta t} = \frac{2G \int_{t_1}^{t_2} \Sigma E}{\int_{t_1}^{t_2} \Sigma M} \quad (9.21)$$

where ΣE is the seismic energy radiated by all events recorded within volume ΔV during the period Δt (Kostrov and Das, 1988). Seismic strain and seismic strain rate can be treated as tensors if moment tensor solutions are available for all events considered. As tensors, seismic stress and seismic strain, or strain rate, have the same principal axes.

Strain rate geometry can only be obtained from events with moment tensor solutions. One can normalise each moment tensor M_{ij} to have a unit Euclidean norm

$$\bar{M}_{ij} = \frac{M_{ij}}{\|M_{ij}\|} \quad (9.22)$$

and then define the normalised strain orientation tensor $\bar{\epsilon}_{ij}$

$$\bar{\epsilon}_{ij} = \frac{\Sigma (\bar{M}_{ij})_k}{\|\Sigma (\bar{M}_{ij})_k\|} \quad (9.23)$$

The normalised moment tensor \bar{M}_{ij} is called the source mechanism (Silver and Jordan, 1982) and it describes the geometry of the strain release for a specific seismic event. The normalised strain orientation tensor $\bar{\epsilon}_{ij}$ describes the geometry of the volumetrically averaged strain rate for a given set of data (Fischer and Jordan, 1991). Seismic events with a considerable volume change should be excluded from this type of strain rate geometry statistics.

The degree to which moment tensors of seismic events are mutually similar within a given area can be measured by seismic consistency, C_s , defined by Fröhlich and Apperson (1992)

$$C_s = \frac{\|\Sigma (\bar{M}_{ij})_k\|}{\Sigma \|(\bar{M}_{ij})_k\|} \quad (9.24)$$

C_s varies from 0, where the individual moment tensors cancel each other out, to unity, where the moment tensors are identical.

The "distance" or the difference between orientations of the normalised moment tensors of two seismic events, say, k_1 and k_2 can

be measured by

$$DOMT_{k_1, k_2} = \cos^{-1}[(\bar{M}_{ij})_{k_1} \cdot (\bar{M}_{ij})_{k_2}] \quad (9.25)$$

where the inner product $[(\bar{M}_{ij})_{k_1} \cdot (\bar{M}_{ij})_{k_2}]$ is called coherence (Kagan and Knopoff, 1985 a,b) and varies from -1, for any pair of opposite moment tensors, to +1, for any pair of identical moment tensors. *DOMT* is an angle and varies from 0, for a pair of identical moment tensors, to π , for an opposite pair. One can then analyze the space or space-time clustering of seismic moment tensor orientations (Willemann, 1993).

9.6 SEISMIC SOFTENING

Fig.9.14 presents schematically the typical stress-strain diagram of a rock sample. After passing through the elastic and strain-hardening regimes, the material softens and further increments of strain are associated with the drop of stress.

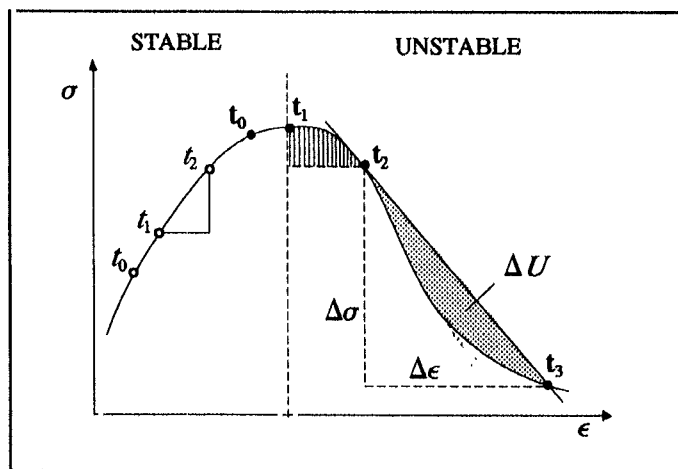


Figure 9.14 Typical stress-strain diagram of a rock sample, volume V.

The deformation is considered to be unstable when the inner product of any infinitesimal increment of stress and strain is negative.

$$d\sigma d\epsilon = d\sigma d\epsilon_e + d\sigma d\epsilon_{in} < 0 \quad (9.26)$$

where ϵ_e and ϵ_{in} are elastic and inelastic strain increments respectively. For the elastic strain increments $d\sigma \cdot d\epsilon_e > 0$ thus instability will occur only when the inelastic term balances the elastic one, so that there is a net strain-softening.

For finite stress and strain departures from the current state at

$t_1[\sigma(t_1), \epsilon(t_1)]$ to the next state at $t_2[\sigma(t_2), \epsilon(t_2)]$, the respective definition of instability of the volume element ΔV , see Fig.9.14, is

$$\int_{\Delta V} \int_{\epsilon(t_1)}^{\epsilon(t_2)} [\sigma(t_2) - \sigma(t_1)] d\epsilon(t) dV < 0 \quad (9.27)$$

Since σ and ϵ are, in general, tensors, there are different stress components that may be influential in causing the instability. In general the possibility for instability arises when one or more stress components within a volume are able to decrease with increasing strain – strain localisation. Alternatively, strain localisation can be caused by relative strain softening, where material within a localised strain zone hardens at a lower rate than the adjacent body of rock (Hobbs et al. 1990; Jessell and Lister, 1991).

One can consider the seismic version of the instability criterion (9.27) with the following assumptions:

$$\sigma(t_2) \approx \sigma_s(\Delta V, t_2 - t_1) = 2G \frac{\sum E}{t_1} / \frac{\sum M}{t_1} > 0$$

$$\sigma(t_1) \approx \sigma_s(\Delta V, t_1 - t_0) = 2G \frac{\sum E}{t_0} / \frac{\sum M}{t_0} > 0$$

$$\int_{\epsilon(t_1)}^{\epsilon(t_2)} d\epsilon(t) \approx \epsilon_s(\Delta V, t_2 - t_0) = \frac{\sum M}{t_0} / (2G\Delta V) > 0$$

If $t_2 > t_1 > t_0$, then for $\Delta V = dV$

$$S_s(\Delta V, \Delta t_1, \Delta t_2) = \frac{\left(\frac{\sum E}{t_1} \frac{\sum M}{t_0} - \frac{\sum E}{t_0} \frac{\sum M}{t_1} \right) \frac{\sum M}{t_0}}{\Delta V \frac{\sum M}{t_1} \frac{\sum M}{t_0}} \quad (9.28)$$

is the measure of seismic softening within the volume ΔV , where: $\Delta t_1 = t_1 - t_0$ and $\Delta t_2 = t_2 - t_1$.

The equation (9.28) will be negative only if

$$\frac{\sum_{t_1}^{t_2} E}{\sum_{t_0}^{t_1} E} < \frac{\sum_{t_1}^{t_2} M}{\sum_{t_0}^{t_1} M} \quad (9.29)$$

The energy released or work done, ΔU , during the instability (t_2, t_3) – see Fig.9.14 – is proportional to stress $\Delta\sigma$ and strain $\Delta\epsilon$ drops

$$\Delta U_{23} = \int_{\Delta V} \int_{\epsilon(t_2)}^{\epsilon(t_3)} [\sigma(t_3) - \sigma(t_2)] d\epsilon(t) dV \quad (9.30)$$

9.7 SEISMIC VISCOSITY AND DEBORAH NUMBER

Rock mass resistance to the flow of coseismic inelastic deformation can be measured by the ratio of seismic stress over seismic strain rate and is called seismic viscosity (Kostrov and Das, 1988)

$$\eta_s(\Delta V, \Delta t) = \frac{\sigma_s}{\dot{\epsilon}_s} = \frac{4G^2 \Delta V \Delta t \sum_{t_1}^{t_2} E}{\left(\sum_{t_1}^{t_2} M \right)^2} \quad (9.31)$$

If one considers seismicity as the turbulent part of the flow of rock towards equilibrium, then the concept of seismic viscosity is similar to the fluid mechanics concept of turbulent or eddy viscosity. Unlike the ordinary or molecular viscosity, the eddy viscosity does not describe the physical properties of the medium but characterizes the statistical properties of the flow, consequentially, it does not have to be constant but can vary in time and space. Seismic viscosity would increase during quiescence, due to the increase in Δt , or during a sequence of high apparent stress (or stress drop) events; it would decrease during a sequence of soft events. The inverse of viscosity is called fluidity.

Lower seismic viscosity (or high fluidity) implies the easier flow of seismic inelastic deformation, or stress transfer due to seismicity, and promotes softer rock mass response to mining.

Having determined seismic viscosity, one can estimate seismic relaxation time τ_s , which governs the rate of decay of seismic stress with time,

$$\tau_s(\Delta V, \Delta t) = \frac{\eta_s}{G} \quad (9.32)$$

The ratio of the dynamic viscosity η to density ρ is called the kinematic viscosity. The seismic kinematic viscosity is then

$$v_s(\Delta V, \Delta t) = \frac{\eta_s}{\rho} \quad (9.33)$$

In general, the viscous term can be divided into two parts of which one is diffusive in character and vanishes when integrated and the other is dissipative and quantifies seismic energy dissipation rate per unit time and per unit mass.

$$e_s = v_s \cdot (\dot{\epsilon}_s)^2 = \frac{t_1}{\rho \Delta V \Delta t} \sum E \quad (9.34)$$

A given rockmass may appear to flow seismically on a time scale, Δt , close to or larger than the relaxation time, τ_s , whereas it will behave as a rigid or elastic solid on shorter time scales. The ratio of the relaxation time τ_s to the time of observation (flow time) is called the Deborah number, De , (Reiner, 1969)

$$De(\Delta V, \Delta t) = \frac{\tau_s}{\Delta t} = \frac{4G \Delta V \sum E}{\left(\frac{t_2}{\sum M} \right)^2} \quad (9.35)$$

The Deborah number, De , may be interpreted as the ratio of elastic to viscous forces. For $De < 1$ viscous effects dominate, whereas for $De > 10$ the system will essentially behave as an elastic solid.

The coseismic viscosity η_{cs} i.e. the viscosity during an individual seismic event at its source could be estimated from $\eta_{cs} = \Delta\sigma / \Delta\dot{\epsilon}_{cs}$ and since $\Delta\dot{\epsilon}_{cs} = \Delta\sigma / (G\Delta t_{cs})$, then $\eta_{cs} = G\Delta t_{cs}$, where $\Delta\sigma$ and $\Delta\dot{\epsilon}$ are stress drop and coseismic strain rate respectively and Δt_{cs} here is the duration of the source. Since the duration of mine seismic sources $\Delta t_{cs} \cong 10^{-2}$ to 10^0 s and $G \cong 10^{10}$ Pa then $\eta_{cs} = 10^8$ to 10^{10} , Pa·s, which is a few orders of magnitude less than the calculated average seismic viscosity η_s for a given volume ΔV and over a given time Δt . The reason is in the intermittent nature of seismic flow of rock, where sometimes large portions of space ΔV and time Δt are not affected.

9.8 SEISMIC DIFFUSION

If a volume of rock, V_m , is mined out at time t_0 and if the altered stress and strain field can readjust to an equilibrium state through seismic movements only, the sum of seismic moments released within a given period of time would be proportional to the excavation closure and in the long term at $t = t_\infty$ (McGarr, 1976a)

$$\sum_{t_0}^{t_\infty} M \approx GV_m \tag{9.36}$$

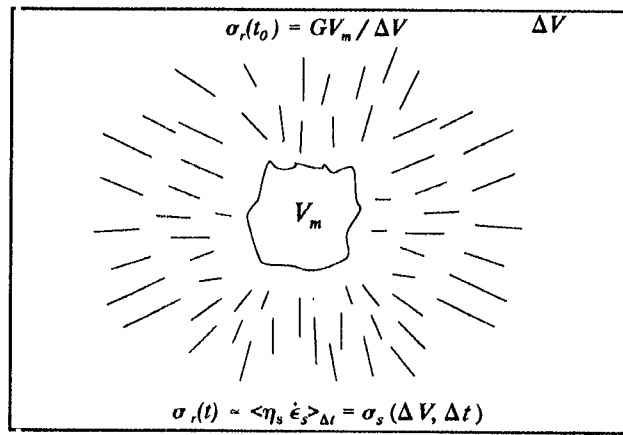


Figure 9.15 Seismic flow of rock into the mined out void V_m

The relative stress level in a given volume of rock ΔV surrounding the excavation Fig.9.15, at the current time t_2 can be calculated from the difference between GV_m and the cumulative moments released to date (McGarr 1976b)

$$\sigma_r = \frac{GV_m - \sum_{t_0}^{t_2} M}{\Delta V} \tag{9.37}$$

The relative stress σ_r decays with the cumulative seismic moment linearly, as shown at Fig 9.16.

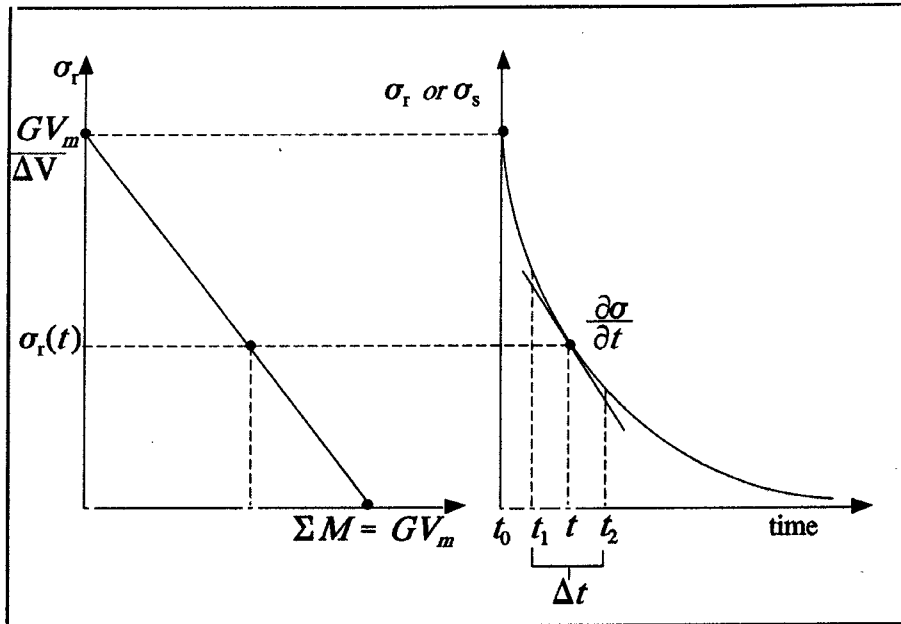


Figure 9.16 Relative stress vs cumulative seismic moments (left) and relative or seismic stress vs time (right)

The average seismic stress during $\Delta t = t_2 - t_1$ within seismically flowing volume of rock ΔV is $\langle \eta_s \dot{\epsilon}_s \rangle$, thus for $t_2 > t > t_1$

$$\sigma_r(t_2) = \frac{GV_m - \sum M}{\Delta V} \approx \langle \eta_s \dot{\epsilon}_s \rangle_{\Delta t} = \frac{2G \sum E}{\frac{t_2}{t_1} \sum M} = \sigma_s(\Delta t) \tag{9.38}$$

The following conclusions can be deduced from equation (9.38):

- an increase in $V_m/\Delta V$ for the same type of rock will increase seismic strain rate and seismic stress.
- higher rock mass viscosity will increase the amount of radiated seismic energy per unit deformation yielding, on average, higher apparent stress events.

If, after removing volume V_m , the rock mass is left undisturbed, entropy is generated since all dissipative irreversible processes involve the loss or dissipation of useful energy. In statistical mechanics the entropy of a state is related to the probability of the occurrence of that state among all possible states. Entropy measures the disorder of the system and increases as the system tends towards equilibrium.

A non-equilibrium situation which is moving towards equilibrium at the rate governed by its distance from equilibrium is described by the diffusion equation,

$$\frac{\partial \sigma_s}{\partial t} = D_s \nabla^2 \sigma_s \quad (9.39)$$

where: $\partial \sigma_s / \partial t$ is change of stress with time [Pa/s],

$$\nabla^2 \sigma_s \equiv \frac{\partial^2 \sigma_s}{\partial x^2} + \frac{\partial^2 \sigma_s}{\partial y^2} + \frac{\partial^2 \sigma_s}{\partial z^2},$$

and for the seismically active cube $\Delta V = l \cdot l \cdot l$, where at the centre $\sigma_0 = 0$, Fig.9.15, and where the average seismic stress within ΔV during $t_2 - t_1$ is σ_s , one can show after triple integration over ΔV that:

$$\nabla^2 \sigma_s = (\sigma_s - \sigma_0) \frac{24}{l^2} = \sigma_s \frac{24}{l^2} = \frac{2G \sum E}{t_1} \frac{24}{l^2} \quad (9.40)$$

D_s is the diffusivity with dimension of m^2/s and is interpreted in terms of a characteristic distance of the process which varies only with the square root of time. The average seismic diffusivity D_s within the volume ΔV over time $\Delta t = t_2 - t_1$ can be defined as:

$$D_s(\Delta V, \Delta t) = \frac{l^2}{\tau_s} = \frac{l^2 G}{\eta_s} = \frac{l^2 \left(\frac{\sum M}{t_1} \right)^2}{4G \Delta V \Delta t \sum E} = \frac{\left(\frac{\sum M}{t_1} \right)^2}{4G l \Delta t \sum E} \quad (9.41)$$

where τ_s and η_s are seismic relaxation time and seismic viscosity respectively.

In terms of seismic source parameters, diffusivity increases with the square of seismic moments and decreases with an increase in seismic energies for the same events, *i.e.* diffusivity is higher when seismic events are softer (of low apparent stress) and decreases with an increase in seismic viscosity. Seismic diffusivity is to be considered as a function of space and time.

One can consider an alternative definition of seismic diffusion coefficient d_s based on Einstein's diffusivity relation,

$$d_s = \frac{(\bar{X})^2}{t} = (\bar{X})^2 \cdot \lambda \quad (9.42)$$

where \bar{X} is an average distance between consecutive sources (including source sizes, Fig.9.17) of interacting seismic events, \bar{t} is an average time between events and λ is an activity rate (s^{-1}). The interaction or correlation between consecutive events is required to ensure they belong to the same process.

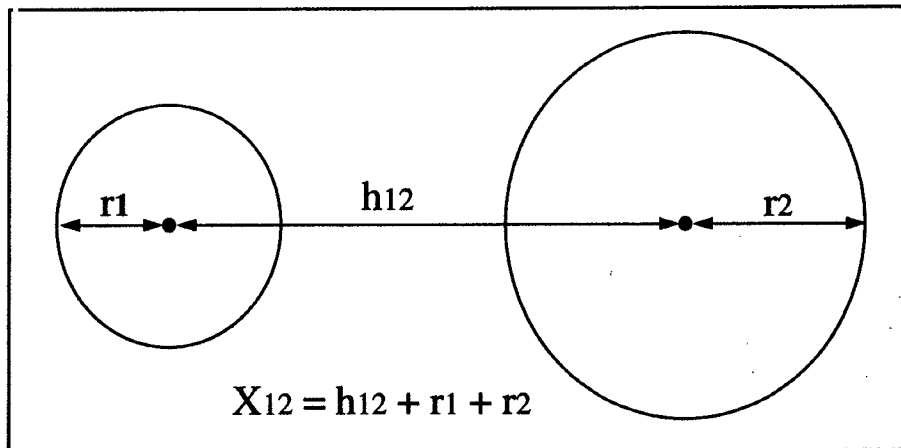


Figure 9.17 An average distance (including source sizes r_1 and r_2) of two consecutive seismic events.

An average velocity of diffusion [m/s] can be given by

$$V_{Ds} = \sqrt{D_s/\tau_s} \quad \text{or} \quad V_{ds} = \sqrt{d_s \lambda} \quad (9.43)$$

The diffusion coefficient given by equation (9.42) and its velocity given by equation (9.43) can be decomposed in x, y and z components. This could be a very useful tool in quantifying migration of microseismic activity and associated fracturing processes in space and time.

9.9 SEISMIC SCHMIDT NUMBER

One can combine seismic viscosity and seismic kinematic diffusion into one parameter called seismic Schmidt number (Sc_s)

$$Sc_s(\Delta V, \Delta t) = \frac{v_s}{d_s} = \frac{\sigma_s \bar{t}}{\rho \dot{\epsilon} \{\bar{X}\}} = \frac{4G^2 \Delta V \Delta t (\bar{t}) \overset{t_2}{\Sigma} E}{\rho \{\bar{X}\} \overset{t_2}{\Sigma} M \overset{t_1}{\int}} \quad (9.44)$$

Please note that Sc_s encompasses four independent parameters

describing seismicity, namely:

- \bar{t} average time between events
- \bar{X} average distance between consecutive events
- ΣE cumulative seismic energies
- ΣM cumulative seismic moments

9.10 UNSTABLE DEFORMATION AND UNSTABLE SYSTEM

The surface which bounds all stress states that correspond to elastic deformation is called the yield or damage surface. The evolution of the yield surface with continued deformation specifies the manner in which the material hardens or softens during the deformation. The direction of the inelastic strain increment beyond the yield surface is determined by inelastic potential. The inelastic potential surface is always normal to the inelastic strain rate vector $\dot{\epsilon}_{in}$ in six dimensional stress space.

The associated flow or normality rule applies to the material where yield and potential surfaces coincide, *i.e.* the inelastic strain rate vector is always normal to the yield surface.

Under normal conditions, *i.e.* for associated flow with a smooth yield surface (Fig.9.18), one would expect a strain softening behaviour before the instability. This could be described by the classical instability criterion formulated by Hadamard in 1903 and then rediscovered by Pearson (1956) and Hill (1957, 1958)

$$\int_{V_n} \dot{\sigma} \dot{\epsilon}_e dV + \int_{V_n} \dot{\sigma} \dot{\epsilon}_{in} dV < 0 , \quad (9.45)$$

where:

- $\dot{\sigma}$ - rate of change of stress
- $\dot{\epsilon}_e, \dot{\epsilon}_{in}$ - elastic and inelastic strain rates
- V_n - volume of nucleation of instability

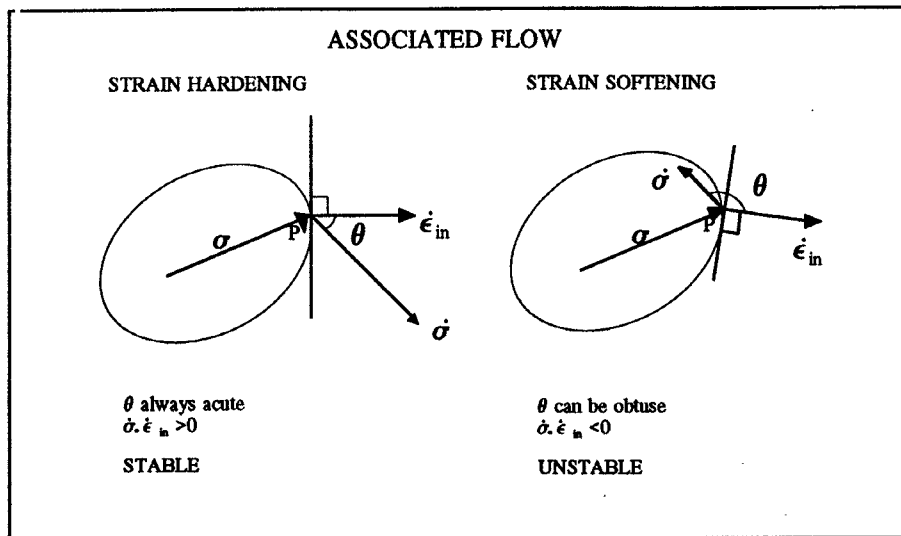


Figure 8.18. Yield surfaces for associated flow (the plastic potential surface coincides with the yield surface). σ is the state of stress at P where the stress rate vector is $\dot{\sigma}$ and the plastic strain-rate vector is $\dot{\epsilon}_n$. In the strain hardening situation the angle θ between $\dot{\sigma}$ and $\dot{\epsilon}_n$ is acute so that $\dot{\sigma} \cdot \dot{\epsilon}_n$ is positive resulting in stable deformation. In the strain softening situation θ can be obtuse so that $\dot{\sigma} \cdot \dot{\epsilon}_n$ is negative. If then $\dot{\sigma} \cdot \dot{\epsilon}_n > \dot{\sigma} \cdot \dot{\epsilon}_e$ where $\dot{\epsilon}_e$ is the elastic strain-rate then $\dot{\sigma} \cdot \dot{\epsilon}$ in this case is negative leading to unstable deformation (after Hobbs et al., 1990).

Although fault- or joint-related seismic events are generally localised it is assumed here that the inelastic deformation is more broadly distributed prior to instability.

The criterion 9.45 states that the inner product of the next increment of stress with the next increment of strain should be negative for unstable deformation within volume V_n ,

$$d\sigma \cdot d\epsilon = d\sigma \cdot d\epsilon_e + d\sigma \cdot d\epsilon_n < 0 \quad (9.46)$$

For the elastic strain increments $d\sigma \cdot d\epsilon_e > 0$. The deformation will be unstable only when the inelastic term balances the elastic term, so that there is a net strain-softening. Near the end of the hardening regime, however, almost all further strain increments are inelastic.

Fig.9.19 shows an example of a triaxial experiment at confining pressure of 94MPa and strain rate of 1.4×10^{-7} /s performed on a sample of fine-grained granite (Yokutake, 1992). One can see the potential onset of instability as defined by equation (9.45) from 1000 sec before the failure. The amount of stress drop from peak stress to fracture is more than 20MPa. Note the dramatic stress decrease and displacement jump just prior to the breakdown instability.

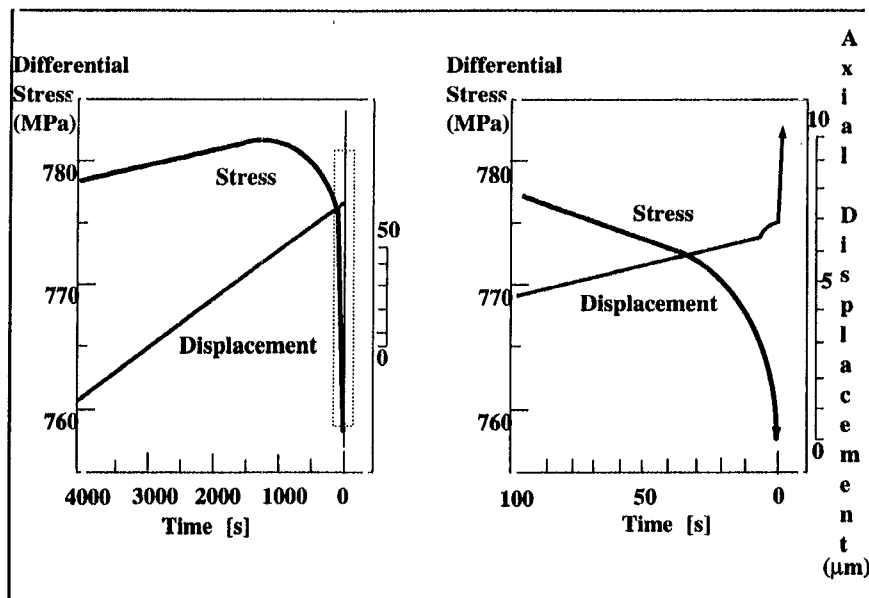


Figure 8.19. The change in the differential stress and in axial displacement versus time for the sample of fine-grained granite during triaxial compression with confining pressure of 94MPa (after Yukutake, 1992).

As stress and strain are tensors, there are many different components that may be influential in causing the instability. One should distinguish between the stability of deformation defined by the stress-strain response of the material and the stability of the system being deformed. In some cases or at some stage the system ceases to deform in a homogeneous mode and undergoes bifurcation. In general, bifurcation refers to a qualitative change of the object under study due to a change of parameters on which the object depends - in this case it is non-uniqueness of the deformation path. A bifurcation mode may or may not be amplified by continued deformation past the bifurcation point. After the displacement corresponding to the bifurcation point more than one incremental displacement field exists, satisfying the equilibrium and boundary conditions. If $\dot{\sigma}_1$ and $\dot{\sigma}_2$ are the stress rate fields corresponding to two such solutions and $\dot{\epsilon}_1$ and $\dot{\epsilon}_2$ are the respective strain rates, then the necessary condition for bifurcation to occur is that there exists an incremental displacement field such that

$$\int_v \Delta \dot{\sigma} \Delta \dot{\epsilon} dV = 0 \tag{9.47}$$

where: $\Delta \dot{\sigma} = \dot{\sigma}_1 - \dot{\sigma}_2$, $\Delta \dot{\epsilon} = \dot{\epsilon}_1 - \dot{\epsilon}_2$

If the bifurcation grows it may be symmetrical or asymmetrical. A symmetrical bifurcation (e.g. barrelling of the specimen) is stable, so $d\sigma d\epsilon > 0$, i.e. the deformation is stable when it is easier to start

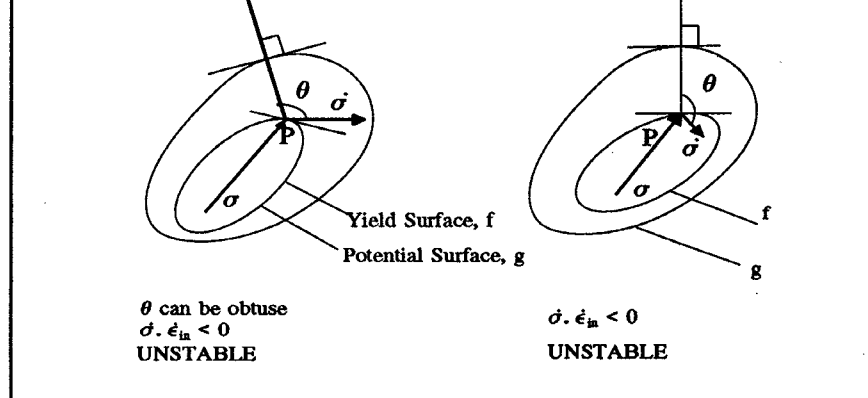


Figure 8.20. Yield surfaces for non-associated flow (the plastic potential surface, g , does not coincide with the yield surface, f). At the point P on the yield surface, σ and $\dot{\sigma}$ are the stress state and stress-rate respectively. At P the plastic strain-rate is $\dot{\epsilon}_{in}$ and this is normal to the plastic potential surface. In both strain-hardening and strain-softening situations $\dot{\sigma} \cdot \dot{\epsilon}_{in}$ can be negative (after Hobbs, et.al., 1990).

At a vertex, the inelastic strain increment vector will tend to follow the stress increment vector - see Fig.9.21. Vertices which cause that localization can happen at smaller overall deformations and at a significantly more positive tangent modulus (stiffer system).

inelastic volume strain and the inelastic shear strain

h - a hardening modulus

They showed that a bifurcation was possible in a triaxial test when the hardening modulus had attained a critical value h_{cr}

$$h_{cr} = \frac{G(1+\nu)}{G(1-\nu)} (\beta - \mu)^2 - \frac{1+\nu}{2} \left(\frac{1}{\sqrt{3}} + \frac{\beta + \nu}{3} \right)^2 \quad (9.48)$$

where ν is the Poisson's ratio.

For relatively constant μ and β , observed at large inelastic strains, localization was predicted to occur post peak *i.e.* during strain softening regime. For axisymmetric compressive loading the decrease in μ and β results in an increase in the angle of the shear band to the maximum principal stress.

Fredrich et.al., (1989) conducted the first laboratory study to quantify all the constitutive parameters in both the brittle and semibrittle regime. Their measured μ , β , ν and h for Carrera marble deformed at room temperature and at different confining pressure. At a confining pressure of 5MPa they showed brittle failure mode and at 40-190 MPa semibrittle failure was observed. In the brittle region, shear localization was not evident until the sample was deformed well into the postfailure region. In the semibrittle regime, with increasing confining pressure, h increases whereas μ , β and ν decrease. The theoretical values for h_{cr} at the onset of localization decrease with increasing confining pressure and are constantly negative for axisymmetric compression. Thus, the bifurcation model predicts that

localization is becoming unstable depends on the energy release and the dissipation inside the softening zone and on the exchange of mechanical energy between the softening zone and the ambient rock. Stress drop due to the softening within the nucleation zone induces some elastic unstraining and redistribution of stresses in the ambient rock. Energy released by elastic rebound of the surrounding rock is fed into the softening region and accelerates its deformation. The amount of energy fed into the nucleation zone correlates positively with its size and with the strain rate or, rather, rate of unstraining in the ambient rock. As soon as an input of elastic energy exceeds the energy dissipation due to the inelastic processes in the growing nucleation zone the system becomes unstable.

One can consider an interpretation of instability in terms of the relative stiffness of the components of the system - an instability will occur when the stiffness of the nucleation volume is equal to or exceeds the stiffness of the external body. Thus instability results from the interaction of the strain weakening constitutive relation of the nucleation zone with the variable stiffness of the unloading surrounding body - see Fig.9.22.

$\Delta\epsilon, \Delta\sigma$ - strain and stress drops during the instability
 ΔE - energy released during instability

It is assumed in Fig.9.22 that the surrounding rock mass is more dilatant (thus having stiffer response) than the nucleation zone and undergoes strain hardening at the time when nucleation zone softens. If the surrounding rock maintained its stiffness the systems would be stable. Fig.9.22 also illustrates the acceleration of deformation preceding instability - see increasing increments of displacement within the nucleation volume, points FG to GH, corresponding to equal increments of stress within the surrounding rock mass (see also Rudnicki, 1988).

In general, the development of instability within the rock type material is a complicated process involving changes in its stiffness, strain rate, influence of temperature and water (Hobbs et.al., 1986). Let us analyse the following constitutive law

$$\sigma = \sigma (\epsilon, \dot{\epsilon}, T, f_{H_2O}), \quad (9.49)$$

where T is the temperature and f_{H_2O} is the fugacity of water. Fugacity measures the chemical potential of a substance and correlates positively with changes in temperature, pressure and concentration.

If, for any small fluctuation in any or all the parameters in (9.49), the stress decreases with continued deformation, *i.e.* $d\sigma/d\epsilon < 0$, then the potential exists for the system to become unstable. From equation

Sufficiently high strain rate sensitivity (low n) can counter balance the tendency to instability due to strain softening (negative θ). An instability can then be delayed because the short time response of the material surrounding the nucleation zone is stiffer than its long time response and/or because the volume of the nucleation zone increases faster than the rate fluid can flow in. This in turn increases the friction and decreases the pore pressure making rock masses much harder and inhibits further dilatancy (Frank, 1965; Rudnicki, 1977, 1988), see Fig.9.5. The amount of dilatant strengthening which can be affected is limited by diffusive instability. If the rock mass is fluid infiltrated, dilatant hardening (and elastic stiffening) in an initially very narrow weakened zone will cause adjacent regions to sustain greater stress and consequently to undergo inelastic dilatant deformation - dilatancy diffusion (Rice 1975).

due to the stiffer short time response of the surrounding rock (SR) and dilatancy hardening within the nucleation zone (NZ).

$\frac{d\dot{\epsilon}}{d\epsilon}$ is the change in strain rate with continued straining; for homogeneous steady-state deformation this is zero, but for deformations in which strain is localized it becomes non zero,

$\frac{\partial\sigma}{\partial T}$ is stress response to change in the temperature; it has a destabilizing effect since stress tends to relax with an increase in temperature,

$\frac{dT}{d\epsilon}$ is the temperature increase due to straining; in general it is positive,

$\frac{\partial\sigma}{\partial f_{H_2O}}$ is the stress response to changes in the fugacity of water; an increase in fugacity decreases the stress so this parameter is destabilising; fluctuations in f_{H_2O} would arise from local fluctuations in pressure or temperature or both,

$\frac{\partial f_{H_2O}}{d\epsilon}$ is the water-fugacity response to change in strain. This could arise from local regions of dilatation developing during deformation where a transient pressure decrease could arise in the vapour phase. This leads to a decrease in f_{H_2O} and an associated increase in σ and stabilises the deformation.

mass the higher the stress drop and the higher the ratio of the stress drop over strain drop associated with instability.

The amount of postpeak deformation in the weakened nucleation zone prior to instability strongly depends on the deviatoric state of stress induced within the nucleation zone and on the degree of inhomogeneity. In particular, instability is predicted much nearer the peak load for very narrow weakened zones and for states of deviatoric simple shear than for states of axisymmetric compression (Rudnicki, 1977).

The overall size of the nucleation zone increases with the size (seismic moment) of the potential instability (Scholz, 1990), increases with the degree of inhomogeneities and decrease in viscosity of the rock mass and decreases with the increase in the strain rate (Kato et.al., 1992).

It can be deduced from Fig.9.22 that the duration and magnitude of mechanical precursory phenomena, specifically the deformation and the deformation rate, increase with an increase in mechanical heterogeneity of the rock mass (Mogi, 1985; Tang and Hudson, 1993).

9.11 NUCLEATION OF INSTABILITY

Critical size of the fractured rock

Breakdown instability will not occur until a quasi-static or quasi-dynamic inelastic deformation has occurred within the critical volume of rock. The growth of the deformation processes up to the point of

Since the development of the nucleation zone is associated with overall strain softening, sources of seismic events located within the nucleation zone would be, on average, of a slower or softer nature, characterized by larger source volumes. This effect would be magnified in cases when the nucleation zone interfaces with the opening. In the laboratory experiments, crack branching and distributed damage associated with the seismic source are observed only if the strength variation in the source region is greater than the stress concentration (Labuz et.al., 1985; Cox and Patterson 1990).

A small but statistically significant decrease in seismic activity (quiescence) has been observed at the beginning of the strain softening stage, followed by an increase just before the instability (Brady, 1977; Main et.al., 1992). Outside the nucleation zone, one would expect seismic events of a harder or faster nature characterized by higher energy indices.

Accelerated deformation

It is of the nature of rock fracture and friction that the breakdown instability does not occur without some preceding phase of accelerating deformation (e.g. Scholz, 1990; Hirata *et al* 1987; Rudnicki, 1988; Mendecki, 1993).

Frequently observed increase in the rate of coseismic deformation before instability can be due to the increase in the rate of micro seismicity, or, for the same rate of events, due to the softer nature of individual events. Seismic softening and/or accelerated deformation

by the increase in the rate of micro seismicity, or, for the same rate of events, due to the softer nature of individual events.

- lower seismic stress or Energy Index within and higher outside, or at the interface of, the nucleation zone
- an increased distance between consecutive events and/or a decrease in time between consecutive events: this would tend to cause an increase in seismic diffusion, its velocity and acceleration

If accelerating deformation coincided with the development of the nucleation zone then, additionally, one would observe a decrease in the average time between events and an increase in the seismic strain rate. This causes an additional increase in diffusion and a decrease in viscosity of the seismic flow of rock resulting in a dramatic decrease in seismic Schmidt number.

The following equation captures the main feature of the above model and returns three parameters: C , α and t_f : t_f is called time at failure and quantifies the potential for instability:

$$\frac{\sum^n V_A}{(\bar{t})_n (\bar{EI})_n \Delta V} = \frac{C}{(t_f - t)^\alpha}$$

where:

- $\sum^n V_A$ sum of apparent volume over the last n events
- $(\bar{t})_n$ average time between seismic events over the last n events
- $(\bar{EI})_n$ average energy index over the last n events
- ΔV volume of interest

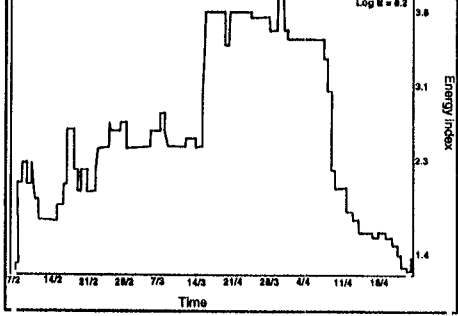


Fig.9.23c

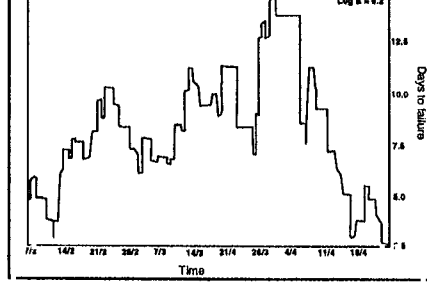


Fig.9.23d

The potential for instability increases with:

High stress An area where stress is anomalously high is at risk of violent failure, either as a result of local instability or in reaction to the stress wave from a more distant tremor.

- Seismic indicators: apparent stress, energy index, seismic stress.

High strain rate Where the rock mass is deforming at a high rate, the area is unstable. Because of the inherent heterogeneity of the rock mass, stress may be concentrated at strain-resistant points over a short period of time.

- Seismic indicators: seismic strain rate, seismic fluidity, seismic Deborah number.

High gradient in cumulative strain A high gradient in strain (or strain rate), or in rock mass fluidity, can be the focus for excess shear stress. Seismic gaps may be recognised as hazardous when surrounded by high strain gradients.

- Seismic indicators: seismic strain, seismic strain rate, seismic fluidity, cumulative apparent volume, seismic Deborah number.

the occurrence of one event alone. This may be required where seismic cover is poor and only the larger events are recorded.

An example is an event of local magnitude 2.0 event which occurred on the Postma dyke (see 10.7.2 below) in the Welkom gold field. The event was recorded by the then 'regional' Welkom Seismic Network with sensitivity down to local magnitude 0.8 in the area of interest. Mining was nearing completion on the north side of the dyke and preparations were being made to mine through to the south. The relatively high apparent stress of 20 bar of the event was sufficient information for the rock mechanics department of the mine to declare the dyke a hazardous structure and recommendations for special mining procedures were issued. These proved appropriate because several rockbursts occurred along the dyke over the following 4 years.

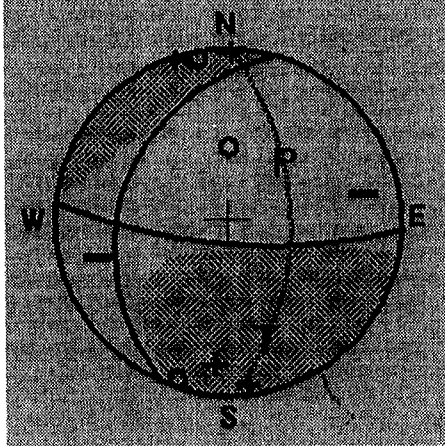
10.3.2 Location, source parameters and mechanism

An example case where the analysis of the source mechanism of event FR951004.0915 (Fig.10.2) proved to be important to justify the continuation of a particular mining practice is described here.

Fig. 10.2 The location of FR951004.0915 relative to the Brand fault and a pillar being mined. The symbol sizes depict variation in apparent stress.

In this case, a pillar was being mined against the Brand fault. Although many such pillars against faults have in the past been mined without problems, this particular fault did once before slip to yield a local magnitude 4.6 earthquake (see 10.1.1 above). Subsequently the fault was considered unlikely to yield a major tremor immediately adjacent to the particular pillar to be mined because experience in the Welkom gold field suggest that the major faults do not yield more than one major slip event in the same place. Furthermore, underground exposures of the fault in the immediate of the pillar showed it to be a rather weak fault zone, characterised by clay rich gouge. It was not expected to sustain high shear stress. The strategy was to mine a slot against the fault to unlock whatever clamping forces may still be active, to effectively make the weak structure even weaker and to avoid a highly stressed remnant locking up the structure during the final extraction phase. If the fault, however, showed signs of excessive shear stress during the early phase of cutting the strip, the whole operation could be in jeopardy - the above assumptions about the ability (or, rather, inability) of the fault to sustain high shear stress in the immediate vicinity of the pillar would be invalid.

Event FR951004.0915 occurred close to the northern cut against the fault. Fig.10.2 shows the location of the event to be some 20 m in the hangingwall of the pillar and very close the fault. The high apparent



(Seismic Moment = $4.09e+12$ Nm)

0.51 -0.52 0.71
 -0.52 -0.24 0.06
 0.71 0.06 -0.38

Diagonalized Tensor		Isotropic		DC		CLVD
-0.23 0.00 0.00		1 0 0		0 0 0		-1 0 0
0.00 -0.00 0.00	= -0.04	0 1 0	+0.69	0 -1 0	+0.19	0 -1 0
0.00 0.00 1.04		0 0 1		0 0 0		0 0 2

Best Double Couple Solution:

1.Plane: Strike = 203, Dip = 37, Rake = -159

2.Plane: Strike = 95, Dip = 77, Rake = -55

QI_configuration = 0.578 Correlation Coefficient = 0.792

Moment Tensor Quality Index = 0.358

Fig.10.3 Seismic moment tensor for FR951004.0915.

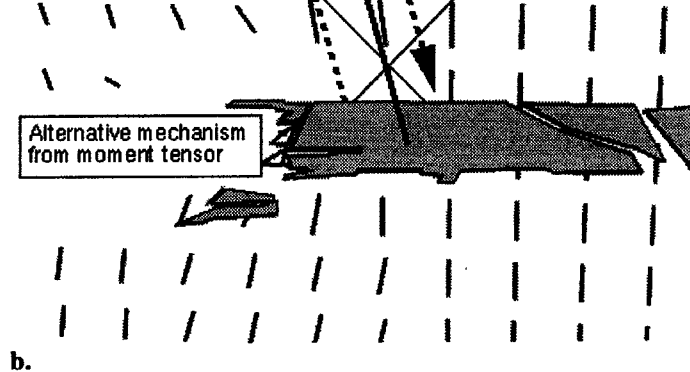


Fig.10.4 The position of FR951004.0915 relative to shear stress vectors on the Brand fault (a) and the principle stress trajectories in a north-south vertical plane through the event (b).

Although plane 1 has a strike close to that of the Brand fault, the dip is too shallow. Plane 2 is very close to the general orientation of the minor dykes which transect the pillar. The slip vector on plane 1 indicates right lateral strike slip. This is incompatible with the expected direction of slip in terms of three observations:

- i) during the 1989 earthquake the fault slipped in a normal sense (this is the case in all major fault slip events in the Welkom gold field);
- ii) simple consideration of the induced shear stress expected in the case of this particular event would suggest that the fault should slip along dip; and
- iii) numerical modelling substantiates observation (ii), indicating that

McGarr (e.g. 1976) introduced the quantification of seismicity in South African mines when he compared the cumulative seismic moment with expected (modelled) elastic stope closure. It took many years since for calibrated seismic monitoring systems in mines to develop to the level that such measurements can be made routinely and continuously. In the example described here it is shown how the rockmass response to mining can be compared in different areas using some of the seismicity parameters described in Chapter 9 and reference is also made to an appropriate statistical procedure to test the significance of differences.

The example includes 2 sets of 3 equally sized and shaped areas from a part of the Welkom gold field. The spatial distribution is shown in Fig.10.5. It is a largely mined out region with scattered pillars. Total extraction in each of the areas of interest here are about the same, but each area is unique in terms of specific geological structure, mining pattern, present production rate and depth below surface. Because the sensitivity of the regional network varies spatially, only events above local magnitude 1.0 recorded during the same period of time were taken into account, ensuring a complete catalogue of data in each case. The volume of interest was fixed symmetrically around the reef being mined in each case.

The results of the analysis are given in Table 10.1. The significance of the difference in seismic stress and seismic viscosity between each area pair is given in Table 10.2. These tables are rich in information and only a few pertinent points are raised here:

seismic strain rate is explained by a known higher rate of production. The higher average energy index in the case of area A probably relates to the 300 m greater depth of mining.

Areas D and F may be directly compared because of similar numbers of events and similarly measured values of M_{max} . In general, area F releases more energy for given moment than area D. Seismic stress in area F is significantly higher, as is average apparent stress and energy index. Seismic strain is lower. Seismic damage is more highly clustered in area D. This suggests that seismic events in area F is generally more violent and special care should be taken. In the case of area D the larger events can be expected to be less violent, but, as seen from the high clustering, there could be a well defined nucleation zone evolving which may be delineated, i.e. it may be possible in this area to establish *where* a major tremor could be expected and mining practice could be appropriately adapted. In general the differences between areas D and F may be attributed to the differences in the depth of mining, although the lower seismic viscosity could reflect inherent differences in rock strength.

Area E is clearly the most hazardous amongst D, E and F. A higher seismic strain rate coupled with a higher seismic viscosity (reflected also in higher apparent stress and energy index) renders more violent seismic events. The differences between areas E and F must be a result of particular mining practice or local geology because depth of mining and general geographical setting are the same.

TABLE 10.1. QUANTITATIVE ANALYSIS OF SEISMICITY BY AREAS OVER A 0

AREA NAME	[m**2]	A	B	C
AREA	[m**3]	961168	961168	961168
VOLUME	[m below surface]	.15E10	.15E10	.15E10
AVERAGE DEPTH		1000	2000	2300
NUM. EVENTS		34	33	98
Mmin (imposed)		1.0	1.0	1.0
Mmax (data)		2.0	2.5	3.6
CUM. MOMENT	[N.m]			
CUM. ENERGY	[J]	.73E13	.92E13	.79E14
		.28E08	.25E09	.24E11
CUM. APPAR. VOL	[CUB m]	.53E08	.11E08	.56E08
CUM. DAMG. VOL	[CUB m]	.50E08	.10E08	.49E08
UNITD. DAMG. VOL	[CUB m]	.47E08	.10E08	.46E08
CSD		.0630	.0279	.0663
SEISM. STRESS	[MPa]	.2330	1.626	17.975
Std. Deviation		.089	.696	22.723
S. VISCOSITY	[Pa.s]	.93E20	.51E21	.66E21
Std. Deviation		.43E20	.28E21	.89E21
SEISMIC STRAIN	[]	.79E-07	.10E-06	.86E-06
S. STRAIN RATE	[/s]	.25E-14	.32E-14	.27E-13
AV. APP. STRESS	[bar]	1.04	4.12	5.66
MED. APP. STRESS	[bar]	0.62	2.80	2.76
AV. ENERGY. INDX	[]	.64	2.97	4.10

TABLE 10.2 THE SIGNIFICANCE OF DIFFERENCES IN SEISMIC STRESS AND

SEISMIC VISCOSITY	SEISMIC STRESS		
	A	B	C
	.98	.78	SEIS
	.93	.76	VISC
	.74	.27	--

(The above significance test is based on a probability deviations of the paramaters - see Chapter 7.7)

10.4.2 Contouring seismicity parameters - some principles

Standard statistical procedures rely on randomness of sampling. The distribution of seismic events in space and time is not random - the degree of non-randomness could be one of the features the analyst may want to visualise through contouring. The contouring of seismic data is, in the first place, a way to enhance the visual appearance of a plot of seismic events. The statistical techniques should be kept as simple as possible in order not to introduce artifacts into the image.

In order to contour, the data must be placed onto a regular grid. There are several considerations involved in gridding the seismic data: grid spacing, physical seismic source size and smoothing functions and their parameters. In addition, the algorithms used for contouring values obtained from individual seismic events (for example: radiated seismic energy, apparent stress) is different from the algorithm used to contour values derived from a number of seismic events (such as seismic viscosity, seismic stress).

The sample rate (grid spacing) must be small enough to retain the detail in the data. However, for large areas, a small sample rate will require a significant amount of data and computer power (speed and memory size). Therefore the analyst must choose the data in such a way that a satisfactory sample rate can be maintained such that the required detail in the data is not lost or aliased.

Information from each event in the data set must contribute to

apparent stress, the seismic events could be seen as point samples of the stress field and each 'sample' should carry equal spatial weight. The smoothing functions are forced to have constant diameter regardless of the source size.

Generally, the shape of the smoothing function should be quite sharp. Examples of such functions are a Gaussian or exponential curves with a small standard deviation, or an inverted distance squared function.

Contouring a seismic parameter derived from individual seismic events is trivial. Each event's value is simply smoothed onto the grid and standard contouring procedures applied.

The seismicity parameters such as seismic Deborah are more complicated to contour. First, both the radiated seismic energies and seismic moments must be smoothed onto grids using the method already discussed above, then these grids must be combined through a transfer function to produce the desired contour plot. The transfer function converts sums of energy and moment into a seismicity based values. That requires an additional pass through the grids with a summation window. The window sums both the energy and moment values and then places the resultant parameter at the centre of the current window location. The size of this window controls the number of grid points used for the summation.

The contouring of EI over relatively large areas/volumes presents a specific technical problem. By definition, an empirical scaling correlation relation between seismic moment and radiated seismic energy is required to calculate EI . If, for example, the contours are to

practised. Because of the lack of development ahead of the advancing mining face, geological information is often limited. Planar clusters of seismic events are the obvious phenomenon to attract the attention while source parameters can be useful to confirm the fact that a pre-existing structure has been activated or to give information as to the physical nature of the structure.

A particular example, pointed out by Butler (pers. comm., 1994) and described by Van Aswegen and Meijer (1994) is that of a steeply dipping fault recognised ahead of mining at the southern margin of the Western Deep Levels East Mine VCR shaft pillar. Micro-seismicity generally groups closely around active mining faces. One deviation from this occurred in this case. A group of seismic events (referred to as group N-S) have been observed which are spatially distinguished from another group of events (group E-W). Group N-S define a near vertical, northerly striking plane in a position above and to the west of events in group E-W, the latter being more or less symmetrically distributed above and below a stope along the shallowly dipping, planar ore body. All events used in this analysis have been recorded by at least 8 seismic monitoring stations using triaxial geophone sets resulting in location accuracy of around 20 m.

The mining takes place about 2300 m below surface. The stoping width is about 1.5 m. The ore body, at the contact between the Ventersdorp volcanites and the underlying Witwatersrand quartzites, dips at 20 degrees towards the south-southeast, cutting through the middle of the lower box in Fig.10.6a and 10.6b.

The seismicity grouped around the mining is of a "softer" nature in

(Fig.10.6a).

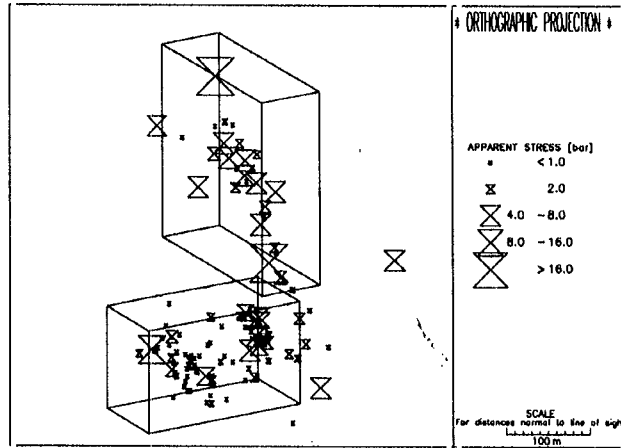


Fig.10.6a An orthographic projection, looking down towards the southwest, of seismic event distribution along an active E-W trending stope, (group E-W) and along a N-S trending plane, (group N-S). The seismic nature of the rock mass in each of the boxes is given in Table I. Note the higher stress conditions, indicated by apparent stress, along the N-S trending zone.

The interpretation is that group N-S events are associated with a fault structure. A higher state of stress in the vicinity of the structure relative to that around the stope is explained by the stress released due to elastic and non-elastic strain in the immediate vicinity of the mine opening. Since no opening exists close to the active part of the fault,

RATIO E_P/E_S 13.27

Table 1. Quantitative comparison of the seismic nature of the two groups of events in Fig.10.6a and 10.6b.

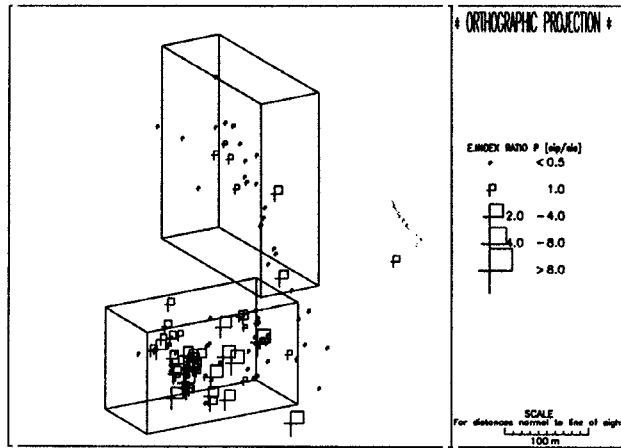


Fig.10.6b. Same as Fig.10.6a, the symbols depict the ratio E_P/E_S reflecting the smaller P- to S-wave energy characteristic of events in the N-S group compared to that of event around the mine opening in the E-W group. The interpretation is that the first group demarcates a fault or fault zone activated by nearby mining.

Although the spatial distribution of the seismic events drew the

the cluster would map out the orientation of the active plane(s) quite clearly. Such a plot would show:

- i) a point concentration being the normal to the active plane(s); and
- ii) a great circle concentration representing the orientation of the active plane(s).

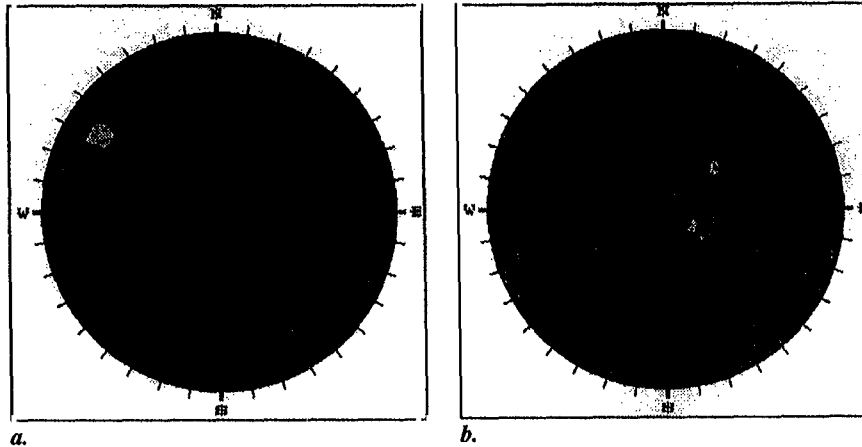


Fig. 10.7 Lower hemispherical projections of (a) the P-axes and (b) the T-axes from a cluster of 126 small seismic events recorded at a New Brunswick mine in Canada. The concentrations depicted by the contour highs coincide with the respective principle stress directions in the area of the cluster.

In general, the most stable parameters from moment tensor analyses are the orientations of the P- and T-axes, i.e. the directions of compression and extension at the model point source. Individually, if the seismic event is caused by slip along a pre-existing plane, there

temporal variations in the elastic and non-elastic properties. Seismic parameters pertaining to stress and strain rate could go a long way towards overcoming such problems because each event spatially associated with the structure and which was properly recorded yields information about what actually happened.

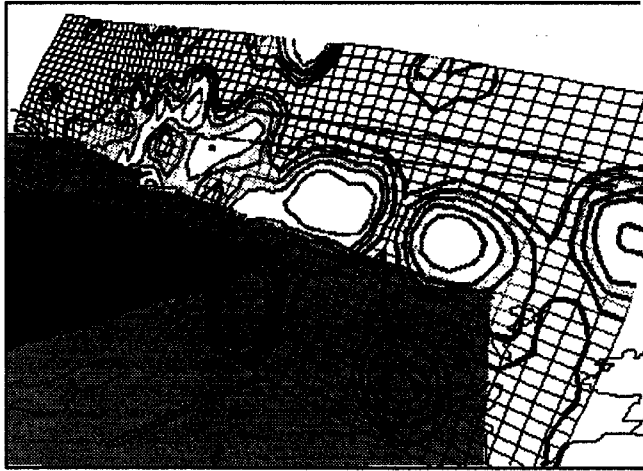


Fig.10.8a A perspective view looking down on the hangingwall side of the Tanton fault (mesh) with contours of EI based on the source parameters of seismicity within 20m of the fault surface. Grey shading depicts a major Basal reef block on the hangingwall side of the fault, with the shaft pillar in a darker shade. The reef blocks on the footwall side, dipping parallel to the line of sight, show up as straight lines behind the fault surface. The grid spacing on the fault mesh is about 20m.

An example of a fault around which mining could have a de-stabilising effect is the Tanton fault at Pres. Steyn Mine No. 4

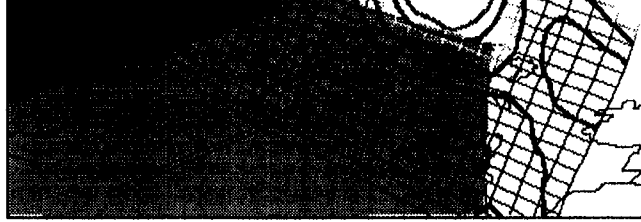


Fig.10.8b. Same as Fig.10.8a but the contours are of inverse seismic Deborah number, thus contour highs indicate high seismic flow.

Fig.10.8a shows part of the Tanton fault at President Steyn Mine No 4 Shaft with contours of *EI* based on seismic events which located on the fault surface ($\pm 20\text{m}$) over a period of eighteen months, ending July 1995. It indicates several areas of relatively high stress along the structure, particularly noteworthy being the concentrations at the lower part of the fault loss area and the area beneath that corner of the shaft pillar closest to the fault. Fig.10.8b shows contours of seismic Deborah number based on the same data set. Note that low seismic Deborah number and high stress (high *EI*) are not mutually exclusive - contour highs coincide in some but not all parts of the structure. As applied today, numerical modelling is unable to predict stress/strain behaviour of geological structures in this detail.

10.4.6 Detection of potential instabilities in space

For special and routine analysis of mining areas/volumes to detect sites

Combining stress and strain indicators Routine spatial analysis is improved if strain indicators are added. Numerous examples can be cited where large tremors occurred at sites of high strain gradients, characterised by high stress. The situation can be recognised where contours of say seismic viscosity or seismic Deborah number are closely spaced and superimposed contours of *EI* show high values.

A classic example is, of course, the well known Trough case (see below) where a full 3D analysis shows how an asperity/seismic gap on a fault yielded after being highly stressed. Most routine spatial analyses on tabular ore bodies will for the foreseeable future, however, be done in 2D because of the ease of application. It may be mentioned here that a simple 2D analysis of the Trough case yield essentially the same results.

Because of limitations imposed by access around tabular ore bodies, seismic monitoring sites are usually poorly configured for providing location accuracy in the direction normal to the mining surface of interest. This is another justification for staying with 2D analyses for routine work in these situations.

Several examples of the detection of potential instabilities in space are described under Section 10.7. Another example is that described under Section 10.4.8, where long term seismic Deborah number contours combine with short term *EI* contours to quite accurately point to the area where a large event occurred.

time history does not have to be treated with additional smoothing. It is therefore also a useful reference curve on a time history plot when comparing the behaviour of other parameters and/or filtering procedures.

Seismic viscosity Seismic viscosity is a robust measure of the nature of seismic rock flow and a decrease in the value of this parameter reflects softening. It is, however, sensitive to the size of the moving time window used. Fairly large time windows (generally several days at least) are recommended to avoid erratic changes due to large events falling in or out of the time window. Cumulative seismic viscosity is virtually the inverse of cumulative apparent volume.

Energy Index A moving median *EI* has been proven a reliable and sensitive indicator of stress variation, especially if the purpose of the analysis is to detect increases in stress. Using a linear scale, a time plot of *EI* does, by definition, emphasise above average values. If the purpose is more general, i.e. to monitor variation above and below average, $\log(EI)$ is the recommended parameter.

Seismic diffusion While ΣV_A and *EI* reflect strain and stress variation, statistical seismic diffusion adds specific information about the spatial distribution of seismicity in time, especially since it can be decomposed into the its coordinate components (see Figs.10.16h, below). By rotation of coordinate axes to coincide with potentially hazardous structures, one could, for example, detect increased seismic migration along a fault.

generally required. In time history analysis this is achieved through median filtering or averaging over a moving time window or a moving window of a particular number of observations (events). For most seismicity parameters, a given time window is required anyway since time of observation is part of the definition. While careful calibration is required for a particular situation, a moving time window of 48 hours, using at least 5 events in the window, has been found to be a good starting point for time history analyses around stope sized areas in South African gold mines.

10.4.8 Definition of clusters

In general, arbitrary polygons around visually recognised clusters of seismic events are adequate for stability analysis through time history plots. As long as the preparation zone of the forthcoming event is included and the specific processes leading up the event is sufficiently dominant, the time history plot will capture the phenomenon. More sophisticated clustering methods are, however, desirable because it could separate non-related noise from the process of interest or even separate more than one process going on more or less simultaneously.

The actual definition and delineation of spatial and temporal clusters of seismicity is, however, not a trivial process. A statistical method of space-time clustering is described in Chapter 7.3. With the development of the concepts of seismic viscosity and seismic Deborah number a new method of space-time clustering presented itself which fits in very easily with standard seismic data analysis procedures,

contours would predict the event. Fig.10.9b shows the location of the event relative to contours of seismic Deborah number. The figure also show the outline of three polygons used for time history data selection. The first polygon is rectangular and represents the local area of seismic activity. The second and third polygons follow the seismic Deborah number 100 and 10 contour lines respectively. Fig.10.9c - 10.9d and Fig.10.9e - 10.9f show the time behaviour of seismicity in each of the three polygons, expressed in terms of ΣV_A , $\log(EI)$, seismic diffusion, seismic viscosity and seismic Schmidt number. The time history plots based on the Deborah number based polygons are clearly superior to that of the general area polygon because:

- i) the drop in EI is more significant;
- ii) it more clearly shows the increase in stress leading up to the ultimate failure (this is important for predicting the event in space - see below);
- iii) an increase in seismic diffusion, not shown in the general area polygon, is observed;
- iv) the drop in seismic viscosity is much more pronounced; and
- v) the combination of (iii) to (iv) leads to a very significantly greater drop in seismic Schmidt number.

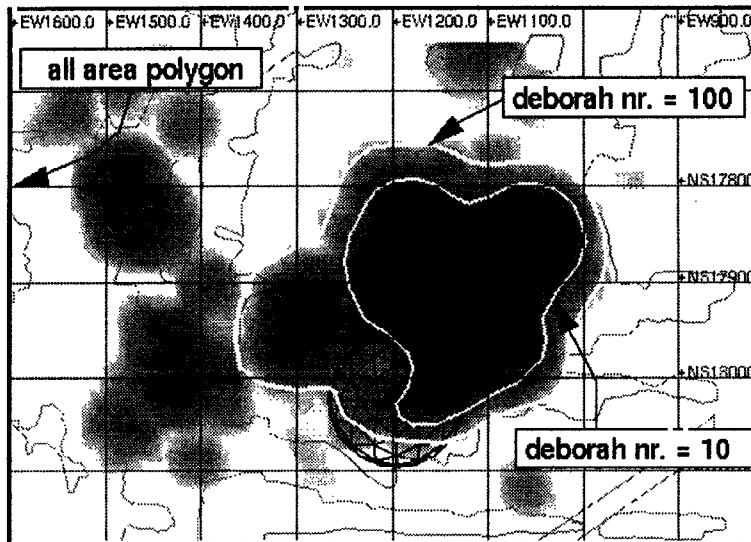


Fig.10.9b Contours of seismic Deborah number for data shown in Fig.10.9a and the outlines of the selection polygons used in the test. The mesh sphere represents V_A of event PS4-950425.

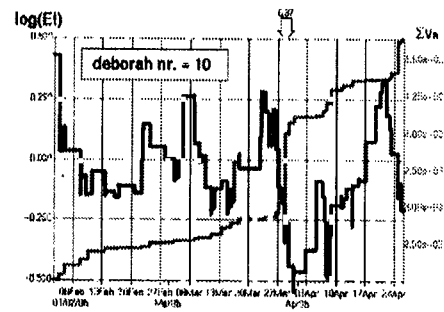


Fig.10.9c Variation in $\log(EI)$ and ΣV_A with time for each of the three polygons described. The plots end with event PS4-950425.

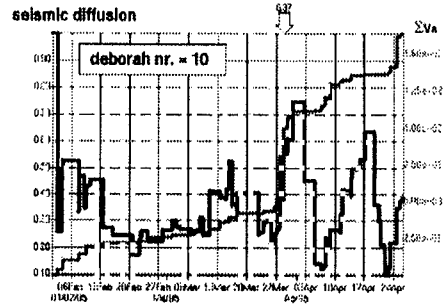


Fig.10.9d Same as Fig.10.9c, the first variable is (statistical) seismic diffusion.

While contours of seismic Deborah number proves most useful for defining appropriate clusters for stability analysis, short term contours of EI are useful to pinpoint the area where the event occurred. Fig. .. shows contours of EI based on the last 10 days of seismicity in the area of interest. An EI high as well as a high gradient in EI spatially coincide with high gradient in seismic Deborah number - a classic 'recipe' for instability.

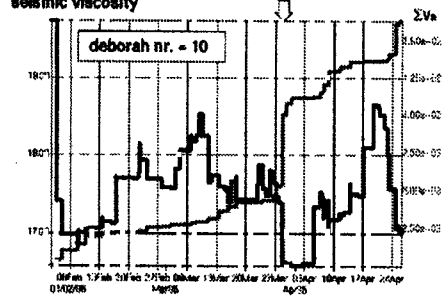


Fig.10.9e Same as Fig.10.9c, the first variable is seismic viscosity.

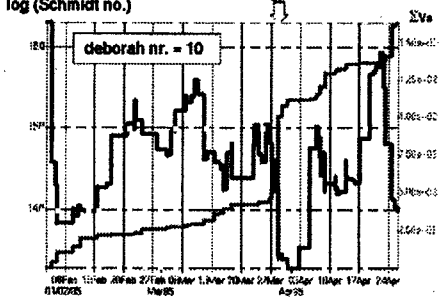


Fig.10.9f Same as Fig.10.9c, the first variable is log(seismic Schmidt number).

10.5 Velocity of Ground Motion Estimates

This section deals with estimates of ground motions based on empirically defined scaling relations. It should be made clear that such estimates are always inferior to actual measurements. Strong ground motions are, however, rarely measured by mine seismic systems simply because seismic monitoring sites are placed where it is accessible and protected against damage. Experiments to directly measure ground motions at sites of rockburst are few and results can be erratic. The application of the scaling laws is at best a rather crude engineering solution, necessitated by the lack of on-line strong ground motion measuring systems.

10.5.1 Scaling laws

Having calibrated records of the velocity of ground motion (most mine seismic networks use cost effective geophones), data bases are growing world wide with the required information to establish empirical relations between some source parameter, distance and peak velocity of ground motion. For rock engineers designing support systems for rockburst conditions this may appear to be the answer to the basic question of what velocity of ground motion to design for. Care should,

taken into account. Furthermore, (Richter) magnitude is an unfortunate choice in the above equations because it is, in many applications, estimated from seismic moment. Radiated seismic energy, by definition, should scale much better with peak ground velocity than seismic moment. Unless magnitude is directly scaled from radiated seismic energy, a more appropriate (although by no means perfect) scaling law would be of the form

$$\text{Log}(V) = a*\text{log}(E) - b*\text{log}(R) + c \quad 10.3$$

where E = radiated seismic energy. From the intermediate and near field terms of seismic displacement the value of b should be > 1 . In the Welkom and Far West Rand gold fields of South Africa, this value was found to be around 1.5 when taking into account a mixture of far field and intermediate field measurements (Butler and Van Aswegen, 1993).

A generally applicable scaling law is not appropriate because

- i) seismic systems differ in the way radiated seismic energy is calculated; and
- ii) because of variable Q , the same seismic energy radiated in different types of rock or under different stress conditions would yield different ground motions for given values of R .

A general recommendation is then to find the applicable empirical relation for the area of interest and not to constrain the value of b in equation (10.3) to 1.0.

in this regard is that very few actual measurements have been made of co-seismic slope closure rates. The estimates made based on observations of physical damage after rockbursts are very useful but suffers from the likelihood that only extreme (and therefore spectacular) cases are examined, resulting in estimates of ground motions of such amplitudes that support design is impossible anyway.

In the intermediated and near fields (where rockburst damage occurs) the peak ground motion dependence on R is extreme, i.e. small differences in R causes large differences in PPV. At the same time, the larger the event, the less meaningful is the hypocentre location provided by the seismic system - for a magnitude 2 event the source size may be well in excess of 100 m in diameter and the hypocentre location normally only reflects the point of rupture initiation (where the first seismic waves to arrive at the seismic stations originated). Although this point could be accurately found, it may be tens of metres away from the volume from which the most energy was radiated (e.g. an asperity on a fault which yielded when the rupture front passed over it).

In general, therefore, PPV scaling relations are of very limited use in support design.

Analysing shakedown damage. Many falls of ground incidents occur outside near/intermediate fields of tremors with peak ground motion way below that required to cause rockburst damage. Correlation with falls of ground incidents provide useful information about the condition of support systems, especially where the correlation is

introduced.

Because of the significant dependence of ground motions to the distance from the seismic source, care must be exercised in the construction of contour plots. Full three-dimensional contouring would generally be the best way to portray the ground motion history of a particular mining volume. In the case of tabular ore bodies a 'two-and-a-half'-dimensional contouring procedure can be followed which is quick and does not require advanced contouring tools. Gridding is taken through two phases, in the first place to establish the value of the third spatial coordinate of the ore body of interest. For example, in the case of the gently dipping, but fault disrupted reefs of the Witwatersrand, a simple reef elevation contour map is first produced. This gives, for every grid point, a reasonably accurate 3D position from which to calculate R to each event of interest. The resultant contour plot then reflects more accurately ground motions in the direct vicinity of the ore body. In the example case shown in Fig.10.10a and 10.10b this latter method has been applied, i.e. the contours reflect ground motion estimates along the undulating reef.

Fig.10.10c is added here to show how the same data set can yield widely different views of seismicity for a given area.

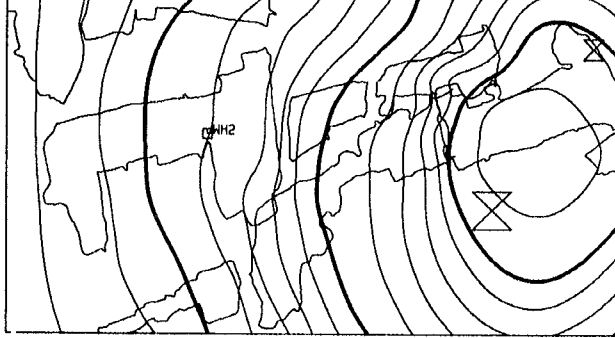


Fig.10.10b Same data set as Fig.10.10a, showing contours of estimated cumulative displacements (estimated $PPV/2\pi f_0$).

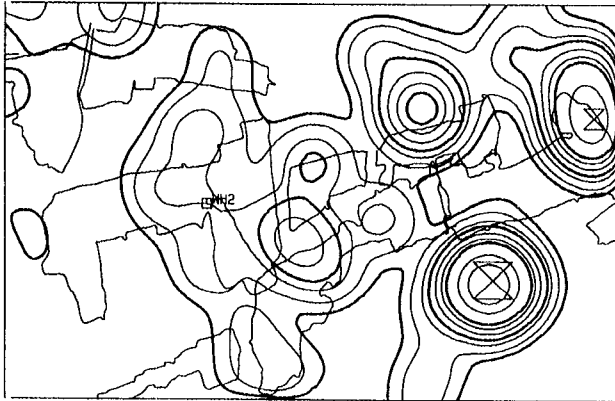


Fig.10.10c For the same data set as Fig.10.10a, contours of ΣV_A .

asperity on a fault can be recognised by observing the apparent stress and *EI* of events along the structure. It has some historical significance since it was the first major mine tremor which was spatially predicted using data from a modern digital system.

Over an eight month period, seismic events spatially associated with a fault east of President Mine No. 2 Shaft, were characterised by above average apparent stress and *EI*. The area along the fault surface thus affected covered approximately 1 km². Away from this area, very few events could be positively associated with the fault. The pattern was recognisable at the end of June 1990.

A comparison with the Trough case (see below) is of interest. An important difference is noted when considering the timing of the warning signs given by the stress indicators. In the case of the Stuirmanspan tremor, the indications of high stress around the asperity already appeared three months before the event - in the case of the Trough fault the comparable time span was less than a day. The main difference in the controlling factors is probably the rate of loading. In the case of the Stuirmanspan fault, scattered mining over a 10 year period could be considered responsible for the shear stress loading of the structure. In the case of the Trough structure, the equivalent loading period was probably less than a year.

10.6.2 The Postma Dyke

The Postma Dyke area is where the first actual ALARMS were issued. Detail descriptions of this have been given in the 1993 and 1994

around 60 MPa, reaching 120 MPa where the dyke and its 10 m pillars either side form the final remnant. All three mentioned structures exhibit excess shear stress in terms of elastic stress modelling which takes into account all mining.

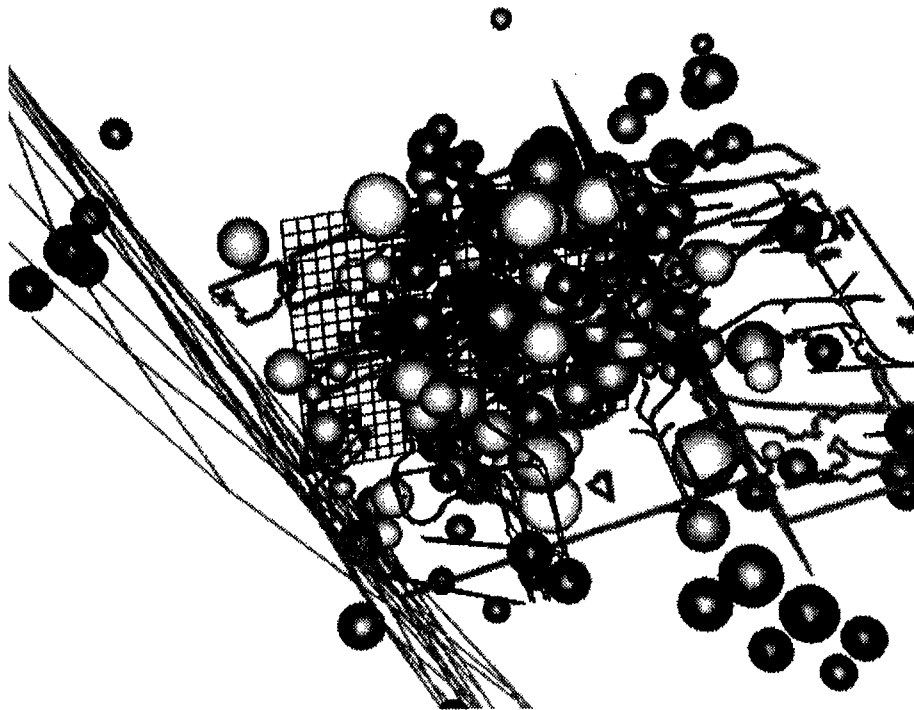


Fig.10.11 The setting of the Postma dyke (vertical mesh) with the Arrarat fault to the east (left) and the Basson fault to the west (right) and some associated seismic events.

behaving in the modern way.

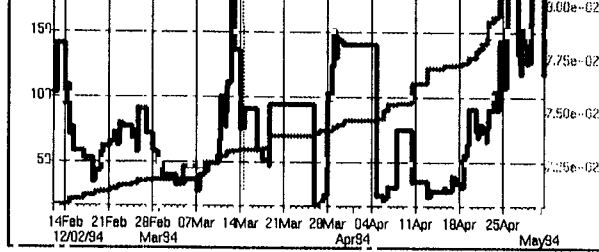


Fig.10.12b Time history of activity rate for seismicity along the Postma dyke for the period 14 February to the end of April 1994.

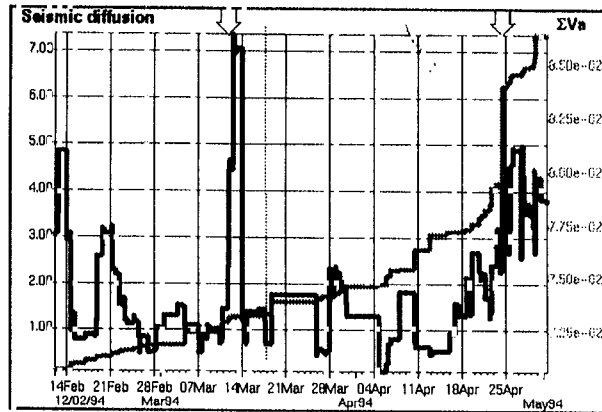


Fig.10.12c Time history of seismic diffusion for seismicity along the Postma dyke for the period 14 February to the end of April 1994.

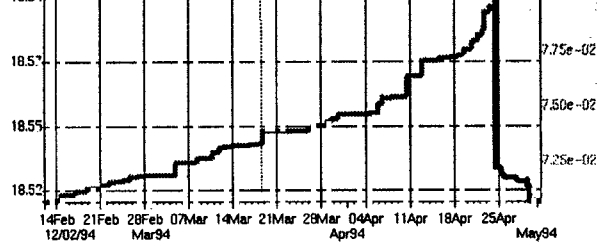


Fig.10.12e Time history of cumulative seismic viscosity for seismicity along the Postma dyke for the period 14 February to the end of April 1994.

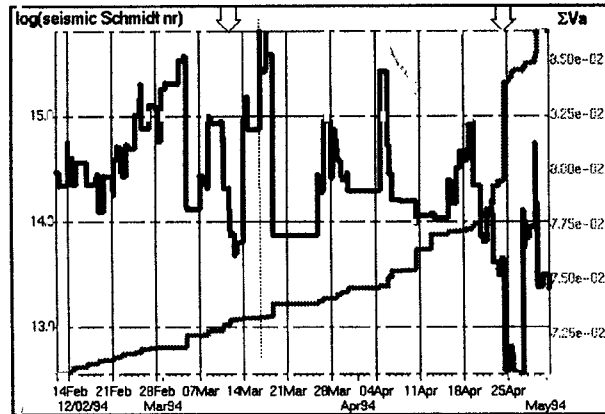


Fig.10.12f Time history of $\log(\text{seismic Schmidt nr})$ for seismicity along the Postma dyke for the period 14 February to the end of April 1994.

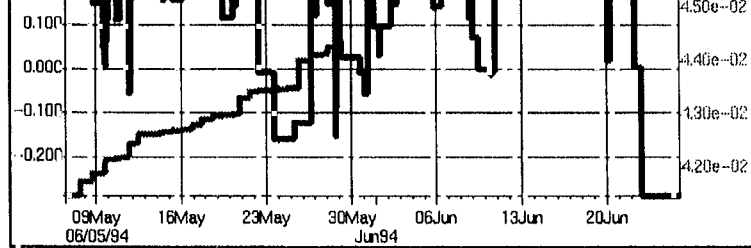


Fig.10.13a Time history plot for $\log(EI)$ and ΣV_A for seismicity along the Postma dyke from 9 May to 27 June 1994.

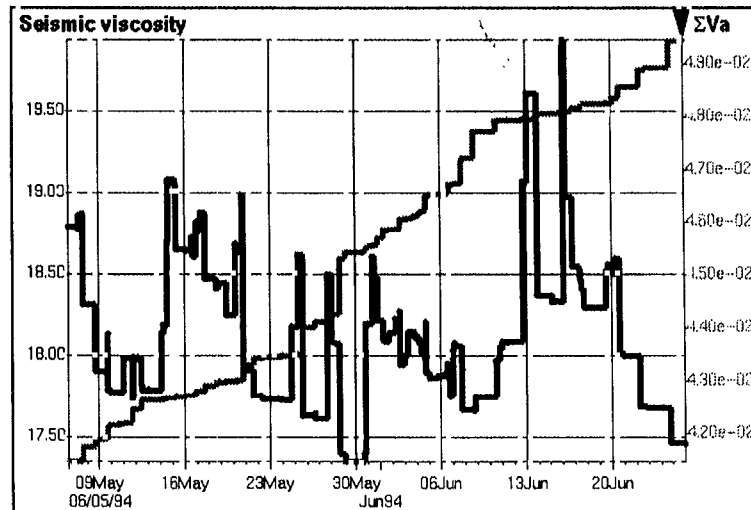


Fig.10.13b Time history plot for seismic viscosity for seismicity along the Postma dyke from 9 May to 27 June 1994.

initiated prior to the large tremor (about 200 km from the epicentre of the event to 26/6/94). Fig.10.14b shows the energy index contours along the POstma dyke, based on the last 6 weeks before the strong tremor. High energy index characterizes the intersection of the Basson fault and the Postma dyke as well as a seismic gap on the dyke east of the intersection between the dyke and the fault.

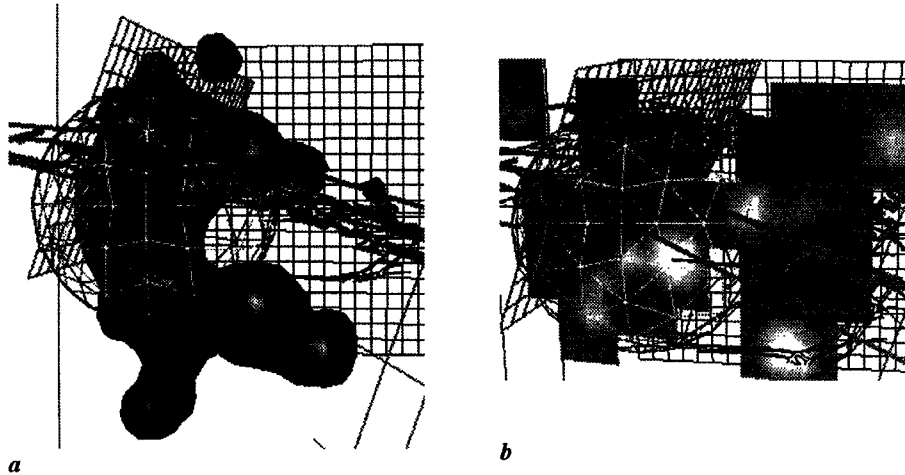


Fig.10.14 a. Iso-surface of seismic Deborah number =10 for the Postma dyke area, based on 6 months' data prior to event WSN-9406270610. The mesh sphere represents the event V_A . b. Contours of $\log(EI)$ (dark is high) along the Postma dyke for the last 6 weeks prior to the major tremor.

fault intersection. Immediate stress redistribution to the east resulted in a severe decline in seismic energy release in the west and a remarkable increase in activity to the east. Fig.10.15 demonstrates this phenomenon quite clearly.

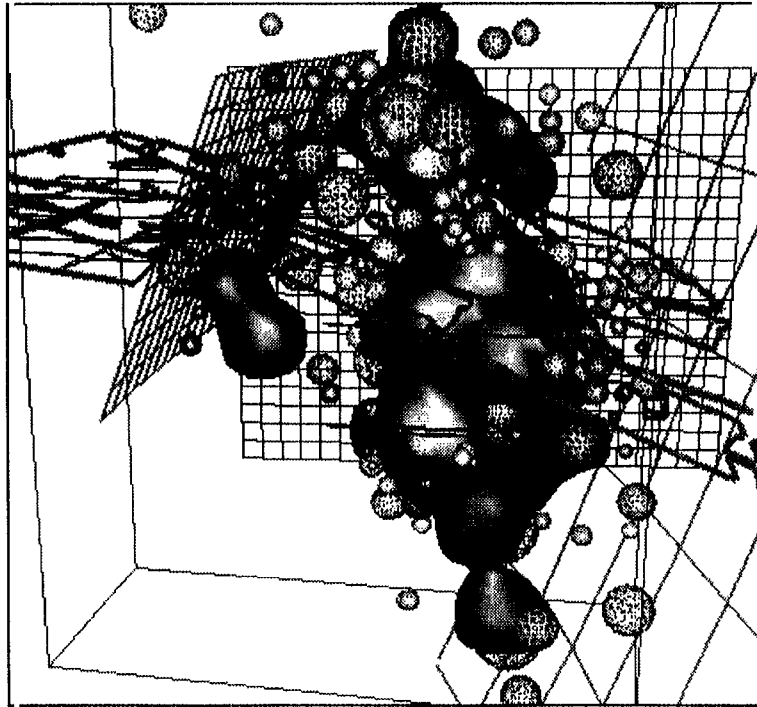


Fig.10.15 Iso-surface of seismic Deborah number and the events contributing to it for the 6 months' period after the WSN-9406270610.

Time history analyses The successful ALARM depicted in Fig.10.11a is not an isolated case. Of the 12 events above Log E 6.8 associated with the dyke during the period Oct. '93 to Dec. 94, 11 display precursory behaviour according to the stability concept, one did not and, in the case of one a lack of data does not allow any conclusions. These results are summarized in Table 10.4

Area = $1.70e^5$ $N_{events} = 1923$ $M_{min} = -0.6(HK)$							
log E	log EI		log Sc_s		CAV	Comments	*** Success
	PP**	P*	PP	P			
8.11	↓↓	↑	—	↓↓	↑		3.5
7.26	↓↓	↑	—	↓↓	↑		3.5
7.82	—	—	↑↑	↓	↑		2
7.34	—	↑	—	↑↑	—	Insuff. data	-3
6.99	—	↓	—	↓↓	↑		3.5
6.85	↓	↓	↓↓↓	↑	↑		3
7.38	↓↑	—	↓↑	↓	—		0
8.20	↓↓	↑	↑	↓↓	↑		3.5
7.15	↓	↑	↑↑	↓↓	↑		2.5
9.90	—	↓↓	↑	↓	↑		3.5
6.96	↑	↓	↑	↓↓	↑		3.5
7.26	↑	↓	—	↓↓	↑		3.5

Table 10.4 Summary of trends of log EI; log (seismic Schmidt number) and ΣV_A precursory to significant events in the Postma dyke study area.

* The arrows indicate clear trends compared to the average.

More than one arrow reflects a very strong trend.

** Two columns are used to tabulate the precursory behaviour of EI and seismic Schmidt number to include the behaviour prior to the very last precursory trend – see text.

*** Scoring of precursory behaviour:

- +1 clear steepening of ΣV_A slope
- 1 flat ΣV_A slope
- +1 clear drop in EI
- 1 clear rise in EI
- +1 strong drop in EI and recovery during final stage
- +1 clear drop in seismic Schmidt number
- 1 clear rise in seismic Schmidt number
- +½ very strong positive trend

10.6.3 Western Holdings No. 6 Shaft

The Western Holdings No. 6 Shaft (WH6#) pillar extraction provided a remarkable mimic of a rock failure test and it serves as a good example case to show the physical meaning of temporal changes in certain seismic parameters, particularly in terms of their value in quantifying the degree of rock mass stability. The mining layout and event distribution over the period 1992 - 1994 are shown in Fig.10.16a.

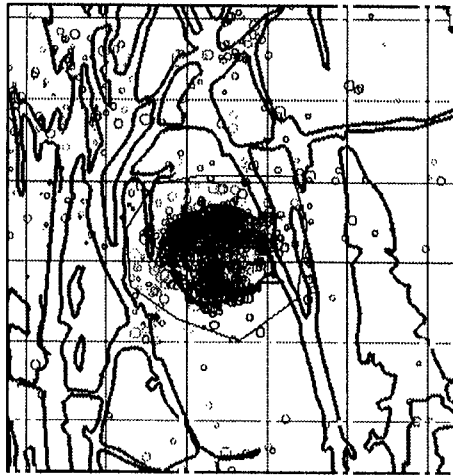


Fig.10.16a Distribution of seismic events at and around the Western Holdings No. 6 Shaft (WH6#). The grey lines outline old mine faces; note the circular shape of the shaft pillar. The black lines at the centre show the positions of the pillar mining faces during two stages. The polygon around the shaft was used for time history analysis event selection. The grey scales depict the age of the events starting from May 1992 (light) to September 1994 (dark). The grid spacing is 250 m.

Seismically, the shaft pillar displayed behaviour similar to that generally experienced in triaxial rock strength tests, namely an initial period of hardening followed by softening and accelerated deformation. Fig.10.16b shows this history in terms of cumulative V_A (apparent volume) and moving median EI (energy index). The moving time window here is large (50 days) to smooth out short term fluctuation. To imitate a stress/strain curve, Fig.10.16c is a plot of moving median EI vs. cumulative V_A showing a 'peak strength' followed by weakening and unstable behaviour.

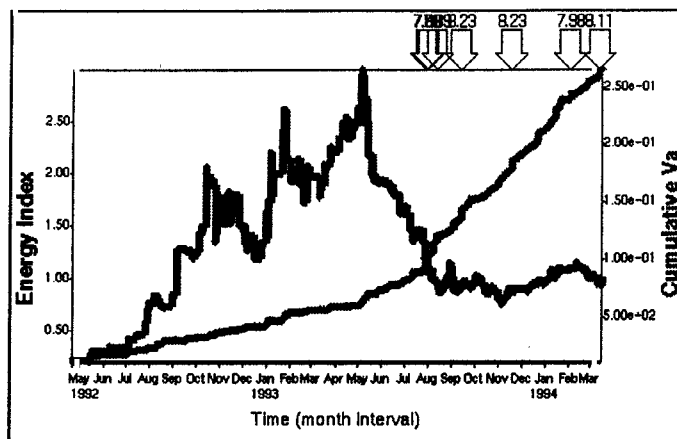


Fig.10.16b Time history of ΣV_A and moving median EI for the seismicity associated with the WH6# pillar mining, May 1992 to March 1994. Please note that all seismic events occurred after the drop in EI and during the increased rate in coseismic inelastic deformation.

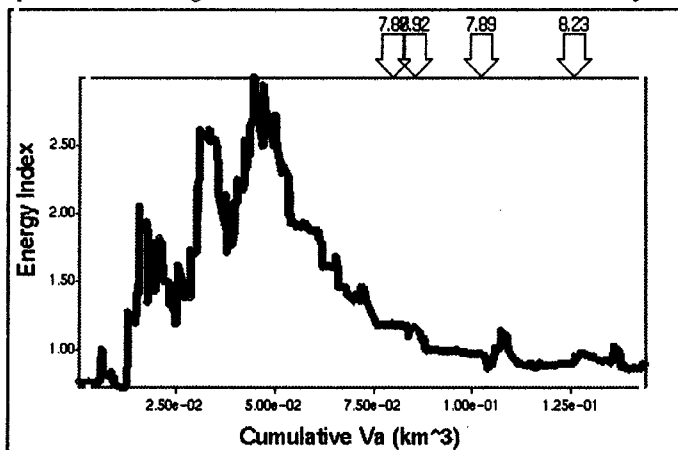


Fig.10.16c The same data as shown in Fig.16a, plotting moving median EI against ΣV_A , yielding a 'stress-strain' curve. Please note that the larger seismic events occurred during softening of the system.

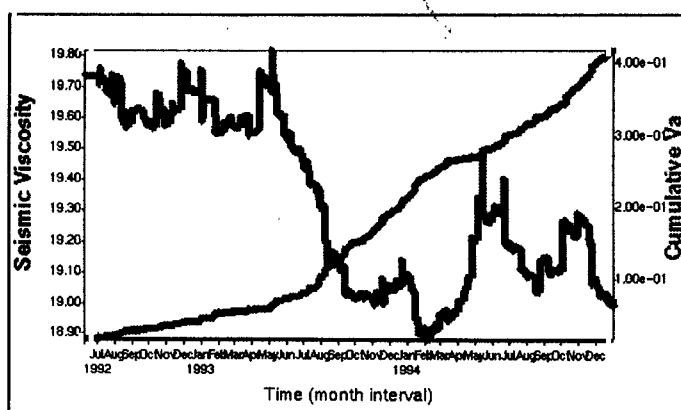


Fig.10.16d The variation of seismic viscosity with time during the mining of the WH6# pillar.

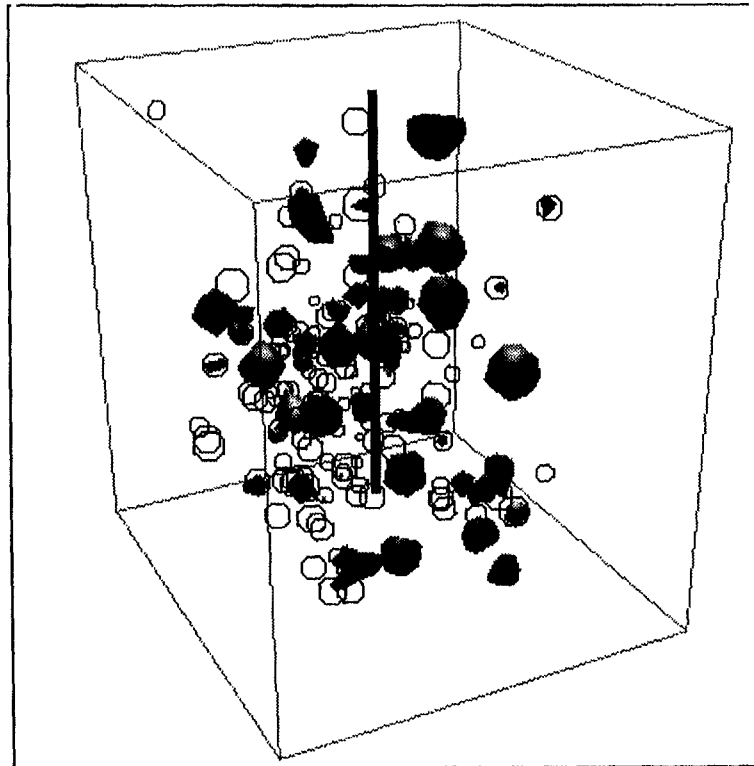


Fig.10.16e Iso-surfaces of above average EI with the seismic events around WH6# for the period January to July 1993. Scale varies in this perspective view.

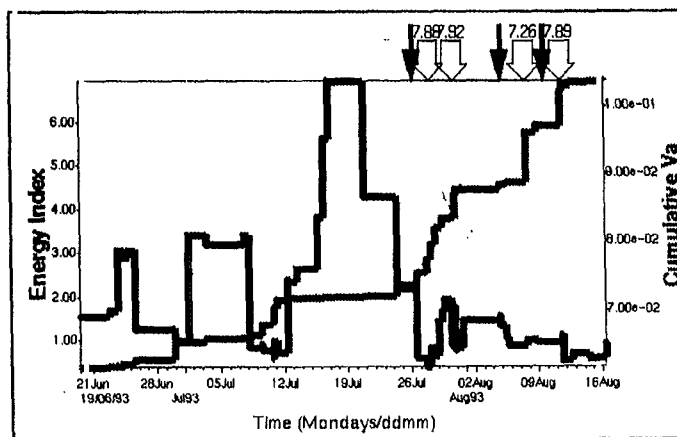


Fig.10.16f Time history analysis from WH6# for the period June to August 1993 showing variation in moving average EI, ΣV_a , the timing of the actual warnings issued (black arrows) and the timing of significant seismic events. The figures above the event indicators give their magnitudes in terms of the radiated seismic energy.

In general, the moving time window seismic viscosity decreased at WH6# from the beginning of mining the shaft pillar until the end of July 1993, after which it fluctuated around the lower level, (Fig.10.16d). Similarly, seismic Schmidt number decreased and remained relatively low after the end of July 1993.

To establish the spatial distribution of the stress increase, as indicated by EI and which culminated during May-June 1993, three-dimensional contours of EI based on events during this time period, is shown in Fig.10.16e. In fact, it indicates that stress had increased throughout the volume of interest, as can be seen by the scattered nature of small volumes of high energy index.

Seismic softening and/or accelerated coseismic deformation in the area of interest (Fig.10.16f), were found to be amongst the most successful indicators of unstable rock mass behaviour.

The two strongest seismic events which occurred during the period 1 June 1993 to 1 October 1993 are well predicted by accelerated seismic deformation as indicated by ΣV_A , drop in stress as indicated by moving median EI , increase in seismic diffusion, drop in seismic viscosity and, as a natural consequence of the latter two, a drop or low values of seismic Schmidt number (Fig.10.16g). Time history analysis of velocity of seismic diffusion is given in Fig.10.16h. Note the added information given by decomposing seismic diffusion between the three coordinate directions. In the case of WH6#, the relative values reflect the E-W geometry of the mining faces and probably the activation of a minor, near-vertical fault zone, also E-W trending, which intersects the reef in the shaft pillar, limiting the seismic diffusivity to the YZ (west-down) plane.

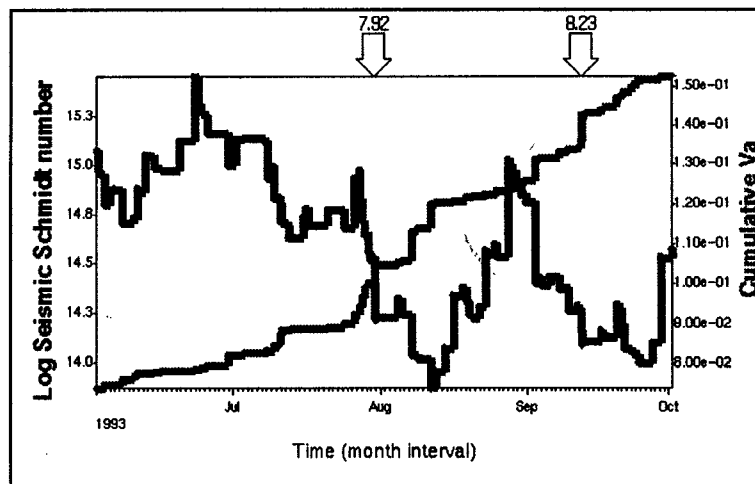


Fig.10.16g The time variation of seismic Schmidt number for the same data set reflected in Fig.10.16h.

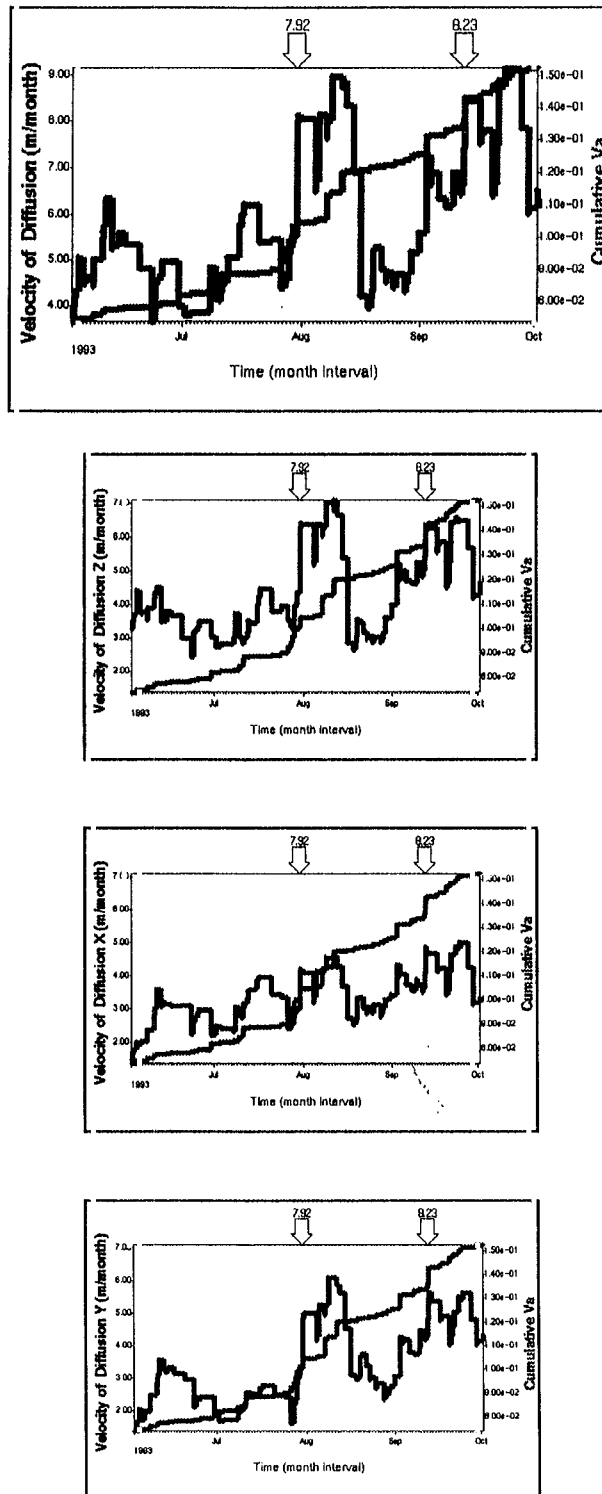


Fig.10.16h The main plot shows the time variation of the velocity of seismic diffusion with respect to two significant seismic events ($\log(E) > 7.9$). The subsequent plots reflect the decomposition of this parameter into the three coordinate directions X (n-s), Y (e-w) and Z (u-d). Note that the seismic diffusion is limited in the north-south direction and is maximum in the vertical direction. (The scale on each of the three smaller plots is the same.)

The occurrence of two particular events in the shaft pillar furthermore serve to point out how the nature of events correlate with the precursory behaviour of the pillar for 18 months prior to the two damaging events. The events were separated in time by 54 hours and in space by 200 metres. Some of the source parameters are shown in Table 10.5.

Local Magnitude	Moment log(N.m)	Energy log(J)	App Stress Bar	App volume m radius
2.5	12.6	7.8	4.90	95
2.0	12.8	7.1	6.07	50

Table 10.5 Source Parameters Examples

Despite the fact that the seismic moment of the first event is nearly one order of magnitude greater than that of the second, the apparent stress of the second is higher than that of the first. Damage caused by the first and larger event was mainly the collapse of the hanging and side walls of a tunnel. The damage associated with the second event was more concentrated and violent, as indicated by the fragment size broken rock and the presence of fresh brittle shears.

Fig.10.16i and Fig.10.16j show the positions of these events in relation to contours of seismic strain rate, seismic viscosity and EI , based on seismic data for the 18 month period ending a week before the events. In Fig.10.16h the EI contours are based on the last three months. The following observations can be made from these plots:

- a. Both events occurred adjacent to local maxima in seismic strain rate.
- b. The larger event with the lower apparent stress occurred in the area of lowest viscosity. The smaller, but more violent, event occurred in an area of high energy index, coinciding with a high gradient in seismic viscosity.

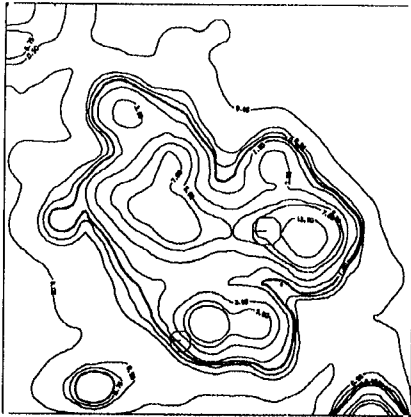


Fig.10.16i Contours of seismic strain rate [as seismic strain rate*1E13] based on an 18 month monitoring period ending a month before the two events shown. The symbol size depicts local magnitude. The box dimension is 600x600 metres.

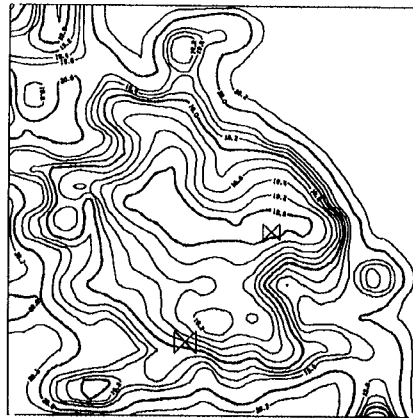


Fig.10.16j As Fig.10.16i, but showing contours of log(Seismic viscosity) and the seismic event symbol depicts apparent stress.

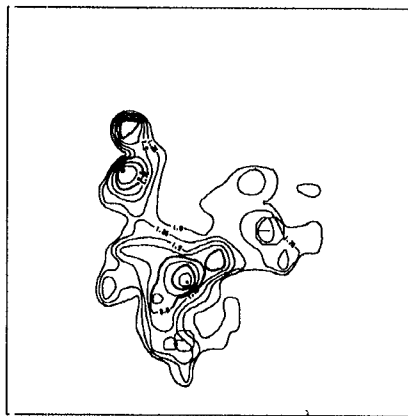


Fig.10.16k As Fig.10.16i, showing contours of average energy index.

10.6.4 The Trough event

The morning of 3 May 1994 the mine seismologist at Western Deep Levels South Mine observed that the routine contour plot of weighted energy index (averaged over four days) indicated an anomalous stress concentration around a large bracket pillar on the Trough structure (referred to as the Trough event). An updated contour plot was produced at mid day. The contours indicated a further increase in stress and a decision was made to evacuate that part of the mine and to keep workers out until the conditions changed. At 18h53 a local magnitude 4 tremor occurred along the Trough structure, followed by several aftershocks in the immediate surroundings. The details of the procedures followed are given in an internal report (Naude 1994). The analysis summarised below is from Mendecki, 1994 and Mayer and Mendecki, 1995.

The Trough structure consists of a west dipping mafic dyke which varies in thickness from 5 to 15 m. The dyke is flanked by faults of small (<20 m) throw. Available data allowed a simplified approximation of the Trough structure geometry as shown in Fig.10.17a.

The precursory behaviour of the Trough structure and environs was studied through spacetime analysis of seismic viscosity and energy index using three dimensional iso-surfaces. The most striking result from the 3D analysis was the recognition of a seismic gap between two lobes of seismic viscosity iso-surfaces, coinciding with the Trough surface. Here, seismic gap is defined as a volume of relatively high seismic viscosity (volume resisting the seismic flow of rock). Such a volume will be characterised by high spatial gradients in seismic stress and seismic strain rates, the gap being slow to deform and accumulating elastic strain. If the gap suddenly fails, a major seismic event may result. This is exactly what happened in the case of the Trough event. The stress history of the last 24 hours may be summarised by two images, the first spanning the period 18h00 on 2 May to 09h46 on 3 May and the second image covering the period 09h46 to 18h50.

During the first period, stress was generally increasing in the seismic gap and along the surrounding part of the Trough structure, as shown by differentially shaded contouring of energy index on the iso-surface of seismic viscosity and additional contour lines on the Trough structure (Fig.10.17b).

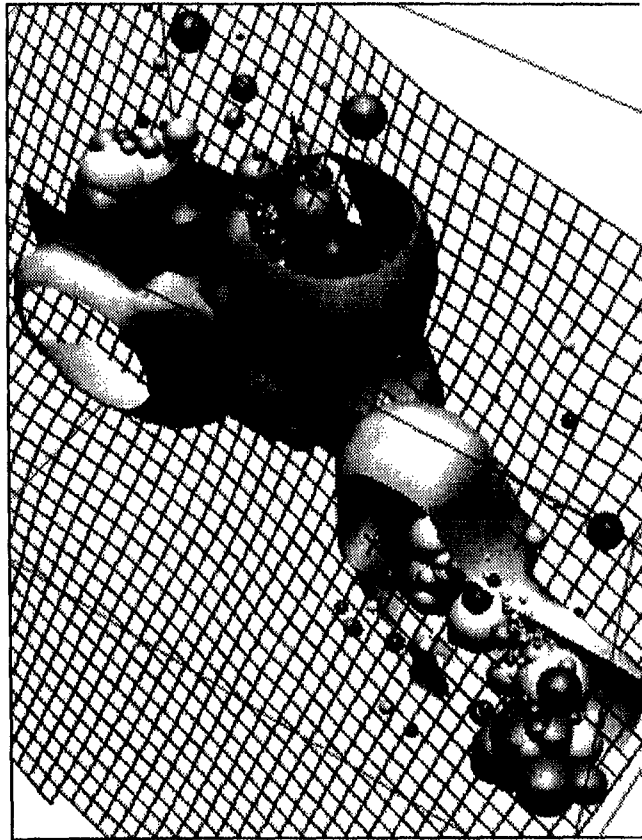


Fig.10.17a Seismic events spatially associated with the Trough structure for the period 1/1/94 - 3/5/94. The cutaway iso-surface is of a particular seismic Deborah number.



Fig.10.17b Iso-surface of seismic viscosity delineating volumes of accelerated seismic flow of rock. A gap is defined where seismic deformation is retarded and it coincides with a particular part of the Trough structure. The iso-surfaces are based on seismic events from 1/1/94 to before the Trough event of 3/5/94. The greyscale shading and contour lines on the fault surface depict variation in EI (the lighter shades reflecting high values) based on seismicity from 18h00 on 25/5/94 to 10h00 on 3/5/94. The mesh lines representing the Trough structure are spaced at 40 m.

During the second period, the stress dropped in the seismic gap reflecting the softening of this part of the rockmass (nucleation volume) where the Trough event occurred (Fig.10.17c).

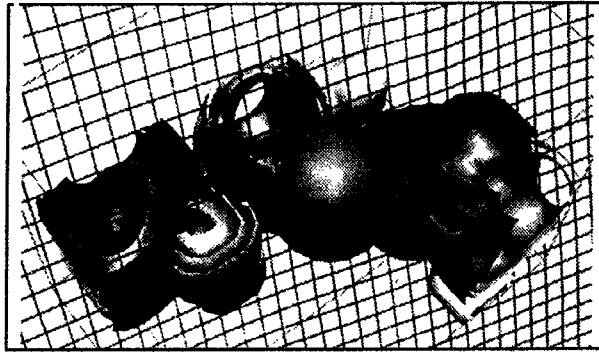


Fig.10.17c Similar to Fig.10.17b, showing isosurfaces for different seismic Deborah number values as well as the Trough event (sphere at centre).

A time history analysis of seismic viscosity and seismic diffusion shows that precursory softening and an increase in seismic diffusivity took place a few hours before the Trough event (Fig.10.17d).

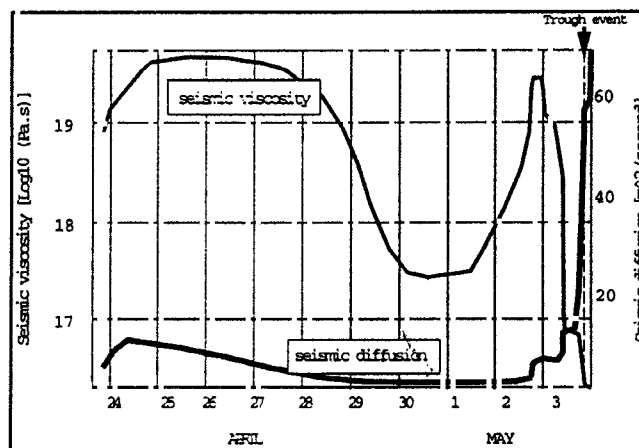


Fig.10.17d A time history analysis reflecting the seismic behaviour of the fault/bracket pillar environment during the 10 day period prior to the Trough event.

10.6.5 81/122 Longwall

The last benchmark case concerns a study area where no significant seismic events occurred during the study period. As part of the research project, the sensitivity of the mine seismic network at Western Deep Levels South Mine was increased in a part of mine which includes the section 122 longwall at 81 level. A sensitivity of

moment magnitude -0.8 was achieved, i.e. all events of moment magnitude -0.8 and larger were recorded by at least 5 three-component seismic monitoring sites. The mining was towards a potentially hazardous complex of geological structures and large events ahead of the mining face were anticipated. No large event occurred in the vicinity of the longwall, but valuable data regarding the rockmass response to production blasting was collected. The area of interest is shown in Fig.10.18a.

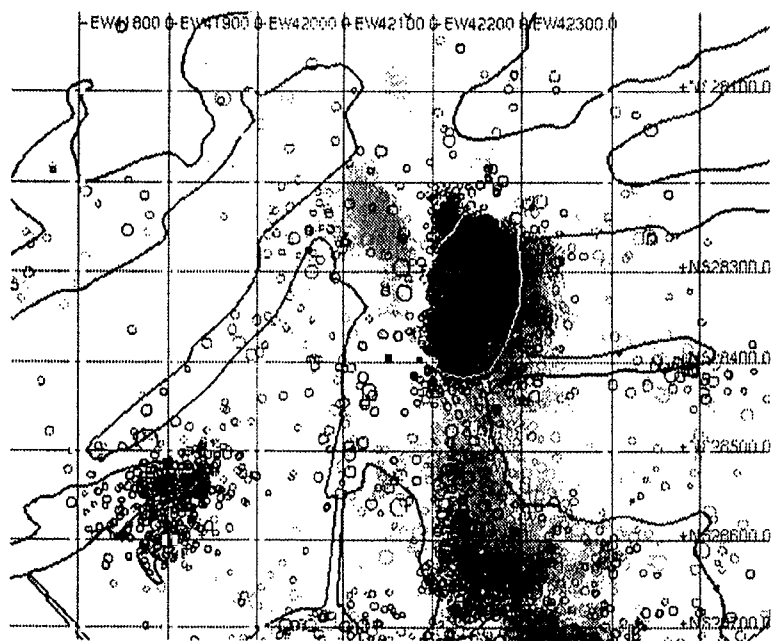


Fig.10.18a The distribution of seismic events over part of Western Deep Levels Mine during 1995. The area of interest here is the dense cluster outlined by the selection polygon.

The seismic record for the area is remarkable because over a 6 month period nearly 4200 events were recorded of which fewer than 100 (<2.4%) occurred outside of blasting time. Each of the 19 events greater than moment magnitude 1.0 were triggered by blasting. The rock mass behaviour prior to two of these rather small events are considered below.

The response to daily blasting is a 'burst' of small seismic events with $\log(EI)$ values which vary by an order of magnitude. The general pattern involves a sudden increase in EI , followed by a decrease (Fig. 10.18b). This is, of course, consistent with what is expected: a sudden increase in the elastic strain in the rockmass ahead of the advancing mining face, followed by some relaxation. The EI values of the last events reflect the level of stress to which the rock mass settled after the blast. In the case of the two events larger than local magnitude 1, it was found that this daily final EI value decreases on a daily basis

prior to the events (Fig.10.18c). The management data with such extreme time distribution presents a special problem for stability analysis.

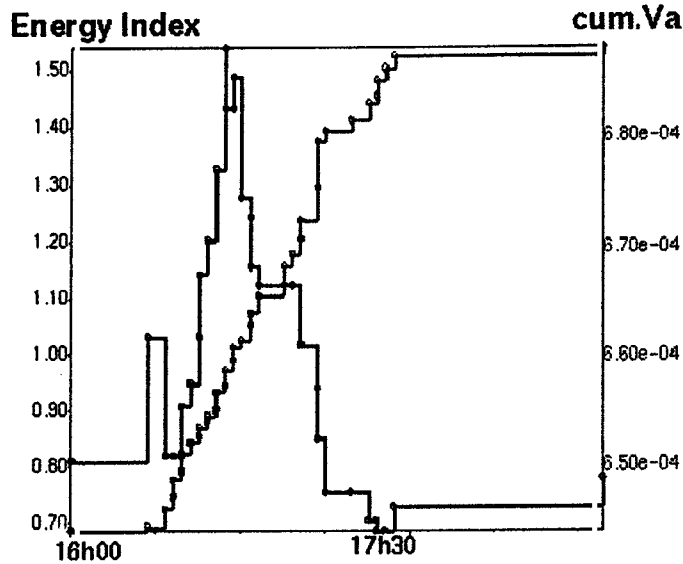


Fig.10.18b A typical response to blasting of a longwall at Western Deep Levels South Mine as measured by cumulative V_A and EI. Note the indicated initial rise in stress level and the gradual relaxation.

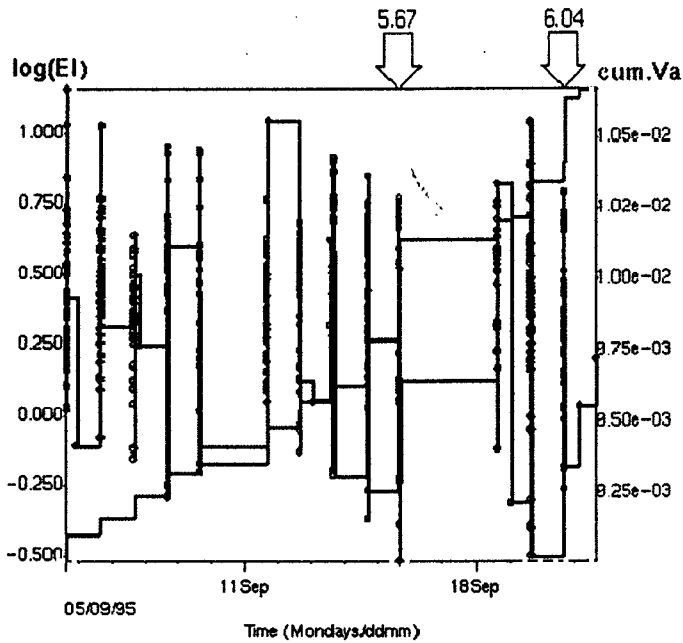


Fig.10.18c Daily response to blasting of a longwall production area at Western Deep Levels South Mine as measured by $\log(EI)$. Note the drop in both parameters prior to larger events.

The calculation of Schmidt number is highly sensitive to the length of the moving time window. By setting this time window at less than 24 hours (20 hours in this case) the specific effect of the daily blasting is quantified. A daily decrease in the value of this parameter is also observed (Fig.10.18d).

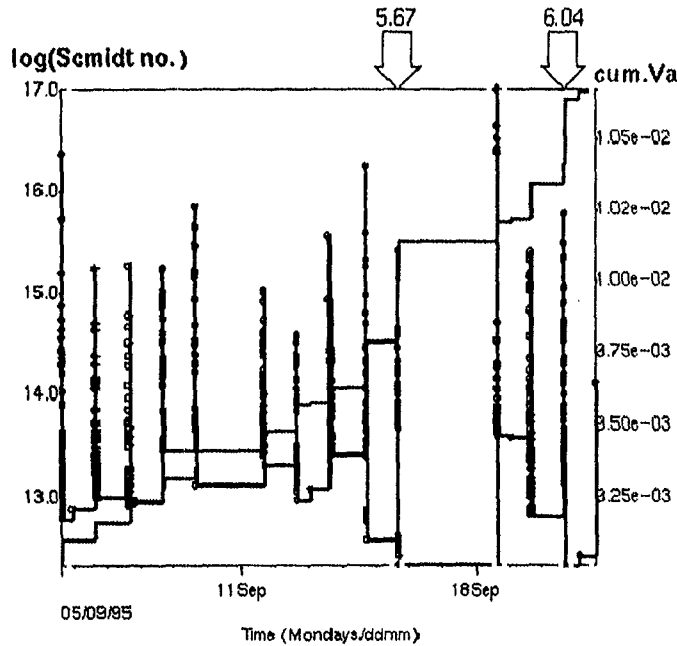


Fig.10.18d Daily response to blasting in a shaft pillar mining area at Welkom as measured by Log(seismic Schmidt number). Note the drop in both parameters prior to a larger event.

The scale invariance of the space/time processes precursory seismic events is illustrated by a 20 minute long seismic history in the study area on 21 October 1995, see Fig.10.18g. Here a local magnitude 0.5 event, triggered by blasting, was preceded by accelerated seismic strain rate (steepened slope of the ΣV_A curve), by a drop in EI and a drop in seismic Schmidt number, Fig.10.18e and 10.18f. In space, the small tremor occurred in a 'seismic gap' with a diameter of 50 metres. The edge of the gap was characterised by high EI . The seismic history prior to this event is therefore similar to that of most large events, but at a different scale in space and time.

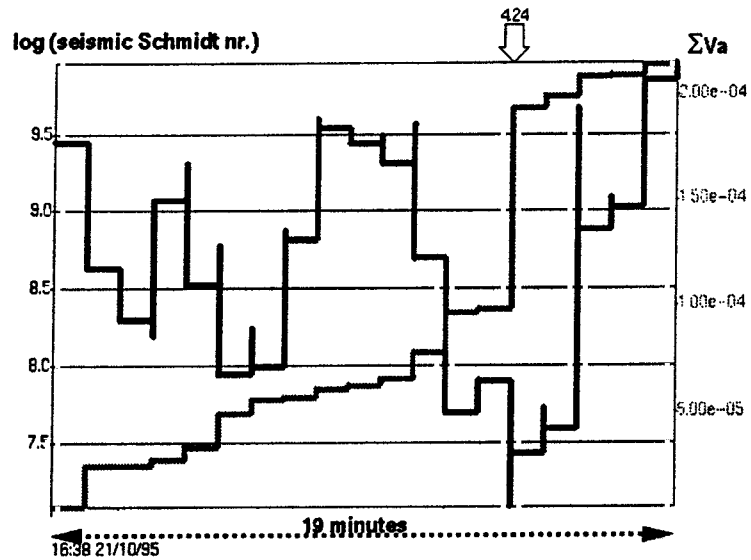


Fig.10.18e Time history plot of log (seismic Schmidt number) for seismicity in the 19 minute period prior to a local magnitude 0.5 event.

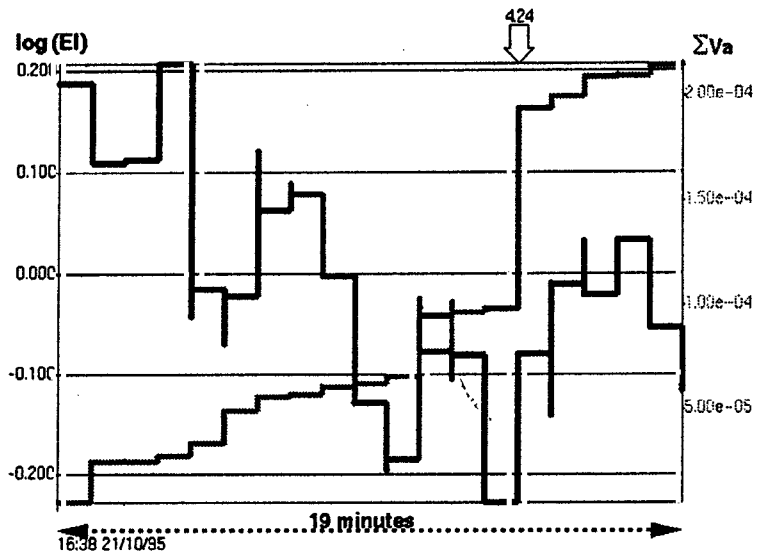


Fig.10.18f Time history plot of log (EI) for seismicity in the 19 minute period prior to a local magnitude 0.5 event.

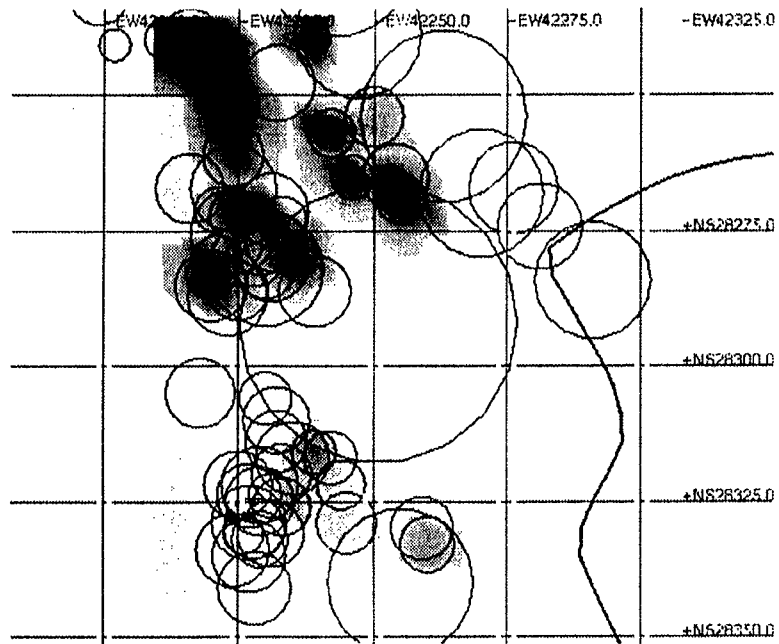


Fig.10.18g The location of the magnitude 0.5 event shown in Fig.10.18e and Fig.10.18f, relative to the seismicity in the 20 minute period prior. The dark shading show high EI along the margin of the seismic gap which was taken out by the tremor.

REFERENCES

- Abarbanel, H.D.I. (1990). Prediction in chaotic nonlinear systems: Methods for time series with broadband Fourier Spectra. *Physical Review A*, **41**, 1782.
- Abercrombie, R.E., Agnew, D.C. and Wyatt, F.K. (1995). Testing a model of Earthquake Nucleation. *Bull. Seism. Soc. Am.*, **85**, 6, 1873 - 1878.
- Abramowitz, M., and Stegun, I.A. (1970). *Handbook of Mathematical Functions*. 9th ed. Dover Publ., New York.
- Aki, K., and Richards, P.G. (1980). Quantitative Seismology. *Theory and Methods*, W.H. Freeman and Company, San Francisco.
- Aki, K., and Lee, W.H.K. (1976). Determination of three-dimensional velocity anomalies under a seismic array using first P arrival times from local earthquakes. 1. A homogeneous initial model. *J. Geophys. Res.* **81**, 4381-4399.
- Aki, M. (1965). Maximum likelihood estimate of b in the formula $\log N = a - bM$ and its confidence limits. *Bull. Earthquake Res. Inst.*, Tokyo Univ. **43**, 237-239.
- Aki, K. (1981). A probabilistic synthesis of precursory phenomena. In: *Earthquake Prediction*, (D.W. Simpson and P.G. Richards, eds.), American Geophysical Union, Washington, D.C., 566-574.
- Alberto, D., Mucciarelli, M., and Mantovani, E. (1989). Use of non-parametric correlation tests for the study of seismic interrelations. *Geophys. J.* **96**, 185-188.
- Alessandrini, B., and Perazzolo, E. (1987). An interactive technique for the deconvolution of seismograms. *Bull. Seism. Soc. Am.*, **77**, 4381-4399.
- Allgower, E.L. and Georg, K. (1990). *Numerical continuation methods, an introduction*. Springer.
- Anderson, J.G., Brune, J.N., Louie, J., Zeng, Y., Savage, M., Yu, G., Chen, Q., and de Polo, D. (1993). Seismicity in the Western Great Basin apparently triggered by the Landers, California Earthquake, June 28, 1992. Preprint, August 3, 1993, 19.
- Anderson, J.G., Louie, J., Brune, J.N., de Polo, D., Savage, M., and Yu, G. (1992). Seismicity in Nevada apparently triggered by the Landers, California, earthquake, June 28, 1992. (abstract), *EOS Supplement*, 1992 Fall Meeting, American Geophysical Union, 393.
- Anderson, K.R. (1982). Robust earthquake location using M-estimates. *Phys. Earth Planet. Interiors* **30**, 119-130.
- Anderson, J.G. (1979). Estimating the seismicity from geological structure for seismic risk studies. *Bull. Seism. Soc. Am.*, **69**, 135-158.
- Backus, G.E. and Mulcahy, M. (1976a). Moment tensor and other phenomenological descriptions of seismic sources. I. Continuous displacements. *Geophys. J.R. Astron. Soc.*, **46**, 341-361.
- Backus, G.E. and Mulcahy, M. (1976b). Moment tensor and other phenomenological descriptions of seismic sources. II. Discontinuous

- displacements. *Geophys. J.R. Astron. Soc.*, **46**, 301-329.
- Backus, G.E. (1977a). Interpreting the seismic glut moments total degree two or less. *Geophys. J.R. Astron. Soc.* **51**, 1-25.
- Backus, G.E. (1977b). Seismic sources with observable glut moments of spatial degree or two. *Geophys. J.R. Astron. Soc.* **51**, 27-45.
- Baher, H. (1990). *Analog and digital signal processing*. John Wiley & sons.
- Bataille, K. and Chiu, J.M. (1991). Polarization analysis of high-frequency, three-component seismic data. *Bull. Seism. Soc. Am.*, **81**, no.2, 622-642.
- Båth, M. (1984a). Correlation between regional and global seismic activity. *Tectonophysics* **104**, 187-194.
- Båth, M. (1984b). Correlation between Greek and global seismic activity. *Tectonophysics* **109**, 345-351.
- Bebbington, D., Vere-Jones, D. and Zheng, X. (1990). Percolation theory: a model for rock fracture? *Geophys. J. Int.*, **100**, 215-220.
- Ben-Menahem, A. and Singh, J. (1981). *Seismic waves and sources*. Springer-Verlag, New York.
- Benade, F. 1994. Seismic index: a study of illuminating hazardous areas on the mine. A case study of the sequence of events on 2 and 3 May 1994. *Internal report, Western Deep Levels South*. 12.
- Ben-Zion, Y. and Rice, J.R. (1993). Earthquake failure sequences along a cellular fault in a three-dimensional plastic solid containing asperity and non-asperity regions, *J. Geophys. Res.* **98**, B8, 14109 - 14131.
- Boatwright, J., Fletcher, J.B. and Fumal, T.E. (1991). A general inversion scheme for source, site and propagation characteristics using multiply recorded sets of moderate-sized earthquakes. *Bull. Seism. Soc. Am.* **81**, 1754-1782.
- Brady, B.T. (1977). Anomalous seismicity prior to rock bursts: implications for earthquake prediction. In: *Stress in the Earth*, M. Wyss (ed.), Special Issue, *Pure Appl. Geophys.*, **115**, 357-374.
- Brady, B.J. (1977). An investigation of the scale invariant properties of failure. *Int. J. Rock Mech. Min. Sci. & Geomech. Abstr.*, **14**, 121-126.
- Brigham, E.O., Smith, H.W., Bostik, F.X., and Duesterhoeft W.C. (1968). An iterative technique for determining inverse filters. *IEEE Trans. Geosci. Electronics*, **GE-2**, 86-96.
- Brink, A.v.Z. (1990). Application of microseismic system at Western Deep Levels. In: *Rockbursts and Seismicity in Mines*, Proceedings of the 2nd International Symposium on Rockbursts and Seismicity in Mines, Minneapolis, Minnesota, Canada, 8-10 June 1988, C. Fairhurst (ed.), 355-361. Rotterdam, Balkema.
- Brune, J.N. (1970). Tectonic stress and the spectra of seismic shear waves. *J. Geophys. Res.*, **75**, 4997-5009, (Correction, *J. Geophys. Res.*, **76**, 5002, 1972).
- Buland, R. (1976). The mechanics of locating earthquakes. *Bull. Seism. Soc.*

- Am.* **66**, 173-187.
- Burmin, V. Y. , (1986). Optimal placement of seismic stations for registration of near earthquakes. *Izv. Akad. Nauk SSR, Earth Phys.* **22**, 366-372.
- Butler, A.G. and van Aswegen, G. (1993). Ground velocity relationships, based on a large sample of underground measurements in two South African mining regions. *Proceedings of third International Symposium on Rockburst and Seismicity in Mines*, Kingston, Ontario, Canada, AA Balkema, Rotterdam.
- Butler, A.G. (1993)a. Application of weighted energy index for routine evaluation of rockburst potential. *Internal Report*, August 1993. ISS International, Welkom.
- Butler, A.G. (1993)b. Large seismic events: minimal precursory seismicity. *ISS International internal report*, November 1993.
- Cao, S. and Greenhalgh, S. (1993). Calculation of the seismic first-break time field and its ray path distribution using a minimum travelttime tree algorithm. *Geophys. J. Int.*, **114**, 593-600.
- Cao, S. and Greenhalgh, S. (1994). Finite-difference solution of the eikonal equation using an efficient, first-arrival, wavefront tracking scheme. *Geophysics*, **59**, 632-643.
- Červený, V. and Firbas, P. (1984), Numerical modelling and inversion of travel times of seismic body waves in inhomogeneous anisotropic media. *Geophys. J.R. Astron. Soc.* **76**, 41-51.
- Cerveny, V., Molotkov, I.A. and Psencik, I. (1977). *Ray methods in seismology*. University of Karlova Press, Prague.
- Chander, R. (1975). On tracing seismic rays with specified end points. *J. Geophys.*, **41**, 173-177.
- Chang, A.C., Shumway, R.H., Blandford, R.R., and Barker, B.W. (1983). Two methods to improve location estimates - preliminary results. *Bull. Seism. Soc. Am.* **73**, 281-295.
- Chiaruttini, C., Kijko, A., and Teisseyre, R. (1980). Tectonic discrimination of the Friuli earthquakes. *Bull. Geofis. Ther. Appl.* **22**, 295-302.
- Christoffersson, A., Husebye, E.S. and Ingate, S.F. (1988). Wavefield decomposition using ML-probabilities in modelling single site three-component records. *Geophys. J.* **93**, 197-213.
- Cosentino, P., Ficara, V., and Luzio, D., (1977). Truncated exponential frequency-magnitude relationship in the earthquake statistics. *Bull. Seism. Soc. Am.* **67**, 1615-1623.
- Cox, D.R., and Snell, E.J. (1989). *Analysis of Binary Data*. Second Edition, Chapman & Hall, London.
- Cox, S.J.D. and Paterson, L. (1990). Damage development during rupture of heterogeneous brittle materials: a numerical study. In Knipe, R.J. and E.H. Rutter (eds) *Deformation Mechanisms, Rheology and Tectonics*. Geological Society Special Publication No.54, 143-165.

- Cox, D.R., and Hinkley, D.V. (1974). *Theoretical Statistics*. Chapman and Hall, London.
- Cox, D.R. (1975). *Partial likelihood*. *Biometrika*, **62**, 269-276.
- Crampin, S., and Fyfe, C.J. (1974). Automatic analysis of tape recordings from seismic networks. *Geophys. J. R. Astron. Soc.* **39**, 155-168.
- Crosson, R.S. (1976). Crustal structure modelling of earthquake data. 1. Simultaneous least squares estimation of hypocentre and velocity parameters. *J. Geophys. Res.* **81**, 3036-3046.
- Crosson, R.S. (1974). Non-linear least squares crustal structure estimation from earthquake data, abstract. *EOS Trans. Am. Geophys. Union* **56**, 1145.
- Crosson, R.S. (1976b). Crustal structure modelling of earthquake data. 2. Velocity structures of the Puget Sound region, Washington. *J. Geophys. Res.* **81**, 3047-3053.
- Cundall, P.A. (1996). *Particle Flow Code*. Itasca Consulting Group, Minneapolis, Minnesota.
- Cundall, P.A. (1990). Numerical modelling of jointed and faulted rock. In: *Mechanics of Jointed and Faulted Rock*, Rossmannith (ed.), Balkema, Rotterdam.
- Darot, M. and Gueguen, Y. (1986). Slow crack growth in minerals and rocks: Theory and Experiments. *PAGEOPH*, **124**, 4/5, 677-602.
- Daubechies I., *Ten Lectures On Wavelets*, SIAM, 1992.
- Dielman, T., and Pfaffenberger, R.C. (1982). LAV (Least Absolute Value) estimation in linear regression: A review. In: *TIMS Studies in Management Science*. (S. Zanakis and J. Rustagi, eds) North Holland, Amsterdam, 31-52.
- Dimri, V. (1992). *Deconvolution and Inverse Theory. Application to Geophysical Problems*. Elsevier, Amsterdam.
- Dorize C., Gram-Hansen, K. (1992). Related Positive Time-Frequency Energy Distributions. in: Meyer Y.(editor), *Wavelets and Applications*, Springer-Verlag.
- Draper, N.R., and Smith, H. (1981). *Applied Regression Analysis*. 2nd ed., John Wiley and Sons, New York.
- Drzezla, B., and Mendecki, A. (1982b). Joint hypocentre location of mining tremors and determination of anisotropy parameters of P-wave velocity. *Acta Geophys. Pol.* **30**, 321-332.
- Drzezla, B., and Mendecki, A. (1982a). The velocity anisotropy of rock mass and location accuracy of mining tremors. *Acta Geophys. Pol.* **30**, 231-241.
- Eadie, W. T., Drijard, D., James, F. E., Roos, M., and Sadoulet, B. (1982). *Statistical Methods in Experimental Physics*. 2nd reprint, North-Holland, Amsterdam.

- Ekblom, H. and Henriksson, S. (1969). L_p -criteria for the estimation of location parameters. *SIAM J. Appl. Math.* **17**, 1130-1141.
- Eneva, M. (1996). *Application of some concepts of nonlinear dynamics to rockburst prediction*. Report to ISS International, Welkom, South Africa, January 1996.
- Fedorov, V.V. (1972). *Theory of Optimal Experiments*, Academic Press, New York.
- Fedorov, V.V. (1974). *Regression problems with controllable variables subject to error*. *Biometrika* **61**, 49-55.
- Fehler, M. and Phillips, W.S (1991). Simultaneous inversion for Q and source parameters of microearthquakes accompanying hydraulic fracturing in granite rock. *Bull. Seism. Soc. Am.* **81**, 553-575.
- Ferber R.G.(1989). Recursive deconvolution filters for seismograph Systems. *Bull. Seism. Soc. Am.*, **79**, No.5, 1629-1641.
- Finnie, G. (1994). A stationary model for time-dependent seismic hazard in mines. *Acta Geophys. Pol.*, **42**, (in print).
- Fischer, K.M. and Jordan, T.H. (1991). Seismic strain rate and deep slab deformation in Tonga. *J. Geophys. Res.*, **10**, 14423-14444.
- Flynn, E.A.(1965). Signal analysis using rectilinearity and direction of particle motion. *Proc. IEEE*, **53**, 1874-1876.
- Forsythe, A.B. (1972). Robust estimation of straight line regression coefficients by minimizing p^{th} deviations. *Technometrics*, **14**, 159-166.
- Fröhlich, C., and Davis, S.D. (1990). Single-link cluster analysis as a method to evaluate spatial and temporal properties of earthquake catalogs. *Geophys. J. Int.* **100**, 19-32.
- Fröhlich, C., and Apperson, K.D. (1992). Earthquakes focal mechanisms, moment tensors and the consistency of seismic activity near plate boundaries. *Tectonic*, **11**, 279-296.
- Fröhlich, C., Riedesel, M.A. and Apperson, K.D. (1989). Note concerning possible mechanism for non-double-couple earthquake sources. *Geophys. Res. Lett.*, **16**, 523-526.
- Fröhlich, C. (1993). Where do "sweet" earthquakes occur? Characteristics of well-determined deviatoric non-double-couple shallow earthquake sources. *Supplement EOS*, 20 April 1993.
- Gibowicz, S.J., Kijko, A. (1994). *An Introduction to Mining Seismology*. Academic Press, New York.
- Gibowicz, S.J. (1979). Space and time variations of the frequency-magnitude relation for mining tremors in the Szombierki coal mine in Upper Silesia, Poland. *Acta Geophys. Pol.* **37**, 39-49.
- Gibowicz, S.J., Harjes, H.P. and Schafer, M. (1990). Source parameters of seismic events at Heinrich Robert Mine, Ruhr Basin, Federal Republic of Germany: Evidence for non-double-couple events. *Bull. Seism. Soc.*

- Am.* **80**, 88-109.
- Golub, G.H., and Reinsch, C. (1971). Singular value decomposition and least squares solutions. in *Linear Algebra*, (J.H. Wilkinson and C. Reinisch, ed.), Springer - Verlag, New York.
- Gonin, R. and Money, A.H. (1985a). Nonlinear L_p -norm estimation: Part I - On the choice of the exponent, p , where the errors are adaptive. *Commun. Statist. - Theor. Meth.* **14**, 827-840.
- Gonin, R. and Money, A.H. (1985b). Nonlinear L_p -norm estimation: Part II - Asymptotic distribution of the exponent p , as a function of the sample kurtosis. *Commun. Statist. - Theor. Meth.* **14**, 841-849
- Gonin, R., and Money, A.H. (1987). Outliers in physical processes: L_1 - or adaptive L_p -norm estimation? In: *Statistical Data Analysis Based on the L_1 -Norm and Related Methods*, (Y. Dodge, ed.), 464-454.
- Green, R.W.E, (1984). Monitoring safety in geotechnical engineering. *Proc. S. Afr. National Group Rock Mechanics Symp.* September 1984.
- Green, R.W.E, (1984). Electronic designs for mine seismic networks. *Elektron S. Afr. Inst. Electrical Engineers* **2(9)**, 5-14.
- Green, R.W.E, (1988). Instrumentation networks for observation of mine-induced seismicity. Keynote Presentation. *Proc. 2nd Int. Symp. of Rockbursts and Seismicity in Mines.* Univ. of Minnesota. 8-10 June 1988, 142-156.
- Gutzwiller, M.C. (1991). *Chaos in classical and quantum mechanics.* Springer, Berlin.
- Hanks, T.C. and Thatcher, M. (1972). A graphical representation of seismic source parameters. *J. Geophys. Res.*, **23**, 4393-4405.
- Hanks, T.C. and Kanamori, H. (1978). A moment magnitude scale. *EOS Trans. Am. Geophys. Union* **59**, 1128.
- Hanyga, A. (1988). Numerical tracing of rays and wavefronts. In: *Seismological algorithms* (ed. D. Doornbos), Academic Press, Inc.
- Hanyga, A. (1991). Implicit curve tracing and point-to-curve ray tracing. *Seismo-series*, **56**, Bergen.
- Hanyga, A. and Pajchel, J. (1995). Point-to-curve ray tracing in complicated geological models, submitted to *Geophys. Prosp.*
- Harter, H.L. (1972). The Method of Least Squares and Some Alternatives. ARL Technical Report 72-0129, Aerospace Research Laboratories, Wright-Patterson Air Force Base, Ohio. AD 752211. (Abstract, *Instit. Math. Statist. Bull.* **1**, 257-258.)
- Hatton, L., Worthington, M.H., and Makin, J. (1986). *Seismic Data Processing. Theory and Practice.* Blackwell Scientific Publishers, Oxford.
- Hawkes, A.G. and Adamopoulos, L. (1973). Cluster models for earthquakes: regional comparisons. *Bull. Int. Stat. Inst.*, **45**, 454-461.
- Heiss, W.D., Nazmitdinov, R.G. and Radu, S. (1995). Periodic orbits and shell

- structure in Octupole deformed potentials. *Physical Review B*, **51**, 1874.
- Herrmann, R.B. (1979). FASTHYPO-A hypocentre location program. *Earthq. Notes* **50**, 25-37.
- Hill, R. (1958). A general theory of uniqueness and stability in elastic-plastic models. *J. Mech. Phys. Solids*, **6**, 236-249.
- Hill, R. (1957). On uniqueness and stability in the theory of finite elastic strain. *J. Mech. Phys. Solids*, **5**, 229-241.
- Hill, D.P., Reasenber, P.A., Michael, A., Arabasz, W.J., Beroza, G., Braumbaugh, D., Brune, J.N., Castro, R., Davis, S., de Polo, D., Ellsworth, W.L., Gomberg, J., Harmsen, S., Hause, L., Jackson, S.M., Johnston, M.J.S., Jones, L., Keller, R., Malone, S., Maunguia, L., Nava, S., Pechmann, J.C., Sanford, A., Simpson, R.W., Smith, R.W., Stark, M., Stickney, M., Vidal, A., Walter, S., Wong, V., and Zollweg, J. (1993). Seismicity remotely triggered by the magnitude 7.3 Landers, California earthquake. *Science*, **260**, 1617-1623.
- Himmelblau, M. (1972). *Applied Nonlinear Programming*. McGraw-Hill, New York.
- Hirata, T., Satoh, T. and Ito, K. (1987). Fractal structure of spatial distribution of micro-fracturing in rock. *Geophys. J.R. Astron. Soc.*, **90**, 369-374.
- Hobbs, B.E., Mühlhaus, H.B. and Ord, A. (1990). Instability, softening and localization of deformation. In Knipe, R.J. and E.H. Rutter (eds) *Deformation Mechanisms, Rheology and Tectonics, Geological Society Special Publication No.54*, 143-165.
- Holcomb, D.J. (1992). *Localisation studies under triaxial conditions*. R.S. Mechanics, Tillerson and Wawersik (eds), Balkema, Rotterdam, 661-670.
- Hopkins, D.L., Cook, N.G.W., and Myer, L.R.. (1990). Normal joint stiffness as a function of spatial geometry and surface roughness. In: *Rock Joints*, (Eds. Barton and Stephansson) Balkema, Rotterdam, 203-210.
- Horii, H. and Nemat-Nasser, S. (1986). Brittle failure in compression: Splitting, faulting and brittle-ductile transition. *Phil. Trans. R. Soc., Land., A*, **319**, 337-374.
- Humphrey, J. R. and Anderson, J.G. (1992). Shear-wave attenuation and site response in Guerrero, Mexico. *Bull. Seism. Soc. Am.* **82**, 1622-1645.
- Ishimoto, M. and Iida, K. (1939). Observations sur les seimes arregistres par le micorseismographe construit dernièrement. *Bull. Earthquake Res. Inst. Tokyo Univ.*, **17**, 443 - 478 (in Japanese).
- Jackson, J. and McKenzie, D. (1988). The relationship between plate motions and seismic moment tensors, and the rates of active deformation in the Mediterranean and Middle East. *Geophys. J.* **93**, 45-73.

- Jackson D.D. (1972). Interpretation of inaccurate, insufficient and inconsistent data. *Geophys. J.*, **28**, 97-110.
- Jackson, D.D.. (1979). The use of a priori data to resolve non-uniqueness in linear inversion, *Geophys. J. R. Astron. Soc* **57**, 137-158.
- Jackson, D.D., and Matsu'ura, M. (1985). A Bayesian approach to nonlinear inversion. *J. Geophys. Res.* **90**, 581-591.
- Jech, J. (1989). Seismic tomography in the Ostrava-Karvina mining region, in: *Seismicity in Mines*, (S.J. Gibowicz, ed.) Special Issue, *Pure Appl. Geophys.* **129**, 597-608.
- Jeffreys, H. (1932). An alternative to the rejection of observations. *Proc. R. Soc. Lond. Ser A*, **137**, 78-87.
- Jessell, M.W. and Lister, G.S. (1991). Strain localisation behaviour in experimental shear zones, *PAGEOHP*, **137**, 4, 421-438
- John, R.C.S. and Draper, N.R. (1975). D-optimality for regression designs: a review. *Technometrics*, **17**, 15-23.
- Johnson, N.L., and Kotz, S. (1972). *Distributions in Statistics: Continuous Multivariate Distributions*. John Wiley & Sons, New York.
- Jordan, T.H., and Sverdrup, K.A. (1981). Teleseismic location techniques and their application to the earthquake clusters in the south-central Pacific. *Bull. Seism. Soc. Am.* **71**, 1105-1130.
- Jordan T.H. and Franklin J.N.(1971). Optimal Solutions to a linear inverse problem in geophysics. *Proc. Natl. Acad. Sci.*, **68**, 291-293.
- Jost, M.L., and Herrmann, R.B. (1989). A student's guide to and review of moment tensors. *Seism. Res. Lett.* **60**, 37-57.
- Joughin, W. 1994. *Elastic Modelling and Quantitative Seismology to Evaluate Seismic Hazard on a Dyke*. Master's Thesis, University of Witwatersrand, South Africa, 1994.
- Julian, B. and Gubbins, D. (1977). Three-dimensional seismic ray tracing, *J. Geophys. Res.*, **43**, 95-114.
- Kagan, Y.Y. (1994). Observational evidence for earthquakes as a nonlinear dynamic process. *Physica D.*, **43**.
- Kagan, Y.Y. and Knopoff, L. (1985a). The first order statistical moment of the seismic moment tensor. *Geophys. J.R. Astron. Soc.*, **81**, 429-444.
- Kagan, Y.Y. and Knopoff, L. (1985b). The two-point correlation function of the seismic moment tensor. *Geophys. J.R. Astron. Soc.*, **83**, 637-656.
- Kagan, Y.Y., and Knopoff, L. (1980b). Dependence of seismicity on depth. *Bull. Seism. Soc. Am.* **70**, 1811-1822.
- Kagan, Y.Y., and Knopoff, L. (1981). Stochastic synthesis of earthquake catalogs. *J. Geophys. Res.*, **86**, 2853-2862.
- Kagan, Y.Y., and Knopoff, L. (1980a). Spatial distribution of earthquakes: the two-point correlation function. *Geophys. J.R. Astron. Soc.*, **62**, 303-320.
- Kagan, Y.Y., and Knopoff, L. (1987a). Statistical short-term earthquake

- prediction. *Science*, **236**, 1563-1567.
- Kagan, Y.Y., and Knopoff, L. (1987b). Random stress and earthquake statistics: time dependence. *Geophys. J.R. Astron. Soc.*, **88**, 723-731.
- Kagan, Y.Y. (1991a). Likelihood analysis of earthquake catalogues. *Geophys. J. Int.*, **106**, 135-148.
- Kagan, Y.Y. (1991b). Seismic moment distribution. *Geophys. J. Int.*, **106**, 123-134.
- Kagan, Y.Y., and Knopoff, L. (1978). Statistical study of the occurrence of shallow earthquakes. *Geophys. J.R. Astron. Soc.*, **55**, 67-86.
- Kagan, Y.Y., and Jackson, D.D. (1991). Long-term earthquake clustering. *Geophys. J. Int.*, **104**, 117-133.
- Kagan, Y.Y. (1994). Observational evidence for earthquakes as a nonlinear dynamic process. Preprint. *Physica D*, 32.
- Kanamori, H. (1977). The energy release in great earthquakes. *J. Geophys. Res.*, **82**, 2981-2987.
- Kanamori, H., and Anderson, D.L. (1975). Theoretical basis of some empirical relations in seismology. *Bull. Seism. Soc. Am.*, **65**, 1073-1096.
- Kato, N., Yamamoto, K., Yamamoto, H. and Hirasawa, T. (1992). Strain rate effect on frictional strength and the slip nucleation process. *Tectonophysics*, **211**, 269-282.
- Keilis-Borok, V.I. (1990). Introduction: Non-linear systems in the problem of earthquake prediction. *Phys. Earth and Planet. Inter.*, Special Issue: *Intermediate-Term Earthquake Prediction: Models, Algorithms, Worldwide Tests*. (V.I. Keilis-Borok, ed.). 1-7.
- Keilis-Borok, V.I., and Kossobokov, V.G. (1990). Premonitory activation of earthquake flow: algorithm M8. *Phys. Earth and Planet. Inter.*, Special Issue: *Intermediate-Term Earthquake Prediction: Models, Algorithms, Worldwide Tests*. (V.I. Keilis-Borok, ed.), 73-83.
- Keilis-Borok, V.I., and Rotwain, I.M. (1990). Diagnosis of time increased probability of strong earthquakes in different regions of the world. *Phys. Earth and Planet. Inter.*, Special Issue: *Intermediate-Term Earthquake Prediction: Models, Algorithms, Worldwide Tests*. (V.I. Keilis-Borok, ed.), 57-72.
- Kijko, A. (1977). An algorithm for the optimum distribution of a regional seismic network. *Pure Appl. Geophys.* **115**, 999-1009.
- Kijko, A. (1980). Statistical test of mutual dependence of seismic activities in two adjacent regions. *Publ. Inst. Geophys. Pol. Acad. Sci. A-10*, (**142**), 125-133.
- Kijko, A., Stankiewicz, T., and Krol, M. (1986). Relative location of mining events. *Przegl. Gorni.* **10**, 219-223. (In Pol.; Engl. abstr.)
- Kijko, A., and Sellevoll, M.A. (1989). Estimation of earthquake hazard parameters from incomplete data files. Part I. Utilization of extreme and complete catalogs with different threshold magnitudes. *Bull. Seism.*

- Soc. Am.* **79**, 645-654.
- Kijko, A. (1993). *Seismological outliers: L_1 or adaptive L_p norm application*. Internal Report. ISS International, Welkom, South Africa. Report Id. ISS/SR/7/VER1
- Kijko, A., Sciocatti, M. (1993). *Optimum spatial distribution of seismic stations in mines*. Internal Report. ISS International, Welkom, South Africa. Report Id. ISS/SR/11/VER1
- Kijko, A. (1994). *Seismological outliers: L_1 or adaptive L_p norm application*. *Bull. Seism. Soc. Am.* **84**, 473-477.
- Kijko, A., Sciocatti, M. (1995). *Optimal spatial distribution of seismic stations in mines*. *Int. J. Rock Mech. and Mining Soc.* **32**, 607-615.
- King, G. (1983). *The accommodation of large strains in the upper lithosphere of the Earth and other solids by self-similar fault systems: the geometrical origin of b-value*. *Pure Appl. Geophys.*, **121**, 761-815.
- Knopoff, L., and Kagan, Y. (1977). *Analysis of the theory of extremes as applied to earthquake problems*. *J. Geophys. Res.*, 5647-5657.
- Koch, M. (1985). *Nonlinear inversion of local seismic travel times for the simultaneous determination of the 3D-velocity structure and hypocenters - application to the seismic zone Vrancea*. *J. Geophys.* **56**, 160-173.
- Korvin, G. (1992). *Fractal Models in the Earth Sciences*. Elsevier, Amsterdam.
- Kostrov, B.V. (1974). *Seismic moment and energy of earthquakes and seismic flow of rock*. *Izv. Phys. Solid Earth*, **13**, 13-21.
- Kostrov, B.V. and Das, S. (1988). *Principles of Earthquake Source Mechanics*. Cambridge University Press, Cambridge.
- Krajcinovic, D. and Mastilovic, S. (1995). *Some fundamental issues of damage mechanics*. *Mechanics of Materials*, **21**, 217 - 230.
- Kuge, K. and Honkura, Y. (1986). *Estimation of the probability of earthquake occurrence on the basis of logistic models: high probability of an earthquake of $M \geq 6.5$ near the arc Junction off northeast Japan*. *Geophys. Res. Letters*, **13**, 709-712.
- Kumar P., Fougoula-Georgiu, E. - *Wavelet analysis in Geophysics: An Introduction*, in: *Wavelets in Geophysics, Wavelet Analysis and Its Applications*. (ed. Fougoula-Georgiu E. & Kumar P.) Academic Press, New York, 1994.
- Labuz, J.F., Shah, S.P. and Dowding, C.H. (1985). *Experimental analysis of crack propagation in granite*. *Int. J. Rock Mech. & Min. Sci. & Geomech. Abstr.*, **22**, 85-98.
- Lambare, G., Lucio, P.S. and Hanyga, A. (1994). *2-D multivalued traveltime and amplitude maps by a uniform sampling of the ray field*. Submitted to *Geophys. J. Int.*

- Lanczos, C. (1961). *Linear Differential Operators*. D. Van Nostrand, London.
- Lasocki, S. (1993). Statistical short-term prediction in mining induced seismicity. In: *Rockbursts and Seismicity in Mines, Proceedings of the 3th International Symposium on Rockbursts and Seismicity in Mines*, Kingston, Ontario, Canada, 16-18 August 1993, R.P. Young (ed.), 211-216, Rotterdam, Balkema.
- Lawrence, D. (1984). Seismicity in the Orange Free State Gold-mining District. In: *Proceedings of the 1st international Congress on Rockbursts and Seismicity in Mines*, (Gay, N.C. and Wainwright, eds.), Symp. Ser. No. 6, 121-130. S. Afr. Inst. Min. Metal., Johannesburg.
- Lawson, C.L. and Hanson, D.J.(1974). *Solving least squares problems*. Prentice Hall, Englewood Cliffs, New Jersey.
- Lee, W.H.K., and Stewart, S.W. (1981). *Principles and Applications of Microearthquake Networks*, Academic Press, New York.
- Lees, J.M., and Crosson, R.S.. (1989). Tomographic inversion for the three-dimensional velocity structure at Mount St. Helens using earthquake data. *J. Geophys. Res.* **94**, 5716-5728.
- Lehner, F.K., Li, V.C., and Rice, J.R. (1981). Stress diffusion along rupturing plate boundaries. *J. Geophys. Res.*, **86**, 6155-6169.
- Lienert, B.R., Berg, E., and Frazer, L.N. (1986). Hypocentre: An earthquake location method using centered, scaled, and adaptively damped least squares. *Bull. Seism. Soc. Am.* **76**, 771-783.
- Lilly, J.M. and Park, J. (1995). Multiwavelet spectral and polarization analyses of seismic records, *Geophys. J. Int.*, **122**, 1001-1021.
- Liptzer, R.S., and Shiryaev, A.N. (1978). *Statistics of Random Processes, Part II*. Springer-Verlag, Berlin.
- Lucio, P.S., Lambare, G. and Hanyga, A. (1995). 3-D multivalued dynamic ray tracing for migration/inversion. *Proc.SPIE*, San Diego, California, **2569**.
- Madariaga, R. (1983). Earthquake Source Theory: a Review. In: *Earthquakes: Observation, theory and interpretation*. Kanamori, H. and E. Boschi (eds), North Holland.
- Madariaga, R. (1973). On the relation between seismic moment and stress drop in the presence of stress and strength heterogeneity. *J. Geophys. Res.*, **84**, 2243-2250.
- Magotra, N.; Ahmed, N. and Chael, E.(1987). Single station seismic event detection and location. *IEEE Trans. Geoscience Remote Sensing*, **27**, 15-23.
- Main, J.G., Meredith, P.H. and Sammonds, P.R. (1992). Temporal variations in seismic event rate and b-values from stress corrosion constitutive laws. *Tectonophysics*, **211**, 233-246.
- Main, I.G. and Burton, P.W. (1984). Information theory and the earthquake

- frequency- magnitude distribution. *Bull. Seism. Soc. Am.*, **74**, 1409-1426.
- Mandelbrot, B.B. (1989). Multifractal measures, especially for the geophysicist. *Pure Appl. Geophys.*, **131**, 5-42.
- Mandelbrot, B.B. (1982). *The Fractal Geometry of Nature*. Freeman, San Francisco.
- Mantovani, E., Mucciarelli, M., and Alberto, D. (1987). Evidence of interrelation between the seismicity of the southern Apennines and southern Dinarides. *Phys. Earth Planet. Interiors* **49**, 259-263.
- Marquardt, D.W. (1963). An algorithm for least-squares estimation of non-linear parameters. *J. Soc. Appl. Math.* **11**, 431-441.
- Matsumura, S. (1984). A one-parameter expression of seismicity patterns in space and time, *Bull. Seism. Soc. Am.* **74**, 2529-2576.
- Maxwell, S.C., and Young, R.P., (1993a). Associations between temporal velocity changes and induced seismicity, *Geophys. Res. Lett.*, **20**, 2929-2932.
- Maxwell, S.C., and Young, R.P., (1993b). A comparison between active source and passive source images. *Bull. Seismo. Soc. Am.*, **83**, 1814-1831.
- Maxwell, S.C., and Young, R.P.. (1994). Application of seismic tomography to induced seismicity investigations. Rock Mechanics in Petroleum Engineering, *Proceedings of Eurock '94*, Balkema, Rotterdam.
- Maxwell, S.C., and Young, R.P., 1996, Seismic imaging of rock mass responses to excavation. *Int. J. Rock Mech. Min. Sc.*; in press.
- McGarr, A. (1976). Seismic moments and volume change. *J. Geophys. Res.* **81**, 1487-1494.
- McGarr, A. (1993). Keynote address: Factors influencing the strong ground motion from mining-induced tremors. *Proceedings 3rd International Symposium on Rockbursts and Seismicity in Mines*, Balkema Rotterdam.
- McGarr, A., (1994). Some comparisons between mining-induced and laboratory earthquakes. *Abstracts of the 89th Annual Meeting, Seismological Society of America*
- McLellan, J.M., Parks, T.W. and Rabinek, L.R. (1973). A Computer Program for Designing Optimum FIR Linear Phase Digital Filters. *IEEE Trans. on Audio and Electroacoustics*, **A4-31**, No.6, 506-576, December 1973.
- Mendecki, A.J. (1981). Methods of the joint hypocentre location for mining tremors and determination of parameters of velocity anisotropy, Ph.D Thesis, Silesian Technical Univ. Gliwice, Poland (In Pol.)
- Mendecki, A.J. (1985). An Attempt to Estimate Seismic Hazard in the AAC Gold Mines Areas. Internal Report, AAC Research and Development Services, Rock Mechanics Department, Welkom, 1-25.
- Mendecki, A.J. and van Aswegen, G. (1986). A Method for the Optimal Design of Mine Seismic Networks in Respect to Location Errors and

- Its Application, Research Report, AAC Research and Development Services, Rock Mechanics Department, 56.
- Mendecki, A.J. (1987). Rock mass anisotropy modelling by inversion of mine tremor data, in *Proceedings of 6th International Congress on Rock Mechanics*, (G. Herget and S. Vongpaisal, eds.), 1141-1144. Balkema, Rotterdam.
- Mendecki, A.J., van Aswegen G., Brown, J.N.R. and Hewlett, P. (1990). The Welkom Seismological Network, *Proc. 2nd International Symposium on Rockburst and Seismicity in Mines*, Minneapolis. 367-377.
- Mendecki, A.J. (1990). *The Integrated Seismic System (ISS)*. Presented at the Seminar on Monitoring and Safety in Civil and Mining Engineering, June 1990. Nancy, France.
- Mendecki, A.J. (1993). Real Time Quantitative Seismology in Mines. Keynote Lecture. *Proceedings of the 3rd International Symposium on Rockburst and Seismicity in Mines*, (R.P. Young, ed.), 16-18 August, 1993, Kingston, Canada. Balkema, Rotterdam, 287-296.
- Mendecki, A.J. (1994). Quantitative Seismology and Rock Mass Stability. In: *Guide to Seismic Monitoring in Mines*, 1994 Edition, A.J. Mendecki (ed.), ISS International, Welkom, RSA.
- Mendecki, A.J., van Aswegen, G., Niewiadomski, J., Stankiewicz, T., Dzhafarov, A.H., Kijko, A., Sciocatti, M., Funk, C., Mountfort, M., Hewlett, P., Green, R.W.E., Brink, A., van Z., Finnie, G. (1994). Seismology for rockburst prevention, control and prediction. *Proc. SIMRAC/SAIMM Symposium*, Johannesburg, South Africa, September 1995.
- Menke, W., Lerner-Lam, A.L., Dubendorf, B. and Pacheco, J. (1990). Polarization and coherence of 5 to 30 Hz Seismic wave fields at hard rock site and their relevance to velocity heterogeneities in the crust. *Bull. Seism. Soc. Am.*, **80**, 430-449.
- Michael, A.J. (1987). Use of focal Mechanisms to determine stress: a control study. *J. Geophys. Res.*, **92**, 357 - 368.
- Michael, A.W. (1992). Initiation of seismicity remotely triggered by the Landers earthquake: where and when. (abstract), *EOS Supplement*, 1992 Fall Meeting, American Geophysical Union, 392-393.
- Milev, A.M., Spottiswoode, S.M. and Stewart, R.D. (in prep.) Automatic location of seismic event doublets by crosscorrelation criteria. Submitted *Bull. Seism. Soc. Am.* (1995).
- Mogi, K. (1983). *Earthquake prediction*, Academic Press, Tokyo.
- Molnar, P. (1979). Earthquake recurrence intervals and plate tectonics. *Bull. Seism. Soc. Am.*, 115-133.
- Molnar, P. (1983). Average regional strain due to slip on numerous faults of different orientations. *J. Geophys. Res.* , **88** B8, 6430 - 6432.
- Money, A.H., Affleck-Graves, J.H., Hart, M.L., Barr, G.D.I. (1982). The linear regression model: L_p norm estimation and the choice of p .

- Commun. Statist. - Computa.*, **11**, 89-109.
- Montalbetti, J.F. and Kanasevich, E.R. (1970). Enhancement of teleseismic body phases with a polarization filter. *Geophys. J. R. Astron. Soc.*, **21**, 413-416.
- Mróz, Z. (1985). Current problems and new directions in mechanics of geomaterials in *Mechanics of Geomaterials* Ed. Z. Bažant. John Wiley & Sons, Ltd.
- Moser, T.J. (1991). Shortest path calculation of seismic rays. *Geophysics*, **56**, 59-67.
- Mucciarelli, M., Alberto, D., and Mantovani, E. (1988). Earthquake forecasting in Southern Italy on the basis of logistic models. *Tectonophysics* **152**, 153-155.
- Mühlhaus, H.-B., Hobbs, B.E. and Ord, A. (1992). Evolution of fractal geometries in deforming material. In: *Rock Mechanics*, Tillerson and Wawersik (eds), Balkema, Rotterdam, 681-690.
- Nakanishi, I. and Yamaguchi, K. (1986). A numerical experiment on nonlinear image reconstruction from first-arrival times for two-dimensional island arc structure, *J. Phys. Earth.*, **34**, 195-201.
- Naude, F.C. (1994). Seismic Index: A method of illuminating hazardous areas on the mine. A case study for the sequence of events on 2 and 3 May 1994. Internal Report, Western Deep Levels, South Mine, May 1994.
- Nelder, J. and Mead, R. (1965). A simplex method for function minimization. *Computer J.* **7**, 308-312.
- Nelson, G.D. and Vidale, J. (1990). Earthquake locations by 3-D finite-difference traveltimes, *Bull. Seism. Soc. Am.* **80**, 295-410.
- Niazi, M. and Mortgat, C.P. (1983). Application of logistic models to earthquake forecasting. *Earthq. Predict. Res.*, **2**, 221-225.
- Niewiadomski, J. (1989). Application of singular value decomposition method for location of seismic events in mines. In: *Seismicity in Mines* (S.J. Gibowicz, ed.), Special Issue, *Pure Appl. Geophys.* **129**, 553-570.
- Nolet, G. (1987). *Seismic Tomography*. (Reidel, Boston).
- Ogata, Y. (1988). Statistical models for earthquake occurrences and residual analysis for point processes. *J. Amer. Statist. Assoc.*, **83**, 9-27.
- Ogata, Y. (1994). Seismological applications of statistical methods for point-process modelling. In: *Proceedings of the First US/Japan Conference on the Frontiers of Statistical Modelling: An Informational Approach*, (H. Bozdogan, ed.), 1994 Kluwer Academic Publishers, 137-163.
- Ogata, Y., and Akaike, H. (1982). On linear intensity models for mixed doubly stochastic Poisson and self-exciting point processes. *J. Royal Stat. Soc. B*, **44**, 102-107.
- Ohnaka, M. (1983). Acoustic emission during creep of brittle rock. *Int. J. Rock Mech. Min. Sci. & Geomech. Abstr.*, **20**, 3, 121-134.

- Olsson, W.A. (1992). The formation of a yield-surface vertex in rock, In: Tillerson and Wawersik (eds), *Rock Mechanics*, Balkema, Rotterdam, 701-705.
- Omori, F. (1895). On the after-shocks of earthquakes. *J. Coll. Sci.*, Tokyo Imp. Univ., 7, 111 - 200
- Onescu, M.C., and Apolozan, L. (1984). The earthquake sequence of Romnicu Sarat, Romania, of 21-22 February 1983. *Acta Geophys. Pol.* 32, 231-238.
- Ortlepp, W.D. (1984). Rockbursts in South African gold mines: a phenomenological view. *Proceedings 1st International Symposium on Rockbursts and Seismicity in Mines*, Johannesburg.
- Ortlepp, W.D. (1984). High ground displacement velocities associated with rockburst damage. In: Young, R P (ed.) *Rockbursts and Seismicity in Mines*. AA Balkmea, Rotterdam, 449.
- Page, R. (1968). Aftershocks and microaftershocks of the great Alaska earthquake. *Bull. Seism. Soc. Am.* 58, 1131-1168.
- Paige, C.C., and Saunders, M.A.. (1982). LSQR: An algorithm for sparse linear equations and sparse least squares. *ACM Transactions on Mathematical Software*, 8, 43-71, 195-209.
- Park, J., Vernon III, F.L. and Lindberg, C.R. (1987a). Frequency dependent polarization analysis of high-frequency seismograms. *J. Geophys. Res.*, 92, 12664-12674.
- Park, J., Lindberg, C.R. and Vernon III, F.L. (1987b). Multitaper spectral analysis of high-frequency seismograms. *J. Geophys. Res.*, 92, 12675-12684.
- Parker R.L.(1972). Inverse theory with grossly inadequate data. *Geophys. J.*, 29, 123-138.
- Pavlis, G.L. and Booker, J. (1980). The mixed discrete continuous inverse: problem: application to the simultaneous determination of earthquake hypocentres and velocity structure. *J. Geophys. Res.* 85 4801-4810.
- Pavlis, G.L. (1986). Appraising earthquake hypocenter location errors: A complete, practical approach for single event locations. *Bull. Seism. Soc. Am.* 76, 1699-1717.
- Pearson, G.E. (1956). General theory of elastic stability. *Quart. Appl. Math.*, 14, 133-144.
- Peterson, D.A. and Simser B.P. (in prep.) Source mechanisms of mining induced seismic events at Brunswick Mine. Submitted to: 4th International Symposium for Rockbursts and Seismicity, Krakow, Poland, 1997.
- Pereyra, V., Lee, W.H.K. and Keller, H.B. (1980). Solving two-point seismic ray tracing problems in a heterogeneous medium. Part 1. A general adaptive finite difference method, *Bull. Seism. Soc. Am.*, 70,79-99.
- Podvin, P. and Lecomte, I. (1991). Finite difference computation of travel times in very contrasted velocity models: a massively parallel approach

- and its associated tools, *Geophys. J. Int.*, **105**, 271-284.
- Podvin, P. (1992). Finite difference computation of multivalued traveltimes, *EAGE annual meeting*, Paris, 502-503.
- Poupinet, G., Ellsworth W.L. and Frechet, J. (1984). Monitoring velocity variations in the crust using earthquake doublets: an application to the Calaveras Fault, California, *J. Geophys. Res.* **89**, 5719-5731.
- Plešinger, A., Hellweg, M. and Seidl, D. (1986). Interactive high-resolution polarization analysis of broadband seismograms. *Geophys.* **59** 129-139.
- Press, W.H., Flannery, B.P., Teukovsky, S.A. and Vetterling, W.T. (1987). *Numerical Recipes in C*. Cambridge University Press, New York.
- Press, W.H., Flannery, B.P., Teukolsky, S.A., and Vetterling, W.T. (1989). *Numerical Recipes: The Art of Scientific Computing*. Cambridge University Press, New York.
- Prothero, W.A., Taylor, W.J. and Eickemeyer, J.A. (1988). A fast, two point, three dimensional raytracing algorithm using a simple step search method. *Bull. Seism. Soc. Am.* **78**, 1190-1198.
- Prugger, A.F., and Gendzwill, D.J. (1988). Microearthquake location: A non-linear approach that makes use of a simplex stepping procedure. *Bull. Seism. Soc. Am.* **78**, 799-815.
- Qin, F., Luo, Y., Olsen, K.B., Cai, W. and Schuster, G.T. (1992). Finite-difference solution of the eikonal equation along expanding wavefronts, *Geophysics*, **57**, 479-487.
- Rabinowitz, N., and Kulhánek, O. (1988). Application of non-linear algorithm to teleseismic locations using P-wave readings from the Swedish seismographic network. *Phys. Earth Planet. Interiors* **50**, 111-115.
- Rabinowitz, N. (1988). Microearthquake location by means of nonlinear simplex procedure. *Bull. Seism. Soc. Am.* **78**, 380-384.
- Radu, S. (1995). Order and chaos in nuclear and metal cluster deformation. PhD Thesis, University of the Witwatersrand, South Africa.
- Reasenberg, P.A., Hill, D.P., Michael, A.J. Simpson, R.W. Ellsworth, W.L. Walter, S., Johnston, M, Smith, R., Nava, S.J., Arabasz, W.J., Pechmann, J.C., Gomberg, J., Brune, J.N., de Polo, D., Beroza, G., Davis, S.D., Zollweg, J. (1992). Remote seismicity triggered by the M7.5 Landers, California earthquake of June 28, 1992. (abstract), *EOS Supplement*, 1992, 1992 Fall Meeting American Geophysical Union, 392.
- Reiner, M. (1969). *Deformation, strain and flow*. H.K. Lewis, London.
- Rice, T.R. and White, T.S. (1964). Norms for smoothing and estimation. *SIAM Rev.*, **6**, 243-256.
- Rice, J.R. (1993). Spatio-temporal complexity of slip on a fault. *J. Geophys. Res.*, **98**, 9885-9907.
- Rice, J.R. (1980). The mechanics of earthquake rupture. In: *Physics of the Earth's Interior*, (A. Dziewonski, and E. Boschi, eds.) Proceedings of the International School of Physics "Enrico

- Fermi", Course 78, 1979. Italian Physical Society, North- Holland Publ. Co., 555-649.
- Rice, J.R. (1992). Fault stress states, pore pressure distributions, and the weakness of the San Andreas fault. In: *Fault Mechanics and Transport Properties of Rocks*, (B. Evans, and T. Wong, eds.), Academic Press, Orlando, Florida, 475-503.
- Richter, C.F. (1935). An instrumental earthquake magnitude scale. *Bull. Seism. Soc. Am.*, **25**, 1-32.
- Rikitake, T. (1976). *Earthquake Prediction*. Elsevier, New York.
- Riznichenko, Yu, V. (1946). Geometrical seismics of layered media, Trudy Inst. Theor. Geophysics, Vol II, Izd, AN SSSR, Moscow (in Russian).
- Roberts, R.G., Christoffersson, A. and Cassidy, F.(1989). Real-time event detection, phase identification and source location using single station three-component seismic data. *Geophys. J.*, **97**, 471-480.
- Robson, D.S., and Whitlock, J.H. (1964). Estimation of a truncation point. *Biometrika* **51**, 33-39.
- Rubin, I. (1972). Regular point processes and their detection. *IEEE Trans. Inform. Theory*, **IT-18**, 547-557.
- Rudnicki, J.W. and Rice, J. (1975). Conditions for the localization of deformation in pressure sensitive dilatant materials. *J. Mech. Phys. Solids*, **23**, 371-394.
- Rudnicki, J.W. (1977). The Inception of Faulting in a Rock Mass with a Weakened Zone. *J. Geophys. Res.*, 844-854.
- Rudnicki, J.W. and Freund, L.B. (1981). On energy radiation from seismic sources. *Bull. Seism. Soc. Am.*, **71**, 583-595.
- Rudnicki, J.W. (1988). Physical models of earthquake instability. *PAGEOPH.*, **126**, 531-554.
- Sadowskiy, M.A., Golubeva, T.V. Pisarenko, V.F. and Shnirman, M.G. (1984). Characteristic dimensions of rock and hierarchical properties of seismicity. *Izvestia, Earth Physics*, **20**, 87-96.
- Sambridge, M. and Galagher, K. (1993). Earthquake hypocentre location using genetic algorithms, *Bull Seism. Soc. Am.* **83** 1467-1491.
- Samson, J.C.(1977). Matrix and Stokes vector representation of detectors for polarized waveforms: theory, with some applications to teleseismic waves. *Geophys. J. R. Astron. Soc.*, **51**, 583-603.
- Samson, J.C. and Olson, J.V.(1980). Some comments on the description of polarization states of waves. *Geophys. J.*, **21**, 115-129.
- Savage, J.C. (1983). Equivalent strike-slip earthquake cycles in half-space and lithosphere-asthenosphere earth models. *J. Geophys. Res.*, **95**, 4873-4879.
- Savage, J.C. (1983). A dislocation model of strain accumulation and release at a subduction zone. *J. Geophys. Res.*, **88**, 4984-4996.
- Scholz, C.H., (1990). *The mechanics of earthquakes faulting*. Cambridge

- University Press.
- Shanks, J.L.(1967). Recursion Filters For Digital Processing. *Geophysics*, **32**, 33-51.
- Shi, Y., and Bolt, B.A. (1982). The standard error of the magnitude frequency b value, *Bull. Seism. Soc. Am.* **72**, 1677-1687.
- Silver, P. and Jordan, T. (1982). Optimal estimation of scalar seismic moment. *Geophys. J.R. Astron. Soc.*, **70**, 755 – 787.
- Singh, S.K., Rodriquez, M. and Esteva, L. (1983). Statistics of small earthquakes and frequency of large earthquakes along the Mexico subduction zone. *Bull. Seism. Soc. Am.*, **73**, 1779-1796.
- Sipkin, A.S., Lerner-Lam, A.L.(1992). Pulse-shape distortion introduced by broadband deconvolution. *Bull. Seism. Soc. Am.*, **82**, No.1, 248-258.
- Slepian, D. (1978). Prolate spheroidal wavefunctions, Fourier analysis and uncertainty, V, the discrete case. *Bell Syst. Tech. J.*, **57**, 1371-1429.
- Slunga, R., Norman, P., and Glans, A.C. (1984). Seismicity of Southern Sweden. *FOA Report C20543-T1*, National Defence Research Institute, Stockholm.
- Smalley, R.F., Jr., Chatelain, J.-L., Turcotte, D.L. and Prevot, P. (1987). A fractal approach to the clustering of earthquakes: application to the seismicity in the New Hebrides. *Bull. Seism. Soc. Am.*, **77**, 1368-1381.
- Spence, W. (1980). Relative epicenter determination using P- wave arrival-time differences. *Bull. Seism. Soc. Am.* **70**, 171-183.
- Spencer, C. and Gubbins, D. (1980). Travel-time inversion for simultaneous earthquake location and velocity structure determination in laterally varying media, *Geophys. J. R. Astron. Soc.* **63**, 95-116.
- Spendly, W., and Hest, G. (1965). Sequential application of simplex design in optimization and evolutionary operations. *Technometrics*, **4**, 441-461.
- Sposito, V.A., Hand, M.L., and Skarpness, B. (1983). On efficiency of using sample kurtosis in selecting optimal L_p estimators. *Commun. Statist. - Computa.* **12**, 265-272.
- Spudich, P.K.P. (1992). On the interference of absolute stress levels from seismic radiation. *Tectonophysics*, **211**, 99-106.
- Stewart, S.W. (1977). Real time detection and location of local seismic events in central California. *Bull. Seism. Soc. Am.* **67**, 433-452.
- Sun, Y. (1992). Computation of 2D multiple arrival travel timefields by an interpolative shooting method, *Expanded Abstracts of the 62-th SEG Annual Meeting* (New Orleans, 1992), 1320-1323
- Takens, F. (1984). *Proceedings of the Dynamical Systems and Bifurcation Conference, Groningen, 1984*. Springer, Berlin.
- Tang, C.A. and Hudson, J.A. (1993). Rock failure instability and related aspects of earthquake mechanisms. Submission to *Earthquake Engineering and Structural Dynamics*.

- Tarantola, A. (1987). *Inverse Problem Theory*. Elsevier, Amsterdam.
- Teisseyre, R. (1980a). Some remarks on the source mechanism of rockbursts in mines and on the possible source extension. *Acta Montana CSAV Praha*, **58**, 7-13.
- Teisseyre, R. (1980b). Earthquake premonitory sequence - dislocation processes and fracturing. *Boll. Geof. Teor. Appl.*, **XXII**, N88, 245-254.
- Thiran J.(1971). Recursive digital filters with maximally flat group delay. *IEEE Transactions of Circuit Theory*, **CT-18**, no. 6.
- Thomson, D. J. (1982). Spectral estimation and harmonic analysis. *IEEE Proc.* **70**, 1055-1096.
- Thorbjarnardottir, B.S. and Pechmann, J.C. (1987). Constraints on relative earthquake locations from crosscorrelation of waveforms, *Bull. Seism. Soc. Am.* **77**, 1626-1634.
- Thornburgh, H.R. (1930). Wavefront diagrams in seismic interpretation, *AAPG Bull.*, **14**,185-200
- Thurber, C.H. (1986). Analysis methods for kinematic data from local earthquakes, *Rev. Geophys.* **24**, 793-805.
- Thurber, C.H. (1985). Nonlinear earthquake location: Theory and examples. *Bull. Seism. Soc. Am.* **75**, 779-790.
- Thurber, C.H. and Aki, K. (1987). Three-dimensional seismic imaging, *Ann. Rev. Earth Planet. Sci.*, **15**, 115-139.
- Tinucci, J.P. and Spearing, A.J.S. (1993). Strategies for clamping faults and dykes in high seismicity tabular miningconditions. In: Young, R.P. (ed.) *Rockbursts and Seismicity in Mines*. A.A. Balkema, Rotterdam.
- Turcotte, D.L. (1992). *Fractals and Chaos in Geology and Geophysics*. Cambridge University Press, Cambridge, U.K.
- Turner, M.E. (1960). An heuristic estimation method. *Biometrics*, **16**, 299-301.
- Um, J. and Thurber, C.H. (1987). A fast algorithm for two-point seismic ray tracing, *Bull. Seism. Soc. Am.*, **77**, 972-986.
- Utsu, T. (1965). A method for determining the value of b on the formula $\log n = a - bM$ showing the magnitude-frequency relation for earthquakes, *Geophys. Bull.*, Hokkaido Univ. **13**, 99-103. (In Japan.; Engl. abstr.)
- van Aswegen, G. (1990). Fault stability in SA gold mines. In: Rossamint, H.P. (ed.) *Mechanics of jointed and faulted rock*. A.A. Balkema, Rotterdam.
- van Aswegen, G. and Butler, A. (1993). Applications of quantitative seismology in SA gold mines. *Proceedings 3rd International Symposium in Rockbursts and Seismicity in Mines*, Balkema, Rotterdam.
- van Aswegen, G. and Meijer, O. (1994). *The mechanisms of seismic events around faults in mines*. Proceedings of Eurock '94, Balkema, Rotterdam.
- Vere-Jones, D. (1994). Statistical models for earthquake occurrence: clusters,

- cycles and characteristic earthquakes. In: *Proceedings of the First US/Japan Conference on the Frontiers of Statistical Modeling: An Informational Approach*, (H. Bozdogan, ed.), 1994 Kluwer Academic Publishers, 105-136.
- Vere-Jones, D. (1977). Statistical theories for crack propagation. *Math. Geol.*, **9**, 455-481.
- Vere-Jones, D. and T. Ozaki (1982). Some examples of statistical inference applied to point process data. *Am. Inst. Stat. Math.*, **34**, 189-207.
- Vere-Jones, D. (1976). A branching model for crack propagation. *Pure Appl. Geophys.*, **114**, 711-726.
- Vermeer, P.A. and de Borst, R. (1984). *Non-associated plasticity for soils, concrete and rock*. Heron, **29**, 1-64.
- Vidale, J.E. (1986). Complex polarization analysis of particle motion. *Bull. Seism. Soc. Am.*, **76**, 1393-1405.
- Vidale, J. (1988). Finite-difference calculation of traveltimes, *Bull. Seism. Soc. Am.* **78**, 2062-2076.
- Vidale, J. (1990). Finite-difference calculation of traveltimes in 3D, *Geophysics*, **55**, 521-526.
- Vinje, V., Iversen, E. and Gjoystadl, H. (1993). Traveltime and amplitude estimation using wavefront construction, *Geophysics*, **58**, 1157-1166.
- Voight, B. (1989). A relation to describe rate-dependent material failure. *Science*, **243**, 200-203.
- Walcik, M.C. and Chael, E.P. (1990). Optimal backazimuth estimation for three-component recordings of seismic events. *Bull. Seism. Soc. Am.*, **81**, 643-666.
- Wesson, R.L. (1971). Travel-time inversion for laterally inhomogeneous crustal velocity models. *Bull. Seism. Soc. Am.*, **61**, 729-746.
- Willemann, R.J., (1993). Cluster analysis of seismic moment tensor orientations. *Geophys. J. Int.*, **115**, 617-634.
- Wolf, A., et al (1985). Determining Lyapunov exponents from a time series. *Physica D*, **16**, 285.
- Woźniakowski, H. (1977). Numerical stability for solving nonlinear equations, *Numer. Math* **27**, 373-390.
- Wu, S-C., Cornell, C.A., Winterstein, S.R (1994). Estimation of correlations among characteristic earthquakes. Preprint. *ICSZ, Stanford*, 9.
- Wyss, M. and Brune, J.N. (1971). Regional variations in source properties in Southern California estimated from the ratio of short-to-long period amplitudes. *Bull. Seism. Soc. Am.*, **61**, 1153 - 1167.
- Wyss, M. and Brune, J.N. (1968). Seismic moment, stress and source dynamics for earthquakes in the California - Nevada region. *J. Geophys. Res.*, **73**, 4681 - 4694.
- Xie, H. and Pariseau, W.G. (1993). Fractal character and mechanism of rock bursts. *J. Rock Mech. Sci. & Geomech. Abstr.*, **30**, 343-350.

- Xu, S., King, M.S., and Worthington, M.H. (1990). Elastic wave propagation and hydraulic properties of cracked rocks. In: *Mechanics of Jointed and Faulted Rock*. (Balkema, Rotterdam).
- Yamashita, T. and Ohnaka, M. (1991). Nucleation process of unstable rupture in the brittle regime: a theoretical approach based on experimentally inferred relations. *J. Geophys. Res.*, **96**, B5, 8351 - 9367.
- Youngs, R.R., and Coppersmith, K.J. (1985). Implications of fault slip rates and earthquake recurrence models to probabilistic seismic hazard estimates. *Bull. Seism. Soc. Am.*, **75**, 939-964.
- Yukutake, H. (1992). Fracture nucleation process in intact rock. *Tectonophysics*, **211**, 247-257.
- Zimmerman, R.W., and King, M.S. (1985). Propagation of acoustic waves through a cracked rock. *Proc. 26th U.S. Symposium on Rock Mechanics*, Rapid City, SD, 739-745.
- Zubelewicz, A. and Mroz, Z. (1983). Numerical simulation of rock burst processes treated as problems of dynamic instability. *Rock Mechanics and Rock Engineering*, **16**, 253-274.